Analysis of Alkali Roasting and Leaching on the Extraction of Metallic Values from Titaniferous Minerals

Stephen Tafadzwa Parirenyatwa

Submitted in accordance with the requirements for the degree of
Doctor of Philosophy

The University of Leeds
School of Chemical and Process Engineering

September, 2018

The candidate confirms that the work submitted is his own and that appropriate credit has been given where reference has been made to the work of others.

All the results that are presented in the papers were obtained and analysed by the author of the thesis. The author of this thesis wrote the draft of the papers. The supervisor (Animesh Jha) revised the papers before sending them for publication.

Acknowledgements

I would like to express my gratitude to my supervisor, Professor Animesh Jha, for his guidance and support throughout the research project. I am grateful to him for making it possible for me to pursue my PhD studies. I am highly appreciative of the financial support provided by the Institute of Materials, Minerals and Mining (IOM^3) and Fodere Titanium.

I would like to thank the following colleagues for their friendship and support throughout my PhD studies: Dr Sergio Sanchez, Terence Makanyire, Kwabena Offeh Gyimah and especially Lidia Escudero Castejon. I am grateful to Dr Yotamu Hara for the guidance and help he provided during the early part of the project

I am thankful to Mr M. Javed for technical support, Mr S. Micklethwaite and Mr J. Harrington for assistance with SEM and Mr. S. Lloyd for support with XRF and chemical analysis.

I am hugely appreciative of the support and encouragement of my family and friends throughout my studies, particularly Lucy.

Finally, I give thanks to God for this opportunity and for seeing me through.

Abstract

A novel process for the recovery of iron, titanium dioxide and vanadium pentoxide from titanium-bearing waste materials has been developed. The methodology has been designed to address the environmental legacy of tens of million tonnes of waste from vanadium oxide extraction that has accumulated in South Africa and around the world. Simultaneous extraction of the metallic values from the waste materials is not achievable with the existing methods.

Recovery of vanadium oxide dissolved in the titaniferous magnetite (TM) matrix is achieved by two processes that generate two distinct waste materials. Alkali roasting-water leach process solely extracts V_2O_5 yielding a roast-calcine tailings (Iron-rich tailing, T1). A low-grade TiO_2 slag (TiO_2 rich, T2) is discarded during co-production of steel and vanadium slag from TM.

T1 and T2 were characterised using scanning electron microscopy (SEM), X-ray diffraction (XRD) and X-ray fluorescence (XRF) to understand the varied and complex mineralogy.

The roast-calcine tailings had a total iron content of 49.7 weight.%, 0.3 weight.% V_2O_5 and contained up to 11 weight.% of TiO_2. Vanadium ions are disseminated in residual magnetite, sodium aluminosilicates and the hematite-ilmenite solid solution observed in the material. By comparison, the low grade TiO_2 slag was composed of up to 35 weight.% TiO_2 and 1.2 weight.% V_2O_5. Varied distribution of vanadium ions in refractory magnesium aluminate and magnesium dititanate and the presence of significant quantities of gangue materials makes the state-of-the art TiO_2 and V_2O_5 extraction technologies unsuitable.

Thermodynamic considerations were adopted for analysing the role of alkali carbonate in the physico-chemical separation of the metallic values.

A summary flowsheet is presented below broadly outlining the process steps. Carbothermic reduction in the presence of Na_2CO_3 was carried out on the roast-calcine tailings (T1) for extracting metallic iron, sodium titanate and water-soluble sodium vanadate in the 1073 K to 1323 K temperature range under reducing atmosphere. Wet magnetic separation of the reduced sample separated the metallic iron into a magnetic fraction, whereas the non-magnetic fraction was dominated by sodium titanate and residual gangue minerals with the sodium vanadate dissolved in the wash water. Water

leaching of the non-magnetic fraction was performed to enhance recovery of sodium vanadate and alkali carbonate.

The magnetic fraction was smelted at 1723 K to produce steel micro-alloyed with vanadium and a titania-slag. 0.5M H_2SO_4 leaching of the non-magnetic fraction was performed to upgrade the TiO_2 content to ca. 75 weight.%. T1 acid leach residue was roasted with $NaHSO_4$ at 923 K followed by water leaching to remove water-soluble sulphated impurities. A TiO_2 residue of up to 92 weight.% was obtained after water leaching.

Although the TiO_2 rich (T2) waste contained a limited amount of iron, up to 10 weight.%, the material was reduced in the presence of Na_2CO_3 at above 1223 K to decompose phases hosting vanadium ions and form water- soluble sodium vanadate. The reduced product was water leached to dissolve water-soluble compounds for recovery by selective precipitation. Alumina (ca. 75 weight.% Al_2O_3) was precipitated from the water leach solution after lowering the pH to 8. Addition of ammonium sulphate to the solution followed by solution pH adjustment to 5 resulted in ammonium metavanadate precipitation, which was calcined at 723 K to give vanadium pentoxide of 93 weight.%. The residual solids from water leaching were leached in 0.5M HCl to yield a $CaTiO_3$-rich residue.

The calcium titanate residue was treated using two different methods:

The first involved roasting the calcium titanate residue with $NaHSO_4$ followed by water leaching. As T2 material contained a limited amount of iron it was necessary to add $FeSO_4$ during the water leaching step to ensure dissolution of $CaSO_4$ in order to yield an 86 weight.% TiO_2 residue.

The second method utilised sulphuric acid baking at 473 K of the titanate residue to form a porous cake consisting of water-soluble $TiOSO_4$ and $CaSO_4$. Ambient temperature water leaching of the porous cake was carried out to dissolve $TiOSO_4$ and separate it from the $CaSO_4$-rich solid residue. Titanium dioxide hydrate was precipitated from the $TiOSO_4$ solution by hydrolysis at 353 K. The TiO_2 precipitate was calcined to produce synthetic rutile with up to 97 weight.% TiO_2.

The flowsheet developed for T2 treatment has formed the basis of a pilot-scale plant designed to scale-up the technology and valorise the waste material.

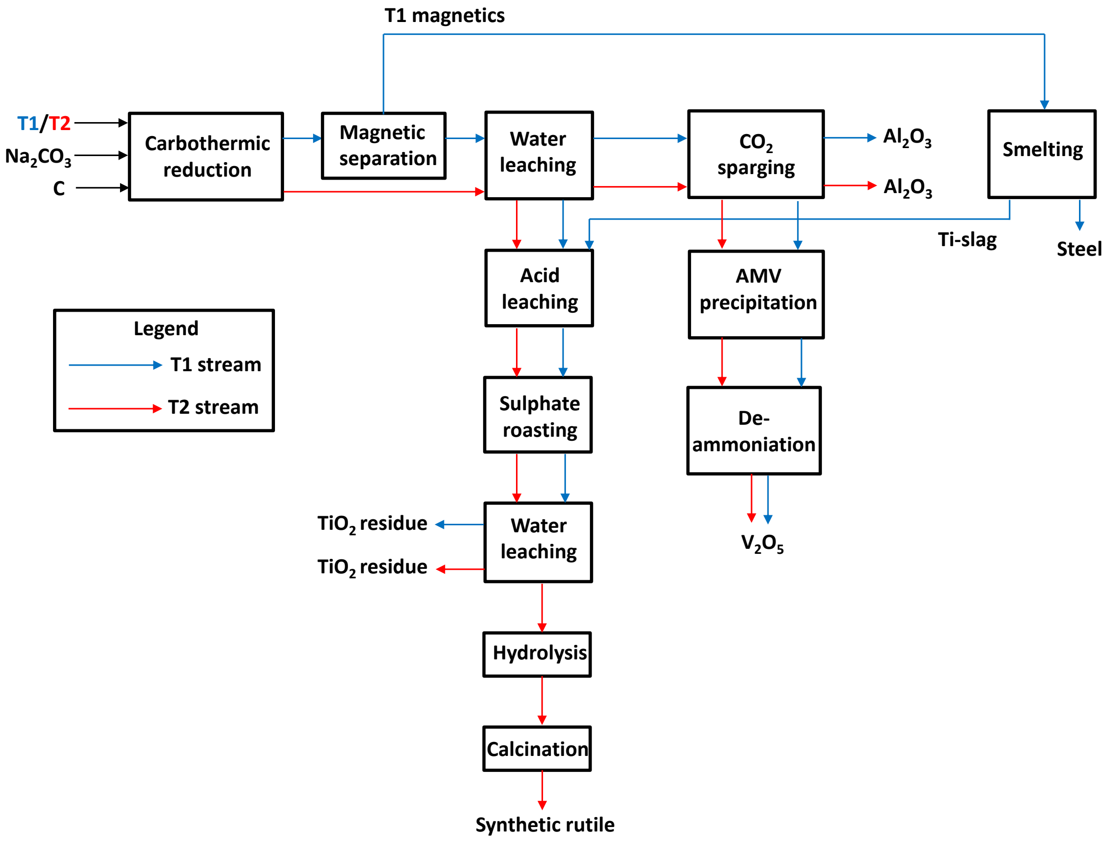
T1 magnetics
T1/T2
Na_2CO_3
C
Carbothermic reduction
Magnetic separation
Water leaching
CO_2 sparging
Al_2O_3
Al_2O_3
Smelting
Ti-slag
Steel
Acid leaching
AMV precipitation
Legend
T1 stream
T2 stream
Sulphate roasting
De-ammoniation
TiO_2 residue
TiO_2 residue
Water leaching
V_2O_5
Hydrolysis
Calcination
Synthetic rutile

Table of Contents

List of Figures

List of Tables

List of Publications

The list of journal and conference paper published are presented below.

- **Parirenyatwa, Stephen, Escudero-Castejon, Lidia, Sanchez-Segado, Sergio, Hara, Yotamu and Jha, Animesh (2015) 'Comparative study of alkali roasting and leaching of chromite ores and titaniferous minerals'. *Hydrometallurgy*.** https://doi.org/10.1016/j.hydromet.2015.08.002. This publication was written in collaboration with Ms. Lidia Escudero-Castejon. Results from alkali roasting in air of ilmenite mineral and chromite ore with NaOH and KOH are evaluated in this paper.

- Parirenyatwa, S., Escudero-Castejon, L., Sanchez-Segado, S., Hara, Y. and Jha, A., 2017. An Investigation on the Kinetics and Mechanism of Alkali Reduction of Mine Waste Containing Titaniferous Minerals for the Recovery of Metals. In *Applications of Process Engineering Principles in Materials Processing, Energy and Environmental Technologies* (pp. 465-474). Springer, Cham. **https://doi.org/10.1007/978-3-319-51091-0_45. Conference paper presented at TMS 2017: 146th Annual Meeting & Exhibition, February 26-March 2, 2017, San Diego, California, USA. The paper discusses the reductive alkaline roasting kinetics and mechanism of T1 material and the segregation of metallic values.**

- Parirenyatwa, S., Escudero-Castejon, L., Sanchez-Segado, S., Hara, Y. and Jha, A., 2016. Investigation of Molten Salt Phase Formation during Alkali Roasting of Titaniferous Minerals with Sodium and Potassium Hydroxide. *Journal for Manufacturing Science and Production*, *16*(4), pp.299-308. **https://doi.org/10.1515/jmsp-2016-0025. An extended article based on a conference paper presented in the Advances in Molten Slags, Fluxes, and Salts: Proceedings of the 10th International Conference on Molten Slags, Fluxes and Salts. 10th International Conference on Molten Slags, Fluxes and Salts, 22-25 May 2016, Seattle, Washington, USA. The article characterise the alkali-rich liquid phase formed during oxidative roasting and determines its impact on the physical chemistry of alkali roasting. Phase equilibria of the Na/K-Fe-Ti-O systems were calculated and compared with experimental results.**

Potential journal articles

- Thermal decomposition and kinetics of Bomar ilmenite
- Physical chemistry of titaniferous magnetite thermal decomposition
- Influence of alkali on phase transformation in titanium – vanadium slag under different atmospheres

Filed patent

Process: Priority date: 04-03-2015 US20180044762A1

The patent relates to the process for recovery of metallic values from titanium-bearing materials using reductive alkali roasting described in this report.

1 Introduction

1.1 Background

Titanium

Titanium can be founded in nature in a large variety of minerals of which ilmenite ($FeTiO_3$), rutile (TiO_2), anatase (TiO_2), brookite (TiO_2), perovskite ($CaTiO_3$) and leucoxene ($Fe_2O_3 \cdot TiO_2$) are the most representative [1]. Ilmenite and rutile are the two most important minerals and are commonly present in igneous and metamorphic rocks. Ilmenite concentrates are sourced from either primary rock deposits or sedimentary deposits.

Primary rock deposits are less commercially exploited largely due to the intergrowth of ilmenite with magnetite in these deposits. As ilmenite is often found with hematite and magnetite the TiO_2 levels can be relatively low and recovery of free ilmenite be made challenging, explaining why these deposits are not commercially exploited to a large degree [2]. A further complication is that rock deposits often have elevated levels of alkali earth oxides such as calcium oxide (CaO) and magnesium oxide (MgO) which if present during the chloride process form liquid calcium chloride ($CaCl_2$) and magnesium chloride ($MgCl_2$) ,respectively, which can lead to operational difficulties during the process [3].

Sedimentary deposits, also known as sands, are the main source of the TiO_2 – bearing feedstock including ilmenite and rutile. Sedimentary deposits are often associated with low mining costs and generally found on coastlines and in river beds where they can often be subjected to weathering that results in the concentration of TiO_2 [2].

Despite the demand for titanium metal from the energy and chemical industries being expected to increase during the next few years, the biggest market for titanium still resides as high purity TiO_2 for the pigment industry accounting for nearly 90% of the worldwide production, owing to its properties such as high refractive index and scattering power. Ti metal, weld fluxes and rods represent the remaining 10% of global production [2, 4]. Ilmenite is the main feedstock for the production of TiO_2 pigment via the sulphate process but increasingly the chloride process, which primarily uses rutile or high grade titanium slag, is being favoured owing to the fact that it appears to be superior in terms of cost and waste management, when compared to the sulphate process [5]. Due to limited supply of natural rutile and increasing usage of the chloride process, it has become necessary to produce synthetic rutile by upgrading ilmenite [6].

Vanadium

Titaniferous magnetite (TM), also referred to as titanomagnetite concentrate, typically containing 1 weight.% to 3 weight.% V_2O_5 is the most important source of vanadium, presently accounting for approximately 85% of the current world V_2O_5 production. Vanadium production is classified under three separate terms [7]:

1. Primary production involves extraction of solely vanadium oxide from titaniferous magnetite by alkali roast – water leach process, accounting for nearly 15% of supply.
2. Co-production occurs when vanadium oxides are recovered with other metallic values during the process. Manufacture of steel and vanadium slag from TM represents the principal source of vanadium. However, vanadium can be a co-product of phosphate, lead, uranium and bauxite ore processes. Co-production is responsible for 70 % of the output.
3. Secondary production includes extraction of vanadium oxide from industrial waste materials such as vanadium-bearing fly ash, petroleum residues, pig iron slag, and spent catalysts. These sources constitute the remaining 15% of vanadium production.

Approximately 90% of vanadium is consumed by the steel industry owing to its ability to enhance key properties including: weldability, toughness, ductility and corrosion resistance. Most vanadium is added to steel as ferrovanadium (FeV). Application as catalysts, chemicals and alloys comprises the remaining 10%. The high strength-to-weight ratio of vanadium-titanium alloys makes them important for the aerospace sector. Vanadium usage in the green technology area is expected to rise due to the vanadium redox flow battery [8].

1.2 Statement of the problem

The process waste from the vanadium extraction using the titanomagnetite concentrates in South Africa has accumulated over the years to more than 50 million tonnes. There are two types of waste products from the vanadium extraction plants: iron-rich tailing (T1) and low-grade TiO_2 slag (T2).

T1 is classed as a roast-calcine waste material from primary vanadium production. Titanomagnetite concentrates containing up to 3 weight.% V_2O_5 are subjected to alkali roasting in air to form water-soluble sodium vanadate ($NaVO_3$) that is extracted during the subsequent water leaching step. Significant quantities of tailings are generated since the remaining solids from water leaching are considered waste products. The 11 weight.% TiO_2 content precludes the material from blast furnace usage, while also being below titanium dioxide beneficiation process requirements. Residual vanadium ions in the tailings are present in the (3+) and (5+) states [9].

T2 is a low-grade TiO_2 slag material discarded during the co-production of steel and vanadium chemicals by Evraz Highveld Steel and Vanadium Ltd in South Africa. Titanomagnetite concentrates are pre-reduced in rotary kilns with the addition of fluxes followed by smelting in an electric arc furnaces. Majority of vanadium present in T2 is transferred into the molten pig iron, whereas TiO_2 is captured into the slag phase, due to the prevalent redox condition. Consequently, up to 1.2 weight.% V_2O_5 is found in the slag typically dissolved in complex and spinel phases.

T1 stockpile has accumulated to 12 million tonnes compared to 45 million tonnes of T2. Significant quantities of metallic values such as iron, titanium dioxide and vanadium pentoxide are contained within these materials presenting a significant commercial opportunity.

As a trace element vanadium is vital to humans, however, studies have indicated it is carcinogenic and toxic at elevated concentrations, to an extent where international agencies have classed vanadium as an environmental risk [10-13]. Increasing numbers of people are affected by vanadium pollution, particularly in South Africa, China, USA and Russia [14]. Vanadium is able to enter the environment from mine tailings along with processing emissions [15]. Pentavalent ions, such as those in T1, represent the most toxic form of the metal [7].

The current methods are either not suitable for extracting the metal constituents, or are not capable of simultaneously extracting each constituent from the waste material. This is because:

- Even though the T1 has a high iron content, it contains too much TiO_2 to be suitable for blast furnace reduction.
- TiO_2 content of the T1 is below what is economically viable for the Becher process and titania slag production.
- T2 is composed of a significant quantity of gangue such as alkali earth oxides and silica that also makes existing beneficiation unworkable.

The aim of research in this thesis is to develop a process, capable of simultaneously extracting iron, titanium dioxide and vanadium pentoxide from a range of low-grade feedstocks, which are primarily derived from the titanium-bearing waste materials from the vanadium extraction operations in South Africa. The process steps have been designed and demonstrated to have a zero-waste and limited adverse environmental impact. Emphasis was placed on designing a process that may allow a lower-cost option for developing a plant with the available power, water supply and raw materials transport infrastructure in South Africa. For this reason, the physical chemistry of the process is required for flow-sheet analysis used for plant design. In this case, the choice of a rotary kiln was considered, following the batch-process analysis of the chemistry of reduction reaction. In this thesis the results of process chemistry using a rotary kiln furnace, developed at the University of Leeds, are reported. The thesis therefore embodies the following parts, as a part of meeting the overall objective on the extraction of metallic values from the titaniferous waste minerals of T1 and T2 classifications:

The aim of this work was completed by carrying out the following tasks:

i) mineralogical phase analysis of the as-received T1 and T2 mineral wastes;

ii) equilibrium thermodynamic analysis of the multicomponent phase equilibria in the Ti-Fe-Ca-Na-O in the presence and absence of reducing agents for the experimental design;

iii) investigation of the phase equilibria, kinetics and mechanism of pyrometallurgical processing of T1 and T2 materials, for ascertaining the separation of major metallic values;

iv) based on the analysis of the process chemistry, study of the overall reaction in a semi-continuous operations using a rotary kiln;

v) thermodynamic analysis of the leaching conditions for the extraction and purification of TiO_2,V_2O_5 and Al_2O_3;

vi) characterisation of magnetic fractions of T1 waste and the melting and ferrous alloy formation;

vii) beneficiation chemistry of T2 slag waste by upgrading the feedstock from nominal 35 weight.% to above 95 weight.% and

viii) developing a block materials and energy flow diagram and undertaking material and energy balances on the processing of the waste materials.

1.3 Structure of thesis document

The thesis is made up of 9 chapters:

Chapter 2: Literature review

Chapter 2 details TiO_2 pigment production techniques and the role of current titaniferous mineral beneficiation is discussed including the constraints of the state-of-the-art processes. Vanadium extraction technology is assessed along with the separation and purification methods employed by the industry. The objectives of the thesis are given in Chapter 2.

Chapter 3: Materials and Methods

Chapter 3 presents the titanium-bearing materials and reagents used for the study, as well as the experimental procedures followed for the investigation. Characterisation techniques and sample preparation methods employed in the study are described.

Chapter 4: Phase analysis of materials

In Chapter 4 TM, T1 and T2 materials are characterised utilising XRF, XRPD and SEM-EDX. Phase equilibria calculations to predict phases formed from previous processing of titanomagnetite concentrates are presented and the results compared with phase analysis of T1 and T2. Phase transformation of TM heat treated in air and inert atmospheres is investigated.

Chapter 5: Thermodynamic considerations

Chapter 5 presents standard Gibbs free energy change calculations and multi component phase equilibria data for carbothermic reduction in the presence and absence of alkali carbonates for T1 and T2 materials.

Chapter 6: Carbothermic reduction of iron-rich tailings and low-grade titanium dioxide slag in the presence of alkali carbonates.

Chapter 6 discusses the kinetics and mechanism studies of reductive alkali roasting of T1 and T2 materials in the thermogravimetric analysis apparatus. Reduced samples are characterised using SEM-EDX and XRPD and the physical chemistry of reduction is studied. Reductive alkali roasting in the rotary kiln was investigated and the effect of parameters on operations is detailed.

Chapter 7: Separation and purification of reduced products

Chapter 7 describes the separation and purification of metallic values from reduced products. Reduced T1 samples were subjected to magnetic samples and the non-magnetic and magnetic fraction. Smelting of the magnetic fraction to produce a ferroalloy was demonstrated. The non-magnetic fraction was subjected to two-stage leaching and sulphate roasting to upgrade the TiO_2 content. Water leaching of reduced T2 sample for extraction of metallic values such as V_2O_5 and Al_2O_3 is shown. Acid treatment and sulphation roasting of the water leached T2 residue is described in Chapter 7.

Chapter 8: Mass and energy balance of iron-rich tailings and low-grade titanium dioxide slag processing

Chapter 8 evaluates the mass and energy for the process steps in the flowsheets designed to treat T1 and T2 materials.

Chapter 9: Conclusions and future work

The final chapter draws conclusions from the results obtained during the experimental work and proposed future work is given.

2 Literature review

Chapter 2 provides an overview of TiO_2 pigment production by chloride process and sulphate processes, including methods developed to produce TiO_2 from T2-type industrial waste. A summary of the state-of-the-art methodologies utilised for beneficiating titanium-bearing feedstock is provided. Technologies developed to extract vanadium oxides from titaniferous magnetite and other sources are presented and the separation and purification of vanadium oxide techniques are detailed.

2.1 Mineralogy

2.1.1 Titaniferous magnetite

Most spinel oxides have the general formula $X^{2+}Y^{3+}{}_2O_4$. In the normal spinel (XY_2O_4), the divalent cations occupy the tetrahedral voids and the trivalent cations occupy the octahedral sites. For each unit cell, eight of the sixty-four tetrahedral sites and sixteen of the thirty-two octahedral sites are occupied by cations. When half of the trivalent cations are replaced by divalent cations in the octahedral sites, then given that the tetrahedral sites are occupied exclusively by divalent cations, an inverse spinel is formed [18].

Magnetite as shown in Figure 2.1a is an inverse spinel structure that can occur as a solid-solution with ulvöspinel ($Ti_xFe_{3-x}O_4$), forming a magnetite – ulvöspinel solid solution at magmatic temperatures [19]. Slow cooling may result in the decomposition of the ulvöspinel to ilmenite and magnetite. The magnetite- ulvöspinel is known as known as titanomagnetite. Ulvöspinel (see Figure 2.1b) is an exsolution lamellae in magnetite that is present in rock deposits [2]. The structure of ulvöspinel is an inverse spinel with the Ti^{4+} and Fe^{2+} ions filling the octahedral sites and the Fe^{2+} ions filling the tetrahedral sites. Charge coupled substitution occurs at the octahedral sites ($2Y^{3+} = M^{4+} + N^{2+}$) because of the mixing of the Ti^{4+} and Fe^{2+} ions that are occupying the site, causing valency disorder [16]. The V ions are largely present in the 3+ valence state, as they occupy the octahedral sites of the spinel forming coulsonite (FeV_2O_4) which is in solid solution with magnetite and ulvöspinel [17, 18]. However, a minor amount may be present as V^{4+} ions that are also able to occupy the octahedral sites [19]. The occurrence of V^{4+} ions is explained by an electron-exchange reaction with Fe^{3+} ions, according to equation 2.1 [20, 21]. It has been reported in literature that V^{4+} is stable in spinels [22, 23].

$$Fe^{3+} + V^{3+} = Fe^{2+} + V^{4+} \qquad 2.1$$

The V^{3+} ion has an octahedral radius of 61 pm which is similar to that of Fe^{3+} (63 pm), implying that it is readily able to substitute for the Fe^{3+} ion in the magnetite matrix, as seen in Figure 2.1c . The substitution is supported by the crystal field stabilisation energy (CFSE) theory where trivalent cations with high octahedral site preference energies (OSPE) are predicted to occupy octahedral sites. V^{3+} ions with an OSPE of -53.5 kJ/mole are likely to favour the octahedral site compared with Fe^{3+} cations that have zero OPSE, with respect to the solid-solution forms of spinels [24].

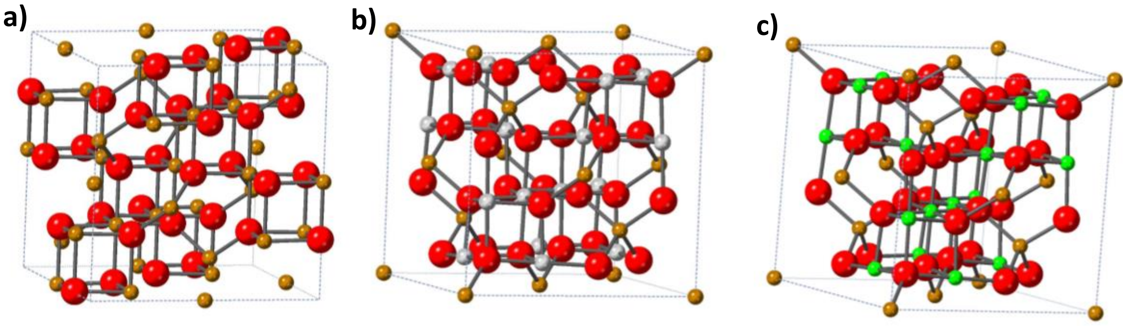

Figure 2.1 Crystal structures of a) magnetite, b) ulvöspinel and c) coulsonite. (Fe=brown, O =red, Ti = grey and V=green)

Spinodal decomposition

Spinodal decomposition is the mechanism of phase transformation where unmixing of a solution into distinct phases with different chemical compositions occurs. For example, a binary alloy would separate into A-rich and B –rich regions when cooled into the unstable region of a miscibility gap (see Figure 2.2a) [25, 26].

A Gibbs free energy curve plotted as a function of composition is given in Figure 2.2b. Spinodal decomposition occurs where the curvature of the Gibbs free energy curve is negative (see equation 2.2), representing a region where the system is unstable. A small composition fluctuation would result in A-rich and B-rich regions, causing in a decrease in Gibbs free energy. Decomposition is governed solely by diffusion as there is no thermodynamic barrier to the decomposition within the chemical spinodal, with diffusion occurring until the equilibrium compositions, X_1 and X_2, are reached [25, 27, 28].

$$\frac{d^2G}{dX^2} < 0 \tag{2.2}$$

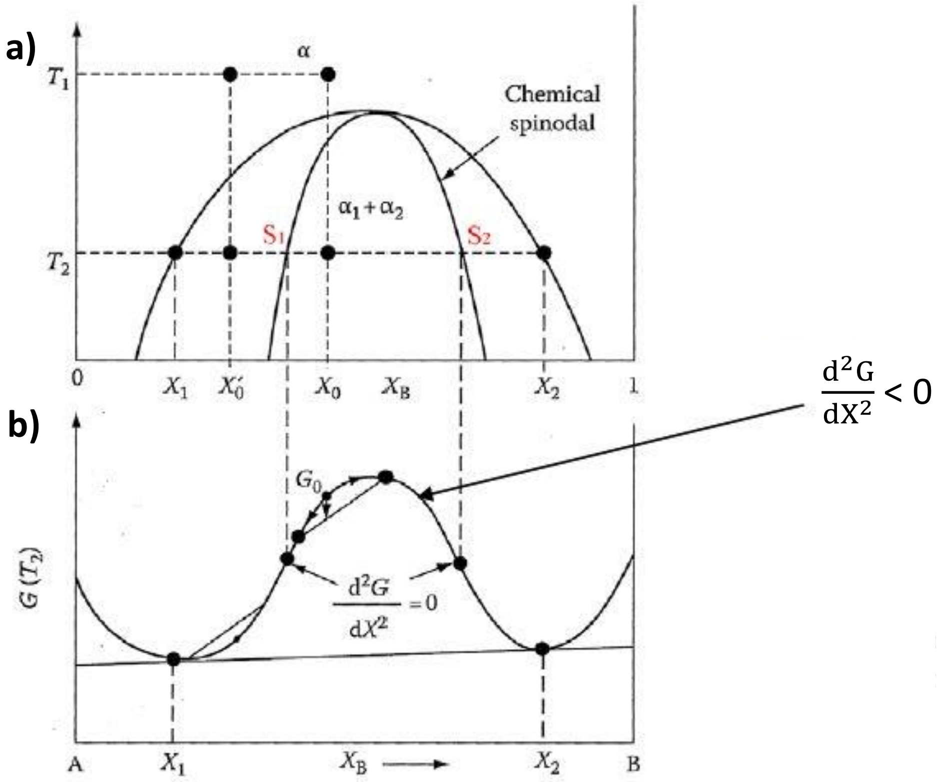

Figure 2.2 a) Phase diagram of binary mixture with a miscibility gap showing a spinodal b) Gibbs free energy against composition plot [25].

Von Gruenewaldt et al [29] explained that the presence of ilmenite in titanomagnetite from the Bushveld complex in South Africa is a result of exsolution of ilmenite from the solid solution. During cooling, unmixing of ulvöspinel and magnetite phases from the solid solution produces a fine-scale two-phase intergrowth [30]. The miscibility gap identifiable in Figure 2.3 illustrates that as the temperature decreases there is unmixing of the ulvöspinel and magnetite phases. The exsolved ulvöspinel lamellae (intergrowths) undergo subsolidus oxidation to form ilmenite [31-33]. The reaction proceeds according to equation 2.3, which is thermodynamically feasible below 973 K and becomes more favourable as the temperature decreases [18, 34, 35].

$$3Fe_2TiO_4 + 0.5O_2(g) \rightarrow 3FeTiO_3 + Fe_3O_4 \tag{2.3}$$

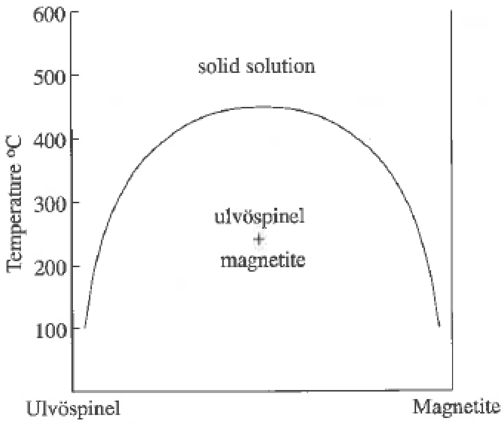

Figure 2.3 Approximate position of the solvus in the magnetite-ulvöspinel solid solution [30, 36].

2.1.2 Ilmenite

Ilmenite has a hexagonal structure containing two cations, titanium and iron, which form alternating bilayers perpendicular to the c axis [37]. $Fe^{2+}$and Ti^{4+} ions are tetrahedrally and octahedrally coordinated, respectively, with the O ions. Ilmenite minerals often contain manganese which is generally present as a substitutional impurity for Fe^{2+}. In the ilmenite lattice both Fe^{2+} and Fe^{3+} can exist, and both ions can be partially or completely substituted by Mn^{2+} and Mn^{3+}, respectively. This is because the size difference between Fe^{2+} (92 pm) and Mn^{2+} (97 pm) is less than 15%, which means that extensive ionic substitution may be possible between these two ions [38]. The crystal structure of ilmenite mineral is presented in Figure 2.4.

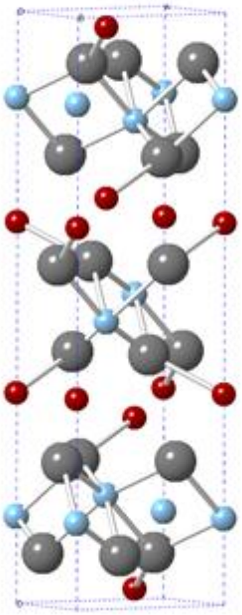

Figure 2.4. Crystal structure of ilmenite mineral (O = grey, Ti = blue, Fe = red) [30, 36].

2.2 Slag chemistry

Slags are mixtures of metal oxides and silicates that form during the smelting of concentrates or ores [39, 40]. The primary role of slags is separation of unwanted compounds, such as unreduced metal oxides and gangue minerals, from the molten metal [39, 41]. Good separation from the molten metal is an important property of a slag [42]. Fluxes such as lime, magnesia and silica are often added to give the slag preferred properties which include:

1. lower melting point than the melt to maintain high fluidity enabling the slag to cover the whole liquid surface.
2. low viscosity.
3. lower specific gravity than molten metal allowing the slag to protect the melt from the furnace gases and atmosphere; inhibiting oxidation of the liquid metal and insulating the melt by limiting heat loss.
4. correct chemical composition in order for the slag to be immiscible with the melt, be able to accept and react with impurities from the molten metal and have the desired chemical properties [40, 42].

Molten slags have silicon atoms that are tetrahedrally coordinated to oxygen anions forming silicate (SiO_4^{4-}) tetrahedral units that polymerise to form a three-dimensional network, as seen in Figure 2.5 [40, 43]. Increasing SiO_2 content of the slag results in increased slag viscosity [44].

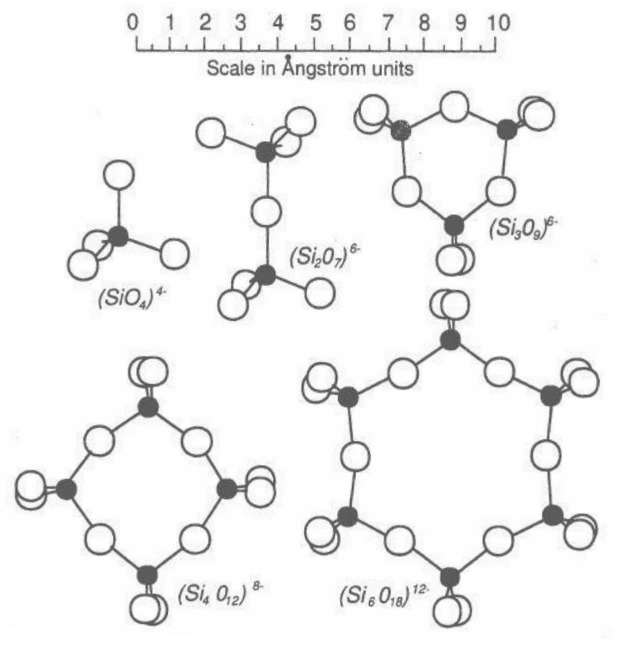

Figure 2.5. Crystalline silicates. Black circle = Si atom, White circle = O atom [42].

Oxides present in the slag can be classified as basic, acidic or amphoteric. Basic oxides donate O^{2-} anions to the slag and are considered to be network-breakers (see equation 2.4). These include: CaO; FeO; MgO; Na_2O and K_2O.

Acidic oxides accept O^{2-} and are considered network-formers (see equation 2.5) and they include SiO_2 and P_2O_5.

Amphoteric oxides behave as either basic or acidic oxides depending on whether they are added to acidic or basic slags, respectively [41]. TiO_2, Al_2O_3, Cr_2O_3 and Fe_2O_3 are examples of amphoteric oxides.

Acidic slags are rich in acidic oxides and have no free O^{2-} anions, whereas basic slags are rich in basic oxides and contain free O^{2-} ions [40, 44].

$$\mathrm{CaO} = \mathrm{Ca}^{2+} + 2\mathrm{O}^{2-} \qquad 2.4$$

$$\mathrm{SiO_2} + 2\mathrm{O}^{2-} = \mathrm{SiO}_4^{4-} \qquad 2.5$$

However, slags can serve as a reservoir for desired metals such as titanium and vanadium oxides, with examples discussed later in chapter 2 [4].

TiO_2 in slag

TiO_2 forms stable $CaTiO_3$ in the presence of CaO. The melting point of $CaTiO_3$ is lowered from 2244 K to 1733 K at eutectic composition of 20 weight.% CaO and 80 weight.% TiO_2, as seen in Figure 2.6a. TiO_2 added to the $CaSiO_3$ composition results in $CaTiSiO_5$ formation which melts at 1673 K, as illustrated by the liquidus isotherm in Figure 2.6b [43]. Titania slags formed from smelting ilmenite concentrates contain 75 weight.% to 90 weight.% TiO_2, where the Ti^{3+} and Ti^{4+} ions may be present.

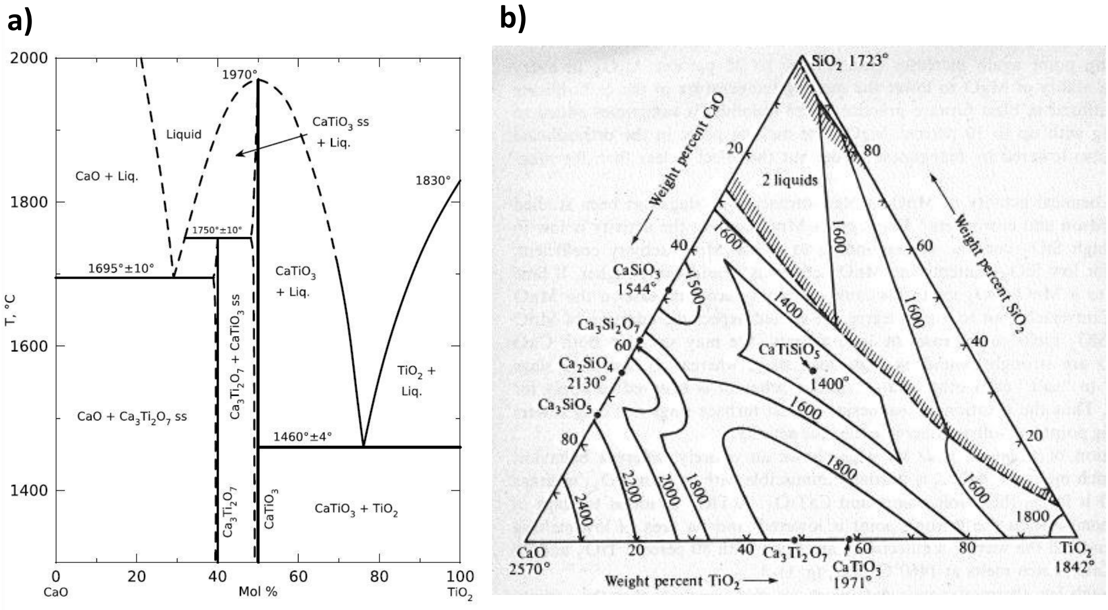

Figure 2.6. Phase diagram of a) $CaO-TiO_2$ and b) $CaO-SiO_2-TiO_2$ system [43, 45, 46].

2.3 Processing of titanium-bearing materials

2.3.1 Production of pigment grade TiO_2

Commercial methods of manufacturing titanium dioxide pigments are based on two well established processes: the sulphate and the chloride processes. However, more recently other processes have also been developed and are at varying stages of the development [41]. The increasingly favoured chloride process requires high-grade TiO_2 feedstocks to be commercially viable and to fully realise environmental advantages over the sulphates process.

The range of feedstock suitable for the chloride or sulphate process is presented in Table 2.1. Some materials are naturally occurring but limited supplies of high-grade feedstock has led to the development of beneficiation processes to meet the demand for high TiO_2 content inputs.

Table 2.1 Feedstock used in the chloride and sulphate processes [2].

Feedstock	**Type**	**Process**	**TiO_2 (weight.%)**
Chloride-grade ilmenite	Natural	Chloride	60
Leucoxene	Natural	Chloride	75-91
Rutile	Natural	Chloride	90-96
Chloride-grade slag	Synthetic	Chloride	85-95
Synthetic rutile	Synthetic	Chloride	90-93
Sulphate-grade ilmenite	Synthetic	Sulphate	44-57
Sulphate-grade slag	Synthetic	Sulphate	75 - 80

2.3.1.1 Chloride Process

The majority of TiO_2 pigment is produced using the chloride process, which was developed in the 1950s, as it has pigment quality, economic and waste management benefits over the sulphate process [5, 6, 47]. Use of high TiO_2 feedstock is particularly preferred for minimising the waste generation. TiO_2 in the raw material is chlorinated in the presence of coke to form titanium tetrachloride ($TiCl_4$), as seen in reaction 2.6. The Fe-Ti-Cl-C-O system in Figure 2.7 illustrates the role CO/CO_2 ratio plays in the chlorination of TiO_2. It can be observed that $TiCl_4$ forms at a phase field where the CO/CO_2 ratio is sufficiently reducing. Iron chlorides are readily formed as they are observed even at lower CO/CO_2 ratios where TiO_2 has not been chlorinated.

$$\mathrm{TiO_2} + 2\mathrm{Cl_2(g)} + 2\mathrm{C} \rightarrow \mathrm{TiCl_4(g)} + 2\mathrm{CO(g)} \qquad 2.6$$

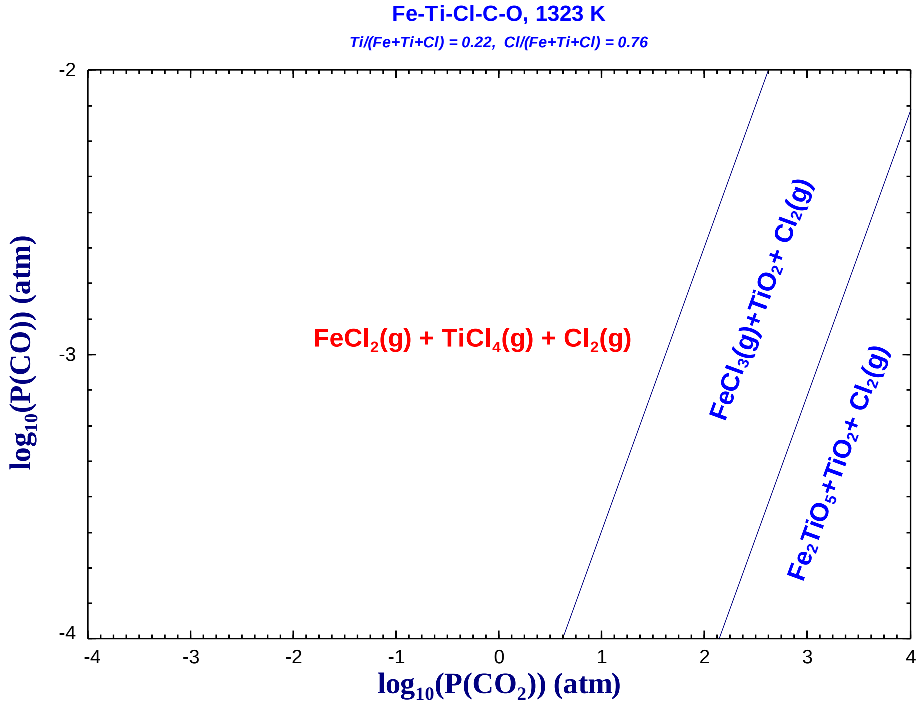

Figure 2.7 Predominance area diagram of the Fe-Ti-Cl-C-O system at 1323 K representing the chlorination of TiO_2 in the presence of carbon [48].

TiO_2 feedstock and coke react with chlorine and oxygen in a fluidised-bed reactor at 1073 K – 1473 K to give $TiCl_4$ and carbon monoxide gas (CO). Minimising the formation of corrosive hydrogen chloride (HCl) gas is ensured by controlling the moisture content of the raw materials. Side-reactions occur during the chlorination process that lead to formation of various chlorides such as AlCl3, $ZrCl_4$, $FeCl_3$, VCl_4, $VOCl_4$ and $SiCl_4$ [49]. The standard Gibbs free energy change versus temperature plot in Figure 2.8 demonstrates that the side reactions become more favourable as the temperature increases.

$$V_2O_5 + 8Cl_2(g) + 5C \rightarrow 2VCl_4(g) + 5CO(g) \qquad 2.7$$

$$V_2O_5 + 3Cl_2(g) + 3C \rightarrow 2VOCl_3(g) + 3CO(g) \qquad 2.8$$

$$Fe_2O_3 + 2Cl_2(g) + 3C \rightarrow 2FeCl_2(g) + 3CO(g) \qquad 2.9$$

$$ZrSiO_4 + 4Cl_2(g) + 4C \rightarrow ZrCl_4(g) + SiCl_4(g) + 4CO(g) \qquad 2.10$$

$$Al_2O_3 + 3Cl_2(g) + 3C \rightarrow 2AlCl_3(g) + 3CO(g) \qquad 2.11$$

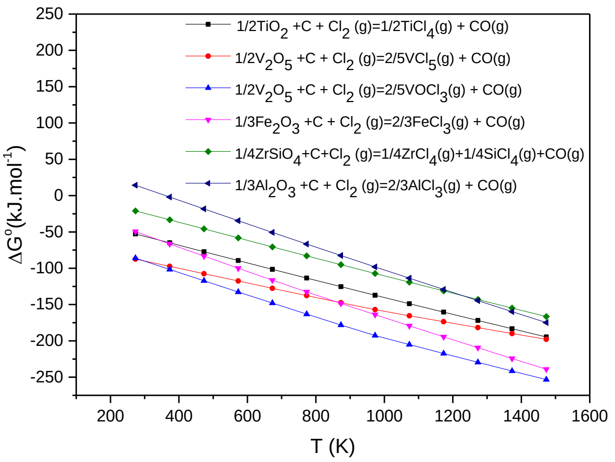

Figure 2.8 Standard Gibbs free energy change against temperature plot for the formation of metal chlorides [35].

After exiting the reactor the product gases are cooled to approximately 423 K causing $FeCl_3$ and $AlCl_3$ to condense, which allows these two species to be separated. The boiling points of $VOCl_3$ and VCl_4 are 400 K and 422 K, respectively, compared to 409 K for $TiCl_4$ and are thus more difficult to remove [50]. $VOCl_3$ and VCl_4 must be reduced in order to be separated, where commonly used reducing agents are copper, hydrogen sulphide or mineral oils [49, 51, 52]. $SiCl_4$, with a boiling point of 331 K, is removed by fractional distillation resulting in pure $TiCl_4$ in liquid form [49, 50].

TiO_2 pigment is formed by oxidation of $TiCl_4$ at 1173 K -1673 K while Cl_2 is regenerated according to equation 2.12. The oxidation reaction is exothermic as ΔH^o ranges from -176 kJ.mol^{-1} to -171 kJ.mol^{-1} in the 1173 K-1673 K temperature range.

$$TiCl_4(g) + O_2(g) \rightarrow 2Cl_2(g) + TiO_2 \qquad 2.12$$

The chlorination of ilmenite is not favourable because of the presence of the iron oxide, which is chlorinated and results in significant consumption of the chlorine gas that is not recycled [53].

$$2FeTiO_3 + 6Cl_2(g) + 6C \rightarrow 2TiCl_4(g) + 2FeCl_2(g) + 6CO(g) \qquad 2.13$$

In addition to TiO_2 pigment production $TiCl_4$ is used for titanium sponge production via the Kroll process [54].

2.3.1.2 Sulphate Process

The sulphate process was developed in the 1910s [47]. Ilmenite and sulphate-slag are used as feedstock.

The raw material is digested with concentrated sulphuric acid, at 423 K – 493 K, to form titanium oxysulphate ($TiOSO_4$), ferric sulphate [($Fe_2(SO_4)_3$)] and ferrous sulphate ($FeSO_4$) and the solution is filtered and subsequently clarified [55].

$$FeTiO_3 + 2H_2SO_4 \rightarrow FeSO_4 + TiOSO_4 + 2H_2O \qquad 2.14$$

Addition of scrap iron to the clarified solution reduces ferric ions to ferrous ions allowing the iron to be crystallised as ferrous sulphate heptahydrate ($FeSO_4.7H_2O$). The Fe-Ti-S-H_2O E_h-pH system in Figure 2.9 demonstrates the stability region where $FeSO_4.7H_2O$ can be crystallised out of solution, between 0.2 and 0.4 volts and in a pH range of 0 to 4. Owing to a lack of $TiOSO_4$ thermochemical data in the FactSage database the titanium present in the solution in the same phase field as $FeSO_4.7H_2O$ is presented as TiO_2 instead of $TiOSO_4$.

$$FeSO_4 + 7H_2O \rightarrow FeSO_4.7H_2O \qquad 2.15$$

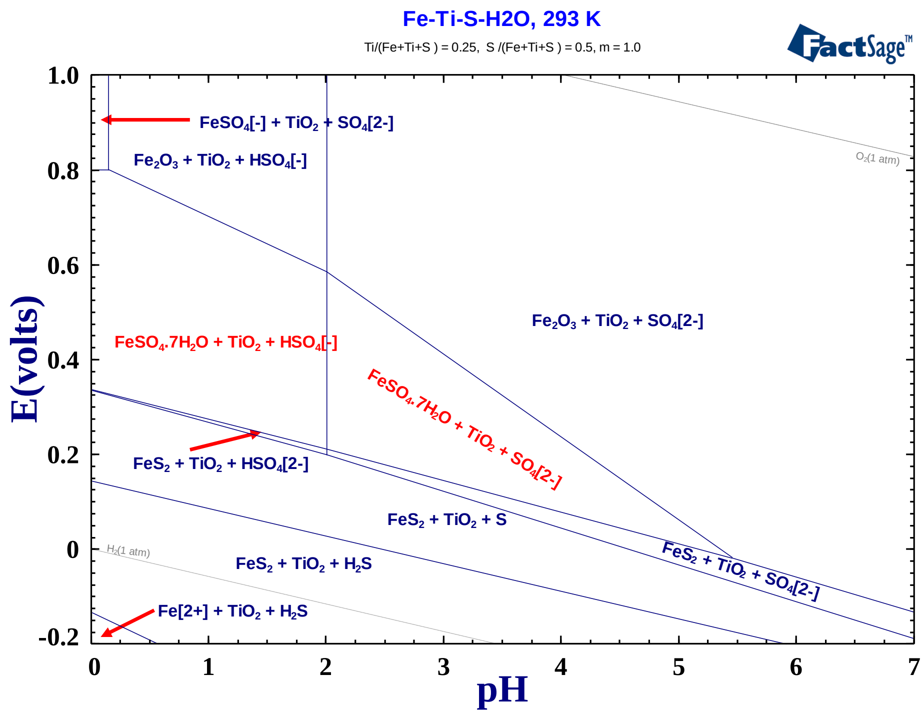

Figure 2.9 E_h-pH diagram of Fe-Ti-S-H_2O system at 293 K computed using FactSage software [48].

The titanyl sulphate containing solution is hydrolysed to form titanium oxide hydrate ($TiO(OH)_2$) (see equation 2.16), which is then calcined in a rotary kiln to form either rutile or anatase [6].

$$TiOSO_4 + 2H_2O \rightarrow TiO(OH)_2 + H_2SO_4 \qquad 2.16$$

The advantages of the sulphate process over the chloride process are that it has lower capital costs and is able to make use of lower quality feedstock. However, the significant generation of dilute sulphuric acid and iron sulphate waste means the process is now less favoured [39]. For example, for every tonne of TiO_2 pigment produced from ilmenite (with 50 weight.% TiO_2) 8 tonnes of dilute sulphuric acid (see equation 2.16), and 3 tonnes of $FeSO_4.7H_2O$ (see equation 2.14) waste products are generated [56]. To overcome the environmental challenges certain companies sell the $FeSO_4.7H_2O$ while others concentrate the dilute H_2SO_4 so that it can be recycled in the sulphate process [57]

Other processes for the production of pigment grade TiO_2 are at various stages of development but are yet to displace the two dominant processes.

2.3.1.3 Avertana and Evraz Highveld Steel and Vanadium processes

Patents have been registered by Avertana Ltd. and Evraz Highveld Steel and Vanadium Ltd. (EHSV) for the production of TiO_2 pigment from TiO_2 waste slag, including EHSV slag (T2), produced from the smelting of pre-reduced titanomagnetite concentrates, [58, 59]. These processes share similarities with the Sulphate process described above.

The initial step of the Evraz Highveld Steel and Vanadium process for TiO_2 recovery from low-grade titania slag is fusion of the T2 with H_2SO_4 at 473 K. Water leaching is carried out below 348 K followed by filtration and clarification of the solution. $CaSO_4$ and residual slag components including SiO_2 report to the solids. $FeSO_4.7H_2O$ is crystallised from the solution, as seen in the Sulphate process. Addition of $(NH_4)_2SO_4$ results in the formation of ammonium aluminium sulphate [$(NH_4)Al(SO_4)_2$]. TiO_2 nuclei are added to the solution which is hydrolysed to precipitate hydrated TiO_2. Calcination at 1223 K followed by conditioning and milling of the TiO_2 precipitate is performed to yield TiO_2 pigment. Ammonia solution is added to the hydrolysed solution to precipitate vanadium oxide present in the solution. However, no indication is given on the purity of the vanadium oxide precipitated.

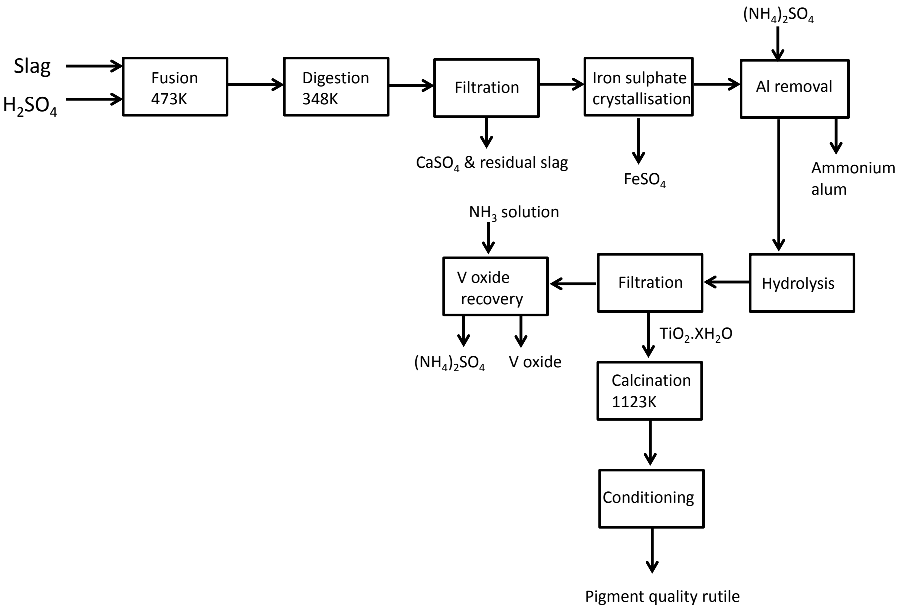

Figure 2.10. Block flow diagram of the Evraz Highveld Steel and Vanadium process for low-grade TiO_2 slag treatment [58].

The Avertana process involves digestion of slag waste material in an autoclave vessel at 323 K - 493 K in order to form $TiOSO_4$ and metal sulphates such as $Al_2(SO_4)_3$, $FeSO_4$, $MgSO_4$, $CaSO_4$ and $VOSO_4$. Pressure filtration is carried out to recover H_2SO_4 that can be recycled in the process. Water leaching of the filter cake is performed below 353 K followed by filtration and clarification of the solution and $CaSO_4$ is recovered from the solids utilising flotation. Similar to the Sulphate process, seeded hydrolysis of the $TiOSO_4$ solution is done to form hydrated TiO_2, which is filtered from the solution. Precipitated TiO_2 is calcined at 1223 K before being subject to conditioning and milling to yield TiO_2 pigment. $Al_2(SO_4)_3$ and $MgSO_4$ are selectively precipitated from the filtrate solution.

The Avertana and H_2SO_4-based EHSV processes for treating T2-like material consume substantial amounts of sulphuric acid owing to the sulphation of TiO_2 and other slag constituents, such as CaO, MgO, FeO and Al_2O_3. Recovery of vanadium oxide from acidic medium often requires use of solvent extraction, as described in 2.4.3.2. The Avertana and H_2SO_4-based EHSV processes would not be suitable for processing of T1-type materials that are rich in iron, as significant quantities of sulphuric acid would be consumed while generating large quantities of iron sulphate waste. Use of alkaline reduction allows for effective recovery of iron from feedstocks containing significant quantities of iron/iron oxide while also allowing for extraction of titanium and vanadium oxides. Reductive alkali roasting of T2 results in the formation of acid-soluble phases, which decreases the overall acid consumption compared to the Avertana and H_2SO_4-based EHSV processes.

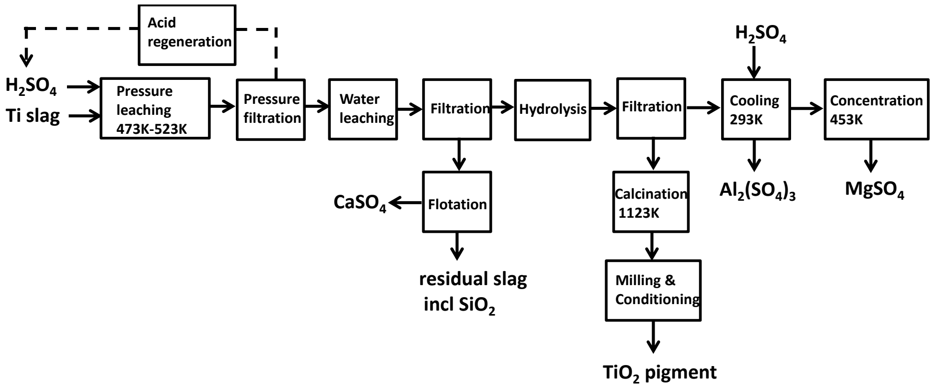

Figure 2.11 Block flow diagram of the Avertana process for low-grade TiO_2 slag treatment [59].

2.3.2 Beneficiation of titaniferous minerals

Increasing use of the chloride process and the limited supply of high-grade feedstock, such as natural rutile, led to the development of a number of processes to upgrade the TiO_2 content of low-grade feedstock [60]. Upgrading the TiO_2 content is primarily achieved by separating iron oxide from TiO_2. New processes have been developed to upgrade titaniferous minerals, however, a limited number are being commercially exploited or have reached an advanced stage [55].

These beneficiation processes are either a pyrometallurgical, a combination of pyrometallurgical and hydrometallurgical or solely hydrometallurgical processes. The Becher process and the Benelite process, which are based on the rotary kiln as the main reactor for treating the titaniferous concentrates, are currently employed to produce synthetic rutile on an industrial-scale.

2.3.2.1 Pyrometallurgical process

Smelting of ilmenite concentrate

Ilmenite concentrates are smelted at 1923 K – 1973 K with anthracite coal in an electric arc furnace to produce pig iron and a slag phase rich in TiO_2 – 75 weight.% - 90 weight.% (see equation 2.17) [49]. Fluxes are not added during the smelting process so that the TiO_2 content in the slag is not effectively decreased [61, 62]. However, reduction of iron oxide is controlled to leave a limited amount of FeO that is able to flux TiO_2 into the slag phase

[61]. The advantage of ilmenite smelting is that the iron present in the ilmenite concentrate is recovered. During smelting, Ti^{4+} ions are often reduced to Ti^{3+} ions to give sub-oxide forms such as Ti_2O_3 [63].

$$\mathrm{FeTiO_3 + C \rightarrow Fe + TiO_2 + CO(g)} \qquad 2.17$$

In some operations ilmenite is pre-reduced in the rotary kiln before being fed into the electric arc furnace with coal for smelting [64, 65]. Smelting ilmenite sands typically produces chloride-grade slag that can be used for the chloride process as the TiO_2 content ranges between 80 and 90 weigh.% while having a low MgO and CaO content. However, undersized chloride slag can be sold to sulphate pigment producers. Rock ilmenite when smelted produces sulphate-grade slag which has 70 weight. % - 80 weight. % TiO_2. However, the high MgO and CaO content means that sulphate slag is only suitable for the sulphate process [66-68]. The higher TiO_2 content of the sulphate-grade slag lowers the amount of waste generated by the sulphate process compared to use of ilmenite concentrate.

The challenges presented by smelting ilmenite are that it operates at high temperatures which is energy-intensive. Titania slag is corrosive to refractory materials requiring formation of a layer of solidified slag, commonly referred to as “freeze lining”, on the furnace lining in the slag zone for protection of the furnace wall [61, 69, 70]. Ilmenite concentrate smelting requires a TiO_2 content greater than 30.% and total Fe composition above 30 % for smelting to be economically viable [66].

T1 with 11 weight.% TiO_2 would clearly not suitable for smelting even though the total iron composition is 50 weight.%. Although the TiO_2 content of T2 is greater than 30 weight.% the limited iron content means smelting is not a viable option for beneficiation of the material.

2.3.2.1 Pyro-hydrometallurgical processes

Becher process

In the Becher process, ilmenite sands that have been weathered or pre-oxidised in air to form pseudobrookite ($Fe_2O_3{\cdot}TiO_2$) and TiO_2 (see equation 2.18) are used. The pre-oxidation of the ilmenite to pseudobrookite causes cracking in the lattice creating a more porous material [66]. However, use of a pre-oxidation step consumes additional energy.

$$\mathrm{4FeTiO_3 + O_2\,(g) \rightarrow 2Fe_2O_3 \cdot TiO_2 + 2TiO_2} \qquad 2.18$$

The lattice changes in the ilmenite due to pre-oxidation increase the rate and extent of reduction of iron oxides to metallic iron during the reduction step (see equation 2.19) [71]. The pre-oxidised ilmenite is reduced with coal at 1373 K-1473 K in a rotary kiln with a residence time of approximately twelve hours forming metallic iron [72]

$$\mathrm{Fe_2O_3 \cdot TiO_2 + 3CO(g) \rightarrow 2Fe + 2TiO_2 + 3CO_2(g)} \qquad 2.19$$

Reduced ilmenite is aerated in order to rust out the metallic iron present in the ilmenite grains according to equation 2.20, ammonium chloride is added as a catalyst to accelerate the aeration process [73, 74]. Subsequently, any remaining iron and impurities are removed by leaching with dilute sulphuric acid to yield a synthetic rutile with approximately 88 weight.% - 93 weight.% TiO_2 [66, 75].

$$\mathrm{4Fe + 3O_2\,(g) \rightarrow 2Fe_2O_3} \qquad 2.20$$

The iron oxide generated by the Becher process is in an unusable form providing no economic value and being classed as a waste product. The Becher process is unable to remove key impurities, such as MgO and CaO, and requires ilmenite concentrate with a TiO_2 content greater than 55 weight.% , however, the process is most effective when ilmenite containing 60 weight.% - 63 weight.% TiO_2 is used. [2, 66, 76]. The feedstock constraints of the process mean it cannot be utilised for beneficiating low-grade feedstock such as T1 and T2.

Benelite and Murso processes

In the Benelite process, ilmenite sands containing 55 - 65 weight.% TiO_2 are reduced in a rotary kiln with heavy oil at 1173 K to ensure any ferric iron (Fe^{3+}) present is reduced to ferrous iron (Fe^{2+}) (see equation 2.21).

$$\mathrm{n\,Fe_2O_3.nTiO_2 + 2CO(g) \rightarrow nFeTiO_3 + 2CO_2(g)} \qquad 2.21$$

Reduced ilmenite is leached in 18 weight.% - 20 weight.% HCl at 293 K – 418 K for several hours in rotary digesters during which the iron oxide (Fe^{2+}) and residual impurities are removed as $FeCl_2$. The acid leaching conditions used during the Benelite process allow for greater removal of impurities compared to the Becher process. The remaining solids are washed and calcined at 1143 K yielding synthetic rutile which is approximately 94 wt.% TiO_2 [60].

$$\mathrm{FeTiO_3 + 2HCl \rightarrow FeCl_2 + TiO_2 + H_2O} \qquad 2.22$$

The spent acid solution is pyrohydrolysed according to equation 2.23 in order to regenerate the hydrochloric acid and produce a fine hematite residue, which is typically a waste product.

The alkali reduction-based process described in this report is shown to be able to treat titanium-bearing feedstock of lower grade than what is required by the Becher, Benelite and Murso processes. Also, the process presented in this report is designed to recovery iron and vanadium oxide from feedstock in contrast to the three processes which are focused on beneficiation of titaniferous feedstock. Furthermore, iron is typically a waste product and the Becher, Benelite and Murso processes are not capable of extracting vanadium oxide.

$$2FeCl_2 + 2H_2O + 0.5O_2\,(g) \rightarrow Fe_2O_3 + 4HCl(g) \qquad 2.23$$

UpGraded Slag (UGS) process

The impurities present in the rock ilmenite feedstock are concentrated in the sulphate-grade slag which reduces the quality and value of the slag. Bearing the quality in mind, the UpGraded Slag (UGS) process was developed by Rio Tinto plc to remove impurities such as FeO, SiO_2, MgO and CaO from the sulphate-grade slag produced by Rio Tinto which is referred to as Sorelslag^{TM}. The objective was to produce a feedstock suitable for the chloride process.

The Sorelslag^{TM} undergoes the following steps [2, 66, 77, 78]:

1. Oxidation at 1273 K for 1 hour of the slag to oxidise all Ti^{3+} ions to Ti^{4+} ions in order to limit titania acid-solubility in step 3. Ferrous ions are oxidised to ferric ions (see equation 2.24) in the process while a significant amount of the glassy silicate phase is decomposed according to equation 2.25.

$$(FeTi_2O_5)_{0.32}(MgTi_2O_5)_{0.33}(Ti_3O_5)_{0.35} + 0.255O_2 \rightarrow (Fe_2TiO_5)_{0.16}(MgTi_2O_5)_{0.33} + 1.55TiO_2 \qquad 2.24$$

$$(Ca, Al, MgFe.Ti)SiO_3 + O_2(g) \rightarrow Fe_2O_3 + CaSiO_3 + Al_2SiO_5 + TiO_2 \qquad 2.25$$

2. Reduction at 1073 K for 1 hour of oxidised titania-rich slag using smelter off-gas (85 volume % CO and 15 vol% H_2) reduces Fe^{3+} ions back to Fe^{2+} ions while enhancing the leachability of the impurities during the succeeding acid leaching.

3. High-pressure acid leaching of the heat-treated slag at 398 K using 18 % to 20% HCl for 5 to 7 hours primarily to remove MgO, FeO, CaO, and Al_2O_3 and SiO_2.
4. Washing of the acid-leached slag followed by calcination in the 873 K to 1073 K temperature range to produce UGS slag with minimum 94.5 weight.% TiO_2.
5. Pyrohydrolysis of spent acid solution for HCl recovery while generating an oxide residue predominantly containing $MgFe_2O_4$ and $FeAl_2O_4$.

An optional step of caustic leaching was included in the original process for removal of excess silica present in the upgraded slag.

Feedstock summary for TiO_2 pigment production

A summary of the feedstock used for the sulphate and chloride processes is presented in Figure 2.12.

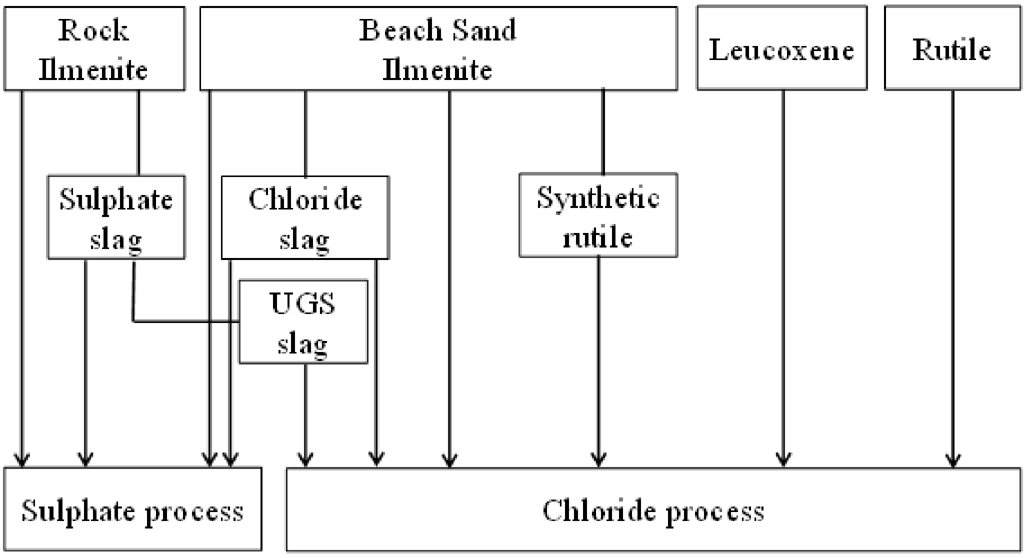

Figure 2.12 Summary of feedstocks for chloride and sulphate processes.

UpGraded Slag (UGS) processing of low grade titania slag

The UGS process was developed to upgrade titania-slag with high levels of alkaline earth oxides, therefore Goso et al. [79] investigated its application for the beneficiation of Evraz Highveld Steel and Vanadium slag (T2). Considering the deleterious consequences on TiO_2 recovery of flux addition during smelting of titanomagnetite concentrate, the authors smelted the concentrate in the absence of any fluxes. The fluxless slag had an initial TiO_2 content of 56 weight.% TiO_2 compared to

33 weight.% for T2 (considered to be the fluxed slag in the study) clearly illustrating the influence of flux on the grade of TiO_2 in the slag. An un-optimised UGS process was applied to both slag materials. However, no comment was made on the effect smelting in without flux smelting had on the separation between the molten iron and the slag material.

Fluxed and fluxless slag material were oxidised at 1148 K and subsequently reduced in a CO atmosphere at 1148 K. Heat treated slag materials were leached with 20 % HCl for 24 hours at 383 K upgrading the TiO_2 content to 67.1 weight.% and 67.8 weight.% for both fluxed and fluxless slag, respectively.

A 2.15M NaOH leaching step at 373 K for 3 hours was adopted for both materials due to the high silica content of the acid leached slag materials. Caustic leached residues were washed and subsequently calcined at 1173 K for 3 hours.

The grade of the treated fluxed slag (T2) was reported to be 74.6 wt. % TiO_2 compared to 74.0 wt. % TiO_2 for the fluxless slag. Major impurities remaining in the upgraded slag materials were MgO and Al_2O_3 which were present as a spinel phase $[Mg(Al,Ti,V)_2O_4]$ and pseudobrookite solid solution ($MgTi_2O_5$-$FeTi_2O_5$-Al_2TiO_5). These phases prevented a higher grade of TiO_2 from being attained.

The study by Lekobotja highlights that the UGS process is limited in its ability to treat the T2 material and is also not capable of simultaneous recovery of TiO_2 and V_2O_5 from the material, in contrast with the alkali reduction based process developed in this report. Use of the UGS process resulted in the need of an additional sodium hydroxide leaching step to remove silica, whereas caustic soda leaching is not required in the alkali reduction based process detailed in this report due to formation of acid-soluble silicate phases during the initial reductive alkali roasting step. Decomposition of the spinel phase remains important for effective beneficiation of the T2 material.

Other processes for the beneficiation of titaniferous minerals have been investigated and are at different stages of development.

Austpac ERMS and EARS processes

The Austpac Enhanced Roasting and Magnetic Separation (ERMS) and Enhanced Acid Regeneration (EARS) process involves roasting in two fluid bed stages.

First, ilmenite concentrate is subjected to oxidative roasting at 1273 K to ensure that the iron oxide is in the trivalent state. In the second stage, reductive roasting is performed at 1273 K with coal to reduce the iron oxide to the Fe^{2+} state, making it easily leachable with the HCl. Roasting enhances the magnetic properties of ilmenite improving separation of ilmenite from gangue and fine char during the subsequent magnetic separation stage.

Leaching the magnetic fraction in hot HCl at atmospheric pressure removes the majority of the iron oxide (see equation 2.22) and other impurities (CaO, MgO, MnO and Al_2O_3). The acid leach residue is washed, dried and calcined in a fluid bed system at around 1073 K giving a synthetic rutile residue which is approximately 96 weight.% TiO_2 [80].

Regeneration of HCl from leach liquors utilising the EARS process is a key component of the process. It is a variation of pyrohydrolysis process with the major difference being that the water in the spent acid is evaporated at 413 K to produce metal chloride pellets that are fed into a fluid bed roaster for pyrohydrolysis at 1073 K to 1173 K regenerating HCl according equation 2.26 [81].

$$2FeCl_2 + 0.5O_2 + 2H_2O \rightarrow Fe_2O_3 + 4HCl(g) \qquad 2.26$$

Reaction 2.26 indicates that all the iron oxide produced by HCl regeneration is solely present as hematite, however, magnetite is also present. The ERMS process would not be suited to the high iron – low titania feedstock (T1) because of significant acid consumption. Austpac has successfully produced direct reduced iron from the iron oxide generated during the process [66].

Magpie process

The Magpie process was developed to process low-grade ilmenite that contain a minimum of 11 weight. % TiO_2 [82, 83]. Ilmenite is first leached with 35% HCl at 348 K under atmospheric pressure in order to dissolve the iron and titanium oxide present and the leach solution is filtered to remove acid insoluble gangue. Excess HCl is removed during an evaporation step that concentrates the filtrate down to a slurry. Titanyl hydroxide ($TiO(OH)_2$) precipitates during evaporation while iron chloride remains in solution.

The slurry is filtered with the filtrate going to solvent extraction, where vanadium and chromium are recovered using solvent extraction. The solution containing ferrous chloride is hydrolysed to regenerate HCl and to produce Fe_2O_3. The $TiO(OH)_2$ precipitate is calcined in order to produce 95.8 weight. % TiO_2.

The disadvantages of solvent extraction are that input of expensive reagents is constantly required, as not all of the organic reagent is recycled. The toxic and flammable nature of solvents poses environmental and safety concerns presenting added costs to operators [84]. Increase in the number of impurities dissolved in solution results in additional steps for separation and purification of metallic values [40].

2.3.3 Carbothermic reduction of ilmenite

Several investigations on the carbothermic reduction of ilmenite have been carried out largely due to the commercial significance of the reaction as it is central to the Becher and Benelite processes. CO gas or solid carbon have been utilised as a reductant where several studies noted that below 1273 K the maximum percentage reduction (%R) attained was 40%. However, above 1273 K the %R achieved approached 100%, explaining why the Becher process is operated at 1473 K [85-88]. As the ilmenite particle size decreased the rate of reduction observed increased [86, 89, 90].

Increasing the carbon addition from the stoichiometric to two times the stoichiometric amount resulted in an increase in the rate of reduction and the extent of reduction by accelerating the Boudouard reaction (see equation 2.27) and reducing the diffusion path for CO gas [88]. However, further increase of the carbon to three times the stoichiometric amount had a minimal effect on the rate of reduction, which agrees with results by Wouterlood [91] that found significantly increasing carbon addition above the stoichiometric requirement did not result in a meaningful increase in extent of reduction.

Increasing reaction temperature causes an increase in the rate of reduction, however, above 1373 K TiO_2 is also reduced to a certain extent [86, 88, 90, 91]. Operating at higher temperatures increases energy costs and causes wearing of refractories.

Kinetics and mechanism of synthetic ilmenite reduction with graphite was studied at temperatures between 1133 K to 1523 K by El-Guindy and Davenport [85] using thermogravimetric analysis (TGA) apparatus under an argon atmosphere. It was observed that as the reaction proceeds a product layer forms resulting in a decrease in reaction rate which was explained as being due to inhibition of the solid-solid reaction (see equation 2.28). Analysis of the SEM images demonstrated phase segregation as reduced iron particles coalesced at the periphery of the particles while the TiO_2 was located between the reduced iron at the periphery and the unreacted ilmenite present at the core of the particle. It was found that an increase in the argon flow rate decreased the gaseous reduction of ilmenite. The study stated this was due to argon gas penetrating the reaction zone, decreasing the concentration of CO and CO_2 gases, ultimately causing the decrease in the Boudouard reaction.

Figure 2.13 illustrates the variation with temperature of the CO/CO$_2$ ratio in equilibrium with solid carbon at atmospheric pressure (see equation 2.27). At lower temperatures CO$_2$ is the dominant component, however, above 1273 K CO is the main gas phase present.

$$\mathrm{CO_2(g) + C \leftrightarrow 2CO(g)} \qquad 2.27$$

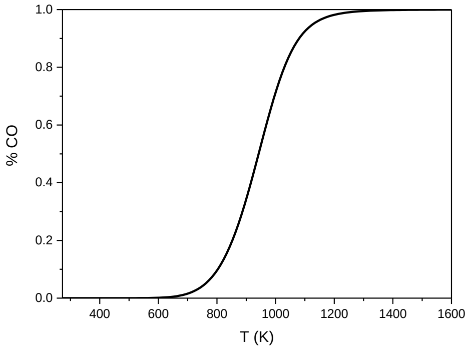

Figure 2.13. Variation with temperature of the concentration of carbon monoxide in equilibrium with carbon dioxide and solid carbon at a total pressure of one atmosphere [92].

El- Guindy proposed that the mechanism for reduction is different depending on the temperature:

Solid state reduction occurring from 1133 K

$$\mathrm{FeTiO_3 + C \rightarrow Fe + TiO_2 + CO(g)} \qquad 2.28$$

Above 1293 K, the principal reaction is the gaseous reduction

$$\mathrm{FeTiO_3 + CO(g) \rightarrow Fe + TiO_2 + CO_2(g)} \qquad 2.29$$

Previous studies noted that above 1273 K the reduction of ilmenite was dominated by gaseous reduction (see equation 2.29) due to the gas being primarily composed of CO, as illustrated in Figure 2.13 [85, 88]. Below 1273 K, the CO$_2$ composition of the gas increase meaning reduction of ilmenite occurs largely due to solid carbon (see equation 2.28) which is slow as a result of the limited solid-solid contact area, whereas CO readily diffuses into the particle explaining why different investigations observed an increased rate of reduction above 1273 K [92, 93].

El-Tawil [86] studied solid-state reduction of ilmenite with charcoal under nitrogen atmosphere in the temperature range 1273 K – 1473 K. At 1273 K, 30%R was the maximum achieved, whereas more than 97 %R was demonstrated at 1473 K and formation of iron precipitate at the grain boundaries was witnessed. At 1473 K the ferrous pseudobrookite phase was observed in the final product along with Ti_3O_5. El-Tawil proposed a similar mechanism to that proposed by El-Guindy and Davenport [85], where the initial stage involved direct reduction of ilmenite with solid carbon giving off CO gas. The second stage involved the gaseous reduction of ilmenite, using the CO generated from the first step. El-Tawil proposed a similar mechanism to that proposed by El-Guindy and Davenport [85], where the initial stage comprised of direct reduction of ilmenite with solid carbon. The second stage involves the gaseous reduction of ilmenite, using the CO generated from the first step.

Wouterlood proposed that reduction of pre-oxidised ilmenite, where Fe_2TiO_5 and TiO_2 phases are present, initially proceeds according to equation 2.30. Subsequently $FeTiO_3$ is reduced to Fe and TiO_2 according to equations 2.28 and 2.29, with CO produced by the Boudouard reaction (see equation 2.27).

$$\mathrm{Fe_2TiO_5} + \mathrm{TiO_2} + \mathrm{CO(g)} \rightarrow 2\mathrm{FeTiO_3} + \mathrm{CO_2(g)} \qquad 2.30$$

However, after reduction at 1453 K ferrous pseudobrookite and metallic iron were observed in the reduction products (see equation 2.31). Magnesium and manganese ions reportedly stabilise pseudobrookite at elevated temperatures [94].

$$2\mathrm{FeTiO_3} + \mathrm{CO(g)} \rightarrow \mathrm{Fe} + \mathrm{FeTi_2O_5} + \mathrm{CO_2(g)} \qquad 2.31$$

Jones [87] reduced ilmenite and pre-oxidised ilmenite using CO gas as the reducing agent at temperatures in the range of 1073 K – 1473 K. While the rate of reduction for the natural mineral was higher the percentage reduction was greater for the pre-oxidised mineral. Jones observed that below 1273 K the chemical reaction controls the rate of reaction but above 1273 K the rate was controlled by diffusion through the external gas film. Wang et al. [88] determined that below 1423 K the chemical reaction was the rate-controlling step but above 1473 K diffusion through the product layer was the rate-controlling step. Both studies observed a similar trend with respect to the controlling regimes but the main difference was the temperature range these regimes were the controlling step.

Jones [87] observed that reduction of natural ilmenite is topochemical, implying that the gas was unable penetrate to the centre of particle until the final stages of reduction. It was suggested that porosity provides better access for the reducing gas. Above 1273 K, significant sintering was observed inhibiting diffusion of gaseous reactants to unreacted minerals; an operational challenge of performing out reduction at elevated temperatures. [87, 91].

Wouterlood [91] carried out reduction of ilmenite and pre-oxidised ilmenite, containing minor amounts of MgO and MnO, using coal char at temperatures in the range 1173 K-1473 K.

Using CO gas as a reducing agent, Zhao and Shadman [96] investigated the kinetics and mechanism of ilmenite reduction between the temperatures 1173 K and 1373 K. The proposed steps are the following:

1. Step 1. CO gas diffusion though the porous product layer of TiO_2 towards the unreacted core of grain particles.
2. Step 2. Reaction of CO gas with ilmenite core to produce TiO_2 and Fe. Accumulated iron at the reaction interface is separated by a layer of nonreactive TiO_2.
3. Step 3. Migration of Fe through the TiO_2 layer away from the unreacted core to the grain boundary.
4. Step 4. Iron nuclei are formed and grow outside and around the reacted grain particles.

Steps 3 and 4 result in complete segregation of iron and TiO_2 and at elevated temperatures it was found that the iron grains coalesce.

The authors' suggestion of metallic iron diffusion to the periphery differs with the study by Kucukkaragoz and Eric [90] that stated that the Fe^{2+} ions diffuses to the periphery.

Kucukkaragoz and Eric [90] investigated the reduction of ilmenite with graphite under argon gas at temperatures between 1523 K and 1623 K. It was proposed that reduction proceeds via two steps:

1. First step happens at a higher rate with Fe^{3+} reduced to Fe^{2+}, followed by the reduction of Fe^{2+} to Fe. Also, Ti^{4+} is reduced to Ti^{3+}.
2. The second step occurs at a lower rate and involves the reduction of Ti^{3+} to Ti^{2+}.

The first step proceeded via a shrinking core reaction with metallic iron present at the periphery of the particle. The authors state that Fe^{2+} ions diffuse to the periphery where they are reduced to Fe resulting in the core of the particles being rich in titanium oxide and low in iron.

Various authors indicate that reduction of pre-oxidised ilmenite and ilmenite containing Fe^{3+} ion proceeds via two-stages, with the first rapid stage being the reduction of Fe^{3+} to Fe^{2+} ions and the second slower stage being reduction of Fe^{2+} ion to metallic Fe [87, 91].

Wang [88] reduced ilmenite with graphite in the TGA system under argon gas system between the temperatures 1123 K – 1673 K. It was observed that the reaction proceeds rapidly in the initial stages before a decrease in the rate of reduction after 30 minutes. The authors observed that presence of impurities such as manganese, silica and aluminium oxides inhibits reduction owing to a barrier effect occurring where Mn^{2+} ions replace Fe^{2+} ions at the reaction interface before forming an enrichment zone that limits CO diffusion and lowering Fe^{2+} activity. Formation of fayalite (Fe_2SiO_4) due to the presence of silica was said to inhibit reduction due to the decrease in iron oxide activity. Cementite (Fe_3C) was formed when reduction when performed at 1573 K.

2.3.4 Alkali roasting of titanium-bearing materials

2.3.4.1 Alkali roasting of ilmenite in air

Alkali roasting of ilmenite concentrates has been studied extensively. Foley and MacKinnon [97] roasted 50 weight.% TiO_2 ilmenite in air, with either Na_2CO or K_2CO_3, at 1133 K. Sodium titanates were formed during roasting in air when Na:Ti mole ratio of 0.34:1 were used. However, as the Na:Ti mole ratio increased ternary compounds Na-Ti-Fe-O became dominant. A similar observation was made when roasting ilmenite in air at 1133 K using K_2CO_3. Acid soluble Fe_2O_3 was formed when using low alkali carbonate ratios even though Fe^{3+} is not as readily leached as Fe^{2+} [98] . The E_h-pH diagram presented in Figure 2.14 shows that a pH below 4 and reduction of Fe^{3+} to Fe^{2+} is favourable for increased dissolution of ferrous ions. Leaching the K-Ti-Fe-O ternary complex with 20% HCl at 383 K for 2 hours yielded a residue that was primarily anatase. Similar results were observed when leaching the Na_2CO_3 roasted products.

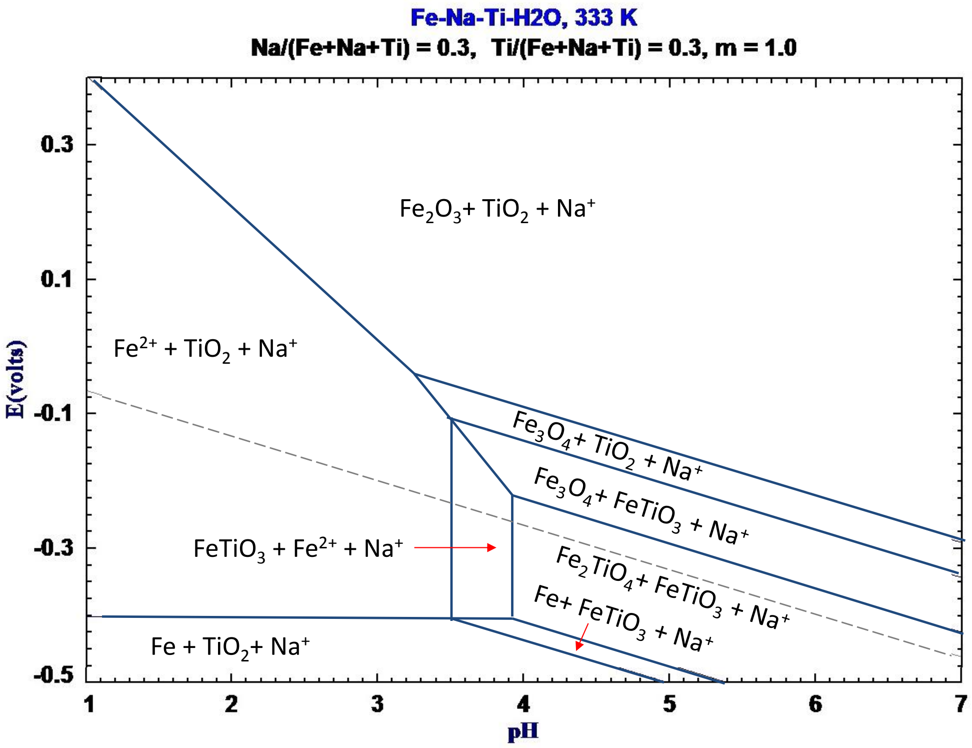

Figure 2.14. E_h- pH diagram for the Fe-Na-Ti-H_2O system [48].

Lahiri and Jha [99] investigated the kinetics and mechanism of soda ash roasting of Bomar ilmenite (69 weight.% TiO_2). It was observed that a product layer formed during the roasting but the presence of a liquid phase prevented the oxygen diffusion resulting in a carbon dioxide gas build-up causing the reaction to stop. Na_2TiO_3, $NaFeO_2$ and sodium iron titanate were the phases observed after roasting.

The proposed mechanism involved two steps. In the first step, ilmenite reacts with soda ash to form sodium titanate and sodium iron titanate ternary compounds. In the second step, the Na-Ti-Fe-O ternary compound rearranges to form sodium ferrite and releases TiO_2 while causing strain in the lattice that results in cracking of the microstructure. Na^+ ions were found to diffuse into the ilmenite lattice by replacing the Fe^{2+} ions, which in turn diffused out was oxidised and reacted with Na_2O to form sodium ferrite (see equation 2.32). Sodium ions caused strain in the ilmenite structure that led to the formation of cracks in the grains. The roasted product was water leached followed by leaching with an oxalic acid and ascorbic acid mixture at a pH below 4 to give a 97 weight.% TiO_2 residue [98, 100].

$$Na_2CO_3 + Fe_2O_3 \rightarrow 2NaFeO_2 + CO_2(g) \qquad 2.32$$

Work by Ephraim and Jha [101] found that when roasting ilmenite with soda ash the surface of the grain was attacked and the pores were formed that allow sodium ions to migrate into the core of the grain.

It was observed that while roasting ilmenite with potassium based alkali salts the K^+ ions diffuse in a similar manner to Na^+ ions, when Na_2CO_3 is used during alkali roasting. Diffusion of the K^+ ions caused strain in the ilmenite lattice resulting in cracking of the microstructure [102]. As K^+ ions (133 pm) are larger than Na^+ (97pm), they result in a greater change in the molar volume during roasting, inducing significantly more strain in the ilmenite lattice [100].

Alkali roasting of ilmenite is more suitable for titanium-bearing minerals with high TiO_2 content and moderate iron oxide content as iron is lost as a waste product during acid leaching. However, roasting in the presence of alkali salts introduces strain into the lattice structure as a result of Na^+/Fe^{2+} cation inter-diffusion and causes macroscopic cracks in the ilmenite microstructure resulting in increased porosity. Any enhancement in porosity for interfacial and diffusion-controlled reactions is beneficial for carbothermic reduction.

2.3.4.2 Alkali roasting of titania slag

Upgrading the TiO_2 content of titania slags using alkali roasting has been extensively investigated.

72 weight.% TiO_2 Sorelslag^{TM} ground to -45μm was roasted between 873 K to 1173 K with alkali salts - such as Na_2CO_3, NaOH or NaCl - using 0.3:1 to 0.6:1 alkali:Sorelslag^{TM} weight ratio.

Roasted samples were wet milled for 30 minutes to dissolve sodium chromates and sodium vanadates, followed by filtration for recovery of the Cr_2O_3 and V_2O_5 from the filtrate. The milled solids were washed and subjected to two-stage acid leaching with 12% - 25% H_2SO_4. Subsequently, acid leached solids were washed and calcined at 1173 K to yield an upgraded slag containing 96 weight.% TiO_2 [103].

Studies of soda ash roasting of titania containing 72 weight.% TiO_2 have been performed by Lasheen [104] and Dong et al. [105]. Lasheen roasted TiO_2slag in the presence of Na_2CO_3 at 1123 K using 0.55:1 Na_2CO_3:slag weight ratio primarily forming $NaFeTiO_4$ and Na_2TiSiO_5. Dong et al. performed roasting at 1173 K using 0.43:1 Na_2CO_3:Slag weight ratio with sodium titanate, sodium ferrite, sodium iron titanate and sodium magnesium titanate being the phases present after roasting.

In both studies roasted products were water leached followed by filtration to separate the water-soluble sodium chromate and sodium vanadate. Lasheen [104] carried out acid leaching of the water leached solids with 20% HCl at boiling temperature to remove impurities, giving an 87 weight.% TiO_2 residue. The high silica content made it necessary to carry out 2M NaOH leaching at 333 K followed by washing and calcination at 1173 K to yield a 97 weight.% TiO_2 synthetic rutile.

Dong et al.[105] performed a two-stage acid leaching with boiling H_2SO_4 to remove impurities while titanium oxide was also dissolved in the solution. Hydrated TiO_2 precipitated from the solution was calcined at 1173 K to produce synthetic rutile assaying over 95 weight.% TiO_2.

Much of the research for alkali roasting of titania slag has focused on treating slag with a TiO_2 content above 70 weight.%, a grade is well above the 30 weight.% in the T2 material - suggesting the existing processes in the literature would not be suitable for the T2 material [103-105]. Where the silica content of titania slag was found to be high, an additional caustic soda leaching step was required [104], which is not the case in the alkali reduction based process described in this report due to the formation of acid-soluble phases during reductive alkali roasting.

Yahui et al. [106] performed NaOH roasting of low-grade titania slag (31 weight. % TiO_2) at 823 K utilising 1.1:1 NaOH:slag weight ratio to form Na_2TiO_3 and $NaMgSiO_4$, while the $MgAl_2O_4$ spinel remained intact. Roasted products were washed and filtered followed by acid leaching of the solids to remove sodium oxide. Acid leached solids were digested with 40% H_2SO_4 to form a $TiOSO_4$ solution that was subsequently hydrolysed to give hydrated TiO_2. Doping and calcination of hydrated TiO_2 yielded pigment grade rutile. While Yahui et al. [106] demonstrated an ability to upgrade the TiO_2 content of slag with a comparable amount of TiO_2 as the T2 material, the authors used significant quantities of sodium hydroxide and were unable to decompose the $MgAl_2O_4$ spinel phase. Characterisation of the T2 material given in chapter 4 highlights the importance of decomposing the spinel phase to liberate vanadium ions present. In contrast, the alkali reduction based process developed in this report uses less alkali salt than Yahui et al. [106] and is shown to breakdown $MgAl_2O_4$. Furthermore, application of NaOH roasting on iron-rich materials, such as T1, would produce significant quantities of iron oxide waste.

2.3.4.3 Sulphation roasting of titania slag

Sulphation roasting of 75.7 weight.% TiO_2 slag has been documented by Elgar et at.[107]. Titania slag was mixed with 14 - 20 weight.% Na_2SO_4 before being contacted with an SO_2 and O_2 gas mixture in the 1073 K-1173 K temperature range for between 2 to 6 hours to convert alkali earth oxides present to sulphates. Sulphated slag was leached in 1 weight.% HCl solution to solubilise MgO, MnO and CaO removing 90.4%, 95.3% and 97.5% respectively. HCl was necessary to aid leaching of $CaSO_4$ due to its limited solubility in water, whereas in the alkali reduction based process described in this report the use of HCl was not required to promote solubilisation of $CaSO_4$ after performing sulphation roasting at a lower temperature for shorter period of time. The lower temperature and shorter time used in this report has energy-saving benefits over the sulphation roasting described by Edgar et al. [107].

2.3.5 Carbothermic reduction in the presence of alkali carbonates

2.3.5.1 Effect of alkali on gasification of carbon

Various authors have investigated the catalytic effect of alkali elements on the gasification of carbon, however the mechanism of catalytic activity has not been clearly explained [108-113]. Promotion of the Boudouard reaction is favourable for carbothermic reduction as stated above due to the resulting increase in the rate of reduction. K_2CO_3 reportedly has superior catalytic activity when compared to Na_2CO_3 [114].

2.3.5.2 Effect of alkali salts during carbothermic reduction of iron ore

Several investigations on the carbothermic reduction of iron ore with alkali salts have observed that the presence of alkali promoted iron grain growth and extent of reduction.

High phosphorus iron ore was reduced in the presence of alkali sulphates by Zhu et al [115], Li et al [116] and Bai et al. [117]. CaO and 15% Na_2SO_4 were added during reduction experiments at 1623 K by Zhu et al. Li et al. [116] carried out the reduction with 7.5 weight.% Na_2SO_4 and 1.5 weight.% borax at 1323 K ; the emission of SO_2 gas is a disadvantage of using Na_2SO_4 with carbothermic reduction. Bai et al. performed carbothermic reduction in the presence of 10% Na_2CO_3 at 1323 K.

The studies observed that alkali promoted growth of the metallic iron grains, aided removal of phosphorus and led to the formation of sodium aluminosilicates. Carbothermic reduction of high alumina iron ore in the presence and absence of Na_2CO_3 was investigated by Chun et al. [118]. Larger iron grains were formed after reduction in the presence of 9 % Na_2CO_3 at 1323 K compared to experiments performed in the absence of Na_2CO_3. Na_2CO_3 reactions with SiO_2 and Al_2O_3 formed sodium silicate and sodium aluminosilicate, damaging the iron ore structure and enhancing separation of iron from alumina during the subsequent magnetic separation step.

2.3.6 Effect of alkali carbonates on carbothermic reduction of ilmenite

Alkali has primarily been used a catalyst during carbothermic reduction of ilmenite with the exception of work by El-Tawil et al. [119] where sodium titanate and metallic iron were intentional formed.

Mohanty and Smith [71] studied the catalytic effect of alkali metals on the carbothermic reduction of ilmenite, focusing on catalysing the Boudouard reaction to increase CO formation which results in an increase in the rate of reduction, as reported earlier in the chapter. The authors state catalysing the Boudouard reaction in the rotary kiln could decrease the operating temperature and eliminate the need for the pre-oxidation stage. Reaction mixtures of ilmenite, graphite and 5 weight.% alkali catalyst were ground to less than 45 µm and reduced in a TGA furnace. Uncatalysed reduction was also carried out and the results compared to experiments utilising the following catalysts: caesium carbonate (Cs_2CO_3); K_2CO_3; Na_2CO_3; lithium carbonate (Li_2CO_3) and rubidium carbonate (Rb_2CO_3).

After reduction the samples were allowed to cool under the flow of argon gas to prevent re-oxidation of the sample. Limited reduction was achieved during uncatalysed reactions at 1133 K, however, significant reduction was observed above 1293 K similar to what was observed by El-Guindy and Davenport [85]. For the catalysed reactions significant reduction was observed below 1293 K as gaseous reduction dominated over solid-solid reduction due to the catalytic effect of alkali.

The authors describe three reaction stages for alkali catalysed reduction:

1. The induction stage where the extent of reduction is small and where the solid-solid reaction is dominant.
2. The acceleration stage where the rate of reduction increases and is dominated by gaseous reduction with the Boudouard reaction being the rate limiting factor.
3. The final stage when the reduction is largely complete and the rate of reduction decreases. The authors state that this is either due to the

challenges of the CO diffusing through the product layer or due to the decrease in the surface area available for reduction.

It was reported that the reduction rate for the catalysed reactions was up to 5 – 20 times greater than the uncatalysed reduction, in the temperature range of 1273 K – 1373 K. The order of highest to lowest catalytic activity determined for the different alkali carbonates was: $CaCO_3 > Rb_2CO_3 > Li_2CO_3 > K_2CO_3 > Na_2CO_3$.

El-Tawil et al. [119] reduced a mixture of ilmenite (42 weight.% TiO_2), sodium carbonate and charcoal in air in the temperature range 1273 K – 1473 K with reactions carried out from 0.25 hours to 3 hours. The disadvantage of performing reduction experiments in air is a failure to de-oxidise the furnace as has been done in previous investigations of carbothermic reduction of ilmenite, where an inert atmosphere was created using purge gas such as nitrogen or argon [59, 86]. The presence of air increases the P_{CO2}/P_{CO} ratio, which decreases the reduction of iron oxide, as seen in Figure 2.15 [39].

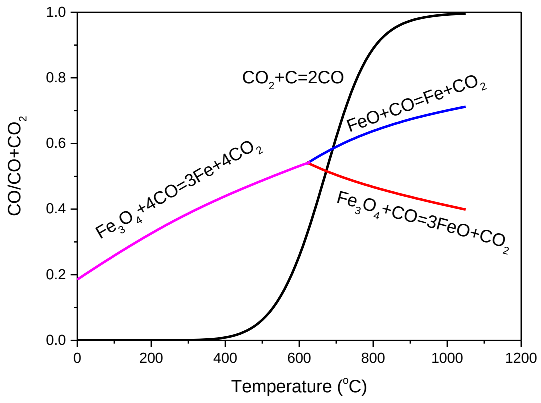

Figure 2.15. Stability of iron oxides in CO-CO_2 atmospheres [39].

Various carbon ratios were studied with the stoichiometric ratio based on the direct reduction ilmenite (equation 2.28).

Maximum metallisation of approximately 85% was achieved when the reaction was carried out at 1473 K with 30 weight.% Na_2CO_3 and 4 times the stoichiometric amount of carbon. Above 20 wt. %, the sodium carbonate was found to have a negligible effect on the iron oxide reduction.

Increasing the stoichiometric addition of carbon up to 4 times the stoichiometric amount improved metallisation, however, above 4 times the stoichiometric amount there was no significant increase in %R. Performing experiments in air may have demanded the stoichiometric excess carbon usage.

At higher temperatures of 1423 K and 1473 K presence of Fe_3C was observed. Formation of sodium titanates was reported to cause breaking of the ilmenite lattice creating a porous structure and promoting the release of iron oxides from the lattice, ultimately enhancing reduction of these iron oxides.

After experiments carried out in the 1373 K - 1473 K temperature range the $Na_8Ti_5O_{14}$, Na_4TiO_4 and Na_2TiO_3 phases were present along with sodium iron titanate compounds. The Na_2O-TiO_2 binary phase diagram in Figure 2.16 indicates three eutectic reactions:

i) $Na_8Ti_5O_{14}$ (N_4T_5) and $Na_2Ti_3O_7$ (NT_3)at 1258 K and 70.6 weight.% TiO_2

ii) Na_4TiO_4 (N_2T) and Na_2TiO_3 (NT) at 1135 K and 45 weight.% TiO_2

iii) Na_2O and Na_4TiO_4 at 1123 K and 24 weight.% TiO_2

The eutectic reactions show that molten titanates were present during the experiment carried out by El Tawil. The presence of liquid phases that can inhibit the diffusion of CO gas adversely affecting reduction is a disadvantage of performing experiments at elevated temperatures [120].

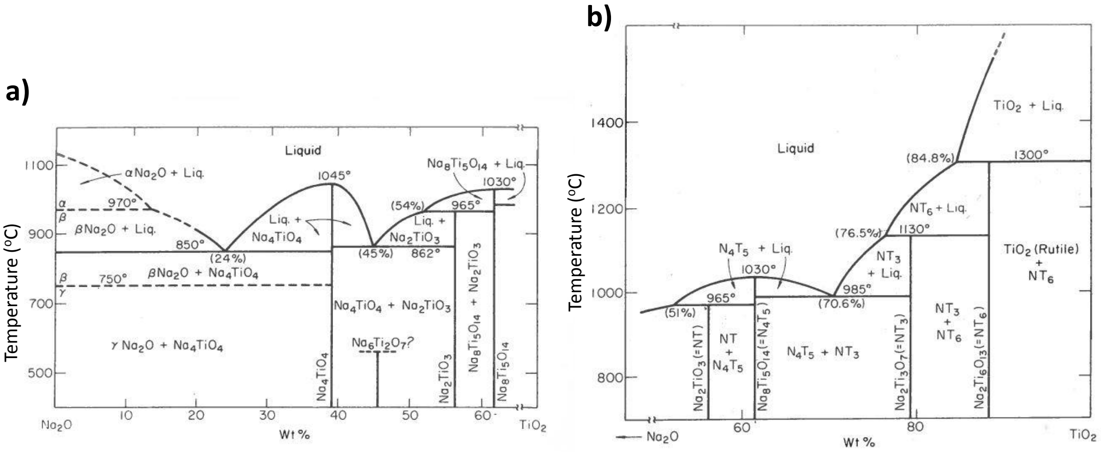

Figure 2.16. Na_2O - TiO_2 binary phase diagram [121].

Wet magnetic separation of the reduced samples was done to give magnetic and non-magnetic fractions. Although the current of the magnetic separator was varied, high recoveries for both iron and titanium dioxide was not demonstrated simultaneously. Table 2.2 shows that at 0.1 ampere significant quantities of iron reported to both the magnetic fraction and non-magnetic fraction while greater than 80% of the TiO_2 reports to the non-magnetic fraction. Formation of sodium iron titanate compounds that would report to the non-magnetic fraction explains the poor recovery at 0.1 ampere. However, increasing the current to 0.5 ampere increased the amount of Fe reporting to the magnetic fraction while also increasing the amount of TiO_2 reporting to the magnetic fraction to greater than 35%. Sintering of sodium titanates at high temperatures owing to the presence of the liquid phase could explain why the TiO_2 content in the magnetic fraction increased meaningfully. Carrying out reductive roasting experiments in air may explain why El-Tawil et al. were unable to achieve good separation as the reaction conditions were inadequate for the complete reduction of iron oxide.

Table 2.2. Separation of iron and titanium dioxide after magnetic separation for sample reduced at 1473 K.

Ampere	**Fraction**	**Weight.% Fe**	**Weight.% TiO_2**
0.1	Magnetic	58.5	16.8
0.1	Non-magnetic	40.9	82.7
0.25	Magnetic	94.8	35.5
0.25	Non-magnetic	5.0	63.8

2.4 Recovery of vanadium oxides

Titanomagnetite concentrates are the source of 85% of the world's vanadium bearing minerals. A range of feedstock comprise the remaining 15% of vanadium chemical supply. Table 2.3 provides a summary of the vanadium bearing minerals and their respective V_2O_5 content. It is evident from the table that the V_2O_5 of the T2 material exceeds that of several vanadium bearing feedstocks [122].

Table 2.3 Vanadium bearing feedstocks [7, 8].

Feedstock	V_2O_5 content, %	Product
Carnotite	18	Co-product
Vanadinite	18	Co-product
Patronite	30	Primary
Titaniferous magnetite / Iron Sands	0.3-3.0	Primary and co-product
Vanidiferous clay	0.3-0.7	Primary
Phosphate rock	0.3	Co-product
Bauxite / Red mud	2-14	Co-product / secondary product
Roscoelite	20-25	Co-product
Fly ash residue	3-7	Secondary product

2.4.1 Pyro-hydrometallurgical processes

2.4.1.1 Processing titaniferous magnetite

The mined ore is subjected to physical beneficiation consisting of : crushing; grinding; flotation (when necessary to remove gangue) and magnetic separation to give a vanadium enriched concentrate. Previously, Otanmäki produced an ilmenite concentrate along with the titanomagnetite concentrate.

2.4.1.2 Primary production of vanadium oxide from titaniferous magnetite

Primary production of vanadium pentoxide involves oxidative roasting of the titanomagnetite concentrate in the presence of alkali salts at 1073 K to 1503 K in a rotary kiln. Sintering of roasted products in the rotary kiln occurs at high temperature due to the formation of the liquid phase and the presence of a liquid phase also inhibits the diffusion of O_2 [123]. Typical alkali salts used for roasting include Na_2CO_3, Na_2SO_4 and NaCl.

Alkali reacts with coulsonite ($Fe_2V_2O_4$) present in the titaniferous magnetite to form water-soluble sodium vanadates and hematite (see equations 2.33, 2.34 and 2.35). Standard Gibbs free energy change calculations presented in Figure 2.17 show that reaction 2.33 is more thermodynamically favourable in comparison to reaction 2.34.

Sodium chloride roasting occurs between 1073 K and 1173 K for maximum effectiveness. However, roasting with NaCl requires the presence of water vapour even though corrosive HCl gas is generated (see equation 2.35) [124]. In the absence of H_2O, reaction 2.36 is less favourable as it has a $\Delta G^o_{1073\,K}$ of -208 kJ.mol^{-1} compared to -273.246 kJ.mol^{-1} for reaction 2.35, as seen in Figure 2.17. Sodium carbonate roasting is carried out in the 1173 K to 1473 K temperature range, whereas sodium sulphate roasting is typically performed in the temperature range of 1473 K-1503 K, owing to its higher melting temperature. A mixture of alkali salts are often utilised to improve the economics of the process, typically Na_2CO_3 and Na_2SO_4 are used in combination [7, 123, 125].

$$Na_2CO_3 + 1.25O_2(g) + FeV_2O_4 \rightarrow 0.5Fe_2O_3 + 2NaVO_3 + CO_2(g) \qquad 2.33$$

$$Na_2SO_4 + 1.25O_2(g) + FeV_2O_4 \rightarrow 0.5Fe_2O_3 + 2NaVO_3 + SO_3(g) \qquad 2.34$$

$$2NaCl + 1.25O_2(g) + FeV_2O_4 + H_2O(g) \rightarrow 0.5Fe_2O_3 + 2NaVO_3 + 2HCl(g) \qquad 2.35$$

$$2NaCl + 1.75O_2(g) + FeV_2O_4 \rightarrow 0.5Fe_2O_3 + 2NaVO_3 + Cl_2(g) \qquad 2.36$$

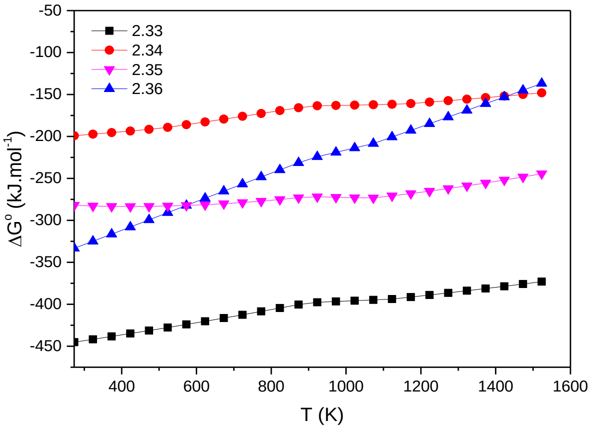

Figure 2.17. Standard Gibbs free energy change calculations for alkali roasting in air of coulsonite [35].

CaO present in the concentrate results in the formation of water-insoluble calcium vanadates which adversely affects the recovery of vanadium oxide during the subsequent water leaching stage. Therefore, CaO content of less than 1.5 weight.% in the titaniferous magnetite is preferred. Feedstock containing less than 3 weight.% SiO_2 is favoured as formation of low-melting sodium iron silicates occurs, trapping vanadium oxides as an insoluble solid solution [123]. The alkali reduction based process detailed in this report is capable of treating material with greater than 3 weight.% SiO_2 and 1.5 weight.% CaO.

The alkaline roasted residue is leached in hot water to solubilise the sodium-vanadate, with the T1- type solids sent to tailings storage. The resulting leach solution is filtered and sent for vanadium oxide separation and purification. The application of alkali roasting in air followed by water leach shall be referred to as alkali roast-water leach process, as this methodology is applied to various feedstocks. Typically, 60% to 80% of V_2O_5 is recovered from titaniferous magnetite using the alkali roast-water leach process [122].

Substantial amounts of iron oxide-rich tailings, such as T1, are generated by the alkali-roast water leach process and highlights its limitations when compared to the alkali reduction based process presented in this report, where TiO_2, V_2O_5 and Fe can be recovered from titanomagnetite feedstocks. Accumulation of significant tailings stockpiles presents an environmental hazard due to the risk of vanadium ions leaching out into ground soil [9]. The iron-rich tailings material is often not suitable for blast furnaces unless it is blended with hematite owing to the TiO_2 content of up to 20 weight.%, except in the case Otanmäki operations where the tailings material is a saleable product [122, 126]. The TiO_2 present adversely affects the viscosity of slag produced during blast furnace operation. Presence of chromite in the titanomagnetite concentrate represents a threat to the environment due to the formation of highly toxic Cr^{6+} ions during oxidative alkali roasting [127] (see equation 2.37).

$$2\mathrm{Na_2CO_3} + 1.75\mathrm{O_2(g)} + \mathrm{FeCr_2O_4} \rightarrow 0.5\mathrm{Fe_2O_3} + 2\mathrm{Na_2CrO_4} + 2\mathrm{CO_2(g)} \qquad 2.37$$

2.4.1.3 Co- production of vanadium oxide from titaniferous magnetite

Co-production of steel and vanadium pentoxide from titanomagnetite concentrates enhances valorisation of the material. Initially, the concentrate is pre-reduced in a rotary kiln with coal in the presence of CaO and SiO_2 at temperature of up to 1413 K. Pre-reduction decreases energy consumption during the subsequent smelting step where the CaO and SiO_2 act as fluxing agents. Smelting of the pre-reduced concentrate at 1623 K in an electric arc furnace produces molten pig iron containing dissolved vanadium along with a low-grade TiO_2 slag, such as T2 [124].

After the low-grade titania slag has been tapped off, the molten pig iron is transferred to a shaking ladle where it is oxygen lanced to transfer the vanadium to the slag phase, forming FeV_2O_4 spinel in the slag [128]. Oxygen addition is controlled ensure a limited amount of molten pig iron is oxidised to FeO, which oxidises V and serves to flux vanadium oxide into the slag phase [126].

Vanadium slag contains between 12 weight.% and 24 weight.% V_2O_5 depending on the origin of the concentrate. Molten pig iron is sent for steel production. Vanadium slag can be used directly for ferrovanadium production or subjected to alkali roasting – water leach process for recovery of vanadium oxides. The presence of chromite spinel presents a considerable challenge as the Cr_2O_3 content in the slag can approach up to 6 weight.% .

China and Russia have developed modified blast furnace operations for the production of steel and vanadium oxides from the titanomagnetite concentrates [129]. The V_2O_5 content of the slag from these countries varies between 10 weight.% and 18 weight.% V_2O_5 [7].

While co-production of vanadium oxide and vanadium chemicals from titanomagnetite concentrate is able to recover iron – as steel – and vanadium oxide present, generation of considerable amounts of low-grade TiO_2 slag is a negative aspect of co-production from titanomagnetite concentrates. The alkali reduction based process presented in this report demonstrates a route for extraction of iron, titanium dioxide and vanadium oxide while not producing the large quantities of waste associated with co-production of vanadium oxide from titanomagnetite concentrates.

Direct reduction of titanomagnetite concentrate

Several studies of titanomagnetite concentrate solid-state reduction have been carried out where it has been determined that reduction is slower compared to magnetite due to the existence of titanium cations that make titanomagnetite more thermodynamically stable [130]. The standard Gibbs free energy change for reduction of Fe_3O_4 (see equation 2.38) at 1473 K is -78 kJ.mol^{-1} compared to -56 kJ.mol^{-1} for reduction of Fe_2TiO_4 (see equation 2.39). Carbothermic reduction of titanomagnetite performed at a temperature of 1623 K was necessary to attain 97% reduction [131].

$$\mathrm{Fe_3O_4 + 4C \rightarrow 3Fe + 4CO(g)} \tag{2.38}$$

$$\mathrm{Fe_2TiO_4 + 2C \rightarrow TiO_2 + 2Fe + 2CO(g)} \tag{2.39}$$

Oxidation roasting of titanomagnetite concentrate before succeeding reduction has been reported to enhance the reduction process, similar to what has been observed with ilmenite [132]. Chen et al. [133] pre-oxidised titanomagnetite concentrate in the 1173 K to 1473 K temperature range to enhance the porosity of the concentrate. Carbothermic reduction of the pre-oxidised concentrate at 1473 K in the presence of

3 weight.% Na_2CO_3 resulted in 97 %R compared to 85 %R for the pre-oxidised concentrate reduced in the absence of Na_2CO_3. Pre-oxidation is an energy—consuming step that is avoided by the alkali reduction based process described in this report whilst still achieving a high degree of reduction.

2.4.1.4 Extraction of multiple metallic values from titaniferous magnetite

Jena et al. [134] smelted titanomagnetite concentrate at 1823 K in the presence of carbon producing 99% pure iron with titanium and vanadium oxides reporting to slag phase. Soda ash roasting of the slag at 1223 K followed by water leaching at 353 K was performed to recover up to 89% of the vanadium present in the slag. Two-stage leaching of the water leach residue utilising 20% HCl at 378 K yielded a 82 weight.% TiO_2 residue. The process given by Jena et al. [134] could not be applied to the T2 material as the material contains a limited amount of iron oxide. The process requires multiple high-temperature stages to produce iron and vanadium oxide, while producing a lower grade of TiO_2 compared to the TiO_2 produced in this report.

An initial step of direct reduction of titanomagnetite concentrate using coal and up to 3 weight.% Na_2CO_3 at 1473 K followed by magnetic separation of the reduced sample to yield an iron concentrate powder and a titanium-vanadium slag has formed the basis of several studies for tri-metal extraction from titanium magnetite concentrate [135-137]. The temperature utilised in the studies for the direct reduction of titanomagnetite concentrates with a catalytic amount of Na_2CO_3 at 1473 K is well above the temperatures used in this report, highlighting the importance of adding sufficient quantities of sodium carbonate during the reduction stage [135-137]. After reductive alkali roasting clear separation of an iron-rich magnetic fraction from a non-magnetic titanium-rich fraction and water-soluble sodium vanadate was demonstrated in this study, avoiding the need for the additional steps used in the existing processes described below.

Chen et al. [135] desilicated the titanium-vanadium slag by flotation and alkaline leaching. The desilicated slag was subjected to sodium hydroxide roasting at 773 K in air using a 1:1 slag:NaOH mass ratio forming sodium titanate, sodium vanadate and sodium ferrite, an additional step that is not required in the process given in this study due to the formation of sodium titanate and sodium vanadate during reductive alkali roasting. Water leaching at 323 K to solubilise sodium vanadate was performed and the solution separated for vanadium oxide recovery. Sulphuric acid treatment of the water leached solids forming a titanium oxysulphate solution was carried out followed by hydrolysis to precipitate $TiO_2.H_2O$. Hydrated TiO_2 was calcined at 1073 K to give an anatase residue containing 98 weight.% TiO_2.

Vanadium-titanium bearing non-magnetic fraction was leached in 6 M HCl solution at 423 K for 4 hours in order to dissolve vanadium, chromium and iron by Zhao et al. [136]. Vanadium and chromium were recovered from the solution using solvent extraction. 4.5 M NaOH leaching at 353 K was performed to remove residual silica present yielding a 93 weight.% TiO_2 slag. However, TiO_2 slag material produced is not suitable for chlorination as the residual V_2O_5 and Cr_2O_3 content of 0.54 weight.% exceeds chlorination feedstock limits. The alkali reduction based process presented in this report avoids the need of additional alkaline leaching for desilication and solvent extraction for vanadium recovery, providing a simpler extraction method over the described literature.

Zhong et al. [137] carried out two-stage HCl leaching on the V-Ti slag for vanadium oxide and titanium oxide extraction. Impurities including CaO, MgO, Al_2O_3 and SiO_2 were extracted during the first stage 5% HCl leaching at 377 K for 2 hours. The second stage leaching using 10% HCl and 30% hydrogen peroxide at 423 K for 1 hour yielded an 83 weight.% TiO_2 slag and an acid leaching solution enriched with vanadium. Calcination of the acid leached slag upgraded the TiO_2 content to 92.5 weight.%.

2.4.2.1 Recovery of vanadium oxides from other feedstocks

The high gangue content of the EHSV TiO_2 slag (T2) makes the alkali roast-water process unsuitable for treating the material. A study by Lekobotja et al. [138] involved roasting the material in air with up to 15 weight.% Na_2CO_3 and in a temperature range of 1373 K to 1473 K followed by water leaching. A maximum vanadium recovery of 27% was attained and the refractory $MgAl_2O_4$ was still present in the material. The low recovery of vanadium oxide demonstrates that the existing alkali salt roast – water leach process is not suitable for treating the T2 material.

Smelting of phosphate rock in the presence of silica and coke at 1473 K – 1773 K produces P_4 gas, which is condensed using water to give white phosphorus. Slag and ferrophosphorus containing up to 7 weight.% V_2O_5 and up to 5 weight.% Cr_2O_3 are by-products. Ferrophosphorus is subjected to the alkali salt roast-water leach process where typical alkali salts used are a mixture of Na_2CO_3 and NaCl [7, 123].

Vanadium clays are subjected to alkali roasting-water leaching process for the recovery of vanadium pentoxide [7, 123].

Gomez-Bueno et al. [139] extracted 85 % of the vanadium in Alberta tar sands fly ash by NaCl roasting with water vapour at 1198 K followed by 2M NaOH leaching at 371 K. Vanadium ions locked in the silica-alumina matrix made alkali roasting more appropriate over the conventional hydrometallurgical processes used to treat fly ash residues.

2.4.2 Hydrometallurgical processes

Hydrometallurgical methods using alkali or acid account for co-production and secondary production of V_2O_5. Alkaline leaching is considered to be more selective and is utilised when acid-consuming gangue are present, however, acid leaching kinetics tend to be superior compared to alkaline leaching [140]. The limited selectivity of acid means that separation is typically achieved by solvent extraction or ion-exchange [7]. The E_h-pH diagram shown in Figure 2.18 demonstrates that vanadium ions are soluble in acidic and alkaline conditions.

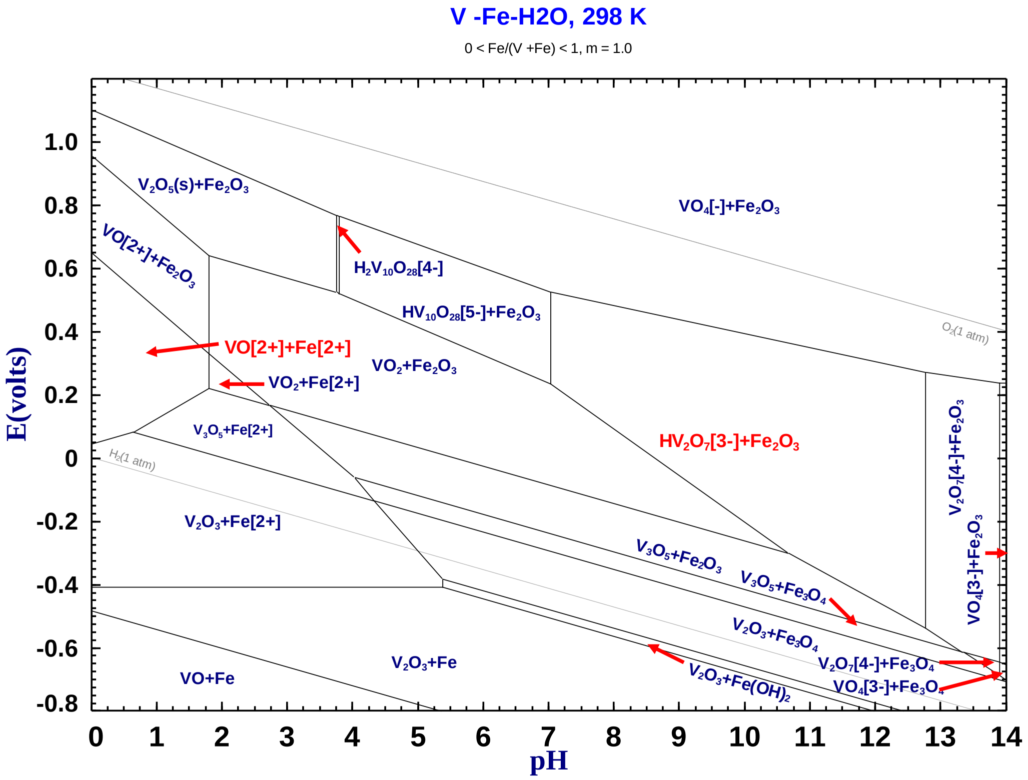

Figure 2.18 E_h –pH for V-Fe-H_2O system at 298 K [48].

Co-production of alumina and vanadium pentoxide occurs from bauxite containing high levels of V_2O_5. In the Bayer process bauxite is digested with NaOH forming sodium aluminate and water-soluble sodium vanadate, where V_2O_5 is purified from the Bayer liquor enriched with vanadium [123]. Further processing of the sodium aluminate yields Al_2O_3 and red mud as a waste product of the Bayer process. Okudan et al. [141] attained 79% vanadium extraction by single stage 353 K water leaching of Bayer process waste. Two stage hot water leaching followed by 2M H_2SO_4 leaching with Na_2SO_3 achieved 95 % vanadium extraction from Bayer process waste containing 14 weight.% V_2O_5 [142].

Alkaline leaching of uranium-bearing minerals, such as carnotite, is appropriate when acid-consuming gangue such as calcite ($CaCO_3$) is present. The greater selectivity of alkaline leaching over acid leaching decreases the quantity of impurities that need to be removed downstream. Use of alkali carbonates, including Na_2CO_3 and $NaHCO_3$, results in the formation of sodium uranyl vanadate. Alkali roasting of the sodium uranyl vanadate yields water-soluble sodium vanadate and an insoluble black oxide of uranium [143].

Carnotite, the uranium-vanadium ore, was a major source of vanadium before significant quantities of titanomagnetite were processed. Acid digestion of carnotite dissolves uranium and vanadium ions. Solvent extraction is performed to first remove the uranium ions from solution. The vanadium ions in the remaining solution are reduced by the addition of iron powder and $VOSO_4$ is separated by solvent extraction and subsequently purified.

Phosphate rock is acid leached with H_2SO_4 during the manufacture of phosphoric acid dissolving the vanadium in the process. The acidified solution is sent for purification for recovery of both vanadium pentoxide and phosphoric acid [7, 123].

Recovery of vanadium oxides from heavy oil and coal fly ash residues from power plants has been extensively researched as these residues contain up to 7 weight.% V_2O_5 and up to 4 weight.% NiO. Oil residues and spent catalysts are typically digested with H_2SO_4, often with the sparing of SO_2 gas to ensure reducing conditions are present, forming $VOSO_4$ which is purified using solvent extraction or ion-exchange.

Alkaline leaching techniques have also been applied for the reclamation of vanadium oxides from fly ash residues, where the choice of lixiviant is dependent on the mineralogy of the fly ash residue. Navarro et al. [144] achieved 98% vanadium extraction after 0.5M H_2SO_4 leaching for 24 hours at room temperature compared to 90 % vanadium extraction after 2M NaOH leaching for 24 hours. However, iron, nickel, aluminium and silicon were also solubilised during acid leaching, whereas only aluminium and silicon were dissolved during alkaline leaching. Vanadium oxide recovery by solvent extraction was demonstrated for both acidic and alkaline leachates. Selective precipitation was effectively applied to alkaline leachate. However, it was not possible to establish optimum conditions for selective precipitation from acidic leachate owing to the presence of impurities.

Pre-roasting of the fly ash before leaching was been found to enhance vanadium recovery provided the roasting temperature did not exceed 1223 K, as above this temperature less leachable V-Ni refractory compounds were formed [145, 146].

A summary of vanadium-bearing feedstock processing and purification is presented in Figure 2.19.

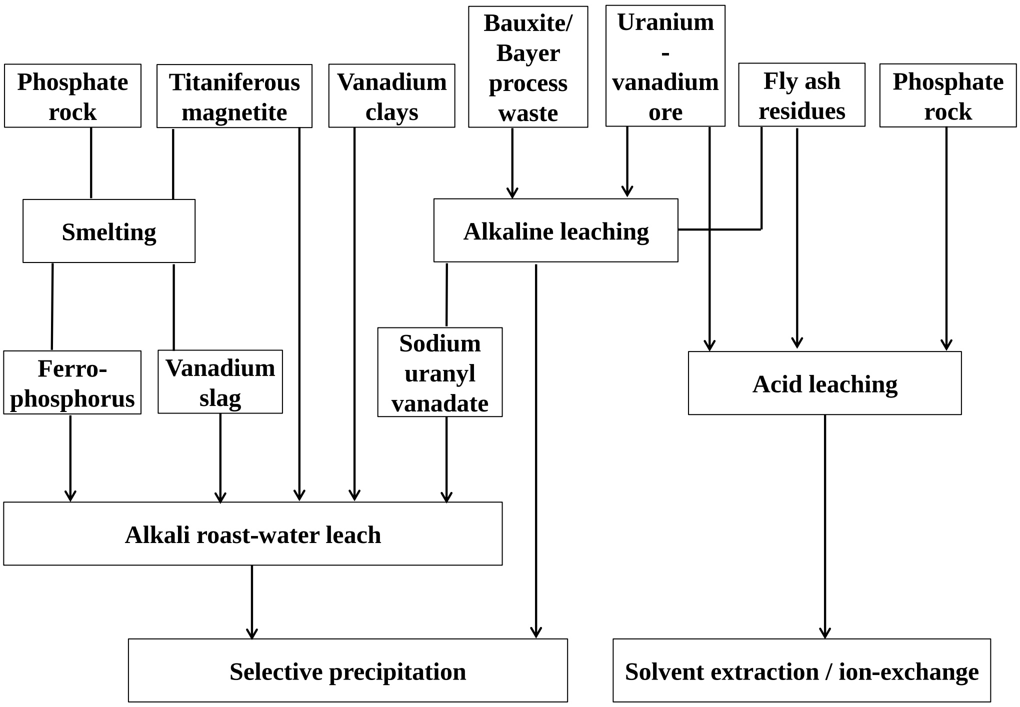

Figure 2.19 Summary block diagram for processing of vanadium-bearing feedstocks.

2.4.3 Separation and purification of vanadium oxides

Separation and purification of vanadium dissolved in solution is typically done by selective precipitation or solvent extraction.

2.4.3.1 Selective precipitation

Vanadium oxides solubilised by alkali roast - water leach process or alkaline leaching are recovered by selective precipitation as ammonium metavanadate (AMV) [147]. The greater selectivity of alkali salts for vanadium oxides results in a solution containing fewer impurities, such as SiO_2 and Al_2O_3 which are present as Na_2SiO_3 and $NaAlO_2$, respectively [123].

The pH of leachate containing sodium vanadates is usually above 12 allowing for selective precipitation of impurities by adjustment of the solution pH. Different plants employ varying methods for removal of impurities from the solution. Addition of the $Al_2(SO_4)_3$ at the appropriate pH can be used for desilication of the alkaline solution, according to equation 2.40. Alternatively, the pH of the solution may be lowered to 8 with a mixture of H_2SO_4 and $Al_2(SO_4)_3$ (see equation 2.41), where desilication is not required the solution pH is decreased to 8 in order to precipitate $Al(OH)_3$.

$$\mathrm{SiO_2 + Al_2(SO_4)_3 \rightarrow Al_2SiO_5 + 3SO_3(g)} \qquad 2.40$$

$$\mathrm{3Na_2O.2SiO_2 + 2NaOH + Al_2(SO_4)_3 \rightarrow Na_2O.Al_2O_3.6SiO_2 + Na_2SO_4 + H_2O} \qquad 2.41$$

Following separation of impurities from the solution, acid is added to decrease the pH from 8 to between 4 and 6. Ammonium salts such as $(NH_4)_2SO_4$ or NH_4Cl are added to the acidified solution which is then agitated to form AMV that precipitates from solution, according to equation 2.42 and 2.43 [148]. Ammonium salt choice is dependent on the acid utilised, where $(NH_4)_2SO_4$ is used in conjunction with H_2SO_4 while NH_4Cl is used with HCl. Utilising H_2SO_4 to lower the solution pH results in the formation of Na_2SO_4, which explains why certain plants perform alkali roasting with Na_2SO_4 or a Na_2SO_4–Na_2CO_3 mixture as it makes the process more economical due to recycling. Alkali roasting processes using NaCl alter the leachate pH with HCl to produce NaCl that can be recycled.

$$\mathrm{2NaVO_3 + (NH_4)_2SO_4 \rightarrow 2NH_4VO_3 + Na_2SO_4} \qquad 2.42$$

$$\mathrm{2NaVO_3 + 2NH_4Cl \rightarrow 2NH_4VO_3 + NaCl} \qquad 2.43$$

Calcination of AMV at 723 K is carried out to yield V_2O_5 of 99% purity and giving off NH_3 and water vapour according to equation 2.44.

$$\mathrm{2NH_4VO_3 \rightarrow V_2O_5 + NH_3(g) + H_2O(g)} \qquad 2.44$$

Selective precipitation of vanadium oxides form acidic solutions can be used, however, the technique is not as effective compared to alkaline solutions [144]. The limitations of selective precipitation of vanadium oxide from acid medium highlight the challenges faced by the sulphuric acid based EHSV process for recover of vanadium oxide during treatment of T2 material [58]. Vanadium ions in solution are oxidised to the pentavalent state by the addition oxidants such as sodium chlorate, sodium hypochlorite, hydrogen peroxide or sodium nitrate. Increasing the solution temperature to 368 K-373 K followed by raising the pH to between 2 and 3 using Na_2CO or NaOH results in the precipitation of sodium hexavanadate ($Na_4V_6O_{17}$) referred to as red cake. Co-precipitation of iron oxides with red cake occurs when iron ions are present in the acidic solution [149].

Air drying of red cake gives a residue containing 83 weight.% to 86 weight.% V_2O_5. Roasting of the air-dried red cake solids yields black cake 86 weight.% - 92 weight.% V_2O_5. Purity of V_2O_5 may be increased by dissolving red cake in Na_2CO_3 solution followed by observing the selective precipitation procedure for recovery from alkaline solutions to produce AMV which can be calcined to give high-purity V_2O_5 [123, 124].

2.4.3.2 Solvent extraction

Recovery of vanadium oxides from acidic solution is typically done by solvent extraction where amines or acidic organophosphorus reagents are used.

Di(2ethlyhexyl) phosphoric acid (D2EHPA), bis(2,4,4-trimethylpentyl) phosphinic acid (CYANEX 272) and 2-ethylexyl phosphonic acid mono 2-ethylexhyl ester (EHEHPA) are examples of common acidic organophosphorus extractants employed, which are often dissolved in kerosene.

Treatment of the leachate in mixer-settler units facilitates extraction of vanadium (IV) and vanadium(V) ions by D2EHPA from the aqueous phase to the organic phase. A pH in the region of 2 is maintained, where the reaction proceeds according to equation 2.45. HA represents acidic organophosphorus reagent [43].

$$\mathrm{nVO^{2+} + m(HA)_2 \rightarrow (VO)_n(A)_{2n}(HA)_{2(m-n)} + 2nH^+} \qquad 2.45$$

Co-extraction of ferric ions is a disadvantage of utilising D2EHPA as an extractant, however, this can be overcome by reduction of Fe^{3+} ions to Fe^{2+} using metallic iron, sodium sulphide or sodium sulphite [150, 151]. However, pentavalent vanadium ions are also reduced to the tetravalent state, which is favourable as vanadium in the tetravalent state is more readily extracted in the presence of D2EHPA [152, 153].

Vanadium complexes are stripped from the loaded organic phase utilising mineral acids or bases [144, 147]. Sodium chlorate is added to the strip solution to oxidise vanadium ions to the pentavalent state and sodium carbonate is added to precipitate red cake. The red cake is re-dissolved in Na_2CO_3 order to give high purity V_2O_5, as described earlier. On the other hand, ammonium salts can be added to the strip solution to precipitate AMV which can be calcined to yield V_2O_5 [151]. The barren organic phase is regenerated so that it can be recycled [4].

Alternatively, anionic amines can be used instead of acidic organophosphorus extractants. However, only pentavalent vanadium ions form complexes with amines, therefore, an oxidant such as H_2O_2 is typically added to ensure that only V^{5+} ions are present. Amines are able to form complexes with vanadium ions over a larger pH range compared to acidic organophosphorus reagents [154], where the reaction proceeds according to equation 2.46, when tertiary amines are utilised.

$$H_2V_{10}O_{28}^{4-} + 4R_3N_{HSO_4}^{H-} \rightarrow 4R_3N_{HH_2V_{10}O_{28}}^{H-} + 4HSO_4^- \qquad 2.46$$

Quaternary amine Alamine 336, primary amine Primene 81R and quaternary ammonium salt Aliquat-336 have proven effective in vanadium oxide extraction [144, 154-156]. Ammonia solution can be utilised to strip vanadium from amine complexes forming AMV as a result [152]. Use of a base to strip vanadium ions can be followed by addition of ammonium salts to the strip solution in order to form AMV [156].

Navarro et al. [144] reported that selective precipitation was more effective for recovery of vanadium oxides from alkaline solutions than solvent extraction.

Solvent extraction often requires several stages before AMV can be precipitated which is a disadvantage compared to selective precipitation [4, 40, 43].

2.5 Chapter Summary

Vanadium is present in solid solution with magnetite as coulsonite (FeV_2O_4), where V^{3+} ions (61 pm) readily substitute for Fe^{3+} ions (65 pm) in the inverse spinel. Ti^{4+} ions occupy octahedral sites in the titanomagnetite matrix where charged coupled substitution with ferrous ions occurs. Ilmenite can occur separately in beach sands but is often present in titaniferous magnetite due to subsolidus oxidation.

TiO_2 pigment production utilising the chloride process is favoured due to lower waste generation compared to the sulphate process. Technologies similar to the sulphate process have been developed for treating T2 material, consuming large quantities of sulphuric acid.

Commercial synthetic rutile production is achieved by Becher and Benelite processing of ilmenite sands, however, a TiO_2 content of greater than 50 weight.% is required, which is greater than the T1 content and iron oxide waste is generated by Becher and Benelite processes.

Smelting ilmenite recovers iron in the form of pig iron and produces titania slag. TiO_2 slag suitable for chlorination is generated by smelting ilmenite sands, whereas smelting rock ilmenite produces sulphate slag. Iron-rich tailings (T1) TiO_2 content is below the limits necessary for smelting. The UGS process developed to upgrade sulphate slag was applied to T2 where a maximum 75 weight.% TiO_2 was achieved, with $MgAl_2O_4$ remaining as a significant impurity. In this report alkaline reduction is shown to decompose the spinel phase, whereas alkali roasting performed by multiple authors failed to breakdown $MgAl_2O_4$, which hosts vanadium ions. Failure by Lekobotja et al. [138] to decompose the spinel may explain their limited vanadium oxide recovery.

Alkali roasting of ilmenite has been shown to enhance its porosity during roasting. Reductive alkali roasting of ilmenite at 1473 K failed to effectively separate iron from titanium dioxide. Addition of alkali salt during the reduction of titaniferous magnetite has been limited to the use of catalytic amounts where carbon gasification was enhanced and increased porosity observed. Methodologies developed for extraction of multiple metallic values from TM have involved several high temperature steps or the use of expensive reagent such as NaOH at >573 K. State-of-the-art technology is unsuitable for simultaneous recovery of metallic values from T1 and T2 materials owing to the gangue content of T2 and the low TiO_2 content of T1, however the process presented in this report has demonstrated recovery of multiple metallic values from the waste materials.

The process described in this report is shown to be able to treat feedstock of varying composition without significant addition of processing steps, as shown by treatment of T1 and T2, whereas the existing processes are often limited to materials that meet certain criteria or require additional steps, such as in the case of caustic soda leaching for silica removal.

2.6 Objectives of the study

- Characterise T1 and T2 materials to determine distribution of metallic values and chemical composition.
- Evaluate thermodynamics of reduction reaction in the presence and absence of alkali carbonates for determining the conditions for separating metallic values.
- Investigate the kinetics and mechanism of reductive alkali roasting of T1 and T2 mineral wastes.
- Study alkali reduction of T1 and T2 in semi-continuous operations using a rotary kiln and determine the influence of operating parameters.

- Demonstrate the conditions for separation and purification of TiO_2, V_2O_5, Al_2O_3 and Fe (only T1) from reduced samples.
- Develop block flow diagram for processing T1 and T2 and perform material and energy balance.

3 Materials and Methods

Chapter 3 details the materials used in this study, together with the experimental procedure and characterisation techniques employed.

3.1 Materials

Iron-rich tailings (T1) from oxidative salt roasting of titanomagnetite concentrate and low-grade titanium dioxide slag waste (T2) from smelting of titanomagnetite concentrate of South African origin were used in this study. Thermal decomposition and characterisation of South African titanomagnetite concentrate has been carried out for this investigation, with results presented in Chapter 4.

A list of the chemicals used is the experiments and analysis is presented in Table 3.1

Table 3.1 List of chemicals used in the investigation.

Chemical	**Supplier**	**Purity (%)**
Sodium carbonate	Alfa Aesar	98
Activated charcoal	VWR	-
Coal	Elitheni	65 (fixed
Activated carbon	Chemviron	-
Sodium bicarbonate	Prime Chemicals	-
Sodium bisulphate	Scientific Laboratory	92+
Ferrous sulphate heptahydrate	Acros Organics	99+
Potassium carbonate	Fischer Scientific	99.78
Lithium borate	Spex sample	66.67 $Li_2B_4O_7$-
Sulphuric acid	VWR	98
Hydrochloric acid	VWR	37
Ammonium hydroxide	Alfa Aesar	28
Argon Pureshield	BOC	-
Carbon dioxide	BOC	-
Iron(III) oxide		-
Calcium oxide	Minerals water	-
Magnesium oxide	Aldrich	99+
Manganese oxide	Alfa Aesar	99.9
Aluminium oxide	Alfa Aesar	99.99
Silicon dioxide	Sigma Aldrich	-
Sodium sulphate	Alfa Aesar	99.0+
Chromium (III) oxide	Alfa Aesar	98+
Synthetic rutile	Standards	92 (TiO_2)

3.2 Experimental Setup

3.2.1 Waste material preparation

Waste material (T1 and T2) up to 90mm in diameter was crushed to less than 3mm using the Retsch® Jaw Crusher BB 200. Waste material sized less than 3mm was milled to the appropriate size using the Retsch® RM200 mortar mill. Milled samples were sorted using sieves of different mesh size to give fractions with the following size distribution:

i) -90 μm
ii) +90 μm -106 μm
iii) +106 μm – 300 μm
iv) +300 μm -500 μm
v) +500 μm -1180 μm

3.2.2 High temperature treatment of feedstock materials

Using a mortar and pestle samples for high temperature treatment were thoroughly mixed with the necessary reagents using the appropriate weights ratios. The mixtures were subjected to carbothermic reduction in three types of furnaces. A summary of the masses of materials studied in the different furnaces is presented in Table 3.2.

Table 3.2 Summary of high temperature experiments.

Type of Furnace	**Material (g)**	**Alkali carbonate (g)**	**Reductant (g)**	**Weight ratio Material:Alkali:Reductant**
TGA	Titanomagnetite concentrate (2)	-	-	
TGA	T1 (1.65)	-	Activated charcoal (0.35)	1:0:0.21
TGA	T1 (1.41)	Na_2CO_3 (0.3)	Activated charcoal (0.3)	1:0.21:0.21
TGA	T1 (1.35)	K_2CO_3 (0.28)	Activated charcoal (0.3)	1:0.27:0.21
TGA	T2 (1.37)	Na_2CO_3(0.30)	Activated charcoal (0.012)	1:0.45:0.009
TGA	T2 (1.38)	Na_2CO_3(0.62)	Activated charcoal (0.055)	1:0.45:0.004
Tube	T2 (50)	Na_2CO_3(20)	Activated charcoal (4.5)	1:0.4:0.009
Tube	T2 (50)	Na_2CO_3(17.5)	Activated charcoal (4.5)	1:0.35:0.009
Tube	T2 (50)	Na_2CO_3(15)	Activated charcoal (4.5)	1:0.3:0.009
Rotary kiln	T1 (200)	Na_2CO_3 (21)	Activated carbon (46)	1:0.21:0.23
Rotary kiln	T1 (200)	Na_2CO_3 (31.8)	Activated carbon (46)	1:0.16:0.23
Rotary kiln	T2 (200)	Na_2CO_3 (90)	Activated carbon (18)	1:0.45:0.009

Thermogravimetric analysis

Thermogravimetric analysis (TGA) was adopted for investigating the weight changes during phase transformation and chemical reactions in waste materials when heated in different atmospheres in the temperature range 1073 K to 1323K. TGA analysis was utilised for studying reaction kinetics and for phase decomposition studies.

A schematic diagram illustrating the TGA apparatus set-up is provided in Figure 3.1. For loading samples in the TGA balance, an alumina crucible was suspended from the hook of a Sartorious microbalance, which has a sensitivity of 0.1mg. A silica tube was used for separating the sample-containing crucible from ambient atmosphere. The tube has an inlet for introducing desired gases to the system and an outlet for removing any gases evolved from reactions.

For heating the sample to a required temperature, the Lenton Furnace was raised using a pulley drive to ensure that the alumina crucible with the sample was positioned within the constant temperature zone of the furnace, as shown in Figure 3.1. The furnace temperature was controlled with a Eurotherm 808 controller and a type-K thermocouple (Nickel-Chromium/Nickel-Alumel) with the end placed near the crucible providing the feedback for maintaining the temperature. For isothermal experiments, the temperature was set to the required temperature before placing the sample-filled crucible inside the silica tube. For non-isothermal experiments, the crucible was placed in the silica tube at ambient temperature and a constant heating rate of 5 K/minute was programmed into the Eurotherm 808 controller to reach the required temperature.

SARTO COLLECT software and myPClab data logger were used for recording the weight and temperature data every 10 seconds, respectively. Experiments in the TGA apparatus were carried out under the flow of argon gas or compressed air utilising a flowrate of 500 mL/min and 1 bar pressure.

The weight and temperature data collected were combined to produce a percentage weight loss curves using ORIGIN PRO 9.1 software.

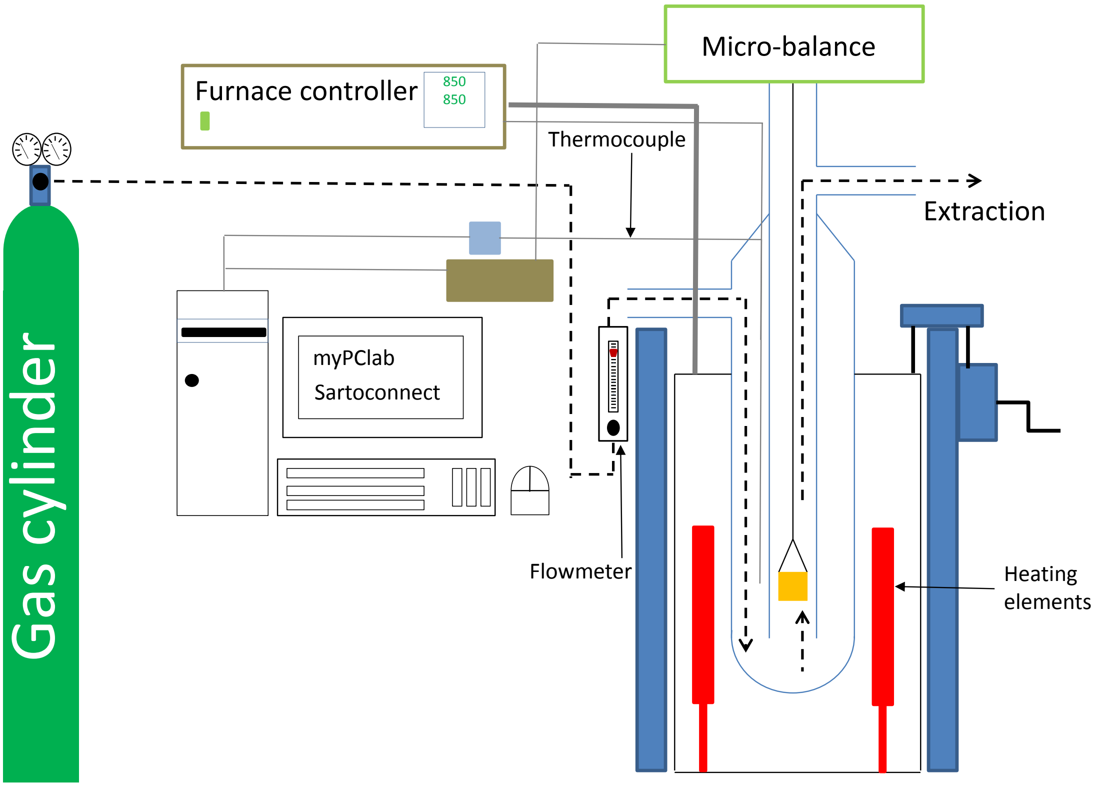

Figure 3.1. Schematic diagram of thermogravimetric analysis apparatus set-up.

Tube furnace

Mixtures (waste material + Na_2CO_3 + activated charcoal) were placed in an alumina crucible that was covered with a graphite block before being placed on a silica cradle. The graphite block was used to create a reducing atmosphere and a small hole was drilled through it to allow evolved gases to escape. Argon gas was purged through the alumina liner throughout the experiment to create an oxygen-free atmosphere with the regulator set to 1.4 bar and the flow rate set to 1 L/min. The Eurotherm controller was used to set the furnace temperature with a type-K thermocouple providing the temperature feedback necessary to maintain the furnace temperature. Once the set temperature was attained the cradle housing the alumina crucible was placed in the alumina tube for isothermal roasting in reducing conditions, as seen in Figure 3.2. Off-gases produced were directed to the extraction hood. After the allotted time the reacted samples were removed from the furnace and allowed to cool to room temperature while covered by an alumina crucible, in order to prevent re-oxidation of metallised iron. A schematic diagram of the tube furnace setup is given in Figure 3.2.

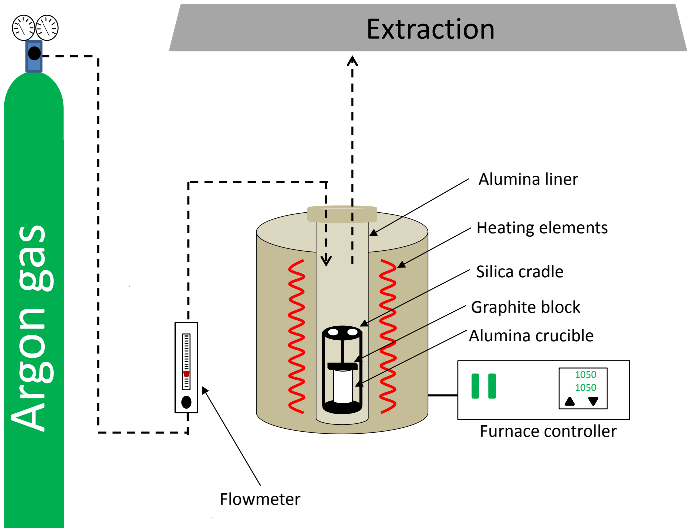

Figure 3.2 Schematic diagram of tube furnace set-up, including argon purge gas and extraction system.

Rotary kiln furnace

Figure 3.3 is a schematic diagram of the rotary kiln furnace setup. The feed (waste material + Na_2CO_3 + activated carbon) for the rotary kiln was prepared by adding the reagents in the required ratios and then mixing well using a mortar and pestle.

The indirect-fired rotary kiln had elements wound into the insulation surrounding the alumina tube, as seen in Figure 3.3. Temperature for the electrically-heated rotary kiln was set using a Siemens Simatic multi panel, with a heating rate of 573 K per hour. Temperature feedback was provided by the type-S thermocouple (platinium-10% rhodium/platinum). Once the temperature had reached the set point the mixture was fed into the hopper of the rotary kiln.

Argon gas was used to maintain an oxygen-free environment in the alumina tube. The regulator on the rotary kiln was set to 300 mbar and the flowrate set to 2 L/min. The Siemens multi panel was used to open the solenoid valve which allowed the purge gas to flow through the tube. A pipe was attached to the nozzle on the rotary kiln to direct the off-gases into the extraction system.

For each experiment, the rotary kiln tube was purged with argon gas for 3 minutes before the tube was raised to the appropriate angle of inclination by referring to the gradometer. The tube rotation, feed screw and hopper vibration were set and activated using the Siemens multi panel and this time was recorded as being the start of the experiment. The feed moved down the tube, through the hot zone and after a certain period of time fell into the collection bottle. The time when the sample began falling in the collection bottle was recorded, to give the residence time. After sample stopped falling into the collection bottle the heating elements and argon gas were turned off. Sample collected in the bottle was allowed to cool down over a period of 20 – 24 hours. The feed screw was removed and any sample present around the screw was placed in a sample bag. The inside of the alumina tube was visually inspected for ring-formation. Any material that remained in the tube was removed using a wooden rod, collected in the collection bottle and the quantity recorded.

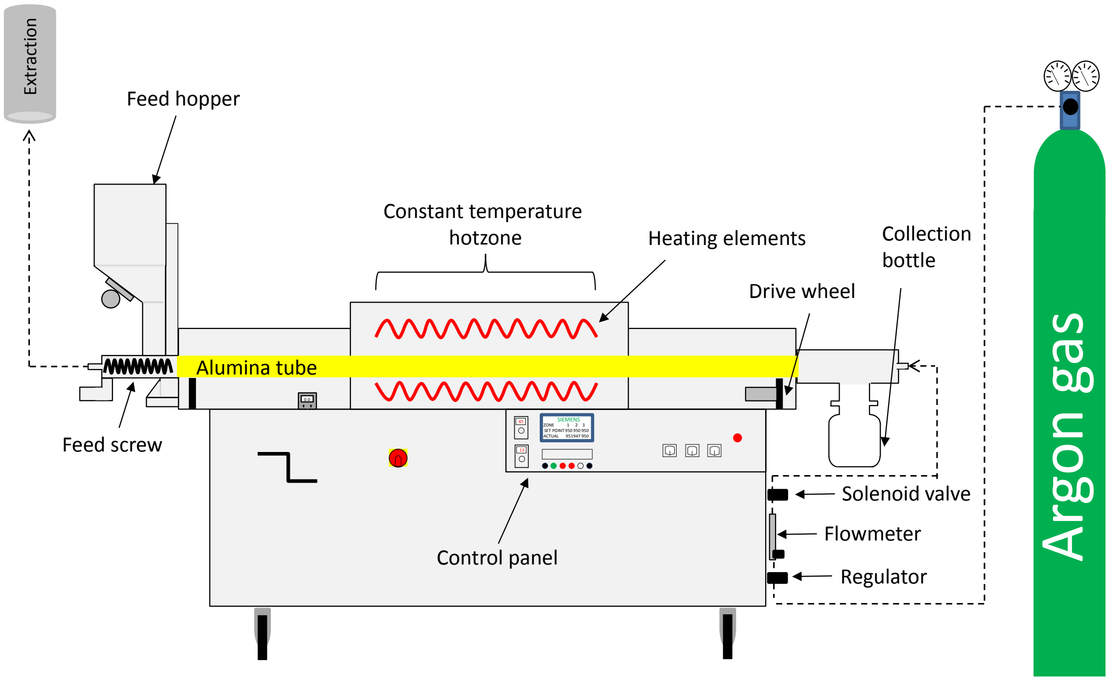

Figure 3.3. Schematic diagram of rotary kiln furnace set-up including argon gas and extraction system.

3.2.3 Processing of waste material reduced in the presence of alkali carbonates

Reduced T1 and T2 samples were ground in the Retsch® RM200 mortar mill for 30 minutes.

Magnetic separation

After grinding the reduced T1 samples were taken separately for magnetic separation so that a magnetic Fe-rich fraction could be physically separated from a Ti-rich non-magnetic fraction. The Wet Test Chute from Master Magnets Ltd, employing a NdFeB magnetic system was used. This activity involved placing the reduced solids that had been previously milled on the chute and washing with water and scrubbing with a brush to liberate the non-magnetics, including water-soluble compounds. The non-magnetics carried by the water were collected in a Nalgene beaker. The magnetic fraction remaining on the chute was removed, dried and milled again so that two-stage magnetic separation could be performed. The milled magnetic fraction was placed on the chute and separation was carried out with the non-magnetics collected in the original Nalgene beaker. The final non-magnetic fraction was then allowed to settle in order to accelerate subsequent filtration. The magnetic fraction after the second separation was dried and kept for smelting. The non-magnetic fraction was treated to recover TiO_2 and the solution processed for alumina and vanadium pentoxide recovery. The T2 material reduced in the presence of alkali carbonates was not subjected to magnetic separation owing to the low iron content.

Water leaching

T1 non-magnetic fractions and reduced T2 samples were water leached separately to solubilise the sodium vanadate and any other water-soluble compounds, namely sodium aluminate. A magnetic stirrer was placed in a Pyrex beaker and water was added to achieve the desired solid:liquid ratio , which varied from 1:5 g/mL to 1:10 g/mL. The beaker was situated on the Stuart® UC152 hot plate. The rotation speed on the magnetic stirrer was set to 200 rpm and the solids were poured into the beaker. The temperature of the water leaching solution was set to 353 K using the hotplate temperature dial. A FiveGo Mettler Toledo pH meter was used to monitor the pH and temperature of the leach solution. At the end of the leaching the solution was filtered using Whatman® cellulose filters. The solutions were kept for recovery of vanadium pentoxide and alumina, while solid leach residues were subjected to acid leaching.

Smelting of magnetic fraction

Fe-rich T1 magnetic fraction was mixed with 0.5 weight percent graphite in a mortar and pestle before being placed in an alumina crucible. The alumina crucible was covered with a graphite block that had a hole drilled in it. The alumina crucible was placed in a larger graphite crucible in order to maintain a reducing atmosphere.

Eurotherm 2132 and 2416 controllers were used to set the elevating hearth furnace temperature to 1323 K. The Type R thermocouple (platinum-13% rhodium / platinum) provided temperature feedback to the controllers. Argon gas was purged throughout the experiment using 2.5 L/min flowrate at 1.4 bar pressure. The alumina crucible was contained inside a graphite crucible that was placed on the furnace platform (see Figure 3.4). The furnace temperature was raised to 1723 K and the sample was held for 2.5 hours. After 2.5 hours the graphite crucible was removed and covered by a larger alumina crucible to prevent re-oxidation of iron.

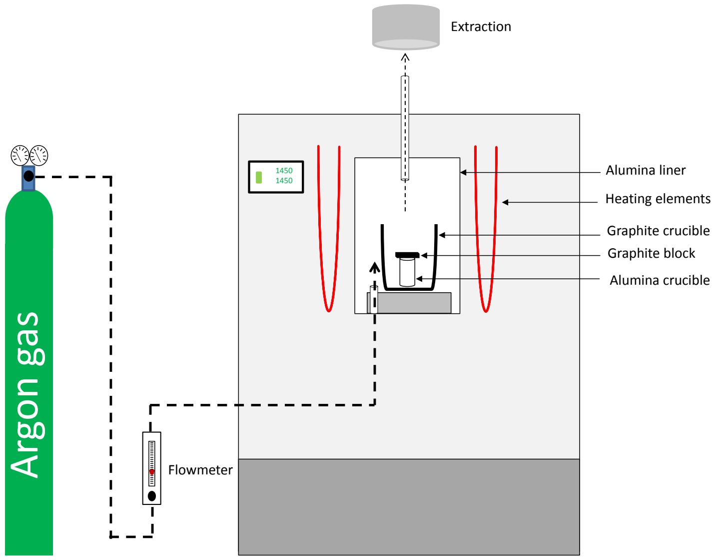

Figure 3.4 Schematic diagram of an elevating hearth furnace.

Acid leaching of water leached residues

Water leached T1 non-magnetic fraction was leached in a 0.5 M sulphuric acid (H_2SO_4) solution for two hours at 313 K. The solid:liquid ratio of 1:30 g/mL was utilised. Acid leaching of the water leached T2 residue was performed in a 0.5 M hydrochloric acid (HCl) solution for two hours at 313 K using a 1:8 g/mL solid:liquid ratio. The pH and temperature of the leaching solution were monitoring throughout the experiment using the FiveGo Mettler Toledo pH meter. The acid leach residues were filtered and water washed to remove any residual acid and water-soluble compounds. The dried residues were characterised using X-ray powder diffraction (XRPD) and X-ray fluorescence (XRF).

Recovery of vanadium pentoxide and alumina from solution

The filtered water leach solutions were evaporated on a hot plate to increase the sodium vanadate concentration in the solution. Once the appropriate volume had been evaporated the solution was filtered to remove any solids that precipitated during evaporation. Carbon dioxide (CO_2) gas was sparged into the solution to decrease the pH from 12 to 8. The regulator on the CO_2 cylinder was set to 1 bar and the flow rate set to 1 L/min. Sodium carbonate was regenerated during this step as alumina was precipitated and solid precipitates were subsequently filtered.

The pH of the filtrate was adjusted to 5 using H_2SO_4 followed by the addition of stoichiometric excess of ammonium sulphate ($NH_4(SO_4)_2$). The solution was agitated for 4 hours during which time the ammonium metavanadate (AMV) precipitated and was subsequently filtered. Precipitated AMV was deammoniated in an ELITE muffle furnace set to 723 K in order to produce a V_2O_5 rich residue.

Sulphate roasting

Acid leached T1 residue was mixed with sodium bisulphate ($NaHSO_4$) using the appropriate ratios with the mixture placed in an alumina crucible. The mixture containing $NaHSO_4$ was heated to 923 K and held for 1 hour. The calcined residue was water leached to yield a TiO_2 rich residue, which was characterised using XRF and XRPD.

Acid leached T2 residue was calcined with $NaHSO_4$ for 2 hours at 923 K. Ferrous sulphate was added during leaching of the roasted residue in order to solubilise calcium sulphate. The resulting TiO_2 residue was analysed using XRF and XRPD.

Alternatively, the acid leached T2 residue was intimately mixed with the H_2SO_4 and heated at 473 K for 3 hours. The resulting porous cake was water leached and filtered. Titanium oxysulphate in the filtrate was hydrolysed at 353 K for 1 hour. The titanium dioxide hydrate precipitate was calcined at 1173 K for 30 minutes to yield synthetic rutile.

Thermodynamic calculations

Thermodynamic calculations were performed using HSC Chemistry 5.1 software [35]. The software contains the necessary thermochemical databases for the standard Gibbs free energy change, mass and energy balance calculations. Graphs representing the thermodynamic data were produced using ORIGIN PRO 9.1 software.

FACTSAGE 6.4 [48] was used to compute E_h-pH diagrams, predominance area diagrams and phase equilibria. FactSage utilises different pure substances and solution databases for thermodynamic calculations, where the following databases were selected: FactPS, SGPS, FToxid, FTsalt and FTmisc.

3.3 Characterisation techniques

As - received and treated samples were characterised by X-ray powder diffraction (XRPD), X-ray fluorescence (XRF) and scanning electron microscopy (SEM) with energy dispersive spectroscopy (EDX).

3.3.1 X-ray powder diffraction analysis

The incident beam generated in the x-ray tube is directed towards the sample. Crystalline phases present have parallel planes of atoms with set interplanar spacing (d), also known as d-spacing, between the planes. Diffracted beams from parallel planes interfere constructively when the path difference between them is an integer multiple of the wavelength, therefore satisfying the Bragg condition (see equation 3.1) [157, 158].

$$n\lambda = 2d\sin\theta \tag{3.1}$$

Where N is the order of reflection, λ is the wavelength of the incident x-rays, θ is the angle of deflection/incidence and d is the space between planes.

A schematic illustration of the X-ray powder diffraction operation is given in Figure 3.5. The incident beam is directed onto the sample. The X-ray source and detector rotate at angle θ while the sample remains stationary. The intensity or counts recorded by the detector are measured against the diffraction angle (2θ).

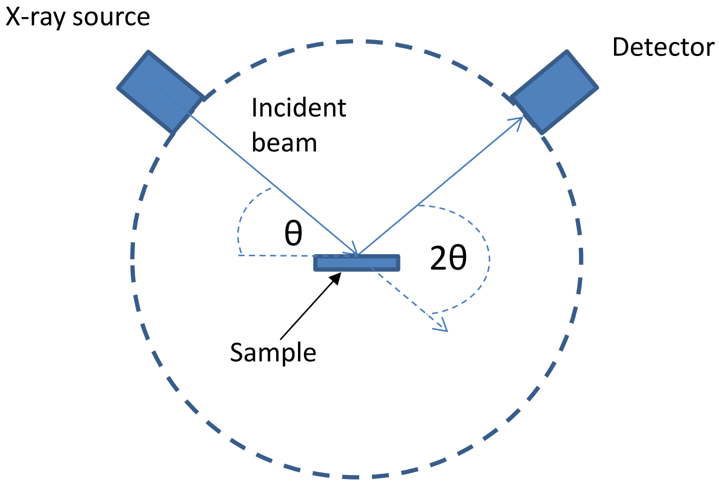

Figure 3.5. Illustration of X-ray powder diffraction operation.

Sample preparation

Waste materials and treated materials were analysed using XRPD. Finely ground samples were analysed with maximum 2θ range between 5° and 85° using the Philips X'pert machine with Cu K_α (0.15417 nm) radiation. The acceleration voltage was 40 kV, the current 40 mA and the step size 2θ = 0.0334225°. Phases present in the powder diffraction patterns were identified using the High score plus software which was supported by the ICDD PDF-4+ database.

3.3.2 Scanning electron microscopy

In scanning electron microscopy an electron beam is directed onto the surface of the sample where it interacts with the specimen and produces different signals, such as backscattered and secondary electrons, that are collected by detectors [159], as summarised in Figure 3.6.

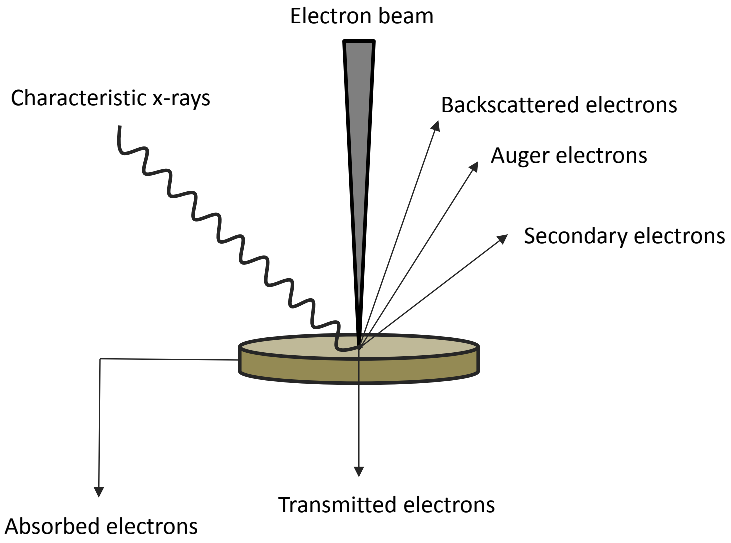

Figure 3.6. Illustration of interaction between electron beam and sample emitting different electrons and X-rays.

Backscattered electrons are high energy reflected electrons that have varying energies depending on the atomic number of elements in the sample. Elements with a high atomic number appear brighter than those with low atomic numbers [160]. The average atomic number contrast makes backscattered electron imaging well-suited to studying samples containing multiple phases and understanding their distribution, particularly minerals. Secondary electrons are used for morphological and topographical analysis of samples, and are emitted at lower energies compared to the backscattered electrons.

Energy dispersive X-ray analysis provides additional information when analysing the samples. Incident beam electrons displace electrons located in discrete orbital shells, creating vacancies in the orbital shell. Electrons from higher energy orbital shells move to fill the vacancy in the lower energy orbital shell releasing characteristic X-rays for each element. The characteristic X-rays are used to produce elemental maps, linescan profiles and EDX analysis results for chemical composition. The elemental composition of the sample is determined by detecting the number and energy of the characteristic x-rays emitted [159]

Sample preparation

Samples were placed in a resin mould (Diameter 2.5cm; Height 3.5cm) with a mixture of 5ml epoxy resin (EpoThin Epoxy Resin, Buehler) and 1.5ml epoxy hardener

(EpoThin Epoxy hardener, Buehler) and allowed to cure for 24 hours. Mounted samples were polished using Silicon Carbide paper (Buehler): P240; P600; P800; P1200: P2500 and P4000 on a Buehler MetaServ® 250 grinder-polisher. Polished resins were placed onto stems, painted with graphite and coated with an 8 nm layer of iridium to prevent charging.

Analysis of mounted samples was carried out using the variable pressure Carl Zeiss EVO MA15 scanning electron microscopy machine, operated using a 20 kV accelerating voltage, 8 mm working distance. An 80mm X-Max SDD detector was used to obtain backscattered images of the samples. The Oxford Instruments AZtecEnergy EDX system was employed to carry out elemental mapping, EDX Point&ID analysis and to acquire linescan data - providing information that could not be obtained by the XRD analysis, as amorphous phases and those present in minor amounts are not be detected by the diffractometer. Limited analysis of samples was performed using the ultra-high resolution Hitachi SU 8230 FE SEM.

3.3.3 X-ray fluorescence

XRF analysis was used to study the chemical composition of the waste material and processed products. Samples are bombarded with high-energy X-rays beams displacing ground state electrons creating vacancies in the orbital shell [161]. Fluorescence occurs as electrons from higher orbital shells move to fill the vacancies emitting characteristic X-rays in the process [162]. X-ray-fluorescence shares similarities with EDX, however, the primary difference is that the wavelength dispersive XRF (WDXRF) machine contains a crystal that diffract X-rays of a specific wavelength into the detector. WDXRF machines are only able to detect one element at a time unless multiple crystals are employed [163]. Wavelength dispersive spectroscopy results have superior resolution, minimal spectral overlaps and greater sensitivity compared to the energy dispersive detection techniques [164].

Sample preparation

As received and treated samples were analysed using X-ray fluorescence to determine their respective chemical compositions. Samples were heated in air at 1173 K to determine the loss on ignition. Subsequently each sample was mixed with a lithium borate flux in a platinum crucible using flux:sample ratio of 19:1 while ensuring a total weight of the mixture was 7 grams. The platinum crucible was placed in the Katanax® K1 Prime fusion furnace where a pre-set programme was operated. The molten flux-sample mixture was poured into a platinum mould by the fusion furnace and allowed to cool, forming a fused bead. Fused beads were analysed using the Rigaku ZSX Primus II multi-element wavelength dispersive X-ray fluorescence spectrometer with the ZSX Primus II software. Samples were analysed using semi- quantitative (EZScan) and quantitative programmes.

The quantitative programme was developed by preparing a series of 23 standards of known compositions with Fe_2O_3, TiO_2, V_2O_5, MgO,CaO,SiO_2,Al_2O_3,MnO, Cr_2O_3, Na_2O (added as Na_2CO_3) and SO_3 (added as Na_2SO_4). A commercial synthetic rutile standard of known composition was used as the 24th standard. The 24 standards were analysed using the EZScan and quantitative programmes with results of the analysis presented in appendix Table A.1 and Table A.2, respectively.

4 Phase analysis of materials

Chapter 4 presents characterisation of titaniferous magnetite, iron-rich tailings (T1) and low-grade TiO_2 slag (T2). Phase equilibria calculation results based on previous processing of TM are compared with T1 and T2 phase analysis. Phase transformations of TM heated in air and argon atmospheres in the 973 K-1273 K temperature are investigated.

4.1 Phase characterisation

The feedstocks, T1 and T2, investigated in this study have been characterised using X-ray fluorescence, X-ray powder diffraction and scanning electron microscopy. T1 and T2 are waste materials from processing South African titanomagnetite concentrate. Therefore, South African titanomagnetite concentrate has been characterised to provide insight into the raw material the waste products were generated from.

4.1.1 South African Titaniferous magnetite (TM) and iron-rich tailings (T1)

4.1.1.1 X-ray fluorescence of TM and T1

Chemical composition of the titaniferous magnetite given in Table 4.1 indicates that the V_2O_5 concentration is within the range of 1 weight.% -2 weight.%, which is typical of South African titanomagnetites [122, 124]. Silica content of 3 weight.% is at the limit of what can be tolerated of the alkali roast-water leach process without adversely affecting recovery of vanadium oxide [123].

Titanomagnetite concentrates subjected to alkali roast-water leach process for primary recovery of vanadium yield iron-rich tailings waste material, such as T1. A mixture of Na_2CO_3 and Na_2SO_4 were used for oxidative roasting at 1473 K of the titanomagnetite concentrate that produced the T1 waste material.

Chemical analysis of T1 is presented in Table 4.1. Expectedly, the V_2O_5 content in T1 is lower than TM as the vanadium ions were extracted as a water-soluble sodium vanadate during the previous processing that generated the waste material. The Na_2O and SO_3 content of T1 is higher than TM owing to the previous alkali roasting which resulted in residual amounts of alkali salts remaining in the solids. Iron oxide content of T1 and TM are comparable.

Table 4.1 Chemical composition of titaniferous magnetite and iron-rich tailings.

Weight. %	Fe_2O_3	TiO_2	V_2O_5	SO_3	Na_2O	Al_2O_3	SiO_2	MnO	CaO	MgO	Cr_2O_3
TM	71.4	13.4	1.9	1.3	4.4	2.8	3.0	0.3	0.6	0.9	0.1
T1	66.5	11.7	0.3	2.1	5.6	5	5.8	0.3	1.6	0.4	-

4.1.1.2 X-ray powder diffraction of titaniferous magnetite and iron rich tailings

The XRPD pattern given in Figure 4.1a shows that TM is a solid-solution of magnetite (Fe_3O_4) and ulvöspinel (Fe_2TiO_4), where both minerals have isometric crystals [165, 166]. Peaks for ilmenite ($FeTiO_3$) are also observed in the XRPD pattern due to sub-solidus oxidation the TM underwent [32].

Evident from Figure 4.1b is that the main phases in T1 are ilmenite, hematite (Fe_2O_3), ulvöspinel and magnetite. The peaks of $FeTiO_3$ and Fe_2O_3 overlap as both minerals have a hexagonal crystal structure [16, 38]. Hematite and ilmenite are present owing to the oxidation of magnetite-ulvöspinel during the previous oxidative alkali roasting that yielded the T1 waste material.

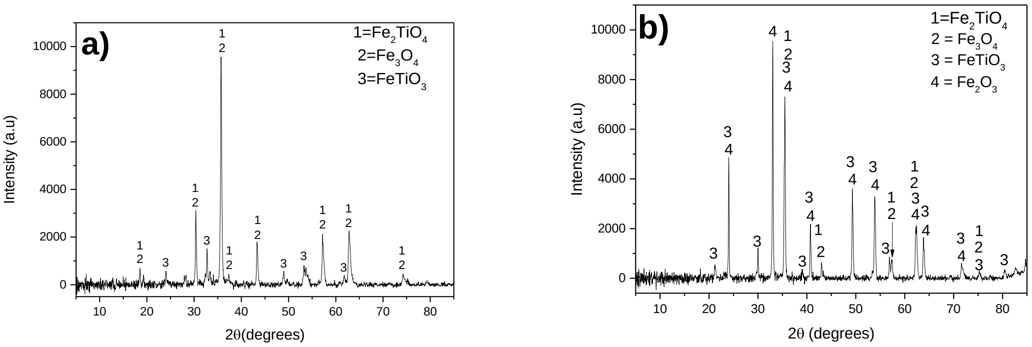

Figure 4.1 XRPD pattern for as received a) titaniferous magnetite and b) iron rich tailings. 1 – Fe_2TiO_4, 2- Fe_3O_4 and 3- $FeTiO_3$ and 4-Fe_2O_3.

4.1.1.3 Scanning electron microscopy of titaniferous magnetite and iron-rich tailings

Titaniferous magnetite

The backscattered SEM image in Figure 4.2 shows the cloth-like interwoven microstructure that is typical of the titanomagnetite concentrates [30].

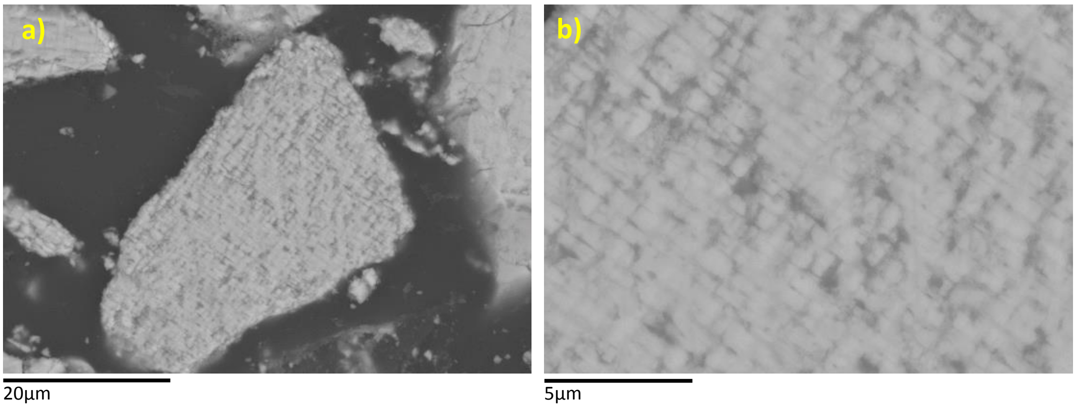

Figure 4.2 Backscattered SEM image of titaniferous magnetite at a) low magnification and at b) high magnification.

SEM-EDX data show a fairly uniform distribution of elements where the composition in Area C of Figure 4.3 corresponds to the magnetite phase enriched with vanadium ions present as coulsonite (FeV_2O_4). Coulsonite is in solid solution with magnetite and ulvöspinel [17]. The dark grey areas represented by A and B in Figure 4.3 are aluminosilicates attached to the magnetite grain. Area B, adjacent to the magnetite grain, contains 32.4 weight.% Fe compared to 1.0 weight.% Fe for area A. XRPD phase analysis shown in Figure 4.1a of TM agrees with the magnetite phase observed in the SEM. However, the aluminosilicates were not observed in the XRPD pattern.

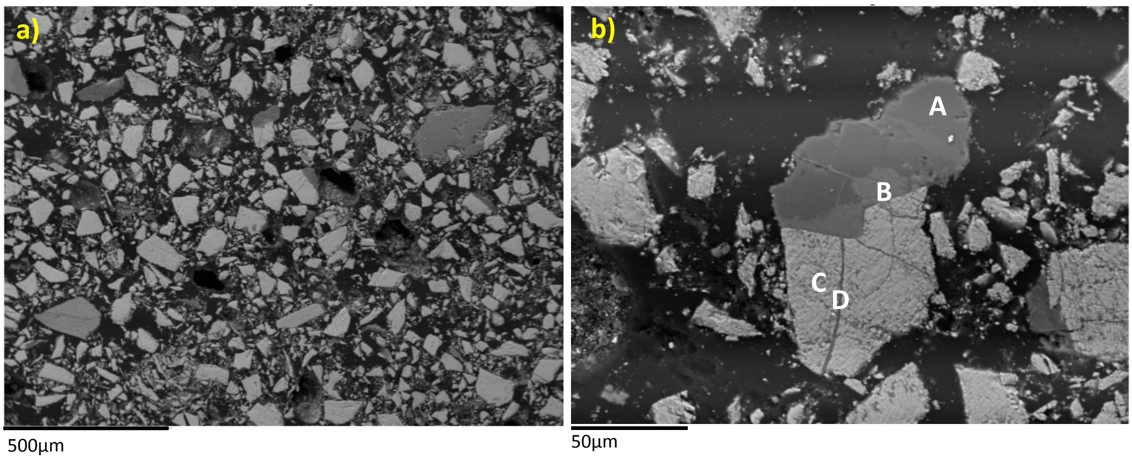

Figure 4.3 Backscattered SEM image of titaniferous magnetite a) low magnification image b) high magnification image.

Table 4.2 Elemental composition of areas A to D on Figure 4.3.

Weight.%	Ti	Fe	O	Na	Al	V	Si	Ca	Mg	K	Mn
A	-	1.0	42.2	3.4	16.4	-	27.1	9.7	-	0.2	
B	0.2	32.4	37.9	-	11.8	-	13.1	0.5	4.1	-	-
C	9.1	60.1	24.5	-	2.2	1.6	1.3	0.1	0.7	-	0.3
D	5.8	35.0	36.7	-	9.4	0.8	6.7	-	5.6	-	-

Iron-rich tailings

Backscattered scanning electron microscopy images of the iron-rich tailings (T1) are presented in Figure 4.4. Analysis of the light grey area (see Area A on Figure 4.4) indicates that this is hematite in solid solution with ilmenite, agreeing with the XRPD results given in Figure 4.1b [16]. The dark grey area (see Area B on Figure 4.4) represents a Na-Ti-Si-Al-Fe-O complex enriched with vanadium oxide, likely owing to formation of a liquid phase [123]. Formation of Na-Ti-Si-Al-Fe-O complex during alkali roasting of the concentrate decreases vanadium extraction during the water leaching as vanadium ions are trapped in the complex.

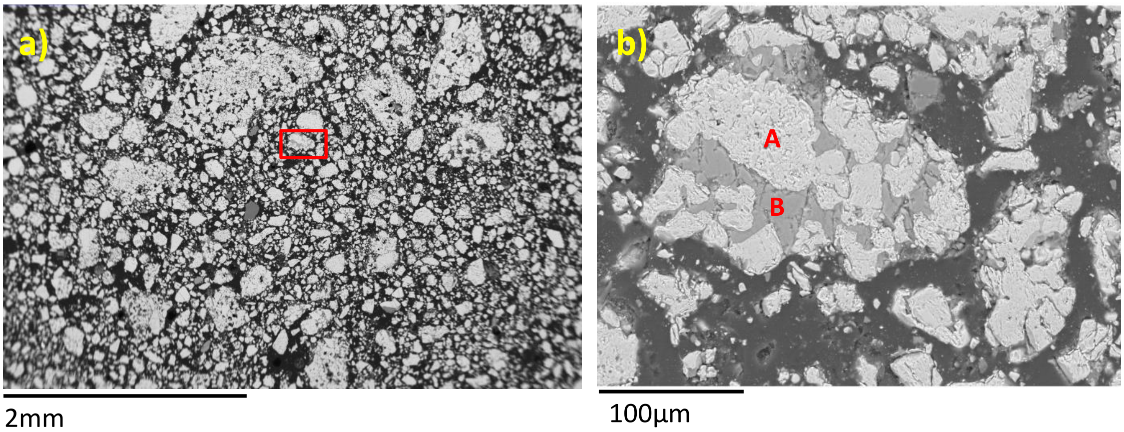

Figure 4.4. Backscattered SEM image of as received iron-rich tailings a) low magnification image and b) high magnification image.

Table 4.3. Elemental composition of areas A and B on Figure 4.4b, as analysed by EDX.

Weight.%	Ti	Na	Fe	O	Si	Mg	Al	Cr	Mn	V	Ca
A	5.1	0.7	52.3	37.9	0.34	0.55	1.46	0.2	0.3	0.2	-
B	11.1	14.5	11.6	39.7	8.9	-	5.9	-	-	6.1	1.7

During alkali roasting of titanomagnetite concentrate the sodium salts react on the surface of the Fe-rich oxides to form phases that react with the low-temperature eutectic sodium aluminosilicates, producing the Na-Fe-Al-Si-O complex observed in the iron – rich tailings microstructure – (see Area A in Figure 4.5) [120]. At the interface between the light grey regions and the sodium aluminosilicate there are dark black phases (see Area B on Figure 4.5), where up to 20.6 weight.% Fe dissolved in the sodium aluminosilicate. The Na-Fe-Al-Si-O complex observed in Figure 4.5 is not enriched with vanadium ions as was seen in Area B on Figure 4.4. The difference in vanadium content is a result of the Al content, where 5.9 weight.% Al is localised in Area B of Figure 4.4 compared to 16.6 weight.% and 12.6 weight.% Al for areas A and B in Figure 4.5. Increased Al content of the Na-Fe-Al-Si-O complex raises the melting temperature of the species, decreasing the amount of vanadium ions dissolved in the complex [123].

The elemental mapping in Figure 4.6 indicates these dark phases are complex sodium aluminosilicates and the light grey phases are Fe-rich oxide with titanium ions dissolved in the matrix. The EDX analysis of Areas C and D of Figure 4.5 demonstrates composition of more than 68 weight.% Fe, approximately 7 weight.% Ti and a limited amount of V (0.1 weight.%), showing that this is magnetite in solid solution with ulvöspinel. The cloth-like interwoven microstructure characteristic of titanomagnetite concentrates, as seen in Figure 4.2, is evidently destroyed during oxidative alkali roasting. Observing T1 material micrographs shown in Figure 4.4 and Figure 4.5 highlights that the interwoven microstructure is no longer visible.

Table 4.4 Elemental composition of areas A to D on Figure 4.5.

Weight.%	**Ti**	**Fe**	**O**	**Na**	**Al**	**V**	**Si**	**S**	**Ca**	**Mg**	**Mn**
A	1.5	6.2	4.8	17.6	16.6	-	17.0	4.7	1.4	-	-
B	3.4	20.6	30.5	15.2	12.6	-	13.0	3.4	1.3	-	-
C	7.3	68.6	20.5	1.1	1.1	0.1	0.5	-	-	0.5	0.3
D	7.6	70.3	20.6	-	0.8	0.1	-	-	-	0.5	0.2

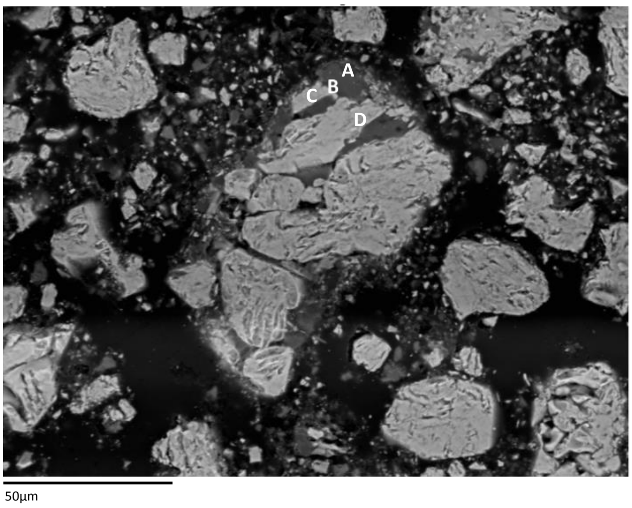

Figure 4.5 Backscattered SEM image of as received iron-rich tailings.

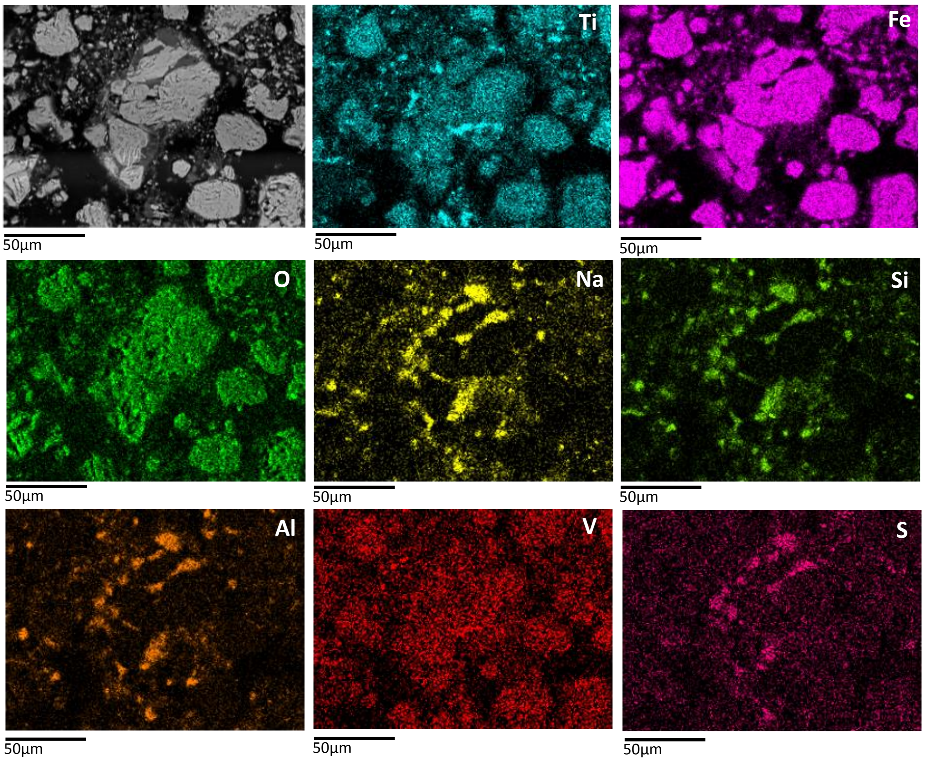

Figure 4.6 Backscattered SEM image of as received iron-rich tailings with elemental mapping.

Disadvantages of the original high temperature processing that yielded T1 waste material are evident from the phase analysis as vanadium ions remain present in Na-Fe-Al-Si-O complexes produced, as shown in Area B of Figure 4.4, and Fe_3O_4-Fe_2TiO_4 solid solutions not completely oxidised. Formation of liquid complexes and phases inhibits the diffusion of O_2 gas [123]; the deleterious consequences are evident in Figure 4.7 where the multi-component system illustrates the importance of O_2 partial pressure as between $-9 < \log_{10}P(O_2)(atm) < -7$ Fe_3O_4 and FeV_2O_4 co-exist in the same phase field. However, at $\log_{10}P(O_2)(atm) > -0.3$ Fe_2O_3 is the stable phase

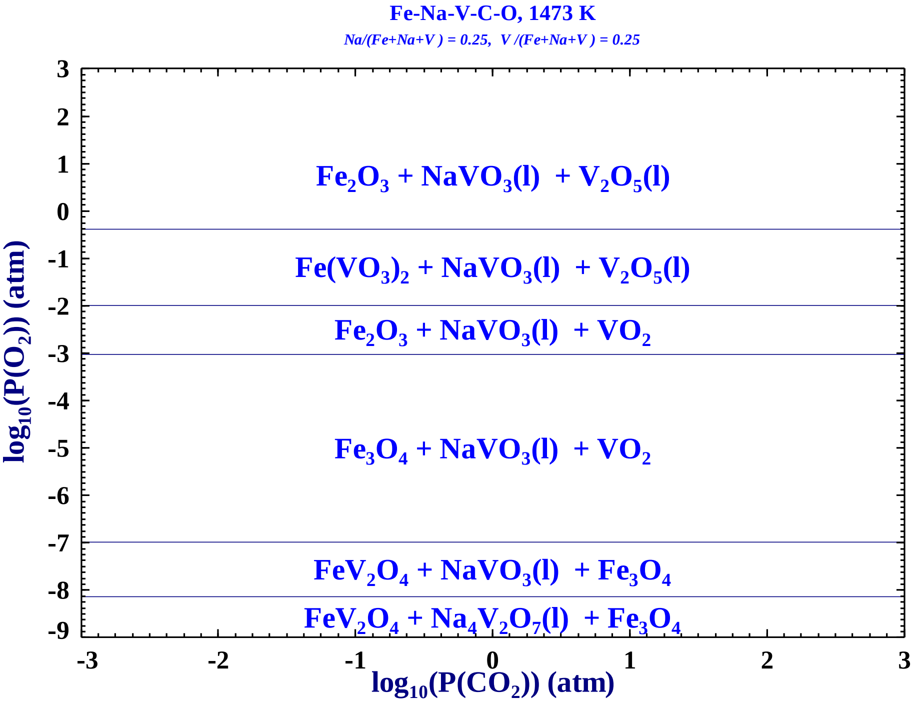

Figure 4.7 Predominance area diagram for the Fe-Na-V-C-O multi component system at 1473 K, computed using FactSage software [48]

4.1.1.4 Phase equilibria calculations iron-rich tailings material

Equilibrium phase compositions deduced from FactSage calculations in order to predict phases from oxidative alkali roasting of the titanomagnetite concentrate are presented in Table 4.5 [48]. Computed results are compared with phase analysis of the T1 material.

The major phase present from the equilibria calculation is Fe_2O_3 which is in agreement with observations of the XRPD pattern for T1 material (Figure 4.1b). Predicted titanium-bearing phases differ from the T1 phase analysis, where Na_2TiO_3, Fe_2TiO_5, $MgTiO_3$ and $CaTiO_3$ were not observed. $NaAlSiO_4$ expected from phase equilibria broadly agrees with the sodium aluminosilicate complexes shown in the micrographs (Figure 4.4 and Figure 4.5). Formation of water-soluble $Na_4V_2O_7$ is expected as shown in Table 4.5. The phase would be extracted during water leaching that follows alkali roasting. Recovery of sodium vanadate during previous alkali roast-water leaching explains the low V_2O_5 content of T1 material. A lack of solution data for complex salt phases in the FactSage software database explains why the complexes observed in the SEM analysis were not predicted by the calculations.

Table 4.5 Phase equilibria for alkali roasting of titanomagnetite concentrate at 1473 K [48].

Input		**Roasting at 1473 K**	
	Mass(kg)	**Phase**	**Mass (kg)**
TM concentrate	1000	Fe_2O_3	587.01
Na_2CO_3	51	Fe_2TiO_5	133.57
Na_2SO_4	12	Na_2TiO_3	59.12
Air	725	$NaAlSiO_4$	42.56
		$Na_4V_2O_7$ (l)	28.57
		$MgTiO_3$	21.22
		$MgAl_2O_4$	20.55
		$CaTiO_3$	19.33
		$MnFe_2O_4$	9.75
		$MgCr_2O_4$	5.06
		Na_2SO_4(l)	4.59

4.1.2 South African low-grade titanium dioxide slag (T2)

Low grade TiO_2 slag (T2) refers to slag that was produced by Highveld Steel and Vanadium Limited, a company in South Africa that co-produced steel, vanadium slag and other vanadium chemicals. Pre-reduction of titanomagnetite concentrate in the direct-fired rotary kiln was performed with dolomite and quartz added to flux the titania into a fluid slag during the subsequent smelting step [65, 122, 124, 126]. Pre-reduced solids were smelted and the low-grade TiO_2 slag tapped off with the molten pig iron, containing vanadium, taken for vanadium slag recovery and steel production [126]. Initial addition of fluxes has negative implications on the processing of T2 and hinders the recovery of metallic values by complexing TiO_2.

4.1.2.1 X-ray fluorescence of low-grade TiO_2 slag

The complex mineralogy and varied distribution of vanadium ions in T2 material affects the recovery of vanadium oxide. Vanadium oxide present in a range of concentrations is found in different mineral and alloy phases, as seen in the scanning electron micrograph data presented below. Bulk analysis given in Table 4.6 is unable to give a specific mineral composition due to the variation expected in the T2 stockpile. However, the V_2O_5 concentration of T2 may be higher than certain deposits (see Table 2.3). The titanium dioxide containing T2 feedstock contains a significant amount of gangue in the form of calcium oxide, magnesium oxide and silicon oxide, as a consequence of their addition as fluxes, which makes processing the T2 material more difficult.

Table 4.6. Chemical composition of low grade TiO_2 slag feedstock presented as a range based on multiple analyses of the material.

Weight.%	Fe_2O_3	TiO_2	V_2O_5	CaO	SO_3	Na_2O	Al_2O_3	SiO_2	MnO	MgO	Cr_2O_3
	3.4 -8.8	29.5 - 34.8	0.8- 1.2	15.6- 17.4	0.5- 1.2	0.3- 5.8	10.4- 12.7	14.8- 19.8	0.6- 0.8	10.6- 10.7	0.1- 0.2

4.1.2.2 X-ray powder diffraction of S.A. low-grade TiO_2 slag

The presence of complex phases in T2 was confirmed in the XRPD analysis given in Figure 4.8. $CaMg_{0.39}Ti_{0.48}Al_{0.87}Si_{1.26}O_6$ was the dominant phase present representing the slag matrix formed during the smelting of pre-reduced titanomagnetite concentrate. TiO_2 in the T2 predominantly crystallised as perovskite ($CaTiO_3$) phase in the presence of significant quantities of lime. A karooite ($MgTi_2O_5$) – tialite (Al_2TiO_5) solid solution formed as a result of the high magnesia concentration in the flux [65]. The magnesia content causes primary phases crystallisation competition between the $MgTi_2O_5$-Al_2TiO_5 solid solution and the Mg(Al,Ti,V)O_4 spinel - which precipitates first owing to it higher melting point [167]. $MgAl_2O_4$ is observed in Figure 4.8.

The rutile phase observed in the XRPD pattern can be explained by increasing the acidity of the slag due to SiO_2 addition, as this was found to promote the formation of the rutile phase over perovskite and the pseudobrookite structure (karooite) [168]. However, rutile crystallises as small agglomerates in the glassy slag matrix [169]. Fassaite ($CaFe_2SiO_6$) is a minor phase present in the T2.

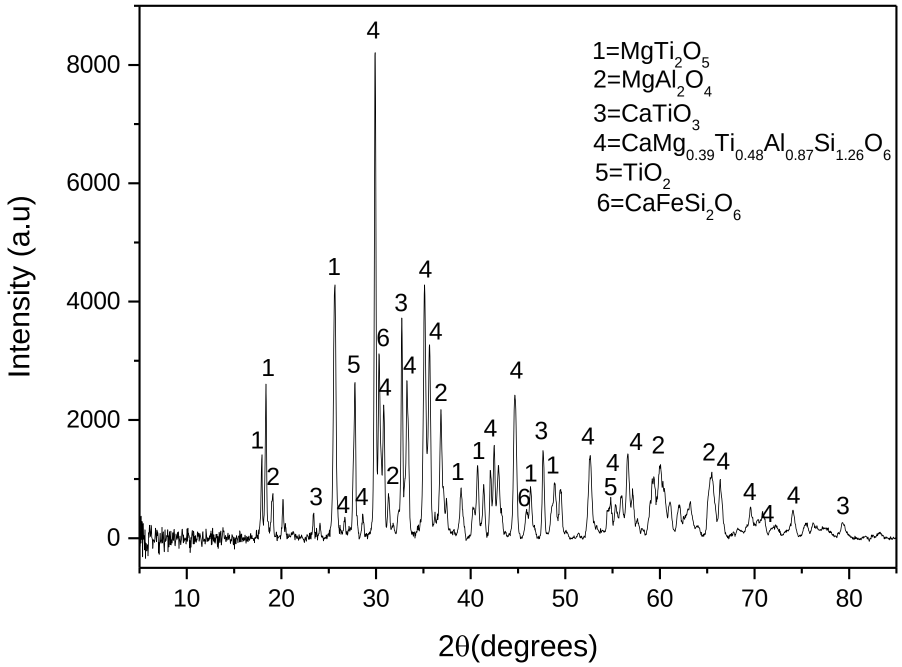

Figure 4.8 XRPD pattern for as received low-grade TiO_2 slag. 1-$MgTi_2O_5$, 2-$MgAl_2O_4$, 3-$CaTiO_3$, 4-$CaMg_{0.39}Ti_{0.48}Al_{0.87}Si_{1.26}O_6$, 5-TiO_2, 6-$CaFeSi_2O_6$.

4.1.2.3 Scanning electron microscopy of low-grade TiO_2 slag

The low-magnification electron micrograph of T2 can be seen in Figure 4.9. Elemental mapping given in Figure 4.10 illustrates that the $MgTi_2O_5$ phase crystallises as rod shaped grains, which is the typical morphology of the pseudobrookite structure [170]. The elemental mapping indicates the vanadium ions are dissolved in the $MgTi_2O_5$ phase.

TiO_2 in slags often form the stable $CaTiO_3$ compound that was observed in the XRPD pattern (see Figure 4.8) [171]. The fine dendritic microstructure dispersed in the slag matrix seen in Figure 4.9 is characteristic of $CaTiO_3$ in titanium-bearing slags, where lime is able to react with TiO_2 giving rise to the dendritic structure [168, 172-175].

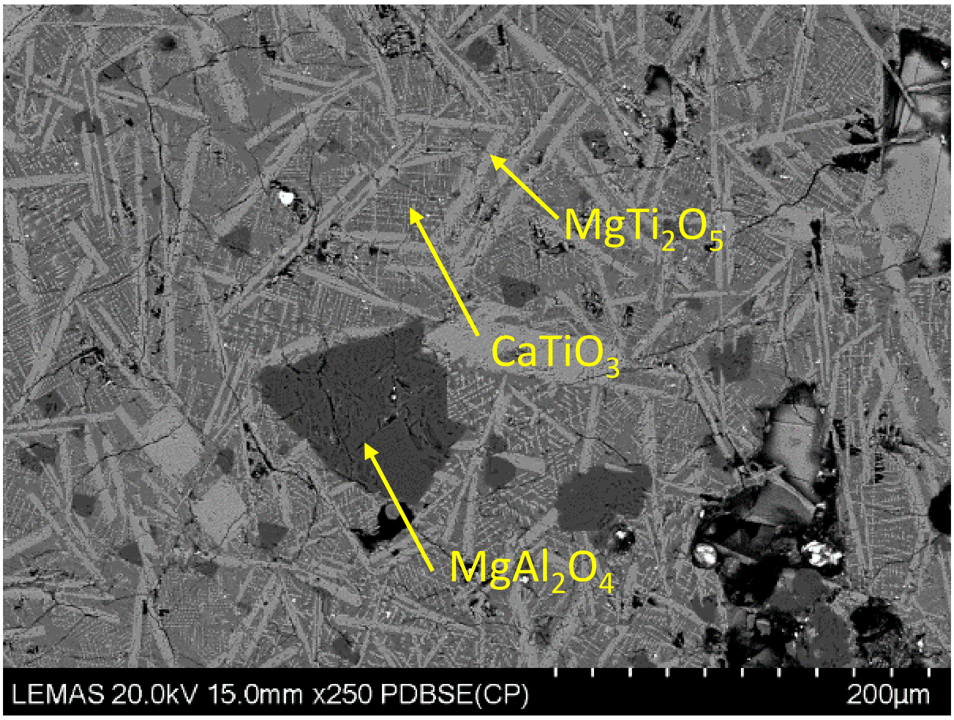

Figure 4.9 Low magnification backscattered SEM image of as received low-grade TiO_2 slag.

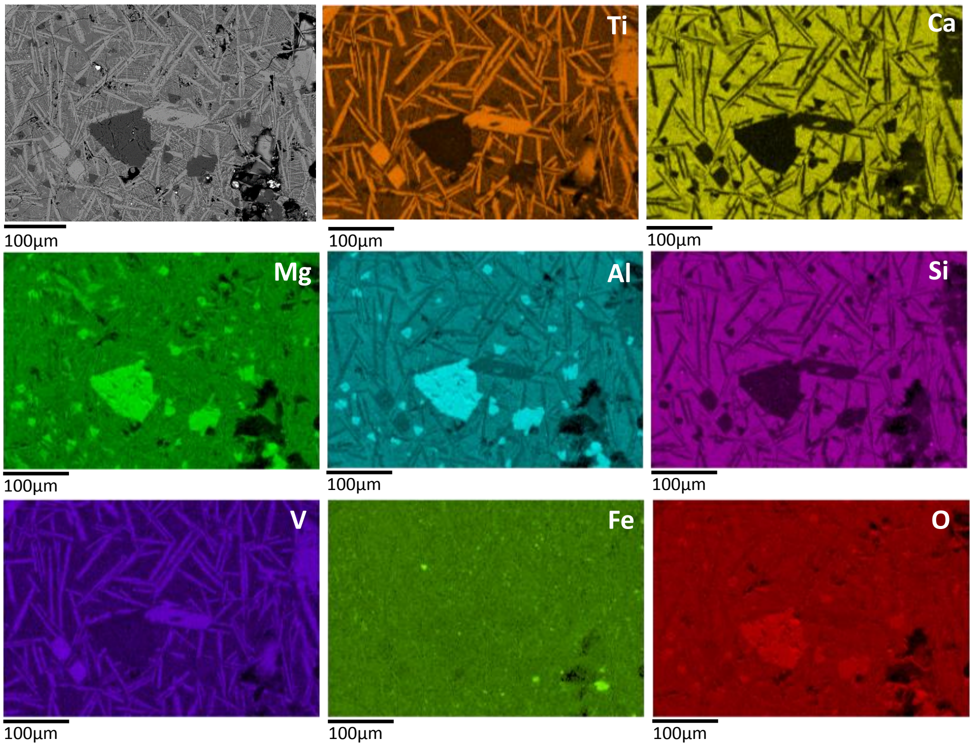

Figure 4.10 Backscattered SEM image of as received low-grade TiO_2 slag with elemental mapping.

The dark region seen in Figure 4.9 represents the $MgAl_2O_4$ phase. Elemental mapping demonstrates that the T2 matrix is composed of Ca-Mg-Al-Ti-Si-O.

T2 material was ground and the particles analysed by SEM-EDX, as represented in Figure 4.11 and Table 4.7. Area A in Figure 4.11 provides the composition of the Ti-rich $MgTi_2O_5$ phase, where the Ti content is 55.7 weight.% and the vanadium concentration is 1 weight.%, as a result of isomorphic substitution at the octahedral sites by V^{3+} ions [176].

The dark region evaluated by EDX analysis (see Area B in Figure 4.11) is the $MgAl_2O_4$ spinel with the vanadium content determined to be 1.2 weight.%. Enrichment of the spinel phase with vanadium ions is similar to what was noted by Diao et al [177], where the authors observed the formation of $Mg_x(V,Ti)_{3-x}O_4$ during the characterisation of vanadium slags. The crystallisation of $MgAl_2O_4$ in an aluminium-deficient slag with respect to magnesium, results in trivalent vanadium ions occupying sites in the spinel forming a $Mg(Al,V)_2O_4$ solid solution [178]. The V^{3+} ion (61 pm) octahedral radius is similar to that of Fe^{3+} (55 pm) and Al^{3+}(54 pm) ions. Therefore, V^{3+} ions readily substitute in ferromagnesian minerals [8, 176]. The occurrence of vanadium ions in the spinel highlights the importance of decomposing the $MgAl_2O_4$ in order to liberate the vanadium ions.

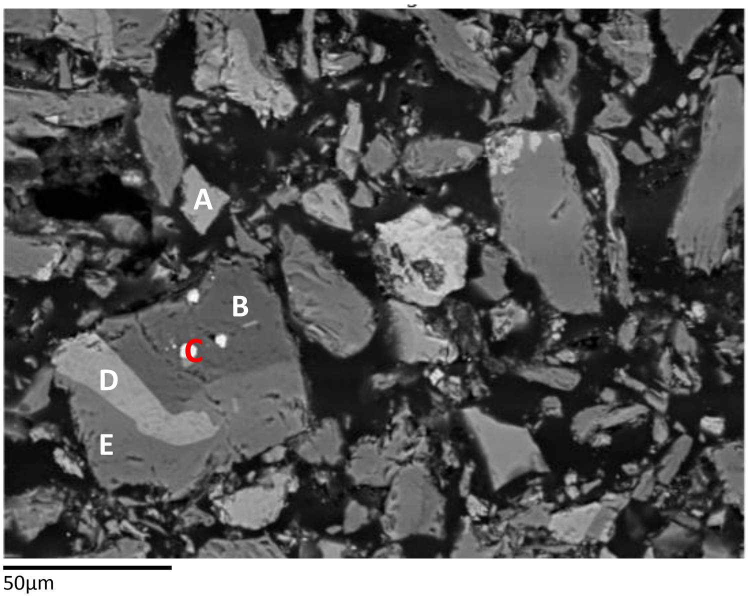

Figure 4.11 Backscattered SEM image of as received low-grade TiO_2 slag, analysed by EDX.

Table 4.7 Elemental composition of areas A to E in Figure 4.11, as analysed by EDX.

Weight.%	**Ti**	**Fe**	**O**	**Al**	**V**	**Mg**	**Si**	**Ca**	**Mn**	**S**	**Cr**	**Na**
A	55.7	0.5	34.9	1.9	1.0	5.5	-	0.4	0.2	-	-	-
B	7.4	0.5	39.2	32.9	1.2	18.0	-	0.1	0.3	0.2	0.2	-
C	1.1	96.7	0.3	-	1.1	-	-	0.2	-	-	-	-
D	35.8	-	34.3	-	-	0.2	-	29.1	-	-	-	0.3
E	8.7	0.5	39.2	6.7	-	10.6	17.9	15.6	0.6	-	-	-

Area C in Figure 4.11 is metallic iron that was entrained in the T2 during smelting of the pre-reduced titanomagnetite concentrate. Although the vanadium content is 1.1 weight.%, the vanadium cannot be extracted by the alkali reductive roast process since the metal is micro-alloyed.

The composition of the $CaTiO_3$ that precipitated in the T2 is given in Area D of Figure 4.11. The vanadium contained in the perovskite is not readily extracted by the process and is typically lost downstream in solid residues or waste solutions. Area E of Figure 4.11 is the chemical composition analysis of the slag matrix, corresponding to the complex $CaMg_{0.39}Ti_{0.48}Al_{0.87}Si_{1.26}O_6$ phase. The line scan data presented in Figure 4.12 illustrates that the Ti ions diffuse out of the $MgTi_2O_5$ rods into the T2 matrix resulting in the formation of the $CaTiO_3$ after reaction with Ca^{2+} ions. As the slag cooled Ti ion diffusion was inhibited by the increased viscosity of the slag matrix [172].

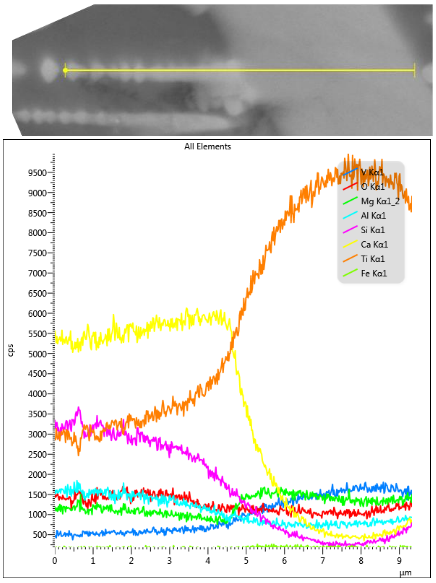

Figure 4.12 Backscattered SEM image of as received low-grade TiO_2 slag with elemental linescan.

4.1.2.4 Phase equilibria calculations for low-grade TiO_2 slag

Gibbs energy minimisation calculations were performed using the FactSage 6.4 software to predict the phases that would form during the pre-reduction at 1413 K and subsequent smelting at 1623 K of titanomagnetite concentrate [48].

Phase equilibria calculations given in Table 4.8 showing the formation of $CaTiO_3$ and $MgAl_2O_4$ at 1623 K broadly agree with the XRPD (see Figure 4.8) and SEM analysis (see Figure 4.9 and Figure 4.11), where $CaTiO_3$ and $MgAl_2O_4$ were observed. Formation of $V_{10}C_8$ confirms why metallic iron entrained in the T2 material was micro-alloyed with vanadium. However, the $CaMg_{0.39}Ti_{0.48}Al_{0.87}Si_{1.26}O_6$ phase was not given from the calculations, likely due to the absence of thermodynamic data in the FactSage software. Transformation of the products seen after pre-reduction at 1413 K to compounds predicted after smelting is evident, where formation of the spinel occurs after smelting at 1623 K.

Table 4.8 Phase equilibria calculations of pre-reduction and smelting of titanomagnetite concentrate [48, 124].

Input		**Pre-reduction at 1413 K**		**Smelting at 1623 K**	
	Mass(kg)	**Phase**	**Mass (kg)**	**Phase**	**Mass(kg)**
TM concentrate	1000	Fe	488.19	Fe	564.40
Dolomite	220	$CaTiO_3$	134.29	$CaAl_2Si_2O_8$	104.85
Quartz	18	$CaAl_2Si_2O_8$	92.58	Mg_2SiO_4	88.54
Coal	450	Mg_2SiO_4	88.54	$Ca_2Ti_2O_5$	74.42
Air	725	Fe_3C	81.68	Ti_3O_5	50.98
		Ti_3O_5	47.69	$CaTiO_3$	49.22
		$Mg_4Al_{10}Si_2O_{23}$	34.87	$MgAl_2O_4$	25.08
		VN	12.14	$V_{10}C_8$	11.32
		MnS	3.68	MnS	3.68

4.2 Phase transformation of South African titaniferous magnetite

4.2.1 Thermogravimetric analysis

Isothermal experiments

The weight loss versus time curves for TM heated isothermally in argon and air atmospheres are presented in Figure 4.13a and Figure 4.13b, respectively. The initial weight loss observed under inert (argon) atmosphere is rapid and then the isotherms begin to plateau within 0.4 hr - 0.55 hr, as seen in Figure 4.13a. Weight loss seen in Figure 4.13a is due to the evolution of H_2O gas from TM. In air atmosphere (see Figure 4.13b) it can be noted there is an initial weight loss for all the temperature curves similar to what was observed for the isotherms in Figure 4.13a. However, as time progresses the TM weight increases. The preliminary weight loss is a result of the release of moisture and the weight gain is due to oxidation of Fe_3O_4 and Fe_2TiO_4, according to equations 4.1 and 4.2. The rate of oxidation observed in Figure 4.13b increases as the temperature increases.

$$Fe_3O_4 + 0.25O_2(g) \rightarrow 1.5Fe_2O_3 \qquad 4.1$$

$$Fe_2TiO_4 + 0.5O_2(g) \rightarrow Fe_2TiO_5 \qquad 4.2$$

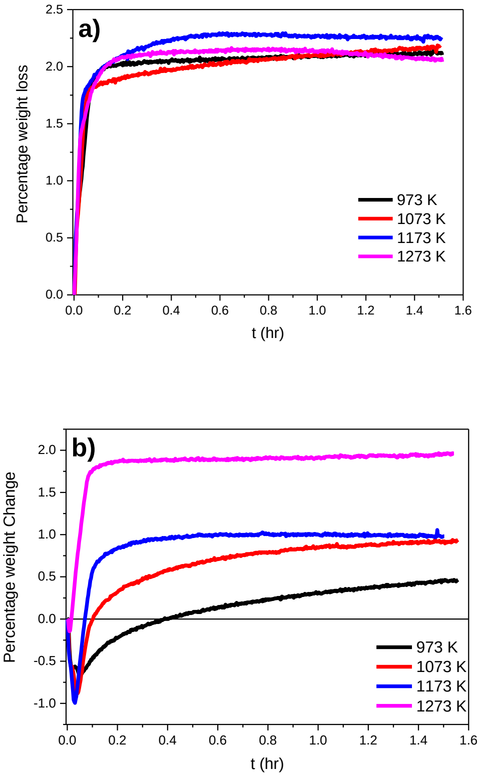

Figure 4.13 Plot of titaniferous magnetite a) percentage weight loss versus time isotherms for 973 K -1273 K under argon atmosphere and b) percentage weight change versus time isotherms for 973 K – 1273 K using compressed air in the TGA equipment.

4.2.2 X-ray powder diffraction and thermodynamic analysis

The dominant phases in TM, as reported in 4.1.1.2, are Fe_3O_4, $FeTiO_3$ and Fe_2TiO_4. The XRPD patterns for the titaniferous magnetite heated under argon and air atmospheres in the 973 K to 1273 K temperature range are presented in Figure 4.14a and Figure 4.14b, respectively.

The main phase observed in the XRPD patterns at all temperatures when heating under argon atmosphere is the Fe_3O_4-Fe_2TiO_4 solid solution, with the ilmenite phase also present at all the temperature ranges. Formation of the titanomaghemite phase (γ-Fe_2O_3) is observed in the XRPD patterns at all the temperatures. It is likely that the vanadium ions are still largely present as V^{3+} ions dissolved in the magnetite matrix as coulsonite, owing to the limited amount of O_2 gas present in the system.

Titanomaghemites are cation deficient spinels ($[Fe^{3+}]<Fe^{3+}_{5/2}\square_{1/3}>O_4$), which have a structure similar to a spinel that contains a limited amount of ferrous ions due to the outward diffusion of Fe^{2+} ions [1, 2]. Titanomaghemites can be defined by the Fe_3O_4-Fe_2TiO_4-$FeTiO_3$- γ-Fe_2O_3 series [3].

The dominant phase observed for the 973 K-1273 K temperature range under air atmosphere is the α-Fe_2O_3 - $FeTiO_3$ solid solution, highlighting Fe_3O_4 and Fe_2TiO_4 were oxidised at high temperature. The XRPD pattern for the 1073 K isotherm also show minor peaks for pseudobrookite (Fe_2TiO_5) and rutile (TiO_2). TiO_2 is observed due to oxidation of ilmenite to rutile and hematite, as given in equation 4.3. At 1173 K and 1273 K, the only peaks visible are those representing Fe_2O_3 and Fe_2TiO_5 ; TiO_2 was not observed above 1073 K owing to the reaction between Fe_2O_3 and TiO_2 to form pseudobrookite (see equation 4.4) [5]. Reaction 4.4 becomes thermodynamically feasible above 873 K and favourability increases as the temperature increases, explaining why there were no peaks for TiO_2 observed above 1073 K [6]. Fe_2TiO_5 is also formed according to equation 4.5 where the $FeTiO_3$ and Fe_3O_4 are oxidised to give Fe_2TiO_5 and α-Fe_2O_3. Since no pseudobrookite peaks were noted at 973 K it is probable that reaction 4.5 proceeds slowly below 1073 K. There is no evidence on the vanadium oxidation state in the TM but it is likely that it has been oxidised from the V^{3+} state to the V^{5+} state according to reaction 4.6 where $\Delta G^{o}_{1273\ K}$ equals -176.26 kJ.mol^{-1}.

$$\mathrm{FeTiO_3 + 0.25O_2(g) \rightarrow TiO_2 + 0.5Fe_2O_3} \tag{4.3}$$

$$\mathrm{TiO_2 + Fe_2O_3 \rightarrow Fe_2TiO_5} \tag{4.4}$$

$$\mathrm{Fe_3O_4 + FeTiO_3 + 0.5O_2(g) \rightarrow Fe_2TiO_5 + Fe_2O_3} \tag{4.5}$$

$$\mathrm{FeV_2O_4 + 1.25O_2(g) \rightarrow Fe_2O_3 + V_2O_5} \qquad 4.6$$

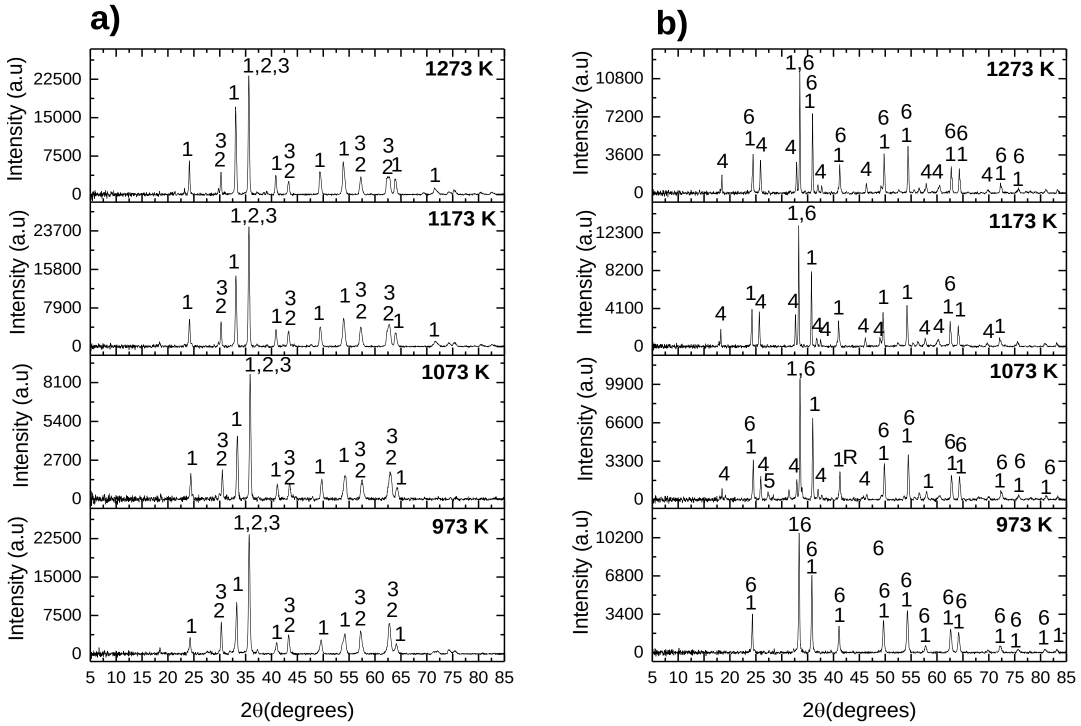

Figure 4.14 XRPD patterns of isothermally heat treated titaniferous magnetite from 973 K – 1273 K a) under argon and b) air atmosphere, using TGA apparatus. 1- $FeTiO_3$, 2- Fe_3O_4-Fe_2TiO_4, 3- γ-Fe_2O_3, 4-Fe_2TiO_5, 5-TiO_2(rutile), 6-Fe_2O_3

Non-isothermal experiments

Weight change versus temperature curves for the non-isothermal heating of the titaniferous magnetite from ambient temperature (295 K-300 K) to 1273 K under argon and air atmosphere are presented below in Figure 4.15. Visible weight loss occurs during the first 0.14 hr for curves in both atmospheres. Under argon atmosphere the curve continually decreases as the temperature increases, which is the evolution of moisture from the as-received sample. However, the curve depicting the air atmosphere begins to gain weight due to oxidation as the temperature increases, similar to what was observed for the isothermal heating in air (Figure 4.13b).

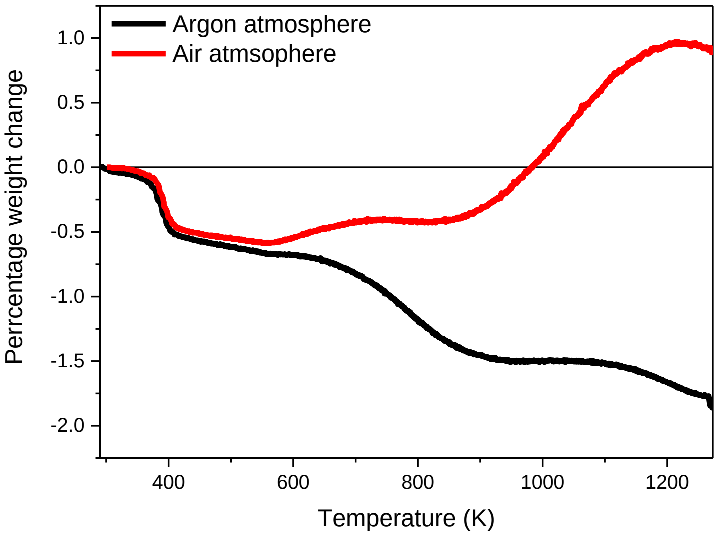

Figure 4.15 Plot of titaniferous magnetite percentage weight change versus temperature from ambient temperature to 1273 K under argon and air atmosphere, using TGA apparatus.

The X-ray powder diffraction patterns from the non-isothermal treatment of the TM under argon and air atmospheres are presented in Figure 4.16a and Figure 4.16b, respectively. In Figure 4.16a, the major peaks visible represent $FeTiO_3$, γ-Fe_2O_3 and Fe_3O_4-Fe_2TiO_4 phases, comparable to what was observed after the isothermal heat treatment (see Figure 4.14a). However, the main difference is that there are only minor peaks for Fe_2TiO_5 present after non-isothermal heating. The formation of γ-Fe_2O_3 can be explained by the reaction between Fe_3O_4 and $FeTiO_3$ (see equation 4.7), as this reaction was observed by Vincent et al [7] up to 1223 K. Above 1223 K, the formation of pseudobrookite was observed, which agrees with the experimental results given. The authors proposed that the $FeTiO_3$-Fe_2O_3 solid solution was exsolved, where $FeTiO_3$ has a gamma-structure [7]. However, at the time of writing their article there was limited knowledge of the γ-Fe_2O_3. Figure 4.16b shows that the high temperature phases formed after non-isothermal heat treatment in air atmosphere are $FeTiO_3$, α-Fe_2O_3 and Fe_2TiO_5.

$$FeTiO_3 + Fe_3O_4 \rightarrow Fe_2TiO_4 + Fe_2O_3 \qquad 4.7$$

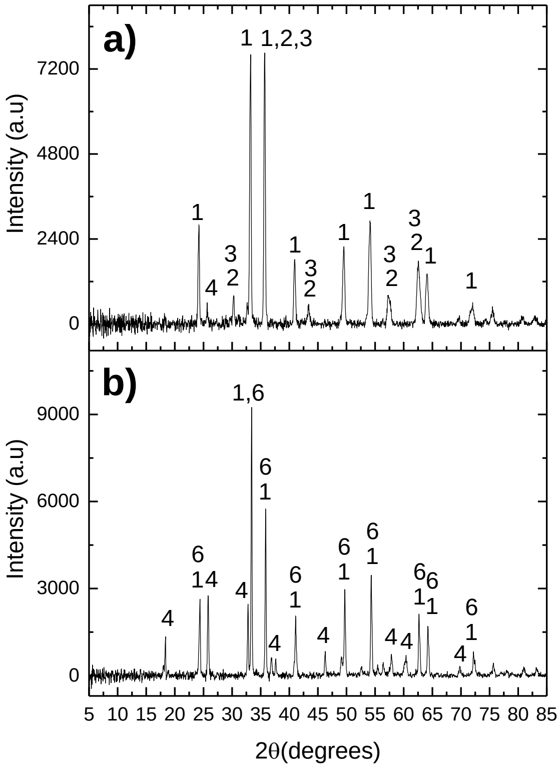

Figure 4.16 XRPD patterns of non-isothermally heat treated titaniferous magnetite from ambient temperature to 1273 K under a) argon and b) air atmosphere, using TGA apparatus. 1- $FeTiO_3$, 2-Fe_3O_4-Fe_2TiO_4, 3- γ-Fe_2O_3, 4-Fe_2TiO_5, 5-TiO_2(rutile), 6-Fe_2O_3.

Predominance area diagrams

The predominance area diagrams (PAD) of the Fe-Ti-Ar-O system at 1073 K and 1273 K are given in Figure 4.17a and Figure 4.17b, respectively, representing heating under argon atmosphere. The key difference between Figure 4.17a and Figure 4.17b is that Fe_2TiO_5 co-exists with magnetite at 1273 K, whereas at 1073 K the two compounds do not co-exist in the same phase field. There is agreement between the thermodynamic calculations and the experimental results in terms of the ability of Fe_3O_4 to co-exist with $FeTiO_3$, as these phases were observed in the XPRD patterns for isothermal heating of TM under argon atmosphere (see Figure 4.14a). The Fe_2TiO_5 phase was observed in Figure 4.16a, the XRPD pattern for the non-isothermal treatment of titaniferous magnetite under argon atmosphere, indicating that there is agreement with the PAD in Figure 4.17b as Fe_3O_4 is shown to co-exist with Fe_2TiO_5 when $\log_{10}P(O_2)$(atm) is equal to -6.

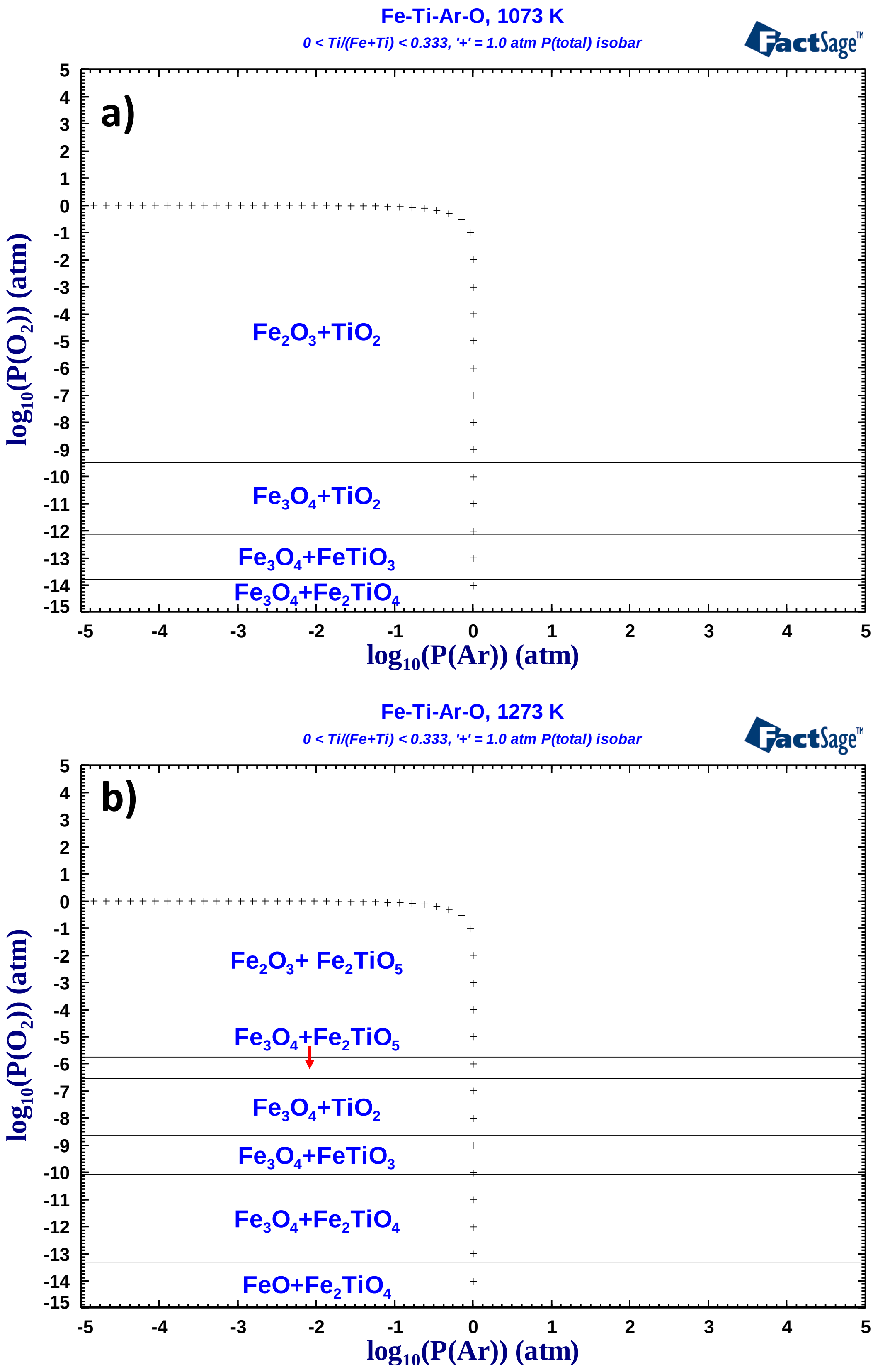

Figure 4.17 Predominance area diagram for Fe-Ti-Ar-O system at a) 1073 K and 1273 K, computed using FactSage software [8].

The heat treatment under air atmosphere is represented in the Fe-Ti-N-O system predominance area diagrams given in Figure 4.18a and Figure 4.18b. Equilibrium phases from the multi-component system predicted for the Fe-Ti-N-O system are similar to those expected in the Fe-Ti-Ar-O system.

There is good agreement between the thermodynamic computation and the experimental results for thermal decomposition in air. Figure 4.18a shows that at 1073 K Fe_2O_3 and TiO_2 co-exist, which agrees with the phases observed in the XPRD pattern in Figure 4.16b. However, a minor peak for Fe_2TiO_5 was also observed at 1073 K and no TiO_2 peak was seen at 973 K. While the exsolution of the TiO_2 from the iron-rich phase is thermodynamically feasible at 973 K, it is likely that kinetics are slow at this temperature. Suggesting that the experiment at 973 K needed to be carried out for longer in order for the TiO_2 to be visible in the XRPD patterns. Above 1073 K, the PAD calculations in Figure 4.18b indicate that Fe_2TiO_5 and Fe_2O_3 co-exist, which agrees with the XRPD patterns in Figure 4.14b and Figure 4.16b.

The characterisation of the iron-rich tailings material indicated that Fe_3O_4 was still present differing with analysis of the titaniferous magnetite heated treated in air where thermodynamic predictions and experimental results show more significant conversion of Fe_3O_4 to Fe_2O_3. This suggests that the original processing conditions are either insufficiently oxidising or that the presence of alkali salt resulted in the formation of a liquid phase that inhibited the diffusion of O_2 gas [123].

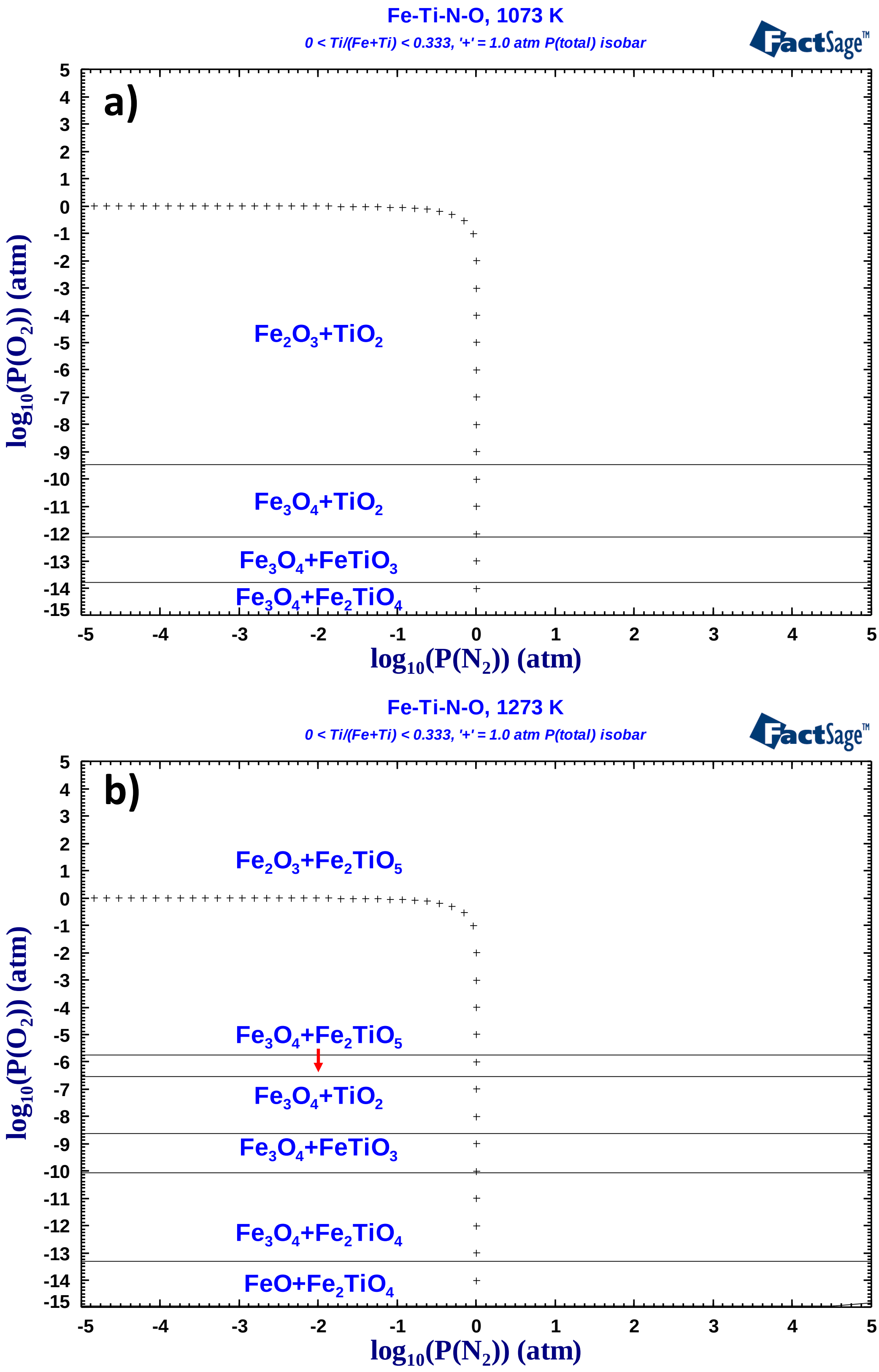

Figure 4.18 Predominance area diagram for Fe-Ti-N-O system at a) 1073 K and 1273 K, computed using FactSage software [8].

4.2.3 Scanning electron microscopy analysis

The microstructure in Figure 4.19a and Figure 4.19b demonstrates that the particles undergo spinodal decomposition, as has been reported for titanomagnetites in literature [15]. However, the decomposition appears to be more extensive in the sample treated in air (see Figure 4.19a), likely due to the role played by the partial pressure of O_2. Diffusion of O_2 gas into the particle results in the oxidation of ferrous iron to ferric iron resulting in extensive fracturing due to the structural transformation [1]. It is also evident that there is disintegration at the periphery of the particle.

It is clear from Figure 4.19b that the grains formed during heat treatment in inert atmosphere are larger than those seen in air atmosphere. Spinodal decomposition occurs in both atmospheres and likely affects the grain coarsening [15,16]. Grains formed (see Figure 4.19b) have a typical spinodal decomposition appearance that demonstrates sinusoidal behaviour, almost appearing to be the product of a computer simulation [17, 18]. The partial pressure of O_2 is lower in the inert environment, suggesting that this influences the grain coarsening and ultimately the grain size. The standard Gibbs free energy change from the spinodal decomposition becomes the rate-determining step as the spinodal curve is approached [19]. The comparison of the $\Delta G^o_{1273\,K}$ of equations 4.5 and 4.6 highlights that there is a more negative value for the decomposition in air atmosphere of -168.64 kJ.mol^{-1} compared to -68.95 kJ.mol^{-1} for the treatment in argon atmosphere. Implying that a greater barrier to diffusion exists in the inert atmosphere and this may contribute to the morphological differences observed in the grains after the isothermal heat treatment in oxidizing and inert atmospheres.

The oxidised microstructure appears to be more porous than the one produced in inert atmosphere. The more porous nature of the particle shown in Figure 4.19a may explain why it appears more uniform versus Figure 4.19b. In Figure 4.19b it appears the particle is made up of three zones, as labelled in the diagram, where the middle zone resembles an interface between the dense particles in the bottom zone and the coarse grains in the top zone. The coarsening of the Fe-rich grains during high temperature treatment in argon atmosphere would be beneficial for the carbothermic reduction in the presence of alkali carbonates, which will be described in chapter 5. Coarse grains may more readily form larger metallic Fe clusters that would be more easily separated from the sodium titanate and sodium vanadium oxide phases, allowing the magnetic separation to be more effective.

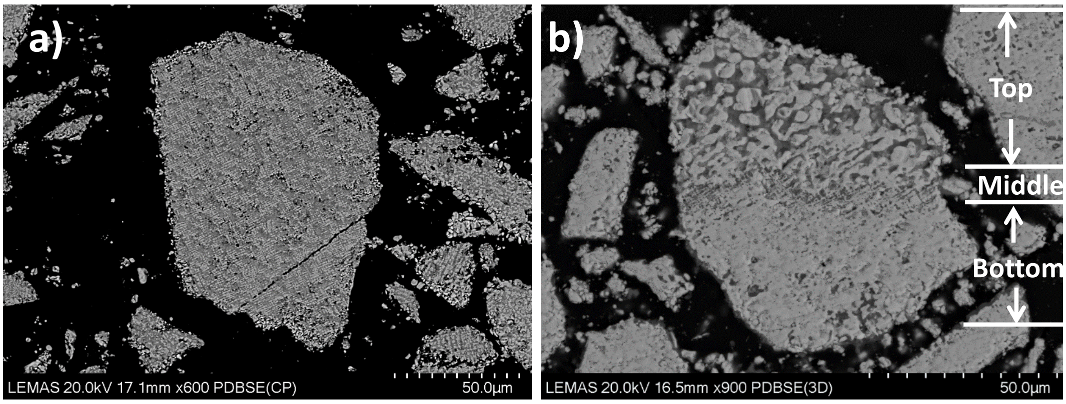

Figure 4.19 Backscattered SEM image of titaniferous magnetite heated isothermally at 1273 K in a) argon and b) air atmosphere using TGA apparatus.

From the linescan data given in Figure 4.20 it can be seen that there is clear spinodal decomposition in which there is unmixing of the Ti-rich and Fe-rich phases during the non-isothermal roasting in air. Evidently, the grain size is larger during non-isothermal heating compared to that noted in isothermal heating (see Figure 4.19a); possibly due to the slower heating rate there is less mass motion within the particles and this allows the grains to coarsen. Vanadium segregation from the iron-rich phase is evident, owing to the limited solubility of V ions in the hematite matrix [18]. This broadly agrees with what was observed in the T1 material microstructure, where the vanadium concentration was lowest in the hematite phases.

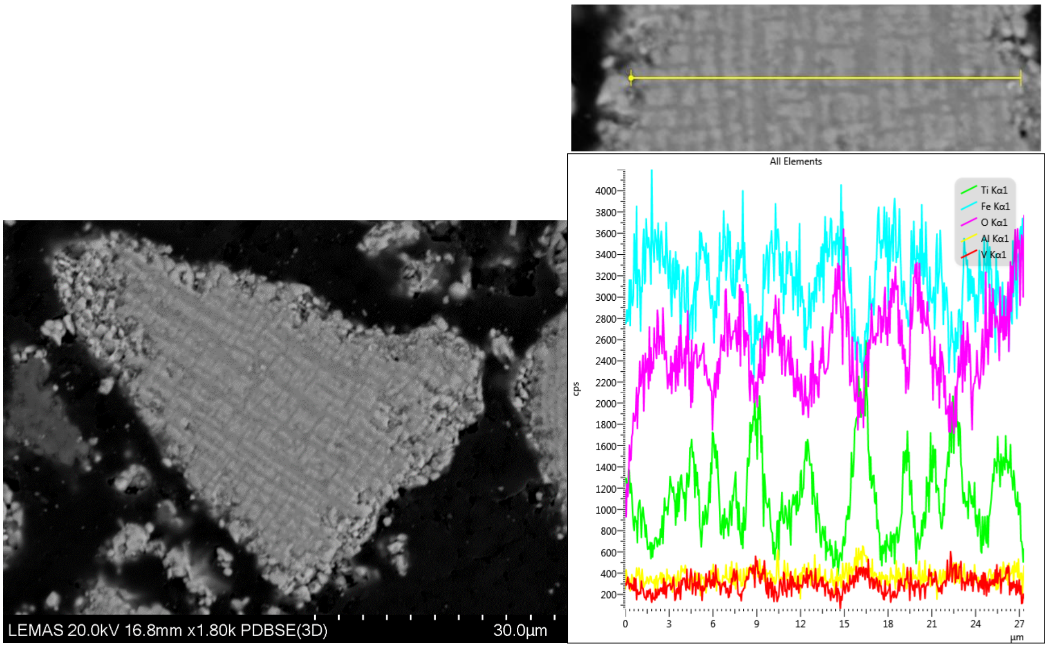

Figure 4.20 Backscattered SEM image of titaniferous magnetite heated non-isothermally from ambient temperature to 1273 K in air atmosphere with line scan data.

4.3 Chapter summary

XRPD analysis of titaniferous magnetite showed that magnetite, ilmenite and ulvöspinel were the major phases present and microstructure investigations indicated that V ions were dissolved in the magnetite matrix. In comparison, hematite, ilmenite and magnetite were observed in the T1 XRPD pattern. SEM analysis revealed that a minor amount of vanadium was dissolved in the $FeTiO_3$-Fe_2O_3 solid solution and sodium aluminosilicate complex. Notably, vanadium was absent in sodium aluminosilicates with a higher Al content. Phase equilibria calculations for predicting phase transformation during alkali roasting of titanomagnetite concentrate showed agreement with phase analysis of T1. Results from FactSage software computation showed the formation of sodium aluminosilicate and hematite phases which where were observed in T1 SEM and XRPD data, whereas formation of ilmenite was not predicted in the FactSage calculations.

TiO_2 in T2 was distributed in the slag matrix, karooite and perovskite, whereas vanadium ions were dissolved in karooite, magnesium aluminate spinel and entrained metallic iron. Phase equilibria predictions agreed with the T2 phase analysis where perovskite and magnesium aluminate were predicted.

Isothermal heating in argon atmosphere of TM resulted in spinodal decomposition with apparent grain coarsening in the particles. SEM of TM subjected to isothermal heating in air showed a more uniform particle with greater porosity. Linescan data from TM heated in air demonstrated segregation between iron oxide and vanadium oxide. Thermal decomposition of TM in air oxidised magnetite to hematite, however, oxidation of T1 was incomplete as magnetite was observed in the XRPD pattern thus decreasing V extraction as the vanadium ions were not liberate from the matrix.

5 Thermodynamic considerations

Chapter 5 considers the thermodynamics of carbothermic reduction of the waste materials in the presence and absence of alkali carbonates and thermodynamic predictions are compared with experimental results. Invariably, the mineralogy of T2 results in multiple complex reactions occurring - which are discussed in this chapter.

5.1 Standard Gibbs free energy change diagrams

5.1.1 Carbothermic reduction of titaniferous minerals

As stated in Chapter 2, carbothermic reduction is carried out on titaniferous minerals as part of the beneficiation of these feedstocks. Ilmenite is reacted with coal in a rotary kiln as part of the Becher and Benelite processes to produce synthetic rutile [75]. Titanomagnetite concentrates are pre-reduced in a rotary kiln with coal before being smelted in an electric arc furnace for steel and vanadium production [126]. Carbothermic reduction of ilmenite proceeds in accordance with reaction 5.1. However, in order to improve the reactivity, ilmenite is often pre-treated with the aim of oxidizing iron to the 3+ state before its reduction according to equation 5.2 [91]. Reduction of the ulvöspinel, magnetite and hematite phases in the titanomagnetite concentrate take place following equations 5.3 - 5.5, respectively. The Boudouard reaction (see equation 5.6) is an important reaction in carbothermic reduction as carbon monoxide is better able to carry out reduction when compared to solid carbon, as CO is able to diffuse more rapidly than solid carbon [39].

$$\mathrm{FeTiO_3 + C \rightarrow Fe + TiO_2 + CO(g)} \qquad 5.1$$

$$\mathrm{Fe_2O_3.TiO_2 + 3C \rightarrow 2Fe + TiO_2 + 3CO(g)} \qquad 5.2$$

$$\mathrm{Fe_2TiO_4 + 2C \rightarrow 2Fe + TiO_2 + 3CO(g)} \qquad 5.3$$

$$\mathrm{Fe_2O_3 + 3C \rightarrow 2Fe + 3CO(g)} \qquad 5.4$$

$$\mathrm{Fe_3O_4 + 4C \rightarrow 3Fe + 4CO(g)} \qquad 5.5$$

$$\mathrm{C + CO_2(g) \rightarrow 2CO(g)} \qquad 5.6$$

The respective standard Gibbs free energy change vs temperature plots for the equations 5.1 to 5.6 are given in Figure 5.1, where it can be observed that the reduction of ilmenite is more thermodynamically favourable than that of the ulvöspinel, with carbothermic reduction of ilmenite becoming feasible above 923 K compared to above 1123 K for the ulvöspinel. Reduction of hematite is thermodynamically feasible above 873 K and the ΔG values become more negative as the temperature increases.

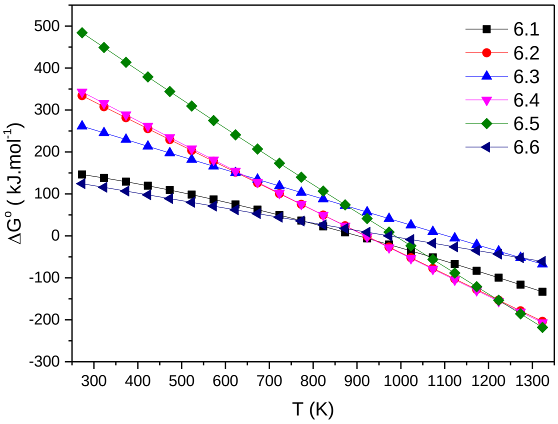

Figure 5.1 Comparison of standard Gibbs free energy change vs temperature curves for reactions 5.1 to 5.6. Values calculated using HSC 5.1 software [35].

5.1.2 Carbothermic reduction of titaniferous minerals in the presence of Na_2CO_3

Computed standard Gibbs free energy change (ΔG^o) values for reactions 5.7 to 5.15 , excluding reaction 5.10, are plotted against temperature in Figure 5.2 and Figure 5.3. Equations 5.7 to 5.15 describe the reactions that may occur during alkali reduction of titaniferous minerals, specifically for T1. Reaction 5.7 involving the reduction of ilmenite with Na_2CO_3 becomes thermodynamically feasible above 973 K. By comparison, reaction 5.8, the alkali reduction of ulvöspinel, becomes favourable above 1073K following a similar trend to what was observed for the carbothermic reduction of these minerals in the absence of alkali carbonates; where carbothermic reduction of $FeTiO_3$ was more favourable than that of Fe_2TiO_4. The standard Gibbs free energy change for the reaction between sodium carbonate and the vanadium oxide present in the South African minerals has been computed according reaction 5.9. In reality, it is expected that the reaction between soda ash and vanadium oxide proceeds according to reaction 5.10 as V^{3+} ions are present. Reaction 5.10 was not computed due to a lack of thermodynamic data available in the FactSage software.

The CaO present in the South African minerals is able to react with the TiO_2 to form $CaTiO_3$, meaning that reaction 5.12 competes with reactions 5.7 and 5.8 for the formation of alkali titanates. Reaction 5.11 requires carbon dioxide gas (CO_2) in order to form sodium permanganate ($NaMnO_4$). Although this reaction is thermodynamically feasible, it is unlikely that it will occur because from Figure 5.6 it is clear that the partial pressure of CO_2 gas must be low in order to form the desired metallic iron. The formation of $CaTiO_3$ over Na_2TiO_3 is undesirable as the CaO is not readily leached out as compared to Na_2O. Above 1250 K, reactions 5.7 and 5.8 become more thermodynamically favourable than reactions 5.12 and 5.13, respectively. The amount of CaO present is less than the amount of Na_2CO_3 added and therefore sodium titanate will likely be the dominant phase formed.

Conventional carbothermic reduction (see reactions 5.1 and 5.3) of ilmenite and ulvöspinel become thermodynamically favourable in a similar temperature range compared to alkali reductive roasting of these minerals (see reactions 5.7 and 5.8), however, as the temperatue increases the alkali reduction reactions become significantly more favourable than those reactions carried out without alkali carbonate.

$$\mathrm{FeTiO_3 + Na_2CO_3 + 2C \rightarrow Fe + Na_2TiO_3 + 3CO(g)} \tag{5.7}$$

$$\mathrm{Fe_2TiO_4 + Na_2CO_3 + 3C \rightarrow Fe + Na_2TiO_3 + 4CO(g)} \tag{5.8}$$

$$\mathrm{V_2O_5 + Na_2CO_3 + C \rightarrow 2NaVO_3 + CO(g)} \tag{5.9}$$

$$\mathrm{FeV_2O_4 + Na_2CO_3 + C \rightarrow Fe + NaVO_2 + 2CO(g)} \tag{5.10}$$

$$\mathrm{2MnO + Na_2CO_3 + 4CO_2(g) \rightarrow 2NaMnO_4 + 5CO(g)} \tag{5.11}$$

$$\mathrm{FeTiO_3 + CaO + C \rightarrow Fe + CaTiO_3 + CO(g)} \tag{5.12}$$

$$\mathrm{Fe_2TiO_4 + CaO + 2C \rightarrow 2Fe + CaTiO_3 + 2CO(g)} \tag{5.13}$$

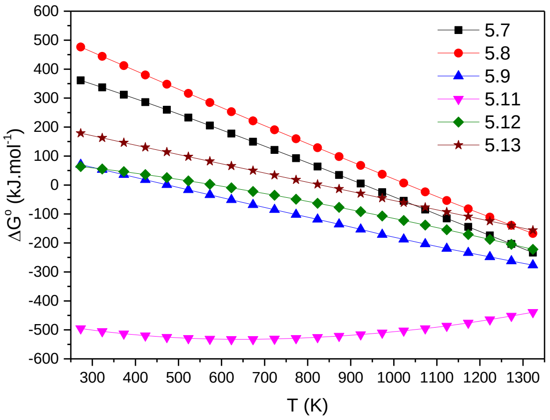

Figure 5.2 Comparison of standard Gibbs free energy change vs temperature curves for reactions 5.7 to 5.13 . Values calculated using HSC 5.1 software [35].

The gangue present in the minerals consume Na_2CO_3 according to equations 5.14 – 5.16. In Figure 5.3, it can be observed that reaction 5.14 is more thermodynamically favourable than both reactions 5.15 and 5.16, suggesting that the sodium aluminosilicate ($NaAlSiO_4$) is more likely to form than either sodium silicate or sodium aluminate.

$$Al_2O_3 + 2SiO_2 + Na_2CO_3 + C \rightarrow 2NaAlSiO_4 + 2CO(g) \quad 5.14$$

$$SiO_2 + Na_2CO_3 + C \rightarrow Na_2SiO_3 + 2CO(g) \quad 5.15$$

$$Al_2O_3 + Na_2CO_3 + C \rightarrow Na_2Al_2O_4 + 2CO(g) \quad 5.16$$

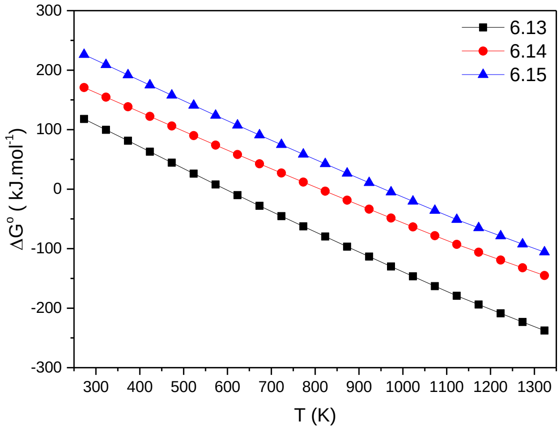

Figure 5.3 Comparison of standard Gibbs free energy change vs temperature curves for reactions 5.14 – 5.16. Values calculated using HSC 5.1 software [35].

5.1.3 Carbothermic reduction of low-grade TiO_2 slag with Na_2CO_3

The complex mineralogy of the T2 different reactions occurring during processing compared to those expected for the iron-rich tailings material.

Decomposition of $MgAl_2O_4$ to form MgO and $Na_2Al_2O_4$ in the presence of Na_2CO_3 and C (see equation 5.17) is thermodynamically feasible above 1023 K. The importance of alkali carbonate is made clear by considering previous work by Goso et al. [167] that failed to decompose $MgAl_2O_4$ even after performing oxidative roasting at 1148 K and reductive roasting at 1148 K on the T2 material. $MgAl_2O_4$ present in chromite ore was decomposed according to equation 5.18 during oxidative alkali roasting [179]. Breaking down of $MgAl_2O_4$ is necessary for release of vanadium ions localised in the spinel.

The significant quantity of lime in T2 is able to react with the vanadium oxide to form water-insoluble calcium vanadate which would adversely affect the recovery of the vanadium oxide in the water leaching step [7]. The reaction between calcium oxide and vanadium oxide (see equation 5.19) is more thermodynamically favourable at lower temperatures than the reaction with sodium carbonate (see equation 5.9). However, as the temperature increases reaction 5.19 becomes less favourable and reaction 5.9 becomes more favourable to a point where above 823 K reaction 5.9 is more favourable than reaction 5.19.

As detailed in chapter 4, the TiO_2 is found as $CaTiO_3$, $CaMg_{0.39}Ti_{0.48}Al_{0.87}Si_{1.26}O_6$ and $MgTi_2O_5$ in the low-grade TiO_2 slag material. $MgTi_2O_5$ is predicted to react with Na_2CO_3 in reducing atmosphere following reaction 5.20 to yield Na_2TiO_3 and MgO as solid products, as the reaction is thermodynamically favourable above 1023 K.

Reactions between the Ca-Ti-Si-O complex and sodium carbonate are expected occur, with two competing reactions involving the formation of either $CaTiO_3$ or Na_2TiO_3 based on reactions 5.21 and 5.22, respectively. Reaction 5.21 becomes feasible at a lower temperature compared to 5.22 and is more favourable at 1323 K, suggesting that formation of $CaTiO_3$ over Na_2TiO_3 is more favoured.

$$\mathrm{MgAl_2O_4 + Na_2CO_3 + C \rightarrow MgO + Na_2Al_2O_4 + 2CO(g)} \qquad 5.17$$

$$\mathrm{MgAl_2O_4 + Na_2CO_3 \rightarrow MgO + 2NaAlO_2 + CO_2(g)} \qquad 5.18$$

$$\mathrm{V_2O_5 + CaO \rightarrow CaV_2O_6} \qquad 5.19$$

$$\mathrm{0.5MgTi_2O_4{}_{(s)} + Na_2CO_3 + C_{(s)} \rightarrow 0.5MgO + Na_2TiO_3 + 2CO(g)} \qquad 5.20$$

$$\mathrm{CaTiSiO_5 + Na_2CO_3 + C \rightarrow Na_2SiO_3 + CaTiO_3 + 2CO(g)} \qquad 5.21$$

$$\mathrm{CaTiSiO_5 + Na_2CO_3 + C \rightarrow CaSiO_3 + Na_2TiO_3 + 2CO(g)} \qquad 5.22$$

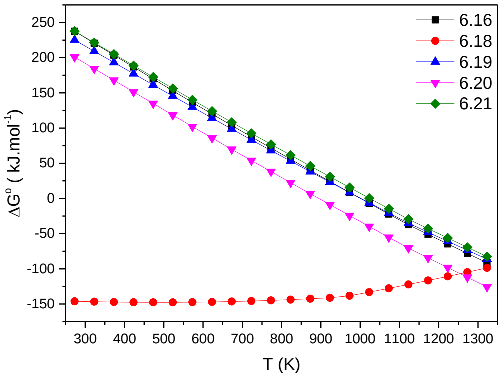

Figure 5.4 Comparison of standard Gibbs free energy change vs temperature curves for reactions 5.17 – 5.22 (excluding 5.18). Values calculated using HSC 5.1 software [35].

5.1.4 Carbothermic reduction in the presence of K_2CO_3

The standard Gibbs free energy change values for carbothermic reduction of ilmenite and ulvöspinel in the presence of K_2CO_3 have been computed and compared with alkali reduction reactions using Na_2CO_3. The main area of interest being the 1223 K to 1323 K range, as this is the typical operating temperature of the reductive alkali roasting process. It can be noted that the reactions involving potassium salts are significantly more favourable than sodium salts. Standard Gibbs free energy change for alkali reductive roasting of titaniferous minerals using K_2CO_3 (see reactions 5.23 and 5.24) is significantly more negative than Na_2CO_3 above 1223 K (5.7 and 5.8). Thermodynamics supports previous studies that found that K_2CO_3 was more effective for alkali reduction of titaniferous minerals than Na_2CO_3 [71].

$$\mathrm{FeTiO_3 + Na_2CO_3 + 2C \rightarrow Fe + Na_2TiO_3 + 3CO(g)} \tag{5.7}$$

$$\mathrm{Fe_2TiO_4 + Na_2CO_3 + 3C \rightarrow 2Fe + Na_2TiO_3 + 4CO(g)} \tag{5.8}$$

$$\mathrm{FeTiO_3 + K_2CO_3 + 2C \rightarrow Fe + K_2TiO_3 + 3CO(g)} \tag{5.23}$$

$$\mathrm{Fe_2TiO_4 + K_2CO_3 + 3C \rightarrow 2Fe + K_2TiO_3 + 4CO(g)} \tag{5.24}$$

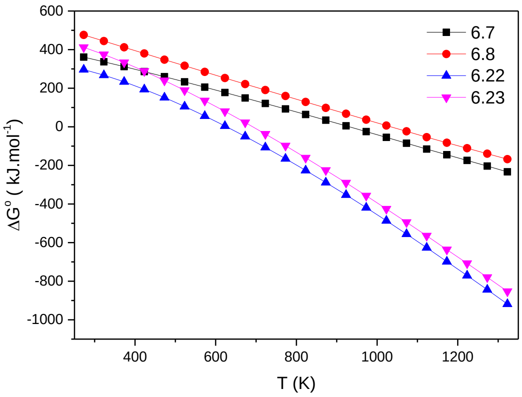

Figure 5.5 Comparison of standard Gibbs free energy change versus temperature curves for reactions 5.7, 5.8, 5.23 and 5.24. Values calculated using HSC 5.1 software [35].

5.2 Predominance area diagrams (PAD)

5.2.1 Titaniferous magnetite and iron rich tailings predominance area diagrams

The Na-Fe-Ti-O-C multi-component system at 1323 K shown in Figure 5.6a, demonstrates that metallic iron is able to co-exist with molten sodium titanate at $\log_{10}P(CO)(atm) \approx -2.5$ and $-4 < \log_{10}P(CO_2)(atm) < -3$. However, the presence of molten sodium titanates would inhibit the diffusion of CO gas decreasing the reduction rate [120]. Figure 5.6b, the Na-Fe-Ti-O-C system at 1223 K, shows that sodium titanate co-existing with iron is a solid at this temperature, highlighting the role that temperature plays in alkali reduction. Magnetic separation of reduced samples would enable the separation of magnetic iron from the non-magnetic sodium titanate phases. El-Tawil et al. [119] performed alkali reductive roasting of ilmenite (42 weight.% TiO_2 and 53.6 weight.% Fe-O) in air but they were only able to achieve 85 % metallisation of Fe at 1473 K. This low metallisation at such an elevated temperature is due to experiments being carried in insufficiently reducing atmosphere, as depicted in Figure 5.6. The un-reduced Fe was lost in the non-magnetic fraction as Na-Fe-Ti-O ternary compounds and hence the overall magnetic separation of iron was limited. Thermodynamic data for sodium iron titanate is not present in the FactSage software database and it is therefore not possible to determine the conditions that would result in its formation.

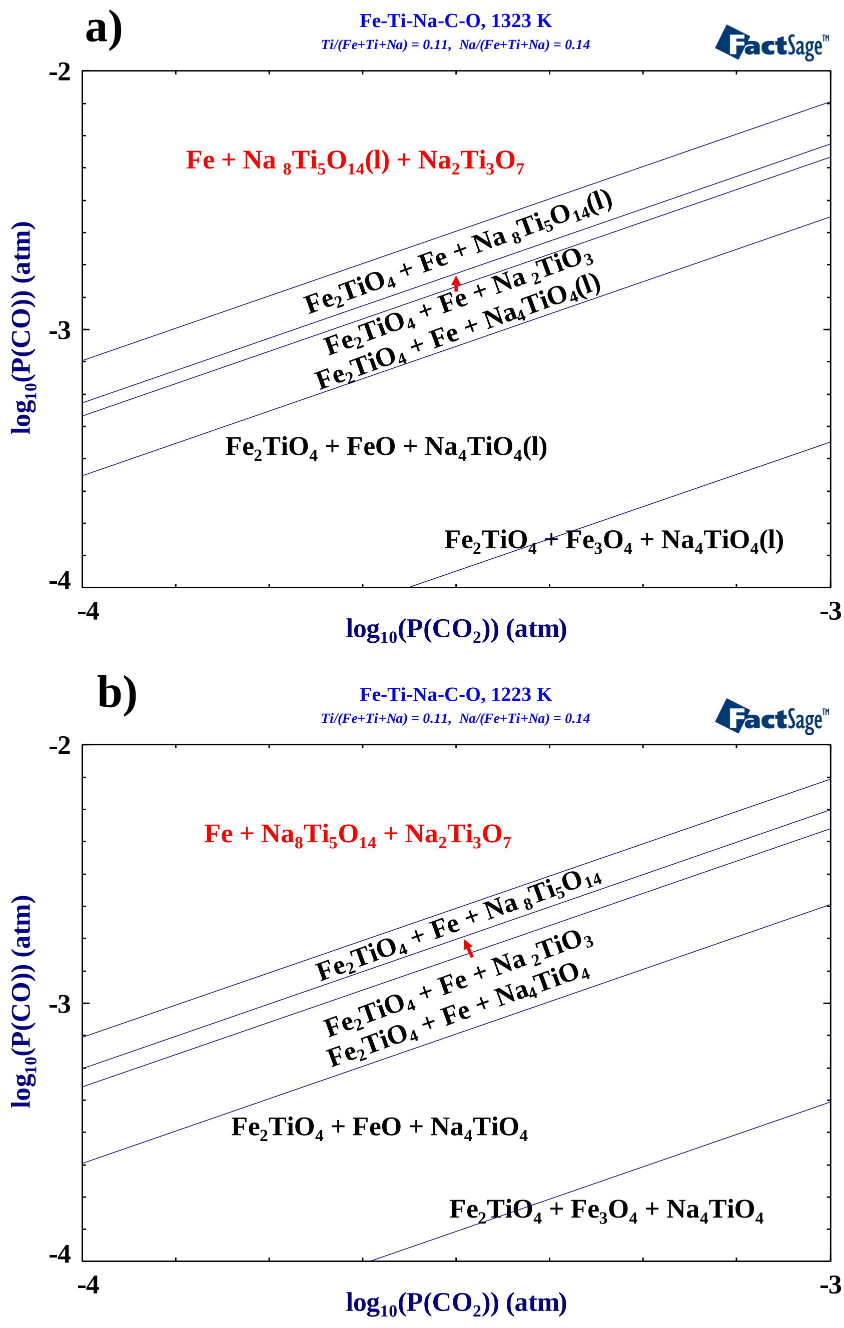

Figure 5.6 Predominance area diagram of Na-Fe-Ti-O-C system at a) 1323 K and b) 1223 K, constructed using FactSage software [48].

The Fe-V-Na-O-C system (see Figure 5.7) shows that at $-4 < \log_{10}P(CO)(atm) < -3.5$ and $-3.5 < \log_{10}P(CO_2)(atm) < -3$ magnetite and coulsonite (FeV_2O_4) co-exist with the sodium vanadate phase. Change in P_{CO} along the red arrow towards the starred region illustrates that metallic iron is able to co-exist with coulsonite and sodium vanadate. Coulsonite is fully decomposed in more reducing conditions of $-3.25 < \log_{10}P(CO)(atm) < -2$ and $-4 < \log_{10}P(CO_2)(atm) < -3.25$ liberating vanadium ions. Figure 5.7 indicates that Fe co-exists with sodium vanadium and vanadium trioxide (V_2O_3), in reality provided sufficient Na_2CO_3 is present the alkali carbonate will react with V_2O_3 to form $NaVO_2$ - a phase that has been reported in the literature [180]. The PAD highlights the importance of operating under a sufficiently reducing environment in order to fully decompose the coulsonite phase and liberate the vanadium ions.

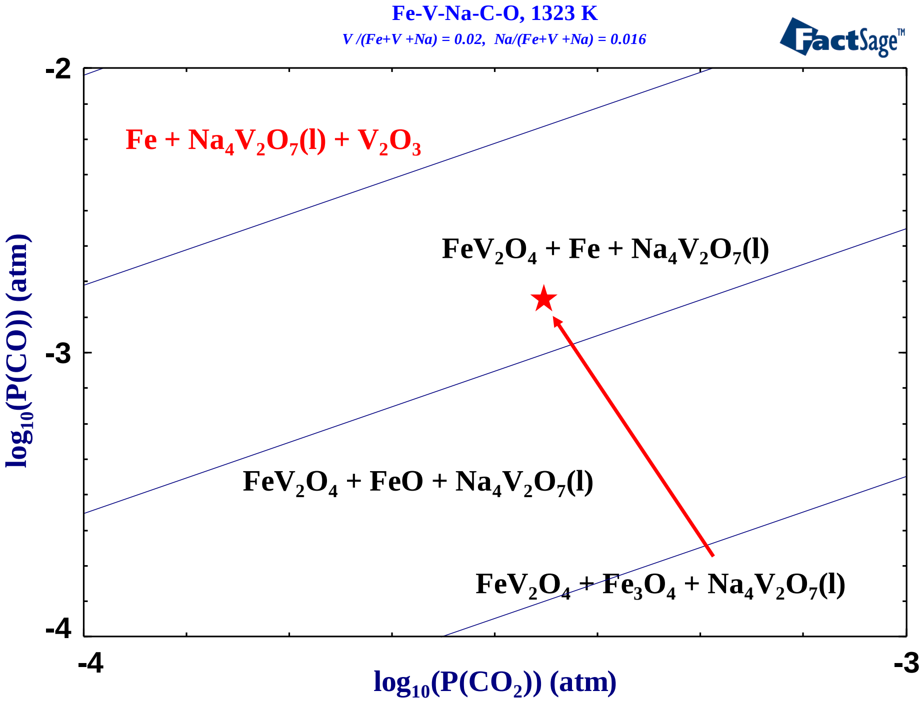

Figure 5.7 Predominance area diagram of V-Fe-Na-O-C system at 1323K, constructed using FactSage software [48]. Red arrow is just an indication.

Figure 5.8 shows the Fe-Ti-O-C system at 1323 K representing carbothermic reduction in the absence of alkali salt. The partial pressure of carbon monoxide needs to be increased with respect to alkali reduction (see Figure 5.6a) in order to achieve complete reduction of iron oxide and physico-chemical separation from titanium oxide ; explaining why the Becher process is carried out at elevated temperatures for a prolonged period of time. The presence of Na^+ ions acts as key driving force to promote the chemical separation of Ti oxide from the Fe oxide. Formation of sodium titanate prevents the reduction of TiO_2 to TiO_{2-x}, which often occurs at higher P_{CO} conditions and temperatures. Sub-oxides of titanium dioxide co-exist with metallic iron, as seen in Figure 5.8.

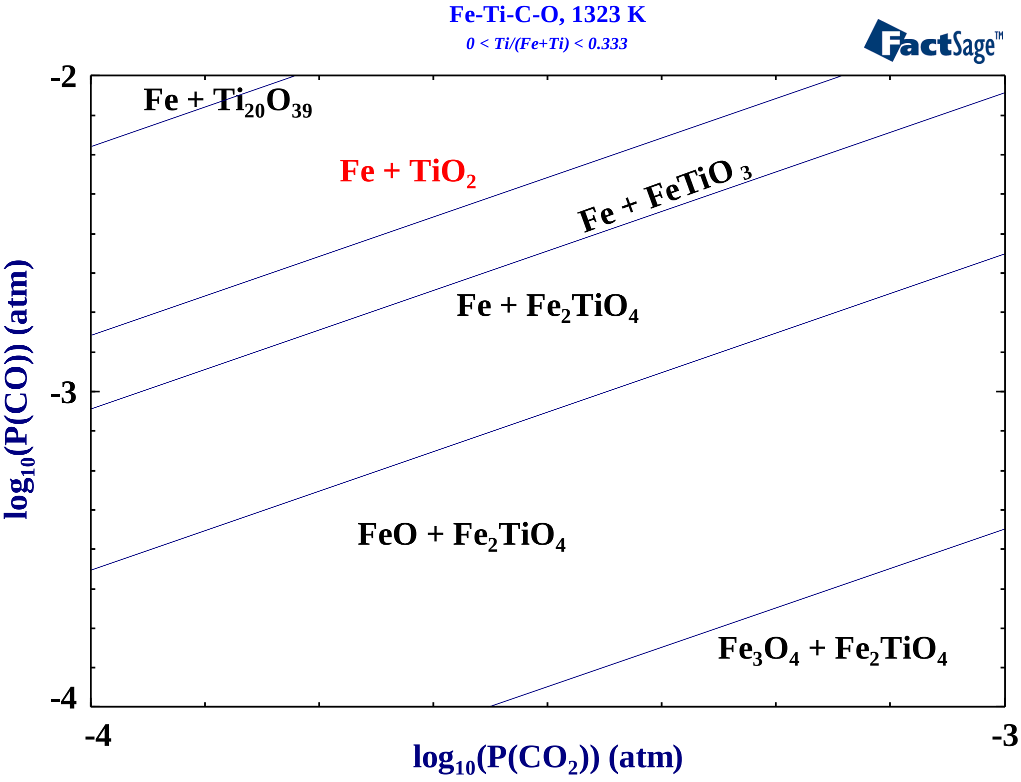

Figure 5.8 Predominance area diagram of Fe-Ti-O-C system at 1323 K, constructed using FactSage software [48].

5.2.2 Low-grade titanium dioxide slag predominance area diagrams

Studying the Mg-Al-Na-C-O-V multi component equilibria system is relevant for processing the T2 material. The $MgAl_2O_4$ spinel is a major component of the T2 material and hosts the V ions as magnesiocoulsonite. Figure 5.9 illustrates that in the presence of sodium ions and carbon at 1323 K the $MgAl_2O_4$ compound decomposes to magnesium oxide (MgO), sodium aluminate ($NaAlO_2$) and sodium vanadate, provided the environment is sufficiently reducing – which may explain why several authors failed to decompose the spinel during alkali roasting in air of titania slag [106, 138]. At $\log_{10}P(CO)(atm) \approx -4$ and $-3.5 < \log_{10}P(CO_2)(atm) < -3$ it can be observed that the $MgAl_2O_4$ phase is still intact, which would be detrimental for vanadium oxide extraction since V ions would remain in the crystal lattice.

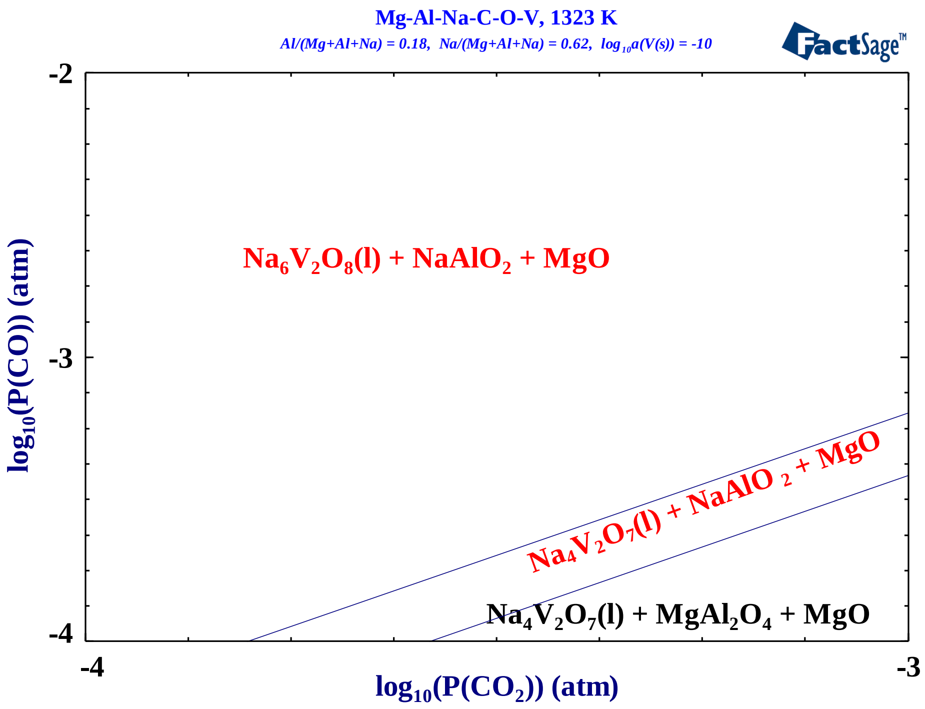

Figure 5.9 Predominance area diagram of Mg-Al-Na-C-O-V system at 1323K, constructed using FactSage software [48].

5.3 Phase equilibria calculations

5.3.1 Iron-rich tailings phase equilibria

Results from the phase equilibrium computation for the alkali reduction of the T1 at 1323 K are given in Table 5.1. The composition of the off-gas is greater than 99 mol % CO. Dominant solid phases obtained are cementite (Fe_3C), Fe and Na_4TiO_4(l). Gangue elements present are predicted to form $NaAlSiO_4$, while the CaO is expected to react with TiO_2 to form $CaTiO_3$. Vanadium is present as vanadium trioxide (V_2O_3) suggesting that no reaction with alkali carbonate occurs.

Table 5.1 Equilibrium products from the theoretical alkali reduction of iron-rich tailings at 1323 K.

Reactants	**Mass (g)**
Iron-rich tailings	100
Na_2CO_3	20.8
Activated charcoal	20.6
Equilibrium phase composition	
Products	**Mass (g)**
Solid	***91.57***
Fe_3C	26.13
Na_4TiO_4(l)	24.27
Fe	20.74
$NaAlSiO_4$	13.71
$CaTiO_3$	3.73
FeS	2.18
MgO	0.37
V_2O_3	0.25
$MgAl_2O_4$	0.11
Gas	***48.23***
CO	47.94
CO_2	0.26
Other	0.03

5.3.2 Low-grade titanium dioxide slag phase equilibria

The solid, liquid and gaseous products expected to be present at equilibrium for the alkali reduction of the T2, as calculated by FactSage 6.4, are detailed in Table 5.2. The off-gas is expected to be rich in CO gas, at over 75 mol percent with CO_2 gas comprising most of the balance ; implying that the off-gas could be used as fuel for combustion and power generation decreasing the overall process energy demand. CO_2 produced from combustion can be integrated into subsequent process steps. Molten sodium titanate is predicted to be the major phase present with $NaAlSiO_4$ and $CaTiO_3$ expected to be present in significant quantities. MgO and Ca-Mg-Si-O compounds are also expected to form along with metallic iron. Critically, vanadium is predicted to in the form of FeV_2O_4.

Table 5.2. Equilibrium products from the theoretical alkali reduction of low-grade TiO_2 slag at 1323 K.

Reactants	**Mass (g)**
Low-grade TiO_2 slag	100
Na_2CO_3	45
Activated charcoal	4.3
Equilibrium phase composition	
Products	**Mass (g)**
Solid	**124.4**
Na_4TiO_4(l)	40.01
$NaAlSiO_4$	24.27
$CaTiO_3$	23.44
MgO	8.41
$Ca_3MgSi_2O_8$	8.33
$CaMgSiO_4$	4.57
Fe	1.8
FeV_2O_4	0.98
MnS	0.77
FeS	0.52
$MgCr_2O_4$	0.18
Gas	**24.93**
CO	18.89
CO_2	6.03
Other	0.01

5.4 Chapter summary

Thermodynamic considerations demonstrate that carbothermic reduction of $FeTiO_3$ and Fe_2TiO_4 in the presence of Na_2CO_3 is more favourable than reduction carried out in the absence of the alkali carbonate. Analysis of competing reactions indicates the consumption of Na_2CO_3 by gangue phases such as Al_2O_3 and SiO_2.

Predominance area diagrams highlight for reduction of iron-rich tailings, metallic iron and sodium titanate co-exist in the sample phase field of $\log_{10}P(CO)(atm) \approx -2.5$ and $-4 < \log_{10}P(CO_2)(atm) < -3$. Mg-Al-Na-C-O-V multi component equilibria system at

1323 K illustrated that at $-3.5 < \log_{10}P(CO)(atm) < -2$ and $-4 < \log_{10}P(CO_2)(atm) < -3$ $MgAl_2O_4$ is decomposed to sodium vanadate, sodium aluminate and magnesium oxide.

Phase equilibria computation for alkali reduction of iron-rich tailings at 1323 K predict the formation of Fe_3C, Fe, $NaAlSiO_4$ and Na_4TiO_4 as dominant phases. Multi component system calculations for low-grade TiO_2 slag reduction in the presence of Na_2CO_3 indicate the presence of $CaTiO_3$, $NaAlSiO_4$ and Na_4TiO_4 among the reduced products.

6 Carbothermic reduction of iron-rich tailings and low-grade titanium dioxide slag in the presence of alkali salts

Chapter 6 focuses on the carbothermic reduction of the iron-rich tailings and low-grade TiO_2 slag in the presence of alkali carbonates. Kinetics and mechanism are studied using the experimental TGA data and the apparent activation energy reported, including the different reaction regimes. Reduced samples are characterised to gain insight into the physico-chemical separation of metal oxides and the impact on subsequent recovery of metallic values.

6.1 Carbothermic reduction of iron-rich tailings in the TGA apparatus

Reaction models

Solid state reactions may be controlled by the reaction at the interface or diffusion of the product and reactant species through the product layer. When the diffusion of species is faster than the chemical reaction, the process is controlled by chemical reaction at the interface and can be described by equation 6.1 [181]. Ginstling and Brounshtein (GB) derived a model for reactions under diffusion control and is written in equation 6.2 [182]. Where X is the fraction reacted (see equation 6.3), k is the rate constant and t is the time in hours.

$$1-(1-X)^{\frac{1}{3}}=kt \qquad 6.1$$

$$1-\frac{2}{3}X-(1-X)^{\frac{2}{3}}=kt \qquad 6.2$$

$$X=\frac{\text{Observed weight loss(g)}}{\text{Theoretical weight loss(g)}} \qquad 6.3$$

A mixed-control model was considered by combining both the Interface and diffusion controlled models to give equation 6.4.

$$1-(1-X)^{\frac{1}{3}}+\;1-\frac{2}{3}X-(1-X)^{\frac{2}{3}}=kt \qquad 6.4$$

6.1.1 Carbothermic reduction of iron-rich tailings in the absence of alkali carbonate

Iron-rich tailings mixed with activated charcoal was reduced in the TGA apparatus between the 1073 K to 1323 K temperature range under argon atmosphere. Reduction of

T1 in the absence of alkali carbonate was performed to compare with carbothermic reduction results obtained from utilising Na_2CO_3.

The percentage reduction (%R), calculated according to equation 6.5 was plotted against temperature and the curves presented below in Figure 6.1. Below 1173 K the %R is limited and is particularly low at 1073 K where 15% reduction is attained. However, %R increases as the temperature increases with 82% being the maximum %R achieved at 1323 K. The reported maximum value is higher than results noted in literature for the solid-state reduction of titanomagnetite concentrates; even when the titanomagnetite is pre-oxidised, as pre-oxidation enhances the extent of reduction [183]. T1 has been pre-oxidised during the previous oxidative salt roasting process. %R observed in this study may have been further enhanced by the presence of residual sodium sulphate salts from the initial treatment, as alkali salts have been reported to increase the extent of reduction [183].

$$\%R = \frac{\text{Observed weight loss(g)}}{\text{Theoretical weight loss(g)}} * 100 \qquad 6.5$$

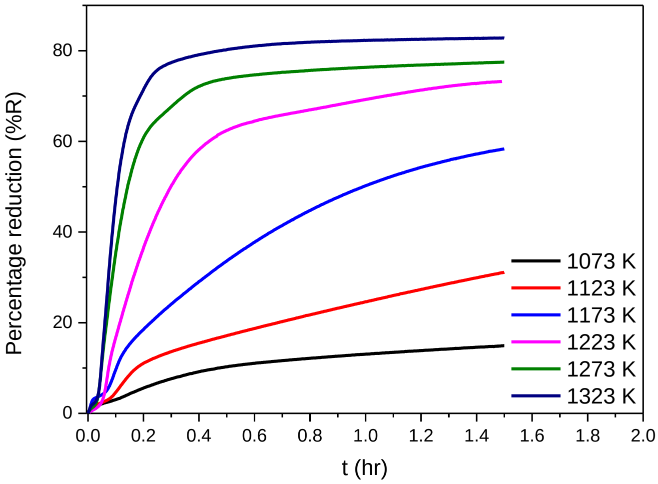

Figure 6.1 Percent reduction curves for the isothermal reduction of iron-rich tailings with activated charcoal from 1073 K to 1323 K.

X-ray powder diffraction analysis

XRPD patterns for the reduced samples are given below in Figure 6.2. Limited formation of Fe is seen at 1073 K, which is to be expected considering the limited %R reported in Figure 6.1. The dominant peaks at 1073 K represent Fe_2TiO_4 and $FeTiO_3$. Intensity of the Fe peak increases as the temperature increases while there is a decrease in the Fe_2TiO_4 and $FeTiO_3$ peaks. However, Fe_2TiO_4 is still present at 1323 K even though Fe is the dominant phase present at this temperature.

Experimental XRPD results broadly agree with the predominance area diagram for the Fe-Ti-C-O system in Figure 5.8 that illustrated Fe could co-exist with Fe_2TiO_4 at $\log_{10}P(CO)(atm) \approx -2.6$ and $-4 < \log_{10}P(CO_2)(atm) < -3$ and with $FeTiO_3$ between $\log_{10}P(CO)(atm) \approx -3$ and $-4 < \log_{10}P(CO_2)(atm) < -3$. Based on the PAD, absence of TiO_2 in XRPD patterns suggests $\log_{10}P(CO)(atm)$ value during TGA experiments was below the required value necessary to form TiO_2.

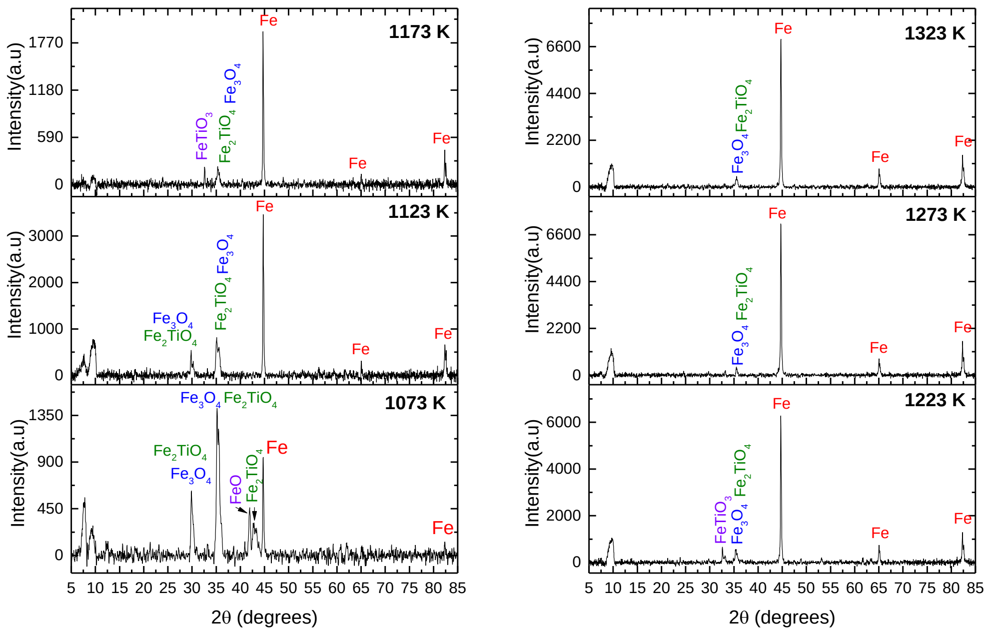

Figure 6.2 Effect of temperature on carbothermic reduction of iron-rich tailings with XRPD patterns presented in the 1073 K to 1323 K temperature range.

Scanning electron microscopy analysis

Figure 6.3 illustrates the microstructure of T1 sample reduced at 1323 K in the absence of Na_2CO_3. Observing the SEM image makes it evident that the metallised iron is largely present at the periphery of the particle showing that carbothermic reduction follows the shrinking core model [184]. Metallic iron particles contain 96.7 weight.% Fe (see Area A on Figure 6.3b).

At the centre of the particle there is evident phase segregation between the dark grey area (see Area B on Figure 6.3b) and the light grey area (see Area C on Figure 6.3b). Dark grey area B is a Na-Al-Mg-Si-O complex which contains a minor amount of dissolved TiO_2. The light grey area C is rich in TiO_2 and it can be noted that the vanadium associated with this phase. Presence of TiO_2 at the core of the particle and metallised iron grains at the periphery is similar to microstructure observed by Kuckkaragoz et al. [83] when reducing ilmenite with graphite.

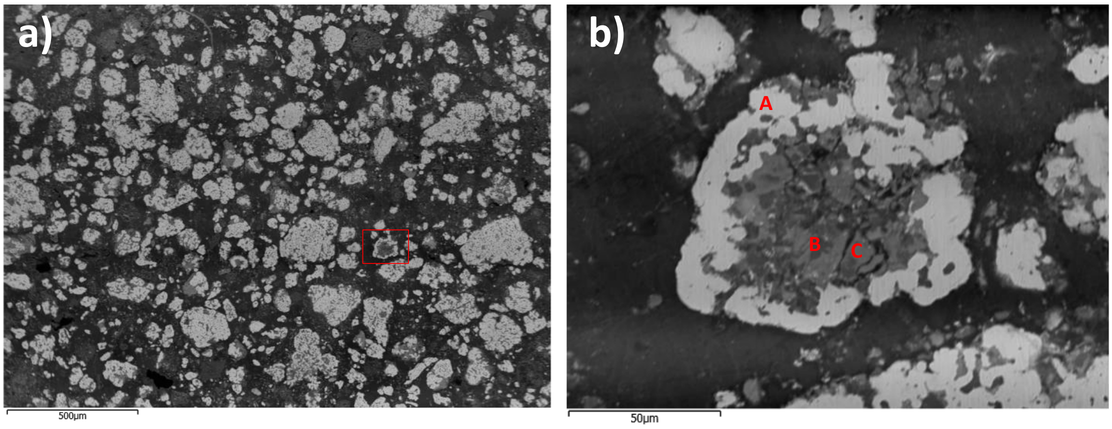

Figure 6.3 Backscattered SEM image of iron-rich tailings reduced in the absence of alkali carbonate at 1323 K, in the TGA apparatus.

Table 6.1. Elemental composition of areas A to C on Figure 6.3b as analysed by EDX.

Weight.%	Ti	Na	Fe	O	V	Si	Ca	Al	Mg	Mn
A	0.7	0.6	96.7	1.8	-	0.2	-	-	-	-
B	5.7	19.4	1.8	37.7	-	11.4	1.2	20.0	2.5	0.4
C	46.1	11.2	4.9	34.0	0.6	0.3	0.6	0.3	0.8	0.8

Kinetic model fitting

Isothermal reduction data was fitted using the kinetic models to determine the mechanism and calculate the apparent activation energy. The fitting results are presented in Figure 6.4 to Figure 6.6 using the Interface, G.B and combined Interface-G.B model, respectively.

Good fitting is observed for both the Interface and G.B models indicating that carbothermic reduction of T1 is under mixed-control. However, improved fitting of the G.B model occurs below 1223 K compared to the results from the Interface model below 1223 K. A combined Interface + G.B model fitting, representing mixed-control, is given in Figure 6.6 where it is evident that linear regression analysis results are superior to both the individual Interface and G.B models. Table 6.2 is a summary of the linear regression analysis of the rate constants for the three different model fitting plots.

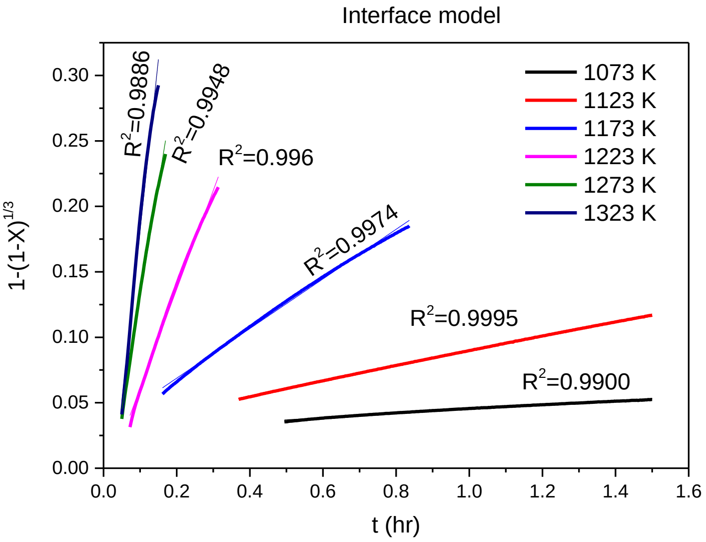

Figure 6.4 Plot of the Interface model versus time (hr) for the carbothermic reduction of iron-rich tailings between 1073 K and 1323 K.

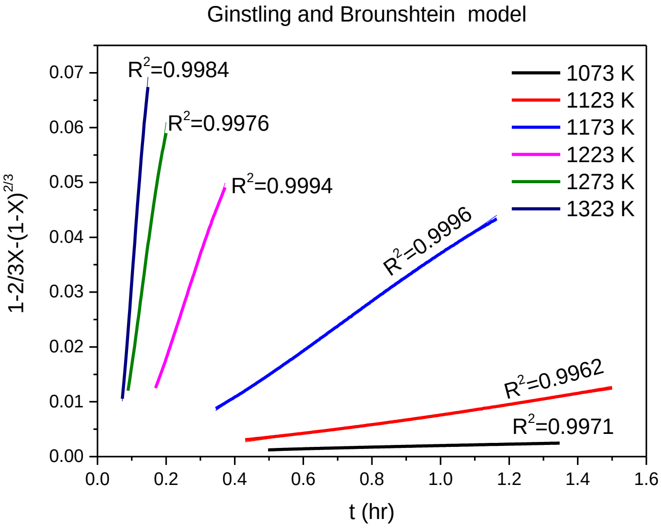

Figure 6.5 Plot of the Ginstling and Brounshtein model versus time (hr) for the carbothermic reduction of iron-rich tailings between 1073 K and 1323 K.

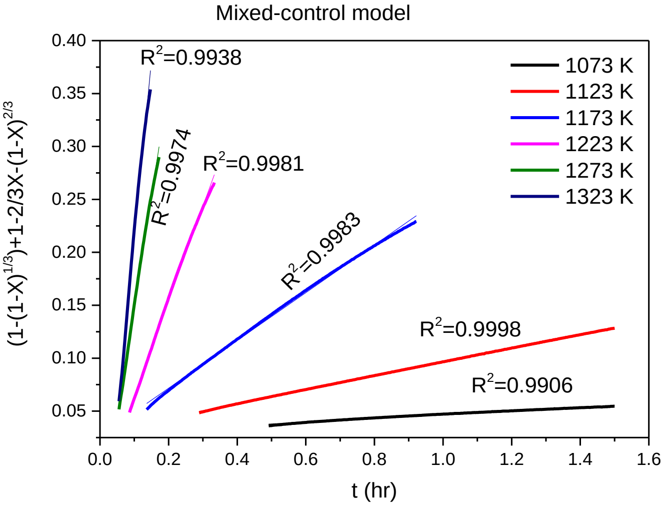

Figure 6.6 Plot of the Mixed-control model versus time (hr) for the carbothermic reduction of iron-rich tailings between 1073 K and 1323 K.

Table 6.2 Linear regression analysis of rate of constants at different temperatures using Interface, Ginstling and Brounshtein (GB) and Mixed-control models.

Temperature (K)	Interface model		G.B model		Mixed-control model	
	k	Standard error	k	Standard error	k	Standard error
1073 K	0.0162	8.5206E-5	0.0014	4.3329E-6	0.0175	8.9144E-5
1123 K	0.0568	6.1493E-5	0.009	2.8395E-6	0.0654	4.5810E-5
1173 K	0.1895	6.2473E-5	0.0435	5.3389E-5	0.2256	5.5442E-4
1223 K	0.7546	0.00513	0.1851	5.4871E-4	0.8943	0.0042
1273 K	1.7158	0.0189	0.4383	0.0034	2.0965	0.0164
1323 K	2.6129	0.0468	0.7885	0.0060	3.3474	0.046

Arrhenius plot and activation energy

Figure 6.7 is the plot of ln k vs 1/T for the carbothermic reduction of iron-rich tailings in the absence of Na_2CO_3, where the activation energy (q) was calculated according to the Arrhenius equation given in equation 6.6 where R is the universal gas constant and A is the pre-exponential frequency factor. As both the chemical reaction and diffusion have a significant influence on the rate of reaction, the rate constants derived from the mixed control model – for which high R^2 values were also observed - were used to determine the apparent activation energy of the global reaction. The apparent activation energy of 258 ± 13 $kJ.mol^{-1}$ derived from the plot is consistent with the C-CO_2 reaction for activated charcoal, where the reported range is between 217 $kJ.mol^{-1}$ and 251 $kJ.mol^{-1}$ [185, 186]. A single reaction regime is visible when using activated charcoal in the absence of alkali salts.

$$\ln k = \ln A - \frac{Q}{R} * \frac{1}{T} \qquad 6.6$$

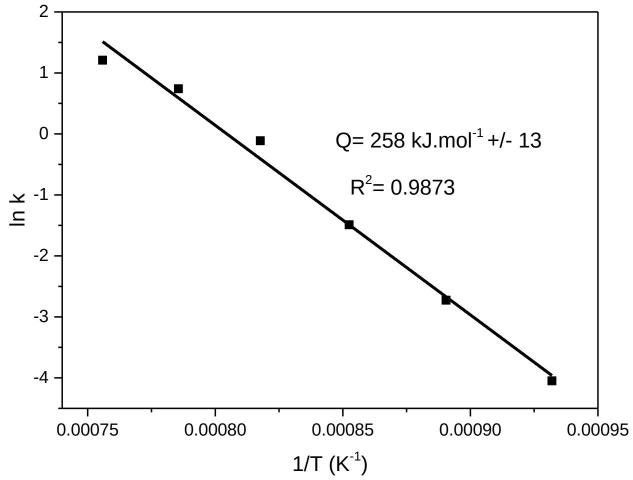

Figure 6.7 Arrhenius plot of ln k versus reciprocal temperature for carbothermic reduction of iron-rich tailings.

6.1.2 Carbothermic reduction of iron-rich tailings in the presence of Na_2CO_3

The iron-rich tailings was ground to – 106 µm, thoroughly mixed with Na_2CO_3 and activated charcoal before being placed in an alumina crucible that was suspended on the thermogravimetric analysis (TGA) balance using a stainless steel wire. Experiments were carried out isothermally and the reaction kinetics were analysed at temperatures between 1073 K and 1323 K. The TGA reaction tube was purged with argon gas at 0.5 l/min in order to maintain the reducing atmosphere. The reduced samples were analysed using scanning electron microscopy – energy dispersive X-ray spectroscopy (SEM-EDX) and X-ray powder diffraction techniques.

The percentage reduction (%R) against time for isothermal reduction in the temperature range of 1073 K - 1323 K is presented in Figure 6.8. The effect of temperature can be seen on the reaction; the %R achieved increases as the temperature increases and a maximum value of 97% reduction is attained at 1323 K. 97 %R is higher than what has been achieved by previous authors that added up to 3% Na_2CO_3 to catalyse carbothermic reduction at 1523 K [183]. Use of sufficient quantities of Na_2CO_3 to react with TiO_2 in titanomagnetite concentrates and titanomagnetite tailings is what distinguishes the work in this report from previous authors. Formation of Na_2TiO_3 lowers the activity TiO_2 to less than unity.

At 1073 K, the rate of reaction is the slowest as this curve is seen to increase gradually with an exponential shape and the %R achieved is below 90%. As the temperature increases the curves change from growing exponentially to increasing linearly. For isotherms 1173 K to 1323 K it can be noted that during the initial period the curves rise steeply before plateauing.

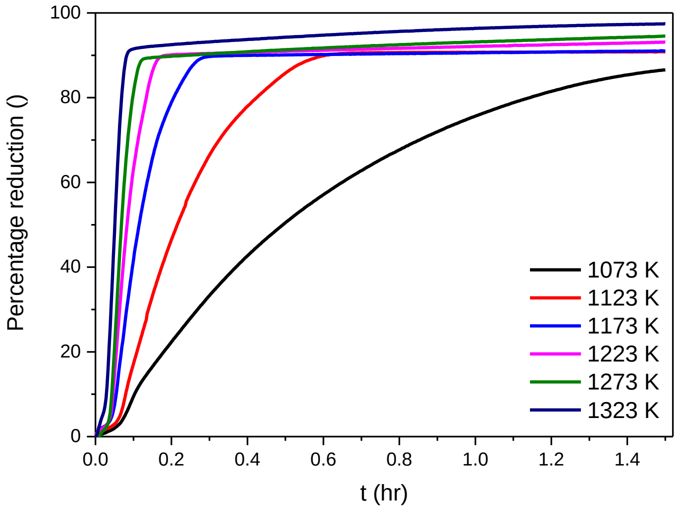

Figure 6.8 Percent reduction curves for the isothermal reduction of the iron-rich tailings in the presence of Na_2CO_3 between 1073 K and 1323 K.

X-ray powder diffraction analysis

The XRPD patterns of T1 reduced in the presence of Na_2CO_3 in the temperature range of 1073K -1323K are presented in Figure 6.9a - Figure 6.9f.

The main phase present at all temperatures is ferrite (α- Fe) showing that the presence alkali carbonate in a reducing environment allows for the significant reduction of iron oxide present, even at temperatures below 1273 K. Below 1223 K, there are minor peaks representing ulvöspinel and sodium titanate.

Sodium aluminosilicate peaks are visible above 1173 K. Formation of the $NaAlSiO_4$ over separate $NaSiO_3$ and $Na_2Al_2O_4$ phases agrees with the thermodynamic considerations given in chapter 5. Standard Gibbs free energy change calculations presented in Figure 5.3 showed that formation of $NaAlSiO_4$ was more favourable than that of both $NaSiO_3$ and $Na_2Al_2O_4$ phases, while phase equilibria computations (see Table 5.1) predicted formation of $NaAlSiO_4$.

The XRPD patterns of T1 reduced in the presence of Na_2CO_3 broadly agree with the predominance agree diagrams (see Figure 5.6) given in chapter 5, which predicted that metallic Fe and sodium titanate co-exist in the same phase field. The PAD also demonstrated that the ulvöspinel phase would be present when the reduction was incomplete.

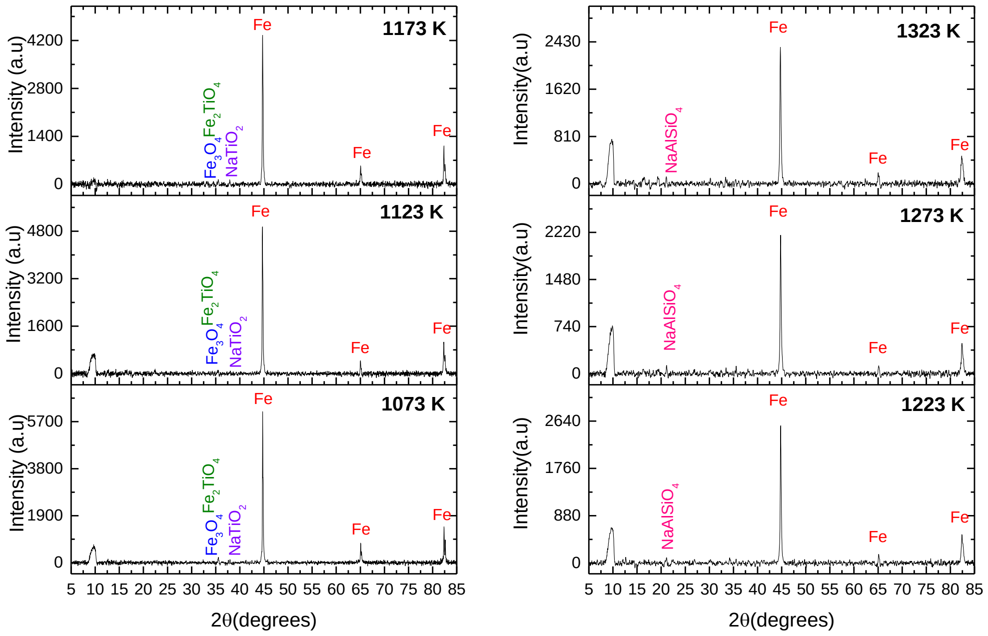

Figure 6.9 Effect of temperature on carbothermic reduction of iron-rich tailings in the presence of Na_2CO_3 in the TGA from 1073 K – 1323 K.

Scanning electron microscopy

Backscattered SEM of T1 reduced in the presence of Na_2CO_3 at 1323K is shown in Figure 6.10. Observing the microstructure it is clear that there are three distinct phases formed during the reaction.

Elemental mapping indicates that the metallic Fe has segregated from the sodium titanate phase [184]. Authors have reported that presence of minor amount of Na_2CO_3 helps promote the growth of iron grains during carbothermic reduction [117, 119]. Large Fe particles are desirable as they enhance the succeeding magnetite separation.

Mapping data demonstrates the formation of a Na-Ti-Mg-Al-Si-O complex and which can be explained by the reaction face between sodium aluminosilicates and Ti-rich phases [120]. The V map shows overlap with the Na-Ti-O phase. Distinct separation of Fe from Ti and V implies that wet magnetic separation of the reduced sample would allow for selective recovery of these metals. Fe would report to a magnetic fraction, whereas Ti and V oxides would be present in the non-magnetic fraction and water solution, respectively.

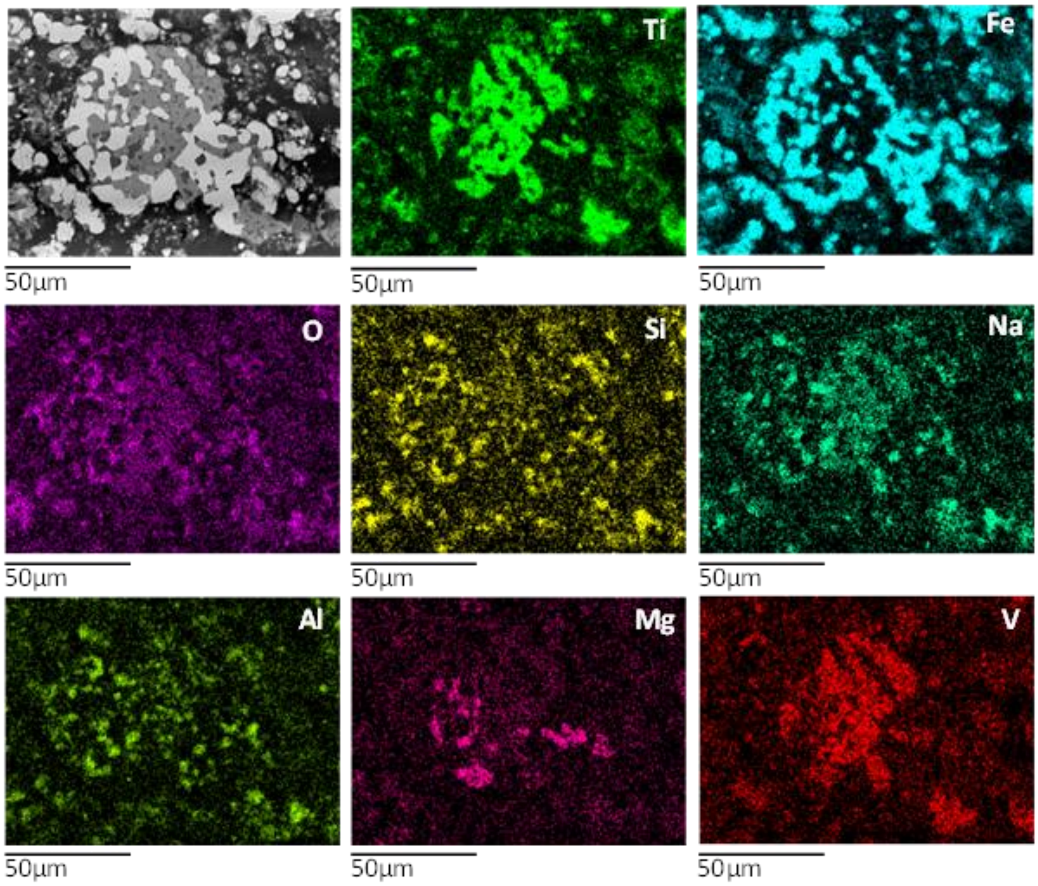

Figure 6.10. Backscattered SEM image and elemental mapping of iron-rich tailings reduced in the presence of Na_2CO_3 at 1323 K in the TGA apparatus.

Kinetic model fitting

The Interface and G.B models were fitted to the isothermal weight loss data obtained from the TGA experiments. Figure 6.11 and Figure 6.12 are plots for the Interface and G.B models, respectively. It can be observed that the experimental data fits well for the G.B model at low temperatures. As the temperature increases, the goodness of fit for the Interface model improves. High R^2 values for both Interface and G.B models implies that the reaction is under mixed-control, which is confirmed by fitting for the mixed-control model given in Figure 6.13. The rate constants derived from kinetic model fitting are detailed in Table 6.3.

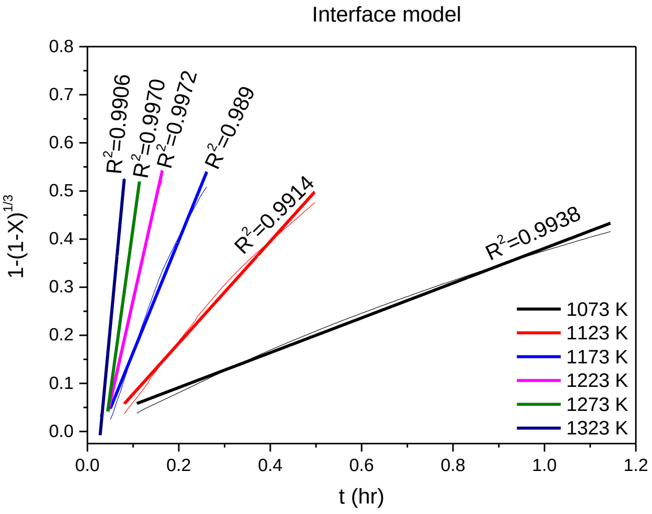

Figure 6.11 Plot of Interface model against time (hr) for carbothermic reduction of iron-rich tailings in the presence of Na_2CO_3 between 1073 K and 1323 K.

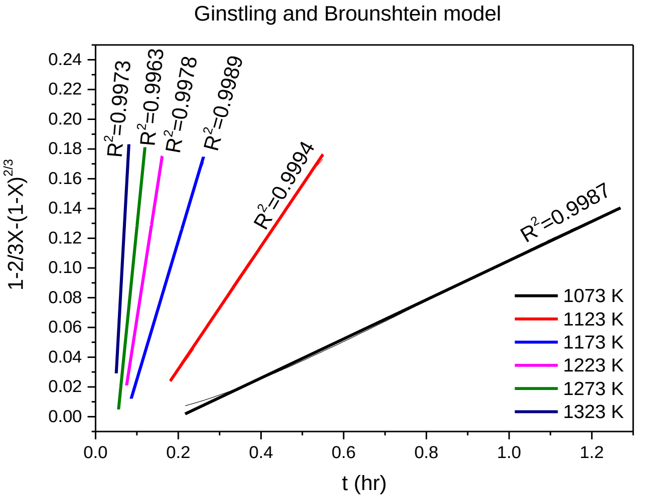

Figure 6.12 Plot of Ginstling and Brounshtein model against time (hr) for carbothermic reduction of iron-rich tailings in the presence of Na_2CO_3 between 1073 K and 1323 K.

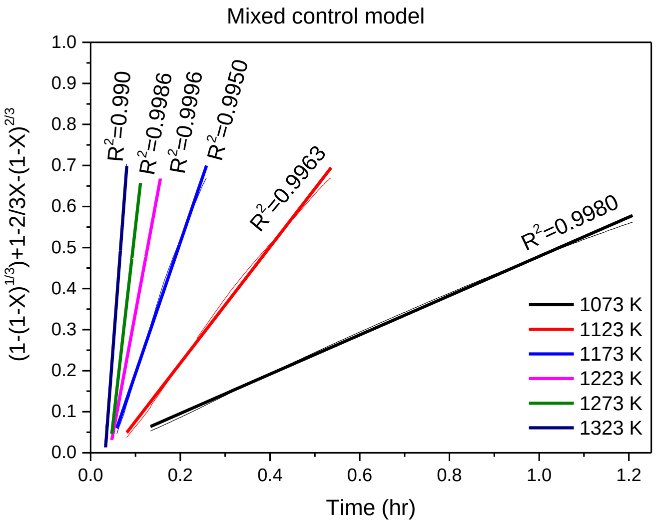

Figure 6.13 Plot of Mixed-control model against time (hr) for carbothermic reduction of iron-rich tailings in the presence of Na_2CO_3 between 1073 K and 1323 K.

Table 6.3. Linear regression analysis of rate of constants at different temperatures using Interface, Ginstling and Brounshtein (GB) and Mixed-control models.

Temperature (K)	Interface model		G.B model		Mixed-control model	
	k	Standard error	k	Standard error	k	Standard error
1073 K	0.3616	0.0015	0.1316	2.4694E-4	0.47836	0.00109
1123 K	1.0573	0.0080	0.4127	8.8008E-4	1.41695	0.00676
1173 K	2.3322	0.0282	0.9300	0.0039	3.20029	0.0267
1223 K	4.2246	0.0344	1.7919	0.015	5.87899	0.01752
1273 K	6.8793	0.0753	2.7610	0.0353	9.56056	0.07365
1323 K	10.0867	0.2249	5.0427	0.0786	14.51883	0.35424

Time interval analysis

Reacted products were removed from the TGA apparatus after 2 minutes and 5 minutes. In Figure 6.14a the reduced Fe is located at the core of the particle after 2 minutes, allowing gas diffusion to occur readily [187]. As the reaction is under mixed-control it implies that during the initial stages the chemical reaction is rate determining. However, after 5 minutes the product layer begins to form as the Fe^{2+} ions have migrated to the periphery of the particle forming a product layer that acts as barrier to the diffusion of gaseous species.

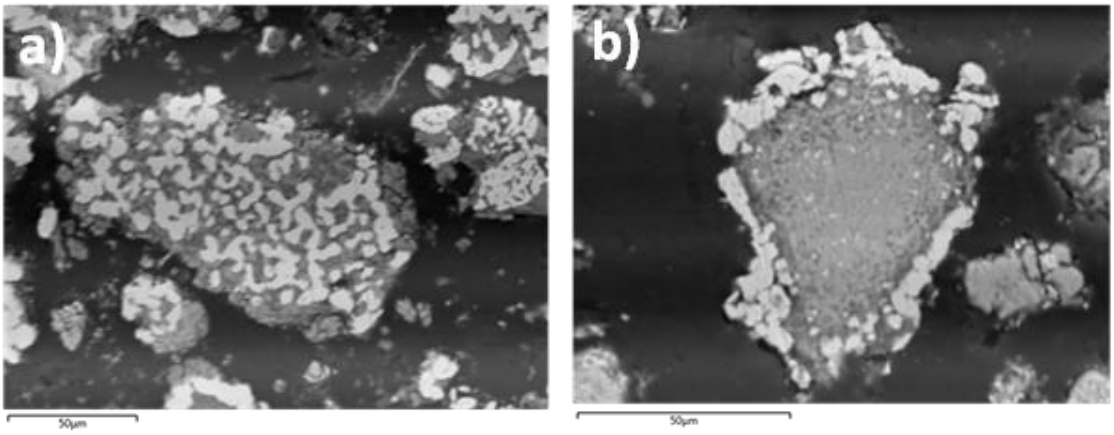

Figure 6.14 Backscattered SEM image and elemental mapping of iron-rich tailings reduced in the presence of Na_2CO_3 at 1323 K after a) 2 minutes and b) 5 minutes in the TGA apparatus.

Arrhenius plot and activation energy

The plot of the natural logarithm versus reciprocal temperature for the alkali reduction is presented in Figure 6.15. The slope of ln k vs 1/T line changes at 1173 K, suggesting that there are two reaction regimes and further illustrating the role of temperature in the reaction. At lower temperatures the apparent activation energy is seen to be 199 ±11 $kJ.mol^{-1}$. The reported value would be consistent with the outward diffusion of O^{2-} ions, which has a reported activation energy of 190 $kJ.mol^{-1}$ [188]. The apparent activation energy at higher temperatures is 130 ± 5 $kJ.mol^{-1}$, which corresponds to the outward diffusion of Fe^{2+} ions that has an activation energy within the range of 117 $kJ.mol^{-1}$ to 140 $kJ.mol^{-1}$ [189]. Observing the microstructure of the T1 reduced particles (see Figure 6.10) confirms the outward diffusion of Fe^{2+} ions as the iron particles are seen at the periphery of the particle. The presence of Na_2CO_3 during carbothermic reduction of T1 lowers the apparent activation energy and results in there being two reaction regimes compared to carbothermic reduction of T1 in the absence of Na_2CO_3 that had an apparent activation energy of 258 $kJ.mol^{-1}$.

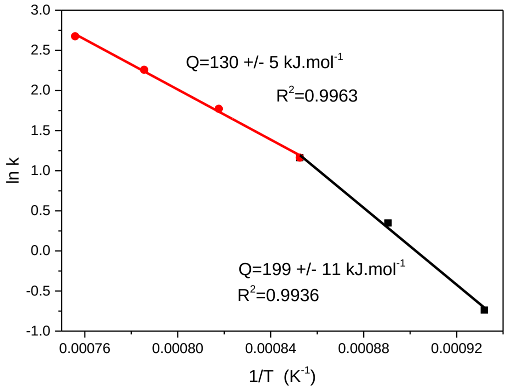

Figure 6.15. Arrhenius plot of ln k versus reciprocal temperature for carbothermic reduction of iron-rich tailings in the presence of Na_2CO_3. The k values used were calculated using the Mixed-control model.

Reaction mechanism

During the carbothermic reduction of T1 in the presence of Na_2CO_3, Na^+ ions from Na_2CO_3 enter the lattice structures of ilmenite and ulvöspinel. As the ionic size of Na^+ is 97 pm it displaces the Fe^{2+} ions whose ionic size is 74 pm, creating strain within the lattice that allows for the formation of sodium titanate [99]. There is outward diffusion of the Fe^{2+} ions towards the periphery of the particles as they form a dense product layer of metallic iron, as the reaction proceeds via the shrinking core model. O^{2-} ions are removed by carbon during the course of the reaction to give CO. Na_2CO_3 reacts with the aluminosilicates and vanadium oxide present to form sodium aluminosilicates and sodium vanadates, respectively.

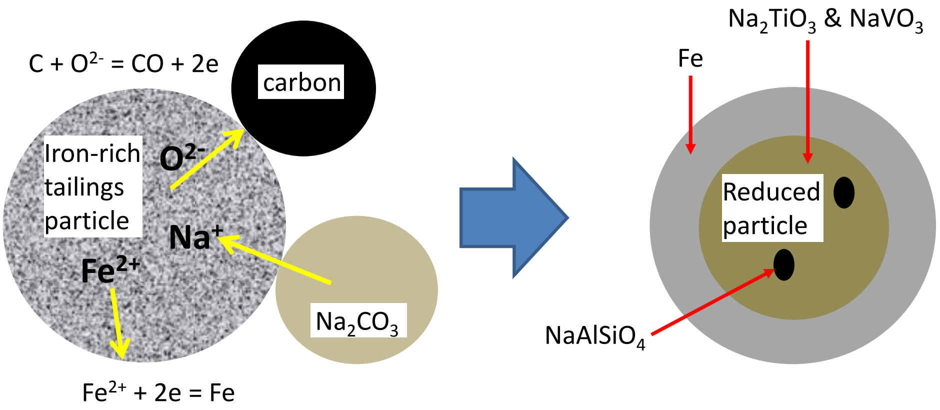

Figure 6.16. Schematic illustration of iron-rich tailings carbothermic reduction in the presence of Na_2CO_3.

6.1.3 Carbothermic reduction of iron-rich tailings in the presence of K_2CO_3

The standard Gibbs free energy change calculations in chapter 5 (see Figure 5.5) showed that reduction of T1 in the presence of K_2CO_3 is significantly more favourable than the reduction of T1 with Na_2CO_3. Experiments were carried out in the TGA apparatus in order to compare the kinetics and mechanism of these two alkali salts.

The reduction of T1 with K_2CO_3 follows a similar trend to what was observed when using Na_2CO_3, as seen in Figure 6.17. The %R increases as the temperature increases. The %R for the 1223 K isotherm in the initial period is greater than for the 1273 K isotherm. However, as the reaction proceeds the 1273 K curves rises above the 1223 K curve.

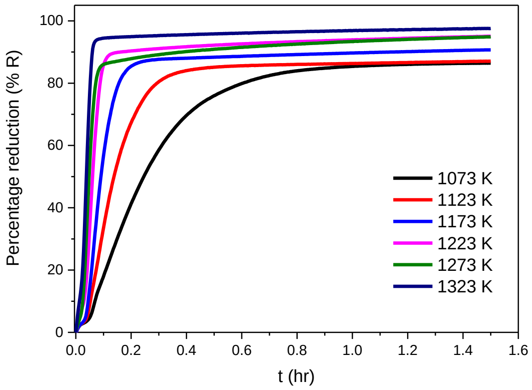

Figure 6.17 Percent reduction curves for the isothermal reduction of the iron-rich tailings in the presence of K_2CO_3 between 1073 K and 1323 K.

X-ray powder diffraction analysis

The XRPD patterns of T1 treated in the 1073 K – 1273 K are given in Figure 6.18. Fe is the dominant phases formed at all the temperatures. Interestingly, no peaks are observed for the ulvöspinel phase, even at 1073 K, differing from the XRPD patterns from reduction with Na_2CO_3 (see Figure 6.9) where Fe_2TiO_4 was observed at temperatures up to 1173 K.

Potassium aluminosilicate is observed in the XRPD patterns for 1073 K, 1123 K, 1173 K and 1323 K experiments. Peaks for the ternary K-Ti-Fe-O ternary complex are also noted indicating that not all the iron oxide has been reduced to metallic iron. Formation of a liquid phase during the reduction may have influenced presence of the ternary complex, as the liquid phase would inhibit the diffusion of gaseous species preventing the reduction the iron oxide to metallic iron [190, 191].

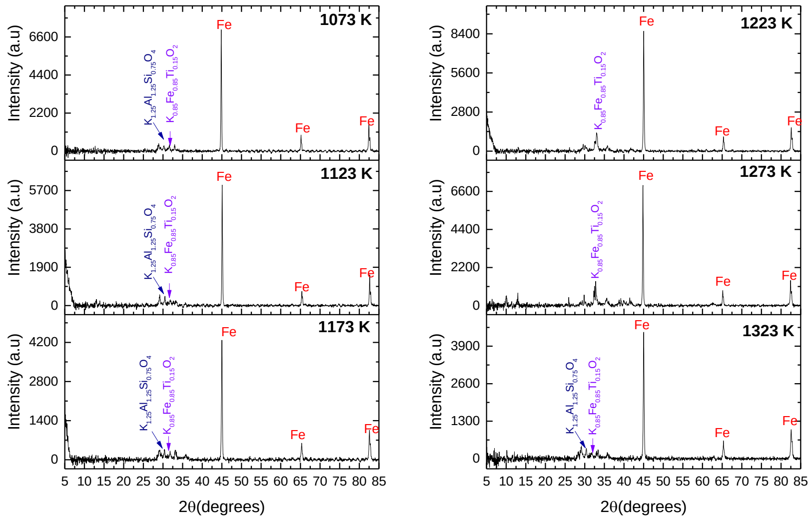

Figure 6.18 Effect of temperature on carbothermic reduction of iron-rich tailings in the presence of K_2CO_3 from 1073 K – 1323 K in the TGA apparatus.

Scanning electron microscopy analysis

In Figure 6.19 the SEM of the sample reduced at 1323 K in the TGA apparatus shows that much of the iron is located at the periphery of the particle. The K-Al-Si-O complex has been segregated from the K-Fe-Ti-O ternary complex, as the elemental mapping shows immiscibility between these complexes.

K-Al-Si-O complex at the core of the particle may inhibit the complete reduction of iron oxide by limiting the diffusion of gaseous species thus the presence of K-Fe-Ti-O ternary complex. The microstructure analysis appears to show that the phase separation during carbothermic reduction of T1 is superior when utilising Na_2CO_3 compared to K_2CO_3.

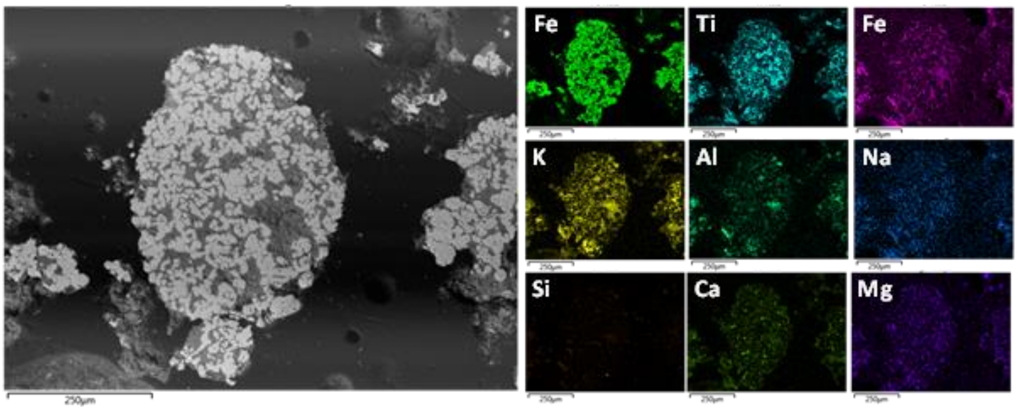

Figure 6.19. Backscattered SEM image and elemental mapping of iron-rich tailings reduced in the presence of K_2CO_3 at 1323 K in the TGA apparatus.

Kinetic model fitting

Kinetic model fitting using the %R data was performed and the results are presented in Figure 6.20 to Figure 6.22. The high R^2 value for the Interface and G.B models indicate that reduction in the presence of K_2CO_3 is under mixed –control ; similar to what was observed for the alkali reductive roasting using Na_2CO_3. The linear regression analysis results detailing the rate constants are given in Table 6.4.

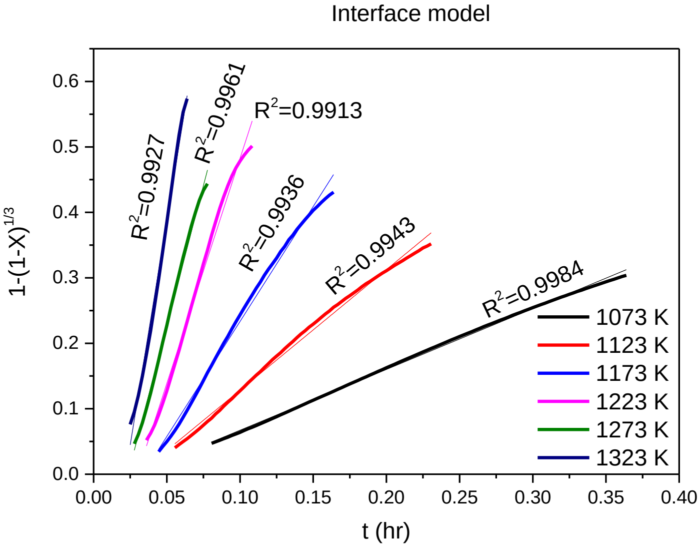

Figure 6.20 Plot of Interface model against time (hr) for carbothermic reduction of iron-rich tailings in the presence of K_2CO_3 between 1073 K and 1323 K.

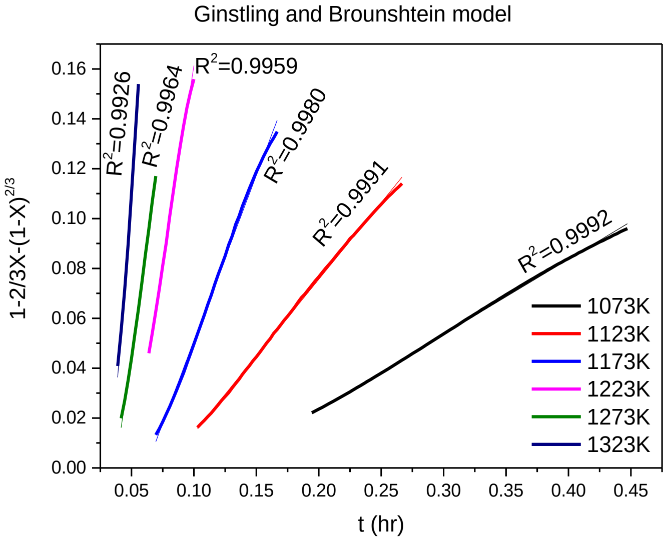

Figure 6.21 Plot of Ginstling and Brounshtein model against time (hr) for carbothermic reduction of iron-rich tailings in the presence of K_2CO_3 between 1073 K and 1323 K.

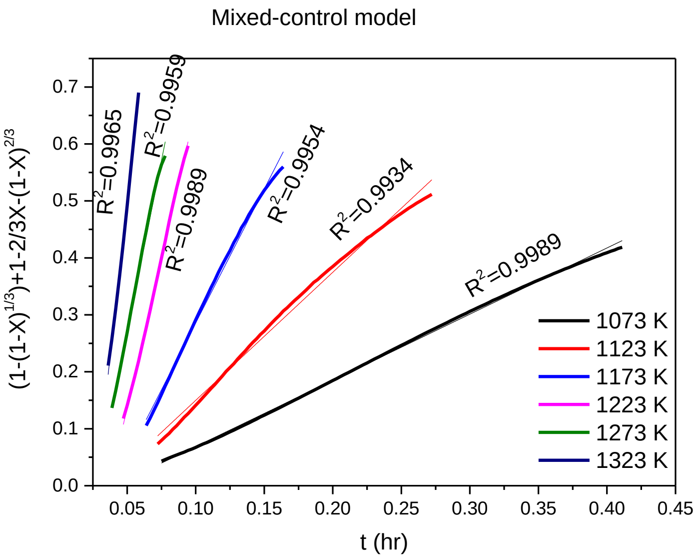

Figure 6.22 Plot of Mixed-control model against time (hr) for carbothermic reduction of iron-rich tailings in the presence of Na_2CO_3 between 1073 K and 1323 K.

Table 6.4 Linear regression analysis of rate of constants at different temperatures using Interface, Ginstling and Brounshtein (GB) and Mixed-control models.

Temperature (K)	Interface model		G.B model		Mixed-control model	
	k	Standard error	k	Standard error	k	Standard error
1073 K	0.9294	0.0037	0.3012	9.0445E-4	1.1623	0.0035
1123 K	1.8417	0.0176	0.6146	0.0024	2.2485	0.0216
1173 K	3.513	0.043	1.3261	0.0101	4.7035	0.0536
1223 K	6.8759	0.1263	3.1832	0.0567	10.5154	0.0846
1273 K	8.564	0.1258	3.5730	0.0676	11.9494	0.2051
1323 K	13.7188	0.3141	6.8282	0.2408	21.8274	0.4547

Arrhenius plot and activation energy

The apparent activation energy for carbothermic reduction using K_2CO_3 is 127 ± 7 $kJ.mol^{-1}$., which corresponds to the outward diffusion of Fe^{2+} ions [189]. A metallic iron product layer observed in the microstructure (see Figure 6.19) confirms the outward diffusion of ferrous ions. One reaction regime is observed in Figure 6.23, contrasted with reduction with Na_2CO_3 where two reactions regimes were visible. This shows the influence of K_2CO_3 is to lower the apparent activation energy at lower temperatures, which is consistent with literature that has stated K_2CO_3 has more catalytic activity than Na_2CO_3 [71].

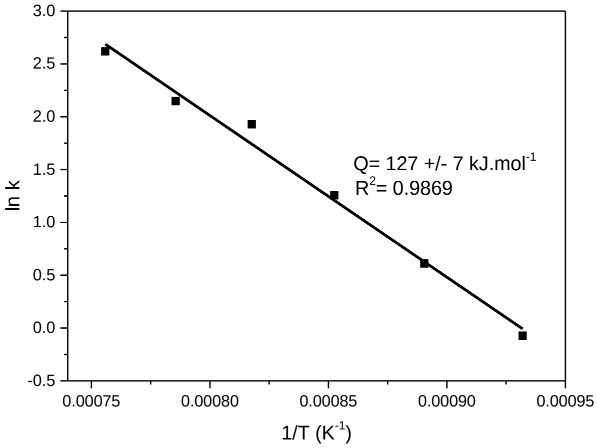

Figure 6.23 Arrhenius plot of ln k versus reciprocal temperature for carbothermic reduction of iron-rich tailings in the presence of K_2CO_3.

6.2 Carbothermic reduction of iron-rich tailings in rotary kiln

Processing of the T1 material was scaled up to 200 g of the waste material, 40.6 g Na_2CO_3 and 46 g activated carbon in the rotary kiln. The study was performed to investigate the behaviour of the reaction during a semi-continuous operation.

Ring formation is a major issue affecting rotary kiln performance and can often lead to full shutdown in order to resolve the problem [192] [193]. The presence of the liquid phase during processing promotes ring formation as particles are able to adhere to the tube wall. In order to limit the ring formation different parameters have been adjusted to determine their effect on accretion formation inside the rotary kiln tube. Owing to the limited length of the rotary kiln hotzone the samples were passed through the kiln multiple times. Any material that remained in the tube and around the screw after each pass was collected and mixed with the sample that was collected in the glass tube. The mixture was re-fed into the rotary kiln hopper.

The inner tube was inspected after each pass to assess the extent of ring formation and the amount of material remaining in the tube as a percentage of the input (%tube) for each pass was calculated. Typically, the samples collected after the fourth pass were collected for analysis using XRPD and SEM techniques. A summary of the rotary kiln experiments is given in Table B.1.

6.2.1 Residence time calculations

An important consideration when treating material in a rotary kiln is the residence time of the mixture in the rotary kiln tube. The empirical model for predicting the residence time of granular materials in a rotary kiln is the Sullivan model (see equation 6.7) [194]:

$$\text{Residence time} = 1.77 \times \frac{L \times \sqrt{\theta}}{D \times N \times \beta} \qquad 6.7$$

Where:
L = Length of rotary kiln
θ = material angle of repose
D = Inner diameter of rotary kiln
N = Tube rotation
β = Slope of rotary kiln

The Sullivan model was used to calculate the expected residence time of the material as it flowed through the rotary kiln at room temperature. Table 6.5 shows that model proved fairly accurate at predicting the residence time.

Table 6.5. Comparison of actual and theoretical residence time in the rotary kiln at room temperature.

Run	Temperature (K)	Tube rotation (rpm)	Slope (°)	Actual residence time (min)	Theoretical residence time (min)
1	Room temp.	2.15	1	120	117
2	Room temp.	2.15	1.5	80	78
3	Room temp.	4.13	1	50	60

Table 6.6, however, shows that at elevated temperatures the Sullivan model is not able to accurately predict the residence of the material in the rotary kiln. The decreased accuracy of the Sullivan model at elevated temperatures is due to the particles in the kiln tube agglomerating to form lumps which then move faster than the granular powders. Agglomeration in the rotary kiln occurs as the particles partially melt and re-solidify

forming bridges between them and growing in size as they move through the kiln tube [195].

Table 6.6. Comparison of actual and theoretical residence time in the rotary kiln at elevated temperatures.

Run	Temperature (K)	Tube rotation (rpm)	Slope (°)	Actual residence time (min)	Theoretical residence time (min)
4	1073	3	1.5	33	56
5	1173	3	1.4	30	60
6	1223	3	1.5	30	56
7	1223	5	1.6	18	31

6.2.2 Effect of temperature

The temperature of the controlled-hotzone in the kiln tube plays an important role in the ring formation and the extent of reduction of the material. Higher temperatures are likely to cause more problems as there is a greater likelihood of melting and liquid phase formation. Liquid phases also inhibits gaseous diffusion which adversely affects reduction of iron oxides. However, the kinetic studies presented in this report detail that the rate and extent of reaction increases with increasing temperature. Carbothermic reduction in the kiln was studied at 1173 K, 1223 K and 1273 K to determine the effect of temperature on the extent of reduction and on ring formation. T1 used at the different temperatures was sized +106 μm -300 μm.

Noteworthy, is that the ring formation occurred at the start of the hotzone. Figure 6.24 shows that the general trend is a decrease in the amount of sample accumulating in the rotary kiln tube with increasing number of passes, except in the case of the first and second pass for experiment carried out at 1273 K. The highest amount of material remains in the kiln after the first pass at 1273 K , which is to be expected as the higher temperature promotes melting of phases that are then adhere to the tube wall. However, there is a significant decrease in the percentage of material in the tube for the second and third pass at 1273 K.

At 1173K the lowest percentage of material remained in the tube after the first pass at 20.23%. The amount of material remaining in the tube after the first pass increases as the temperature increases, as 46.76 % and 57.04 % accumulated in the tube after the first pass at 1223 K and 1273 K, respectively. The decrease in the percentage of material in the tube with each pass shows that reacted material is less prone to causing ring formation.

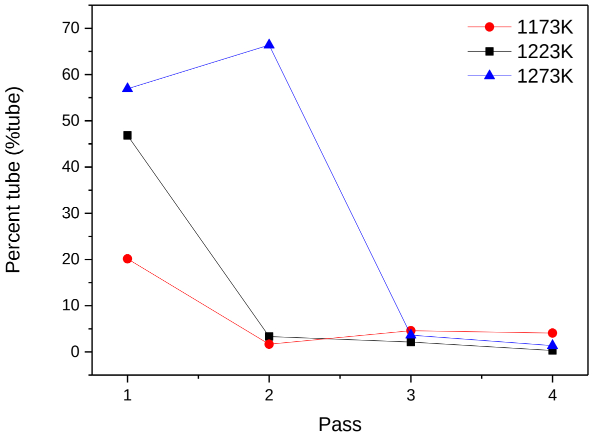

Figure 6.24 Effect of temperature on the percentage of material remaining in the tube after each pass.

The accretion that formed during the first pass of the experiment carried out at 1173 K was collected and analysed using XRPD techniques (see Figure 6.25). It is evident that the mixture has been partially reacted as Fe is the dominant phase present along with minor peaks for $Na_{0.75}Fe_{0.75}Ti_{0.25}O_2$, $CaTiO_3$, FeO and $NaAlSiO_4$. Peaks representing phases observed in the as-received T1 material such as Fe_2TiO_4 -Fe_3O_4 solid solution are also present.

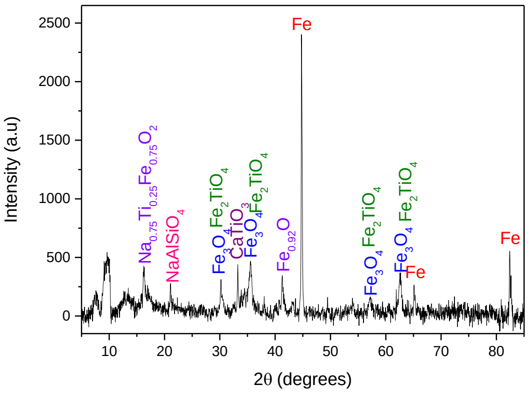

Figure 6.25 XRPD of accretion present at the start of the hotzone for reduction in the presence of Na_2CO_3 carried out at 1173 K.

The XRPD patterns for the samples collected after each pass at 1223 K are presented below in Figure 6.26. After the first pass there is significant formation of metallic Fe along with minor peaks for $Na_{0.75}Fe_{0.75}Ti_{0.25}O_2$, $NaAlSiO_4$ and FeO. For the second and third passes the FeO peaks are no longer observed, indicating that FeO was reduced to metallic iron. Reduction of hematite to wustite occurs rapidly but the $FeO \rightarrow Fe$ reaction is slower [187, 196].

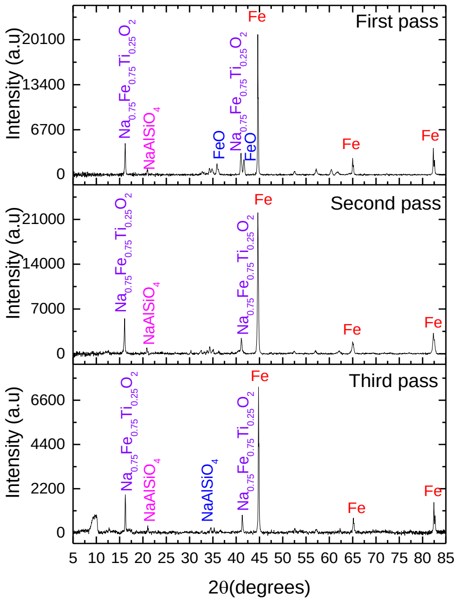

Figure 6.26 XRPD analysis of the sample collected after the first three passes for reduction of iron-rich tailings in the presence of Na_2CO_3 at 1223 K in the rotary kiln.

Phase analysis of the samples collected after the fourth pass at 1173 K, 1223 K and 1273 K is presented in Figure 6.27. Metallic Fe is the dominant phase present from experiments carried out across all three temperatures. Minor peaks for $NaAlSiO_4$ also present for the three temperatures along with minor peaks for $Na_{0.75}Fe_{0.75}Ti_{0.25}O_2$ at 1173 K and 1223 K.

Intensity of the $Na_{0.75}Fe_{0.75}Ti_{0.25}O_2$ peaks are significantly stronger at 1273 K compared to 1223 K and 1173 K XRPD patterns. Minor peaks for Fe_2TiO_4 are observed suggesting the extent of reduction is less at 1273 K, likely a result of significant percentage of sample remaining in the tube after the first two passes. Implying that most of the sample had a limited amount of time in the hotzone compared to the experiments at 1173 K and 1223 K.

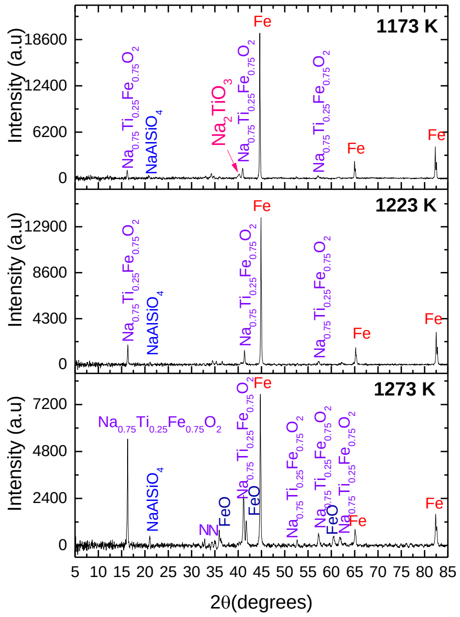

Figure 6.27 XRPD analysis of the iron-rich tailings reduced in the presence of Na_2CO_3 at various temperatures in the rotary kiln.

A photographic image of the sample collected after the first pass in the kiln for experiments performed at 1173 K is presented in Figure 6.28 and it can be seen that grey particles and black particles were collected.

The black particles were the first to fall in to the collection bottle followed by the grey particles. Black particles appear to be the activated carbon that was mixed with the iron-rich tailings and Na_2CO_3. Close observation of the collected samples shows that some of the black particles are located at the core of some of the smaller grey particles.

Figure 6.28 Photographic image of black and grey particles collected after first pass in the rotary kiln at 1173 K.

XRPD patterns of the black and grey particles are given in Figure 6.29a and Figure 6.29b, respectively. Figure 6.29a shows the presence of metallic Fe, Fe_3O_4 and FeO, $NaAlSiO_4$ and $Na_{0.75}Fe_{0.75}Ti_{0.25}0_2$ and broad amorphous peaks illustrating that there is significant amount of carbon present. Amorphous peaks confirm that the black particles are activated carbon particles that have partially reacted with the T1 and Na_2CO_3 and that reduction of the iron-rich tailings was incomplete in the case of the black particles, as FeO and Fe_3O_4 are intermediate phases that are formed during the carbothermic reduction of Fe_2O_3 [195]. Sodium iron titanate ($Na_{0.75}Fe_{0.75}Ti_{0.25}O_2$) phase is an undesirable product as it is non-magnetic and would result in increased iron content of the non-magnetic fraction. $Na_{0.75}Fe_{0.75}Ti_{0.25}O_2$ is an intermediate phase formed during alkali reductive roasting, however, it is presence when the reduction is incomplete.

Figure 6.29b shows that the reduction of the grey particles was more significant than for the black particles. The main phases present in the grey particles are Fe, Na_2TiO_3, $NaAlSiO_4$ and a minor peak for Fe_3O_4-Fe_2TiO_4. Comparison of Figure 6.29a and Figure 6.29b confirms that $Na_{0.75}Fe_{0.75}Ti_{0.25}O_2$ is an intermediate phase that forms during alkali reduction. Black particles appear to serve as a nucleus around which the larger grey particles form.

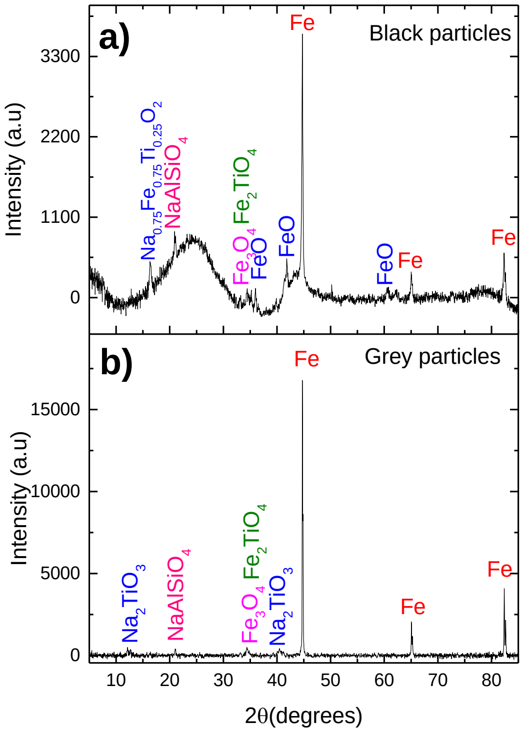

Figure 6.29. XRPD patterns of a) black particles and b) grey particles collected after reduction of iron-rich tailings in the presence of Na_2CO_3 in the rotary kiln at 1223 K.

The phase diagram of the Na_2O-TiO_2 system presented in chapter 2 shows that Na_2TiO_3 becomes partially molten at 1238 K [121] , therefore one of the advantages of performing alkali reductive roasting at 1223 K and temperatures below that is it limits the amount molten sodium titanate present. Molten Na_2TiO_3 would promote ring formation in the kiln tube and inhibit the diffusion of the CO gas, hindering the reduction process and [120, 197].

Figure 6.30a is the backscattered SEM image of the black particles collected from the rotary kiln and three distinct phases are visible. The metallised Fe particles (see Area A on Figure 6.30a) are at the periphery of the particles where they are seen to cluster, increasing the grain size. EDX analysis of the dark grey phase (see Area B on Figure 6.30a) shows that this represents the Na-Fe-Ti-O ternary complex that was observed in Figure 6.29a. The intermediate phase is located at the interface between the partially reacted core of the particle and the metallic Fe at the outside of the particle. Sodium iron titanate was also found to be an intermediate phase while during oxidative roasting of ilmenite with Na_2CO_3 and it was also present during the alkali reductive roasting performed by observed by El-Tawil et al [99, 119]. It is evident that the Na^+ ions diffuse into the lattice forming the ternary phase.

The light grey phase (see Area C on Figure 6.30a) at the core represents the partially reacted Fe_3O_4-Fe_2TiO_4 solid solution. 7.1 weight.% Na in this phase indicating that the Na^+ ions had diffused towards the centre of the particle, where there is phase segregation of the light grey phase from the dark phase.

Figure 6.30b is the SEM image of the grey particles collected from the rotary kiln. The Fe product layer has formed (see Area D of Figure 6.30b) where these particles have a large granular structure, which would make the subsequent magnetic separation more effective. The grey phase (see Area E of Figure 6.30b) is the sodium titanate phase that was observed in Figure 6.30b, confirming that reduction of the intermediate Na-Fe-Ti-O complex is necessary to form sodium titanate and iron.

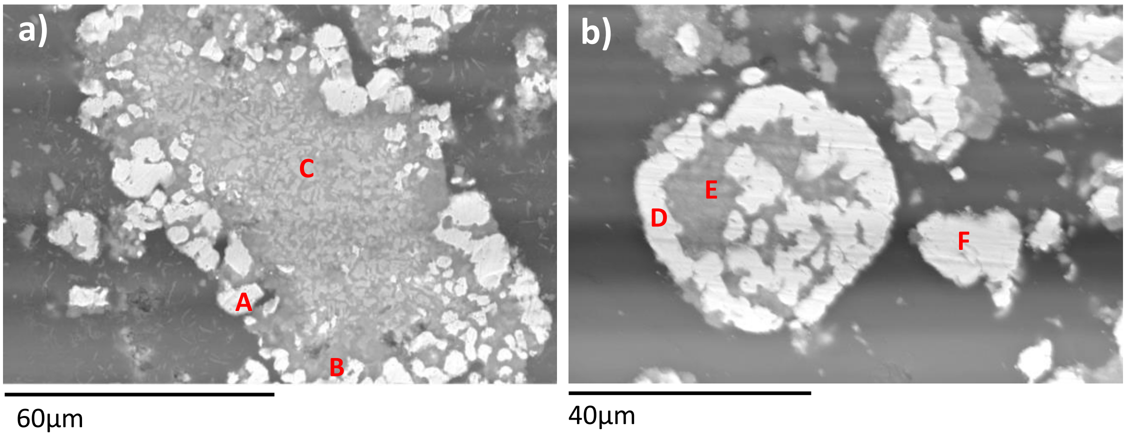

Figure 6.30 Backscattered SEM images of a) black particles and b) grey particles collected after reduction of iron-rich tailings in the presence of Na_2CO_3 in the rotary kiln at 1223 K.

Table 6.7 Elemental composition of areas A to F on Figure 6.30 as analysed by EDX.

Weight.%	Ti	Na	Fe	O	V	Si	Ca	Al	Mg	Mn
A	0.8	3.0	91.3	4.9	-	-	-	-	-	-
B	21.7	13.0	28.6	31.6	0.2	1.7	1.1	1.5	0.6	-
C	2.4	7.3	66.2	22.3	0.1	-	-	0.5	0.4	0.8
D	2.4	2.2	93.4	2.0		-	-	-	-	-
E	35.2	18.0	5.2	35.0	0.6	1.1	0.5	2.7	1.2	0.6
F	2.7	-	96.2	1.1		-	-	-	-	-

6.2.3 Effect of particle size

The effect of T1 particle size on ring formation and reduction was studied by varying the particle size distribution as given below:

i) +106 µm -300 µm
ii) +300 µm -500 µm
iii) +500 µm -1180 µm.

A graphical summary of the percentage material remaining in the tube is presented in Figure 6.31.

Fine particles typically form accretions as they sinter to the tube wall [193]. For the sponge iron production in the rotary kiln the feed size of the ore is generally between 1 mm and 20 mm [197]. The +500 µm -1180 µm size distribution with the largest particles had the highest percentage of material remaining in the tube after the fourth pass at 19.98% and a minor ring formed during the fourth pass, compared to the no rings present after the fourth passes of the other two size distributions. The observation appears counter-intuitive as it would be expected that larger particles result in a decrease in ring formation. However, the increase T1 particle size decreases the reaction surface area and coarse particles react more slowly, resulting in Na_2CO_3 melting and adhering to the kiln wall before being able to react with T1 and activated carbon. The lowest percentage of material in the tube after the fourth pass was for the +300 µm – 500 µm size range at 0.23%, which was slightly lower than the 0.32% of material that remained in the tube after the fourth pass for the +106 µm – 300 µm.

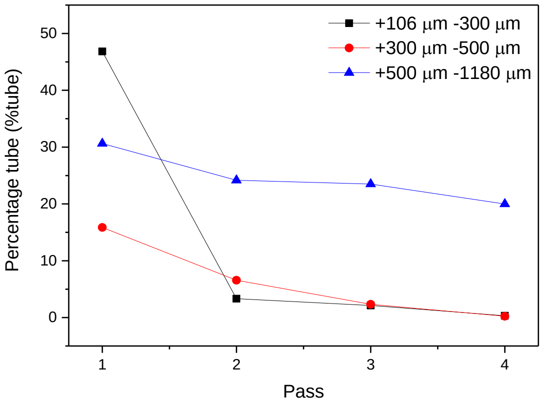

Figure 6.31 Effect of particle size on the percentage of material remaining in the tube after each pass.

The XRPD patterns from the different particle size distributions are presented in Figure 6.32. α-Fe is the dominant phase formed for the varying sized distribution. The intensity of $Na_{0.75}Fe_{0.75}Ti_{0.25}O_2$ peaks are stronger for +300 µm -500 µm and +500 µm - 1180 µm than the +106 µm -300 µm particle size range, implying that the extent of reduction was least for the two particle size distributions (+300 µm -500 µm and +500 µm -1180 µm), even though the +300 µm -500 µm size range had the lowest percentage material remaining in the tube.

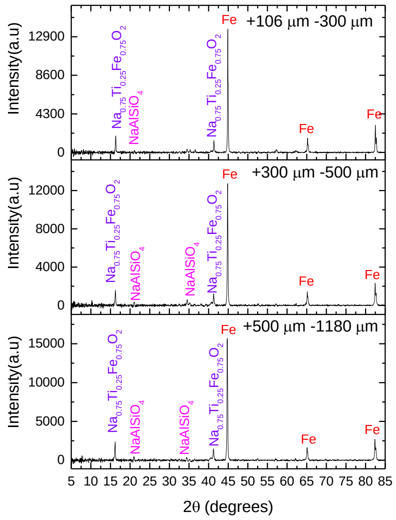

Figure 6.32 XRPD analysis of the different sized iron-rich tailings reduced in the presence of Na_2CO_3 at 1223 K in the rotary kiln.

6.2.4 Effect of Na_2CO_3 weight ratio

The amount of Na_2CO_3 added was decreased to 0.75 times the stoichiometric requirement in order to investigate the effect of T1:Na_2CO_3 on ring formation and reduction of T1. The amount of Na_2CO_3 added was sufficient to react with the TiO_2 present in T1, according to equation 6.7 and 6.8, but was not adequate for reactions with gangue elements. The weight ratio used corresponds to T1:Na_2CO_3:C 1:0.16:0.23 compared the stoichiometric weight ratio of 1:0.2:0.23.

Figure 6.33 illustrates that the percentage of the input material remaining in the tube for the first pass with the T1:Na_2CO_3:C 1:0.16:0.23 weight ratio was 36.98% compared to the 47.49% for the 1:0.2:0.23 weight ratio. It is to be expected that with less Na_2CO_3 there would less ring formation. However, for the second pass the %tube for the T1:Na_2CO_3:C 1:0.16:0.23 weight ratio increases to 48.4% whilst the value decreases to 15.73% for the 1:0.2:0.23 weight ratio, suggestion stoichiometric addition of Na_2CO_3

helps decrease ring formation during the second pass. For the third and fourth pass the %tube values were similar for both weight ratios.

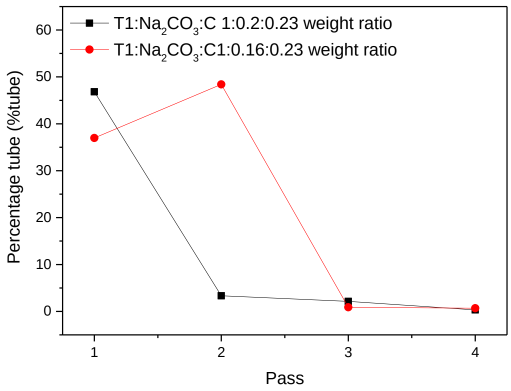

Figure 6.33 Effect of Na_2CO_3 weight ratio on the percentage of material remaining in the tube after each pass.

Samples collected after the fourth pass when using T1:Na_2CO_3:C weight ratio of 1:0.2:0.23 (see Figure 6.34a) had larger nodules compared to those for the 1:0.16:0.23 weight ratio seen in Figure 6.34b. The reduced sample obtained from the 1:0.16:0.23 weight ratio was more friable than the sample from the 1:0.2:0.23 weight ratio.

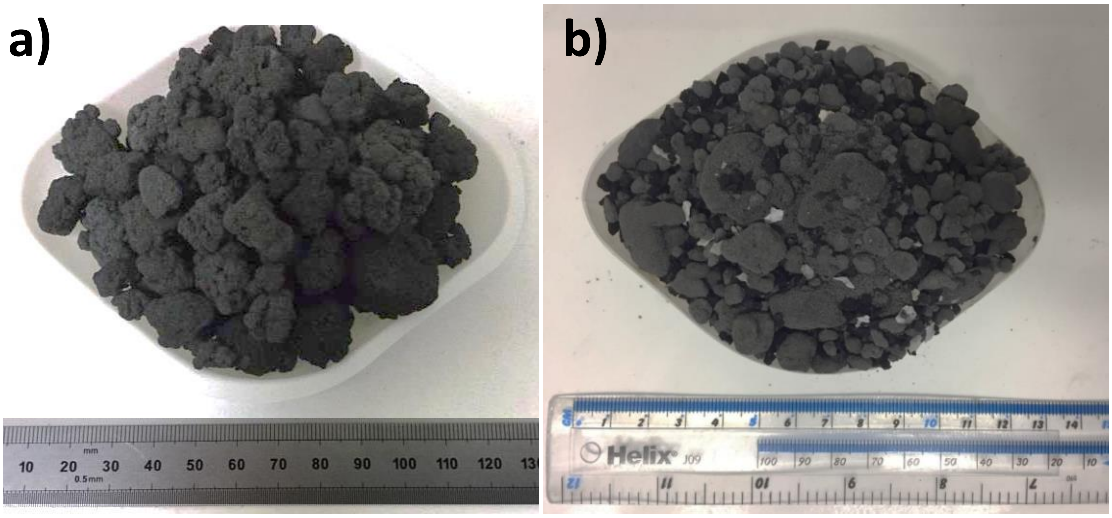

Figure 6.34 Photographic image of samples collected after reduction at 1223 K of iron-rich tailings in the presence Na_2CO_3 using a) 1:0.2:0.23 and b) 1:0.16:0.23 weight ratios.

The XRPD pattern of the two samples are compared in the Figure 6.35. Fe and $Na_{0.75}Fe_{0.75}Ti_{0.25}O_2$ are the dominant phases for both samples. $NaAlSiO_4$ is present in the sample with lower Na_2CO_3 addition, highlighting the importance of adding sufficient Na_2CO_3 to react with the gangue phases otherwise sodium titanate and sodium vanadium oxide formation could be limited.

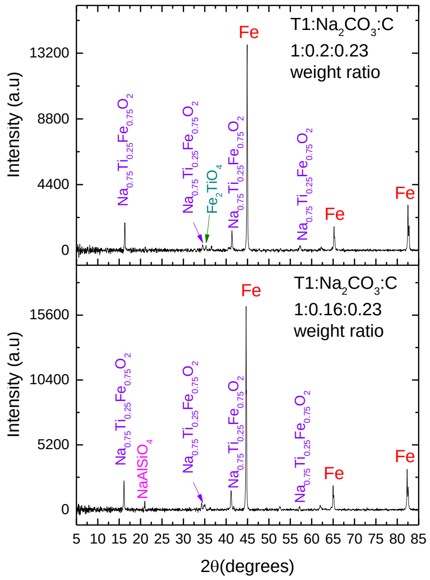

Figure 6.35 XRPD analysis of the iron-rich tailings reduced at 1223 K in the rotary kiln in the presence different Na_2CO_3 weight ratios.

6.2.5 Effect of argon gas flow rate

The effect of changing the flowrate of the argon purge gas was studied by using three different flowrates of 1 L.min^{-1}, 2 L.min^{-1}, and 3 L.min^{-1}.

The samples treated with the three different flowrates follow the same trend as there is a significant decrease from the first to second pass, after which the %tube appears to level out.

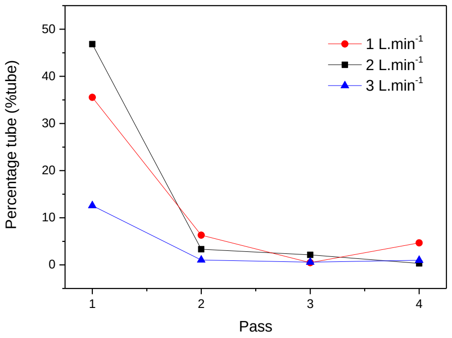

Figure 6.36 Effect of argon gas flowrate on the percentage of material remaining in the tube after each pass.

The major difference between the XRPD patterns is that when using the flow rate of 1L.min^{-1} the peak for sodium titanate is present suggesting that the reduction may have been more effective under these conditions, which disagrees with results by El-Guindy that found increased argon flow rate decrease reduction of ilmenite [85]. It appears that at this flow rate the gaseous species are able to accumulate and enhance the reduction.

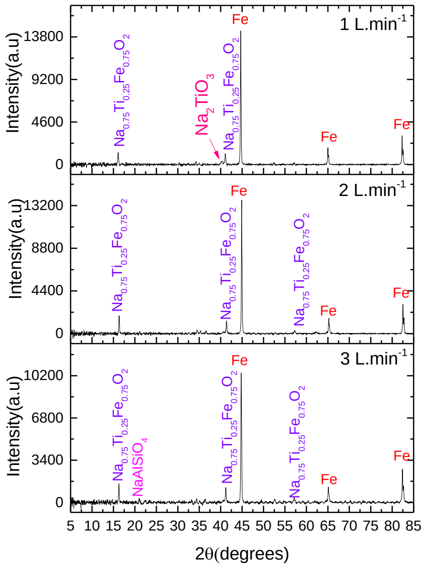

Figure 6.37 XRPD analysis of the iron-rich tailings reduced in the presence of Na_2CO_3 at 1223 K in the rotary kiln using different argon gas flowrates.

6.2.6 Effect of angle of inclination

The residence time in the rotary kiln can be decreased by either lowering the angle of inclination or by decreasing the tube rotation speed. Three different angles of inclinations were trialled to study their impact on ring formation (see Figure 6.38). The three angles of inclination were:

i) 1.2°
ii) 1.4°
iii) 1.6°

After the first pass the %tube for 1.2° and 1.6° angle of inclinations were similar at 47.48 % and 46.83 %, respectively. However, after the second pass the reported values differed more significantly as 15.73 % and 3.33 % remained in the tube for 1.2°

and 1.6° angle of inclination, respectively. By the third pass the all three conditions had similar values as the samples had all been sufficiently reacted.

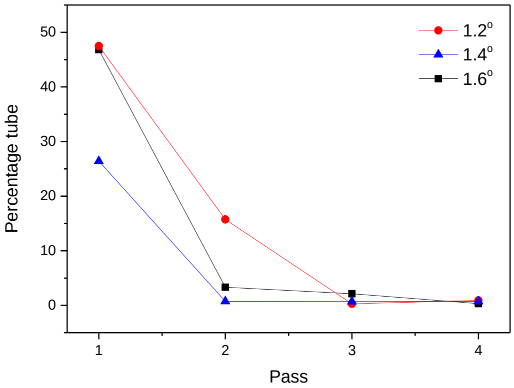

Figure 6.38 Effect of angle of inclination on the percentage of material remaining in the tube after each pass.

Varying angle of inclination does not appear to significantly change the phase observed in the XRPD patterns, as seen in Figure 6.39. The phases observed at the three different angles of inclination are $Na_{0.75}Fe_{0.75}Ti_{0.25}O_2$ and α-Fe.

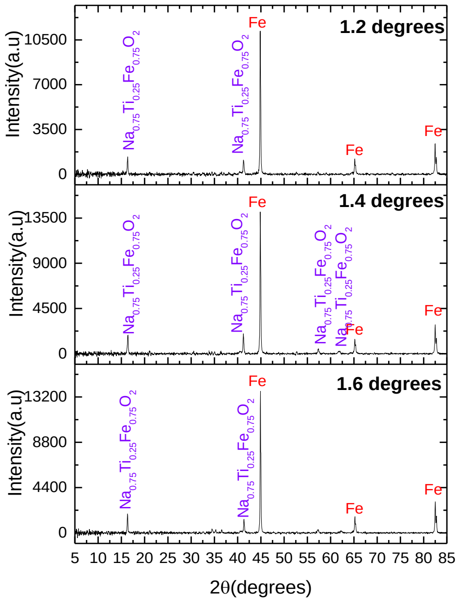

Figure 6.39 XRPD analysis of the iron-rich tailings reduced in the presence of Na_2CO_3 at 1223 K in the rotary kiln using different angle of inclination.

6.3 Carbothermic reduction of low-grade titanium dioxide slag in the presence of Na_2CO_3

6.3.1 Carbothermic reduction of low-grade titanium dioxide slag in TGA apparatus

Thermogravimetric analysis was carried out to measure extent of alkaline reduction of T2 with respect to time. Reduced samples were characterised using X-ray powder diffraction techniques in order to determine the phases formed. Temperature and slag-to-carbon ratio were found to have an effect on the products formed and the reaction kinetics and mechanism. The two carbon weight ratios used include a ratio (Slag:Na_2CO_3:C = 1:0.45:0.04) where the carbon added is equivalent to the amount necessary to reduce iron oxide to metallic iron, assuming all iron oxide is present in the trivalent state according to equation 6.8 . The second ratio (Slag:Na_2CO_3:C = 1:0.45:0.09) ensured there was sufficient carbon in order to satisfy reactions 6.8 and 6.9 .

$$\mathrm{Fe_2O_3 + 3C \rightarrow 2Fe + 3CO(g)} \qquad 6.8$$

$$\mathrm{Na_2CO_3 + C \rightarrow Na_2O + 2CO(g)} \qquad 6.9$$

6.3.1.1 Effect of reduction temperature

The percentage reduction (%R) versus time (t, hr) isotherms for each temperature were plotted for the Slag:Na_2CO_3:C = 1:0.45:0.04 weight ratio in the Figure 6.40. It is evident from Figure 6.40 that the extent of reaction is temperature dependent. Below 1173 K, the curves increase gradually before plateauing. However, at 1173 K and above the gradient of the initial period of the reaction becomes steeper as the temperature increases before levelling out.

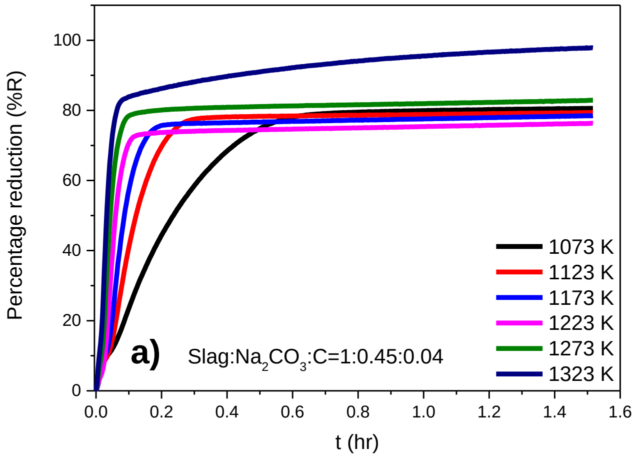

Figure 6.40 Effect of reduction temperature during reduction of low-grade TiO_2 in the presence of Na_2CO_3 and carbon at molar ratio of Slag:Na_2CO_3:C 1:0.45:0.04.

X-ray powder diffraction analysis

After the experiments in the TGA apparatus the reacted samples were analysed using X-ray powder diffraction and scanning electron microscopy techniques. The XRPD patterns for the Slag:Na_2CO_3:C = 1:0.45:0.04 samples are presented in Figure 6.41. The major phase present is calcium titanate ($CaTiO_3$), which is agrees with the thermodynamic predictions made in Figure 5.4 where the formation of $CaTiO_3$ (see equation 5.21) was favoured over the formation sodium titanate from the reaction of Na_2CO_3 (see equation 5.22) with the T2 slag matrix.

Peaks for $MgAl_2O_4$ are present at all the temperature ranges, however, the intensity decreases as the temperature increasing indicating that the decomposition of the $MgAl_2O_4$ to MgO and $NaAl_2O_4$ is incomplete at all temperatures.

The $Na_{1.74}Mg_{0.79}Al_{0.15}Si_{1.06}O_4$ phase formed has the second most intense peaks across all temperature ranges, a phase formed from the reaction between the slag matrix and Na_2CO_3 during reduction.

Above 1173 K, the metallic Fe phase is observed in the XRPD patterns. The intensity of the Fe peaks are low due to the limited amount of iron oxide present in the T2. It is evident that the metallic iron observed in the XRPD patterns was formed during alkali reductive roasting and not Fe previously entrained in the material, as Fe peaks were not observed below 1223 K.

The presence of $Na_{0.75}Ti_{0.25}Fe_{0.75}O_2$ is noted in the diffraction patterns for 1073 K, 1123 K, 1173 K and 1223 K, likely owing to the reaction between $MgTi_2O_5$ and Na_2CO_3.

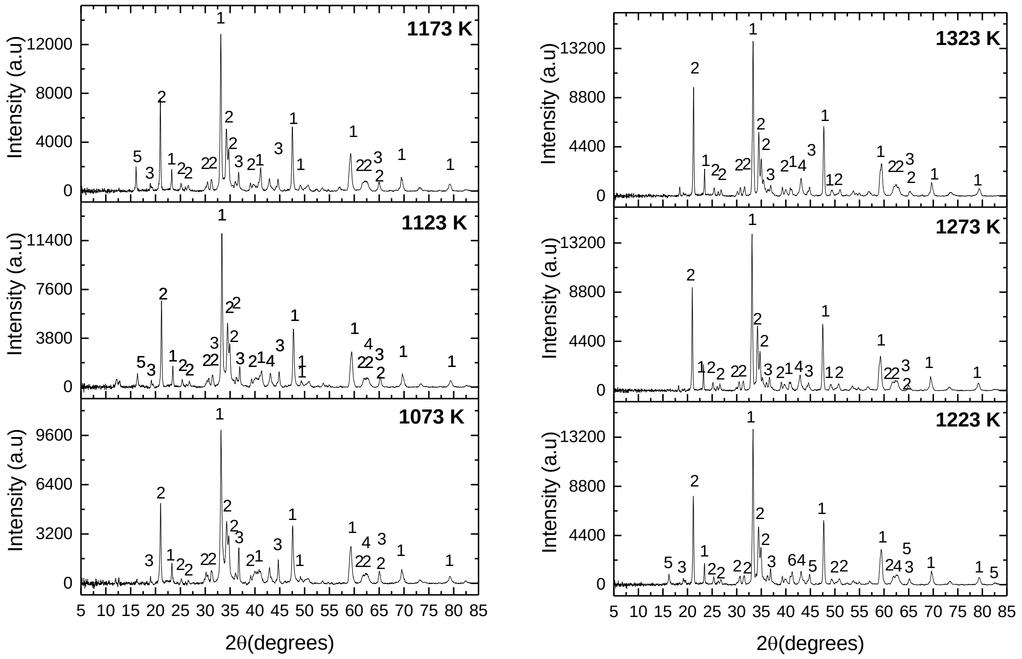

Figure 6.41 XRPD patterns for carbothermic reduction of low-grade TiO_2 in the presence of Na_2CO_3 at a weight ratio of Slag:Na_2CO_3:C 1:0.45:0.04. 1 – $CaTiO_3$, 2- $Na_{1.74}Mg_{0.79}Al_{0.15}Si_{1.06}O_4$, 3 – $MgAl_2O_4$, 4 – Fe and 5 – $Na_{0.75}Ti_{0.25}Fe_{0.75}O_2$.

Scanning electron microscopy analysis

The backscattered SEM image of the low-grade TiO_2 slag reduced with Na_2CO_3 at 1073 K in the TGA apparatus is given in Figure 6.42, with EDX analysis provided in Table 6.8.

The atomic number contrast illustrates that there are multiple distinct phases present in Figure 6.42. Elemental mapping shows that the dark region at the core of the particle (see area D of Figure 6.42) is the $MgAl_2O_4$ that was observed in the XRPD patterns (see Figure 6.41). EDX analysis highlights that 5.8 weight% Ti and 0.8 weight% V are present at area D of Figure 6.42, indicating that the spinel phase is $Mg(Al.V,Ti)O_4$.

Elemental mapping data shows that the sodium is surrounding the $MgAl_2O_4$ phase, suggesting that the Na^+ ions diffuse through the slag matrix towards the centre of the particle. Maps for Mg and Al demonstrate that the intensity of these elements decreases moving away from $MgAl_2O_4$ at the core of the particle. Elemental composition data in Table 6.8 highlights the decrease in Mg and Al weight %, as the values decrease from 17.9 weight.% to 9.8 weight.% for Mg and from 35.4 weight.% to 13.2 weight.% for Al moving from Area D to Area C on Figure 6.42. The apparent shrinking core model reaction suggests that the inward diffusion of the Na^+ ions causes the decomposition of the spinel phase with the Mg and Al oxides dissolving in the decomposed silicate matrix, which is supported by the overlap of Mg and Al maps with Ca, Ti and O maps. Linescan data in Figure 6.43 confirms that a limited amount of Na^+ ions diffused into the spinel matrix.

EDX point ID analysis of the light grey phase (see Area A of Figure 6.43) shows that this phase is $MgTi_2O_5$ that has not been fully decomposed. However, the presence of 5 weight.% Na demonstrates that the Na^+ ions react with $MgTi_2O_5$ by diffusing into the lattice. The Mg^{2+} ions diffuse out of the lattice towards the reacted slag matrix, while the Na^+ ions react with the V ions localised in the $MgTi_2O_5$ lattice to form sodium vanadium oxide.

Area F of Figure 6.42 is metallic iron. The spherical nature of the particle and its location at the centre of the particle suggest that this iron was formed from the iron rejected from the T2 matrix after the addition of the Na_2CO_3. Work by Goso et al [79] did not achieve reduction of iron oxide in the T2 material during reductive roasting of the material. It was possible to metallise the iron during experiments performed in this study owing to the role played by Na_2O in increasing the activity of FeO by combining with SiO_2 [117, 198]. Considering the iron present in the slag matrix as fayalite ($FeSiO_3$) allows for simplification of the reaction chemistry. Reaction 6.10 is significantly more thermodynamically favourable than reaction 6.11 with standard Gibbs free energy change values of $\Delta G^o_{1323\ K}$ -186.41 kJ.mol^{-1} and -41.36 kJ.mol^{-1} , respectively [35].

$$FeSiO_3 + Na_2CO_3 + 2C \rightarrow Fe + Na_2SiO_3 + 2CO(g) \qquad 6.10$$

$$FeSiO_3 + C \rightarrow Fe + SiO_2 + CO(g) \qquad 6.11$$

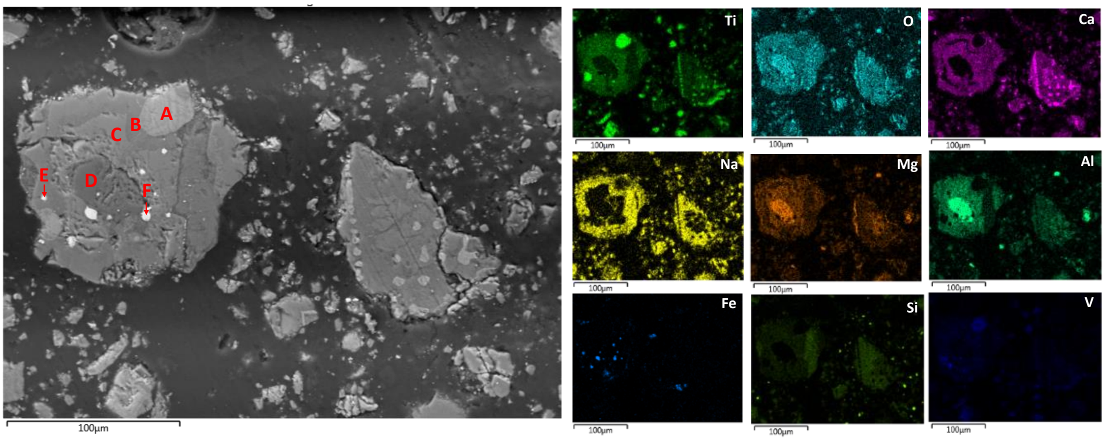

Figure 6.42 Backscattered SEM image with elemental mapping and EDX point and ID analysis of low-grade TiO_2 reduced in the presence of Na_2CO_3 at 1073 K in the TGA apparatus.

Table 6.8 Elemental composition of areas A to F on Figure 6.42.

Weight.%	**Ti**	**Fe**	**O**	**Na**	**Al**	**V**	**Si**	**Ca**	**Mg**	**Mn**	**Cr**
A	53.5	-	33.5	3.7	0.3	2.5	-	0.4	5.8	0.4	-
B	15.5	-	36.3	13.3	10.1	0.8	6.1	7.5	10.2	0.2	-
C	19.1		37.8	-	13.2	0.8	8.0	11.0	9.8	0.3	-
D	5.8	0.2	39.2	-	35.4	0.8	-	-	17.9	0.4	0.2
E	1.3	89.9	2.6	1.4	0.4	1.2	0.3	0.6	0.9	0.3	1.1
F	0.9	95.5	1.1	0.8	-	0.5	-	0.3	0.3	-	0.5

.

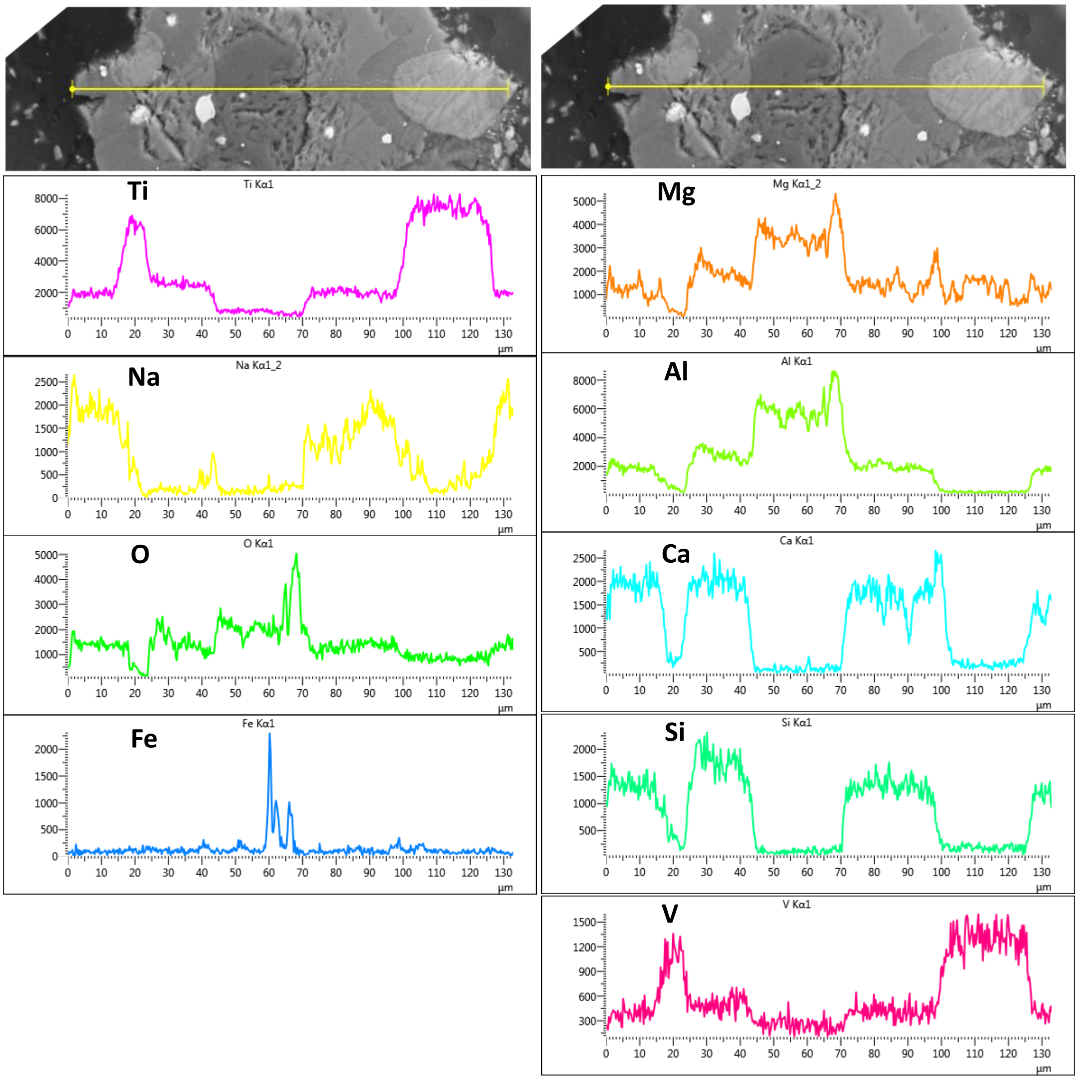

Figure 6.43 Backscattered SEM image with linescan data of low-grade TiO_2 slag reduced in the presence of Na_2CO_3 at 1073 K in the TGA apparatus.

Studying the electron micrographs (see Figure 6.44) of T2 treated at 1323 K in the TGA apparatus shows that there is phase segregation that occurs as a result of Na^+ ions diffusing in the matrix to form the Na-Mg-Al-Si-O compound observed in Figure 6.41. The high magnification image shown in Figure 6.44b illustrates that there are three distinct phases visible. The light grey phase crystallised out of the slag matrix, with the EDX point and ID analysis showing it to be $CaTiO_3$ (see Area A on Figure 6.44b). Formation of $CaTiO_3$ from the slag matrix agrees with thermodynamic calculations which indicated that the formation of $CaTiO_3$ from the T2 matrix was more favourable than the formation of Na_2TiO_3 [35]. $CaTiO_3$ evolution from the slag matrix explains why the intensity of the $CaTiO_3$ peaks increases in the XRPD patterns after the experiment compared to the as-received. The bright specks are areas enriched with iron that has been released from the slag matrix. The dark grey areas correspond to the $Na_{1.74}Mg_{0.79}Al_{0.15}Si_{1.06}O_4$ phase (see Area B on Figure 6.44b), which is further evidence that Na^+ ions diffuse through the T2 matrix. Low concentrations of V are seen dissolved in the slag matrix, which may limit the extraction of the oxide during the water leaching stage. When Mg, Al and Ca are present in significant quantities they typically react with V to form water-insoluble alkali vanadates [7].

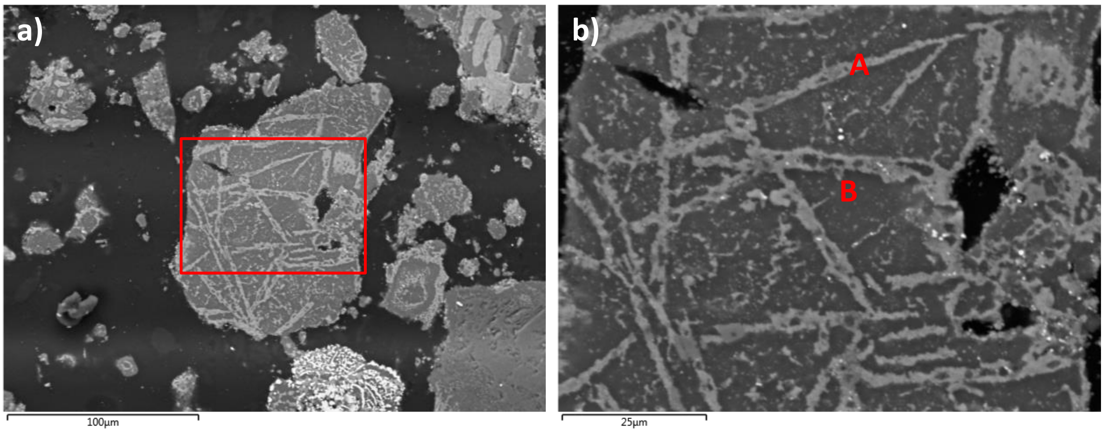

Figure 6.44 Backscattered SEM image with elemental mapping and EDX point and ID analysis of low-grade TiO_2 slag reduced with activated charcoal in the presence of Na_2CO_3 at 1323 K in the TGA apparatus.

Table 6.9 Elemental composition of areas A and B on Figure 6.44b.

Weight.%	Ti	Fe	O	Na	Al	V	Si	Ca	Mg	Mn
A	26.2	0.4	37.8	7.7	2.6	0.5	3.8	18.8	1.9	0.2
B	8.3	0.3	40.0	18.9	8.5	-	12.5	5.2	6.0	0.3

Kinetic model fitting

The percentage reaction against time data for the T2:Na_2CO_3:C = 1:0.45:0.04 weight ratio was fitted using the three models to determine the mechanism and to calculate the apparent activation energy.

Figure 6.45 and Figure 6.46 are plots for the Interface and G.B models, respectively. It can be observed that the experimental data fits well for both models, indicating that the reaction can be considered to the under mixed-control. The R^2 values are at least equal to 0.99 across all the temperatures for the G.B model. However linear regression analysis is best at lower temperatures, 1073 K and 1123 K, suggestion that diffusion is the rate limiting factor at lower temperatures. The goodness of fit for the

Interface model at the lower temperature is modest but improves as the temperature increases. Although, there is good fitting for the mixed-control model across all the temperatures, as given in Figure 6.47, the GB model fits the best. A summary of the linear regression analysis is provided in Table 6.10.

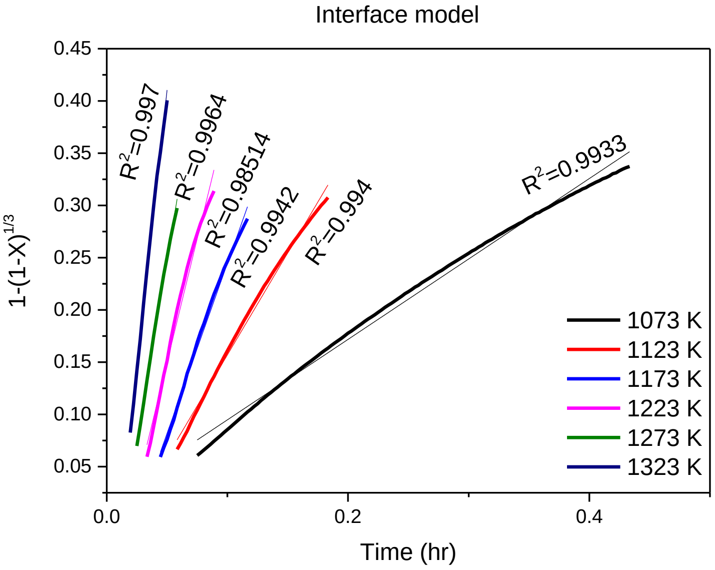

Figure 6.45 Plots of Interface model against time (hr) for the low-grade TiO_2 slag isothermal data at between 1073 K and 1323 K.T2:Na_2CO_3:C 1:0.45:0.04.

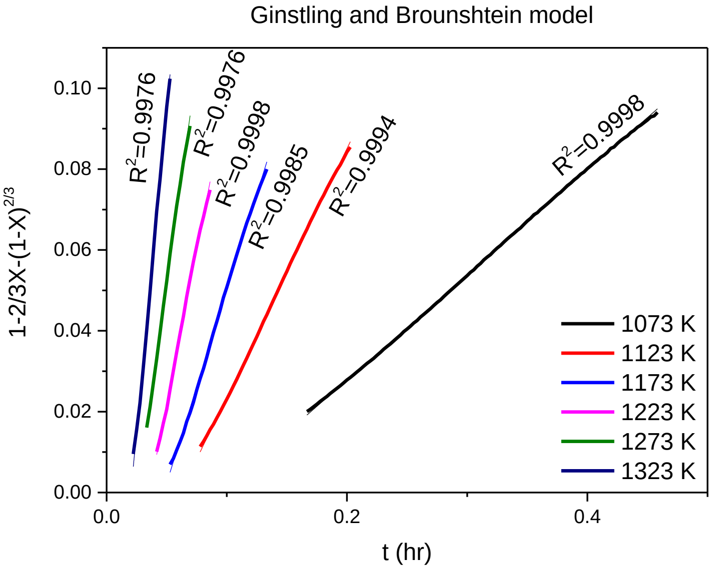

Figure 6.46 Plots of Ginstling and Brounshtein model against time (hr) for the low-grade TiO_2 slag isothermal data at between 1073 K and 1323 K.T2:Na_2CO_3:C 1:0.45:0.04.

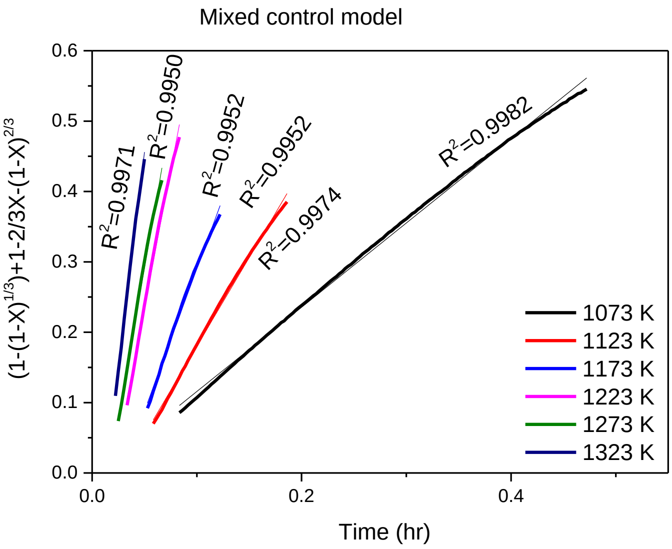

Figure 6.47 Plots of Mixed-control model against time (hr) for the low-grade TiO_2 slag isothermal data at between 1073 K and 1323 K.T2:Na_2CO_3:C 1:0.45:0.04.

Table 6.10 Linear regression analysis of rate of constants at between 1073 K and 1323 K using Interface, Ginstling and Brounshtein (GB) and Mixed-control models for reductive roasting of T2:Na_2CO_3:C 1:0.45:0.04.

Temperature (K)	Interface model		G.B model		Mixed-control model	
	k	Standard error	k	Standard error	k	Standard error
1073 K	0.7699	0.0055	0.2597	3.9803E-4	1.1970	0.0042
1123 K	1.9512	0.0226	0.6142	0.0023	2.5183	0.0189
1173 K	3.253	0.0486	0.9536	0.0068	4.0427	0.0563
1223 K	4.4734	0.1299	1.5196	0.0179	7.808	0.1276
1273 K	6.957	0.1211	2.1366	0.0289	8.4910	0.1556
1323 K	10.638	0.1760	3.1747	0.0470	12.3100	0.2104

Arrhenius plot and activation energy

The plot of the natural logarithm versus reciprocal temperature for the alkali reductive roasting of T2 using the T2:Na_2CO_3:C = 1:0.45:0.04 weight ratio is presented in Figure 6.48. The plots shows that there is one reaction regime. The apparent activation energy is 114 ± 6 kJ.mol^{-1}. The value is comparable with the diffusion of Na^+ ions in soda-lime glass, which has been recorded as 96 kJ.mol^{-1} to 113 kJ.mol^{-1} [188]. SEM results which showed Na^+ cations had diffused into the slag matrix, agreeing with the kinetic model results.

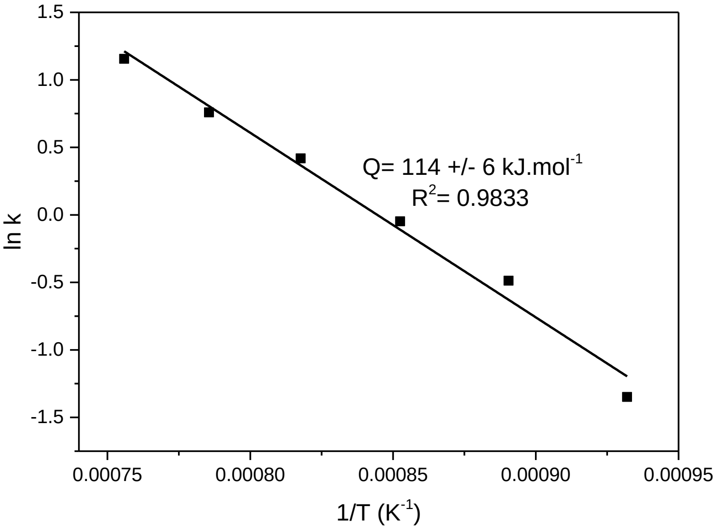

Figure 6.48 Arrhenius plot of the ln k versus reciprocal temperature for carbothermic reduction of low grade TiO_2 slag in the presence of Na_2CO_3 for T2:Na_2CO_3:C 1:0.45:0.04.

6.3.1.2 Effect of carbon ratio

Addition of excess carbon helps promote a more reducing atmosphere that aids with the decomposition of the phases present in the T2. The carbon ratio affects the shape of the curve, particularly at lower temperatures. The %R v time curves for T2:Na_2CO_3:C = 1:0.45:0.09 weight ratio seen in Figure 6.49, follows a similar trend to what was noted in Figure 6.40. At 1273 K, the initial period of the curves becomes steeper as the temperature increases before the rate of reduction plateaus. However, the isotherms at 1073 K and 1123 K increase more gradually compared to isotherms at the same temperature for the T2:Na_2CO_3:C = 1:0.45:0.04 ratio.

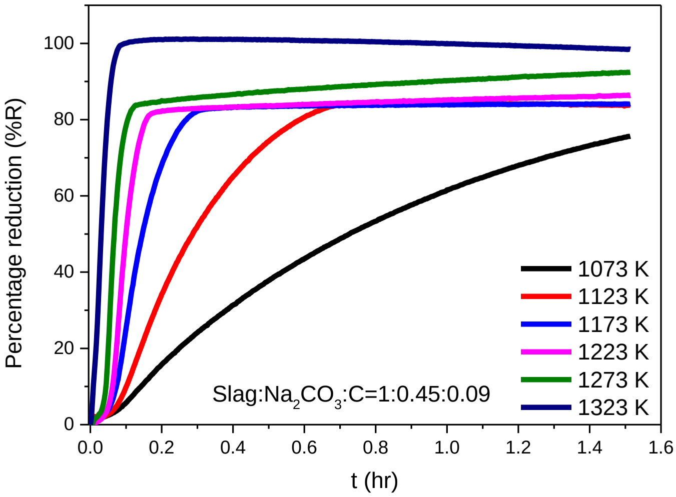

Figure 6.49 Effect of reduction temperature during reduction of low-grade TiO_2 slag in the presence of Na_2CO_3 and carbon at weight ratio of T2:Na_2CO_3:C 1:0.45:0.09 in the TGA apparatus.

X-ray powder diffraction analysis

The XRPD patterns of the high carbon samples are given in Figure 6.50. As the temperature increases the intensity of the Fe peaks increase, even though this is a minor phase. $CaTiO_3$ is the dominant phase formed, similar to what was observed with the T2:Na_2CO_3:C 1:0.45:0.04 ratio samples. The $Na_{1.74}Mg_{0.79}Al_{0.15}Si_{1.06}O_4$ phase intensity can be seen to increase as the temperature increases. It is evident that the $MgAl_2O_4$ begins to decompose at a lower temperature when using the T2:Na_2CO_3:C 1:0.45:0.09 weight ratio compared to the T2:Na_2CO_3:C 1:0.45:0.04 weight ratio, as above 1223 K there are no peaks visible for the $MgAl_2O_4$ phase. The decomposition of $MgAl_2O_4$ agrees with the Mg-Al-Na-C-O-V multi component phase equilibria shown in Figure 5.9 which demonstrated that in the presence of alkali the spinel becomes less stable in a more reducing atmosphere.

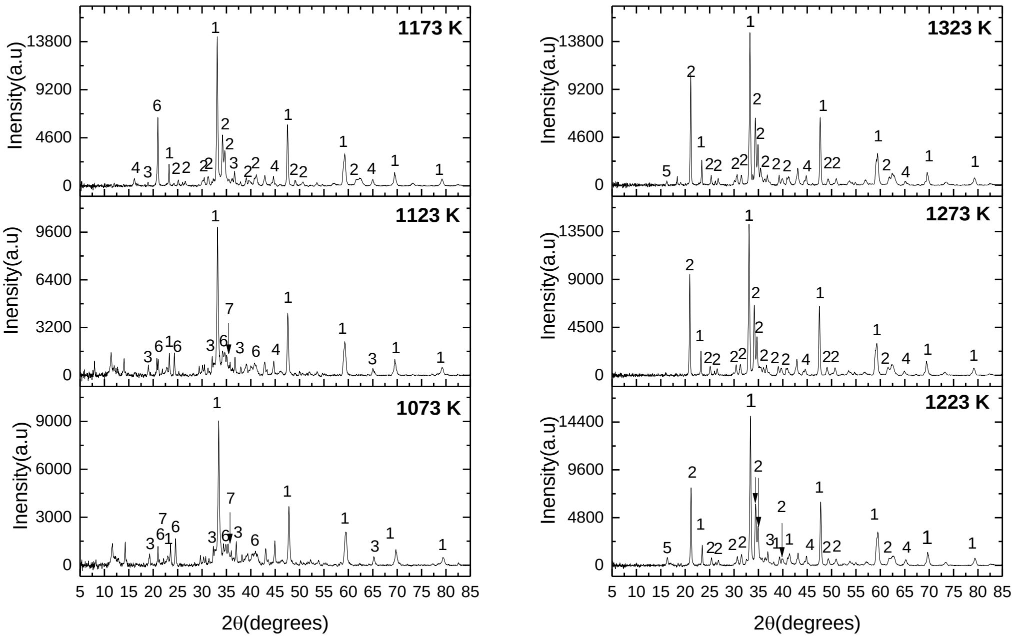

Figure 6.50 XRPD patterns for carbothermic reduction of low-grade TiO_2 slag in the presence of Na_2CO_3 at a weight ratio of T2:Na_2CO_3:C 1:0.45:0.09. 1 – $CaTiO_3$, 2- $Na_{1.74}Mg_{0.79}Al_{0.15}Si_{1.06}O_4$, 3 – $MgAl_2O_4$, 4 – Fe, 5 – $Na_{0.75}Ti_{0.25}Fe_{0.75}O_2$, 6 – $Na_{0.5}AlSiO_{4.25}$ and 7- $Na_2Mg_2Si_2O_7$

Kinetic model fitting

The kinetic model fitting using the results from the T2:Na_2CO_3: C 1:0.45:0.09 weight ratio experiments are presented in Figure 6.51 to Figure 6.54 using the Interface, G.B and Mixed-control models, respectively. The reaction is under mixed-control as the goodness of fit is high across the three models similar to what was observed with the T2:Na_2CO_3:C 1:0.45:0.04 weight ratio experiments. Linear regression analysis of the rate constants is presented in Table 6.11.

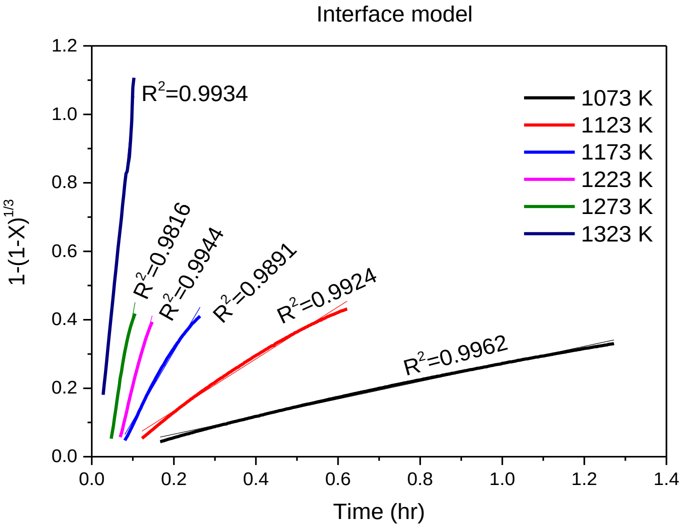

Figure 6.51 - Plots of Interface model against time (hours) for low-grade TiO_2 slag isothermal data at various temperatures T2:Na_2CO_3:C 1:0.45:0.09.

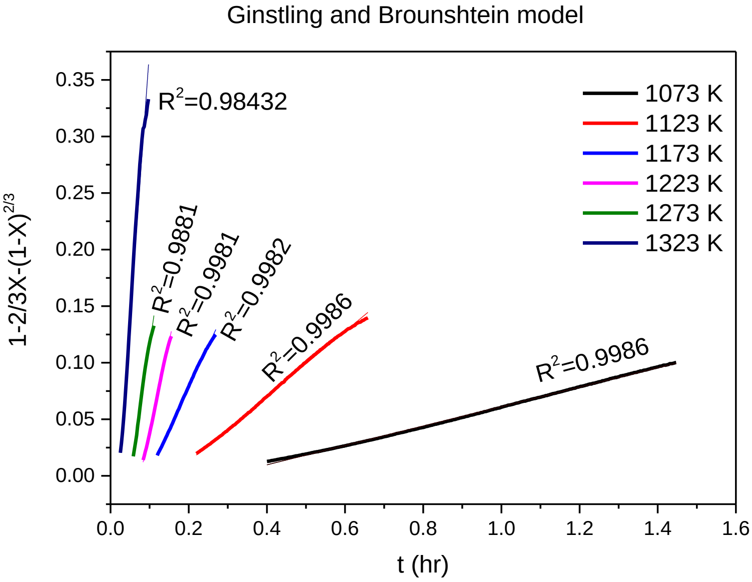

Figure 6.52 Plots of Ginstling and Brounshtein model against time (hr) for the low-grade TiO_2 slag isothermal data at various temperatures T2:Na_2CO_3:C 1:0.45:0.09.

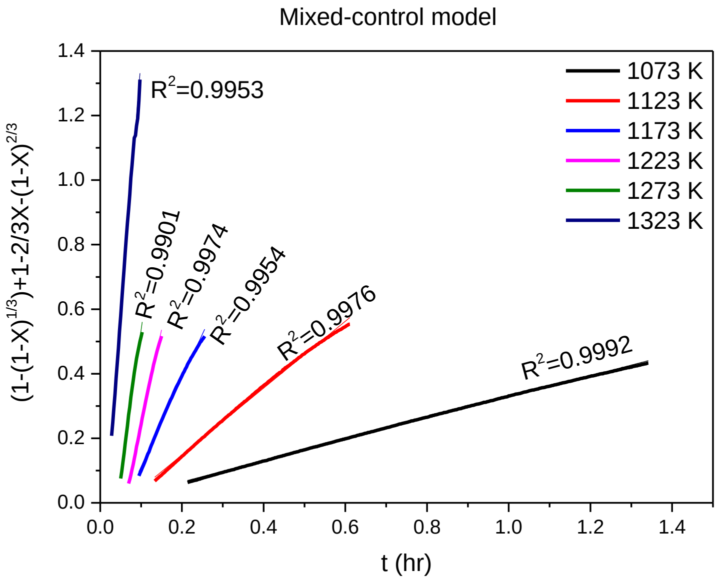

Figure 6.53 Plots of Mixed-control model against time (hr) for the low-grade TiO_2 slag isothermal data at various temperatures T2:Na_2CO_3:C 1:0.45:0.09.

Table 6.11 Linear regression analysis of rate of constants at between 1073 K and 1323 K using Interface, Ginstling and Brounshtein (GB) and Mixed-control models for reductive roasting of T2:Na_2CO_3:C 1:0.45:0.09.

Temperature (K)	Interface model		G.B model		Mixed-control model	
	k	Standard error	k	Standard error	k	Standard error
1073 K	0.2567	7.9469E-4	0.0858	1.6056E-4	0.3291	4.6464E-4
1123 K	0.7600	0.0049	0.2873	8.6486E-4	1.0358	0.0039
1173 K	2.0278	0.0262	0.7400	0.0042	2.7390	0.0243
1223 K	4.4527	0.0631	1.6000	0.0136	5.9001	0.0557
1273 K	6.5164	0.1944	2.2990	0.0577	8.9550	0.2058
1323 K	11.6125	0.1821	4.7551	0.1177	15.9754	0.2203

Arrhenius plot and activation energy

In Figure 6.54 the slope of ln k versus 1/T line shows that there is a single reaction regime for the T2:Na_2CO_3:C 1:0.45:0.09 weight ratio. From the slope, the apparent activation energy has been calculated to be 184 ± 11 kJ.mol^{-1} which is higher than the T2:Na_2CO_3:C 1:0.45:0.04 weight ratio and further illustrates the role of carbon in the reaction. The value corresponds to the gasification of carbon with the reported values being 159 kJ.mol^{-1}to 251 kJ.mol$^{-1,}$ including in the presence of alkali salts [199-201]. Kindly note that the activation energy has increased with an increase in carbon ratio and this is due to the gasification of carbon. In short, the C – CO_2 reaction dominated at the higher carbon ratio. Furthermore, the contact areas between Na_2CO_3 and slag decreased as carbon concentration increased. Nonetheless, at lower carbon concentration, the activation energy is lower because of increased contact area between Na_2O and slag.

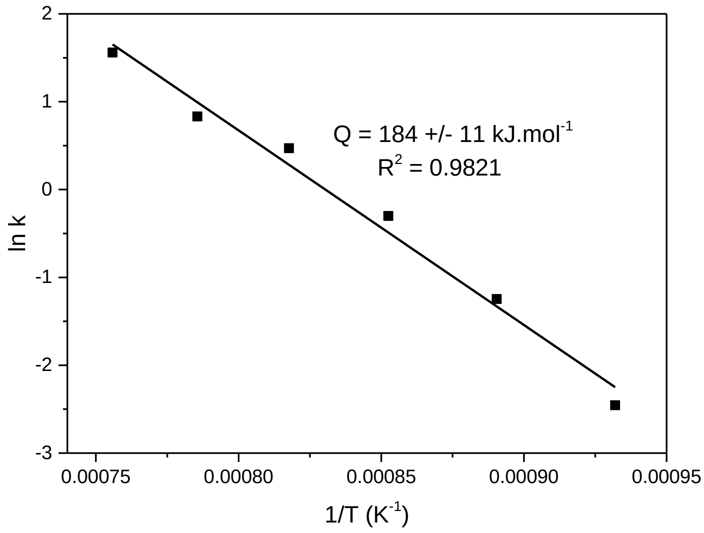

Figure 6.54 Arrhenius plot of ln k versus reciprocal temperature for carbothermic reduction of low grade TiO_2 slag with Na_2CO_3 for T2:Na_2CO_3:C 1:0.45:0.09.

Reaction mechanism

Na_2CO_3 decomposes to Na_2O and CO_2 at elevated temperature resulting in the addition of a basic oxides to the slag matrix, that break the silicate network by adding Na^+ and O^{2-}ions, as depicted in Figure 6.55a. The depolymerisation the silicate network by modifying the bonding from bridging oxygens (left-hand side of Figure 6.55a) to non-bridging oxygens (right-hand side of Figure 6.55a) that have a negative charge. The Na^+ ions and the non-bridging oxygen form an ionic bond giving rise to a partly covalent and partly ionic structure within the slag [41, 202-204].

Divalent Ca^{2+} ions already present in the slag matrix are able to coordinate with two silicate chains (see Figure 6.55b) compared to Na^+ ions, which are only able to coordinate with a single chain. Na^+ cations added to the T2 matrix form stronger bonds with the silicon-oxygen anions than the Ca^{2+} ions, resulting in Ca^{2+} ions being liberated from the silicate network [51]. The depolymerisation of the silicate network also results in the release of Fe and Ti ions from within the matrix [205]. Release of the Ca^{2+} ions promotes the crystallisation of $CaTiO_3$ as Ca^{2+} ions are able to react with TiO_3^{2-} ions [206], as illustrated in Figure 6.56. The electron micrograph in Figure 6.44b confirms perovskite crystallisation as $CaTiO_3$ particles are seen to be finely distributed throughout the reacted slag matrix, as EDX analysis confirmed that there were areas enriched with $CaTiO_3$ were surrounded by $Na_{1.74}Mg_{0.79}Al_{0.15}Si_{1.06}O_4$.

Formation of $CaTiO_3$ from the slag matrix increases the amount of TiO_2 that can be recovered from the T2 material. Direct sulphation either by acid baking or acid digestion of the T2 material is not able to recover the titanium dissolved in the silicate network. However, it must be noted that after alkali reductive roasting of the T2 material there is a residual amount of TiO_2 is still present in the decomposed slag matrix, which is recoverable in this report because of the dilute acid leaching that occurs before the sulphation reaction.

CO_2 gas released from the Na_2CO_3 decomposition is converted to CO gas via the Boudouard reaction [207-209]. The iron oxide rejected from the silicate system is reduced to metallic Fe by the CO gas. Iron oxide is also present in as magnetite and ilmenite and these oxide are also reduced by the CO gas, with the reduced iron are finely distributed within the slag matrix.

The decomposition of $MgAl_2O_4$ to MgO and $NaAl_2O_4$ results in the $NaAl_2O_4$ combining with the de-polymerised silicate network to form the sodium magnesioaluminosilicates. Al_2O_3 is an amphoteric oxide that behaves as a network former in basic slags, with the Al^{3+} ions incorporated into the silicate network [44, 203, 205]. However, charge-balancing cations , such as Na^+ cations, must be located close to the Al^{3+} ions, as seen in Figure 6.55c [210, 211].

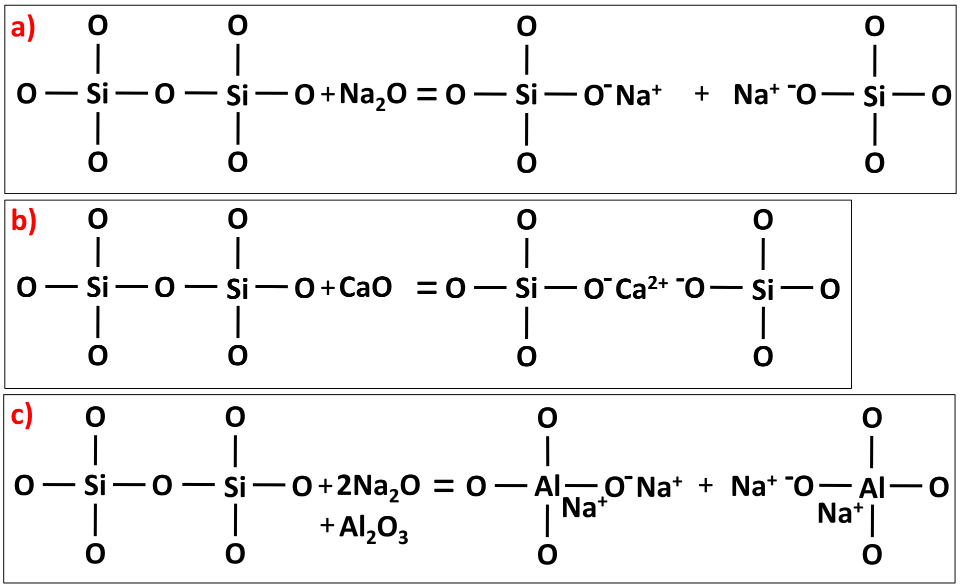

Figure 6.55 Schematic representation of a) sodium oxide addition to silicate network [41] b) calcium oxide in silicate network and c) incorporation of sodium oxide and alumina.

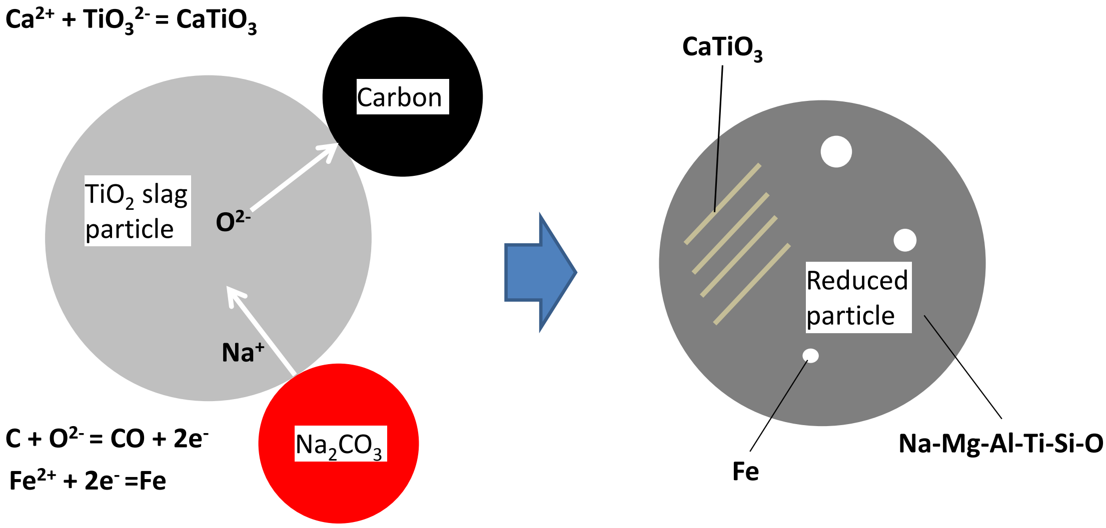

Figure 6.56 Schematic illustration of reaction mechanism of reaction mechanism.

6.3.2 Carbothermic reduction of low-grade titanium dioxide slag in tube furnace

The T2 material was ground with 100% passing through 106 microns and then mixed with Na_2CO_3 and activated charcoal before being fed into the tube furnace at 1323 K.

6.3.2.1 Effect of Na_2CO_3 weight ratio

The effect of weight ratio of Na_2CO_3 during carbothermic reduction of T2 was studied by maintaining a constant T2:C = 1:0.09 weight ratio. Weight ratios of T2:Na_2CO_3 varying from 1:0.3 to 1:0.4 were studied at 1323 K.

The X-ray powder diffraction for the T2:Na_2CO_3:C = 1:0.3:0.09, 1:0.35:0.09, and 1:0.4:0.09 are presented below in Figure 6.57a to Figure 6.57c, respectively. There are obvious similarities in the patterns at the different weight ratios. It can be noted that the peaks for $CaTiO_3$, Fe and $Na_{1.74}Mg_{0.79}Al_{0.15}Si_{1.06}O_4$ are visible at all three weight ratios. The lack of peaks representing for the original T2 as-received material shows that even at T2:Na_2CO_3:C = 1:0.3:0.09 there was sufficient Na_2O available to decompose the slag matrix and promote the formation of $CaTiO_3$. However, the $MgAl_2O_4$ peaks are observed for all the Na_2CO_3 molar ratios. Suggesting that while the Na_2O was consumed decomposing the slag matrix, but there was an insufficient amount to completely decompose the $MgAl_2O_4$ phase as although the spinel peak intensity decreases as the Na_2CO_3 addition increases [212].

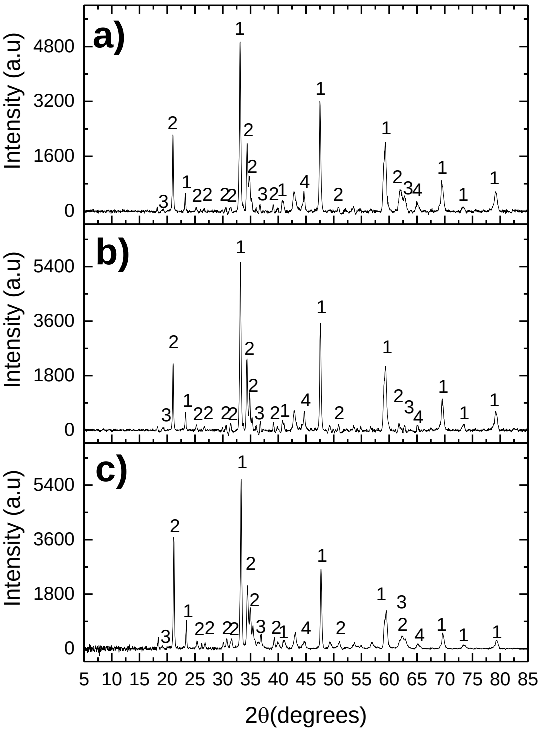

Figure 6.57 Effect of changing weight ratio of Na_2CO_3 at 1323 K for low-grade TiO_2 slag:Na_2CO_3:C reduction a) 1:0.3:0.09 b) 1:0.35:0.09 c) 1:0.4:0.09. 1 – $CaTiO_3$, 2- $Na_{1.74}Mg_{0.79}Al_{0.15}Si_{1.06}O_4$, 3 – $MgAl_2O_4$ and 4 – Fe.

6.3.3 Carbothermic reduction of low-grade titanium dioxide slag in rotary kiln

T2 was processed in the rotary kiln at 1273 K to study the behaviour inside the kiln and determine how suitable a kiln would be for scaling-up treatment of the material. The high Na_2CO_3 burden compared to that used for the T1 is expected to cause operational problems such as accretion formation. Particle size was varied to study the effect on treated sample and operation of the kiln. Treated samples were characterised using X-ray powder diffraction and scanning electron microscopy. T2 was ground and sized to ensure all the particles were in the appropriate range. 200g of T2 was used for each experiment utilising the same weight ratio of T2:Na_2CO_3:C = 1:0.45:0.09. Each reaction mixture was passed through the kiln four times.

6.3.3.1 Effect of particle size

In order to reduce the ring formation inside the rotary kiln the particle size of the T2 material fed into the kiln was varied using an operating temperature of 1273 K for all the experiments. Typically, fine particles result in accretion formation in the rotary kiln so larger particles were used in an attempt to overcome the challenge [197]. The three particle size distributions considered were:

1) +106 μm -300 μm
2) +300 μm -500 μm
3) +500 μm -1180 μm

The comparison of the rotary kiln results is presented in Figure 6.58. Most noteworthy is that as the particle size increases so does the material build up in the kiln tube, which is counter intuitive as fine particles are more likely to adhere to the inside of the tube [93]. The decrease in the available reaction surface area with larger T2 particles results in a portion of the Na_2CO_3 melting before Na_2CO_3 can react with T2 and activated carbon, contributing to a ring forming in the alumina tube. The general trend observed in Figure 6.58 is that the percentage of sample accumulating in the tube decreases with each pass, except when T2 material sized +500 μm -1180 μm was used. The %tube after the first pass for experiment 3) was 80.53% but increases to 87.9% and 83.65% for the second and third pass, respectively and finally the value decreases to 64.18% after the fourth pass.

The percentage remaining in the tube after the fourth pass for T2 material sized +106 μm -300 μm was 1.83% compared 14.8% for after the fourth pass for material sized T2 material sized +300 μm -500 μm. The percentage of sample remaining in the tube decreases as the number of passes increases due to the partially reacted products being less prone to sticking.

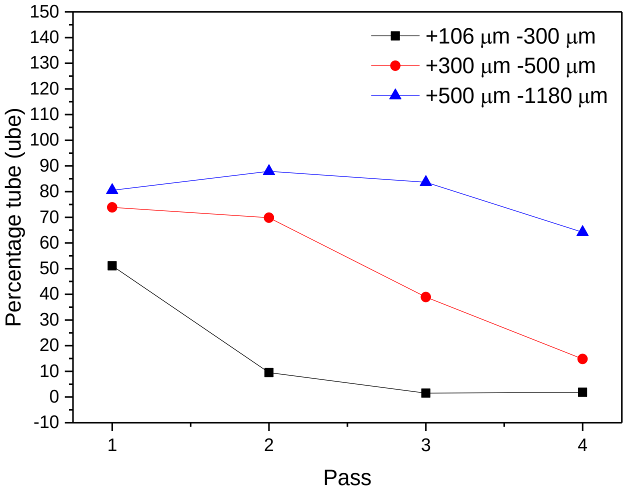

Figure 6.58 Percentage of input material remaining in rotary kiln tube with each pass.

In comparison with the rotary kiln results for treating T1, it can be seen that at all particle sizes there is significantly more ring formation and sample accumulation in the kiln tube after the first pass. This is likely the result of:

i) the larger quantity of Na_2CO_3 used for treating T2.

ii) the higher silica content of the T2 material, which would likely result in the formation of low melting eutectics [213-215].

iii) the ΔG^o_{1273K} value for the reaction between Na_2CO_3 and C with $FeTiO_3$ (equation 5.8) being lower than the reaction with $MgTi_2O_5$ (equation 5.19) where the values are of -233.37 kJ.mol^{-1} and -86.30 kJ.mol^{-1}, respectively. Implying that there may be a greater thermodynamic barrier to the reaction involving T2 ; resulting in liquid Na_2CO_3 coating the outside of the T2 particle instead of having diffused into the particle as seen with T1.

X-ray powder diffraction analysis

Characterisation of the treated samples collected after the fourth pass was performed to understand the influence of particle size on the processing of the T2 material in a rotary kiln. The x-ray powder diffraction patterns for different experiments using T2 are presented in Figure 6.59A to Figure 6.59C where it is evident that the XRPD patterns are comparable to those observed with results from the TGA apparatus (see Figure 6.50).

$CaTiO_3$ is the dominant phase present at all the particle size ranges. However, the peaks at 2θ ≈ 35° are broad and amorphous in appearance for experiments using T2 sized +500 μm – 1180 μm suggesting the silicate-rich slag matrix has not been completed broken down in comparison with the sharp well-defined peaks seen in Figure 6.59A and Figure 6.59B representing $Na_{1.74}Mg_{0.79}Al_{0.15}Si_{1.06}O_4$. The intensity of the $MgAl_2O_4$ peaks is stronger in Figure 6.59C than for Figure 6.59A and Figure 6.59B, implying that the extent of reaction was limited for experiments using T2 sized +500 μm – 1180 μm. The lack of reduction is to be expected as a significant percentage of the material remained in the rotary kiln tube even after the fourth pass.

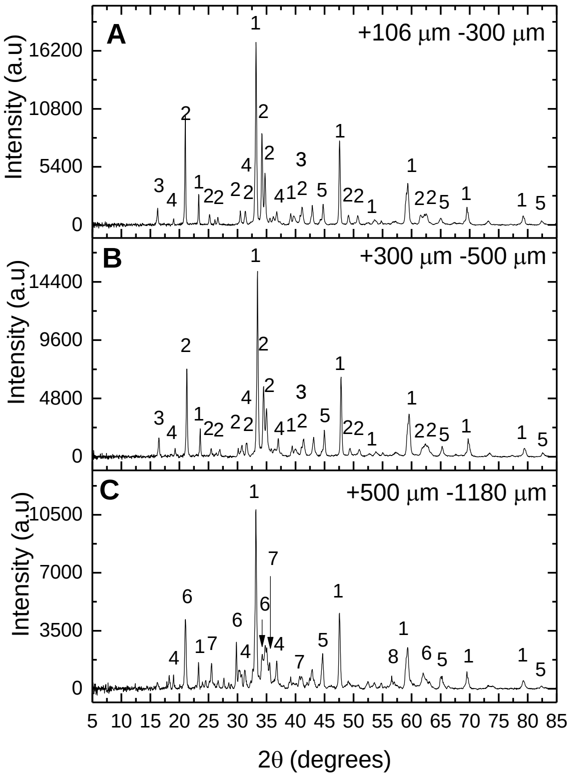

Figure 6.59 Effect of low-grade TiO_2 slag particle on the carbothermic reduction with Na_2CO_3 in the rotary kiln using T2 sized A) +106 μm -300 μm B) +300 μm -500 μm C) +500 μm – 1180 μm. 1 – $CaTiO_3$, 2- $Na_{1.74}Mg_{0.79}Al_{0.15}Si_{1.06}O_4$, 3- $Na_{0.75}Ti_{0.25}Fe_{0.75}O_2$, 4 – $MgAl_2O_4$, 5 – Fe, 6-$Na_{0.875}Al_{0.875}Si_{0.125}O_2$ 7-$Ca_{0.95}Na_{0.04}Mg_{0.65}Fe_{0.23}Ti_{0.10}Al_{0.01}Si_{1.69}Al_{0.31}O_6$.

Scanning electron microscopy analysis

Figure 6.60 is the SEM of the sample collected after the fourth pass from alkali reductive roasting in the kiln using T2 sized +500µm - 1180µm. Elemental mapping indicates that the Na^+ ions have diffused throughout the slag matrix. Intense Mg and Al overlap in regions of the maps represents the $MgAl_2O_4$ phase noted in Figure 6.59b. The Fe map show that the iron is largely present at the periphery of the particle. However, the iron has not formed large particles like those seen in Figure 6.61.

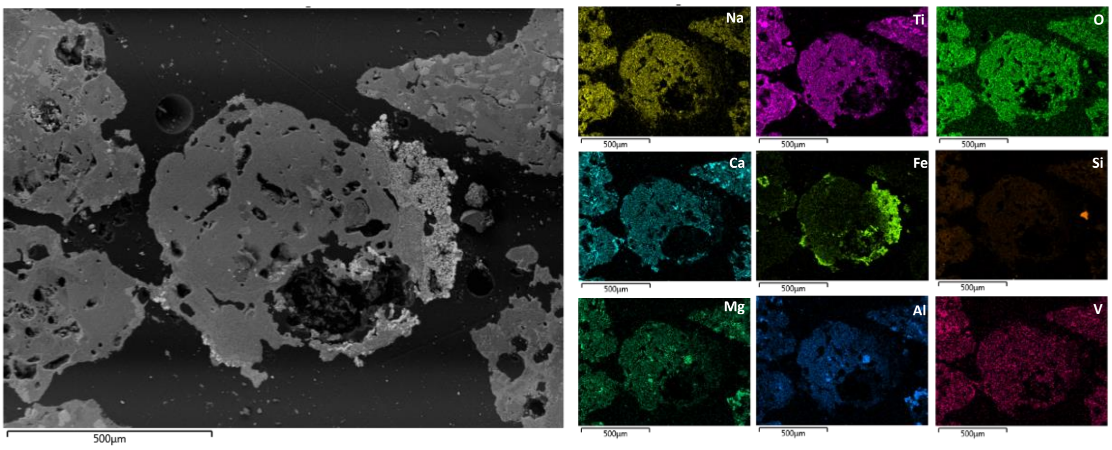

Figure 6.60 Backscattered SEM image with elemental mapping of low-grade TiO_2 slag (+500µm - 1180µm) reduced with activated carbon in the presence of Na_2CO_3 at 1273 K in the rotary kiln collected after the fourth pass.

Backscattered scanning electron micrographs of the treated sample collected after the fourth pass for the T2 particle size distribution +300 µm – 500 µm are given in Figure 6.61. Three distinct phases are visible in the electron image. The light grey phase (see Area C on Figure 6.61) presents metallic iron, which agrees with what was observed in the XRPD patterns (see Figure 6.59d). The metallised iron particles have an Fe content of 94 weight.%. The larger size of the iron particles and the apparent spinodal decomposition nature of the iron grains suggests that the iron may have formed from the reduction of Fe_2TiO_4 that remained in T2. While much of the iron has migrated to the periphery of the particle, it can be seen that much of the iron remains dispersed throughout the particle microstructure. The composition of the reacted slag matrix is given by Area B on Figure 6.61 with 0.3 weight.% V dissolved in the matrix. Area A on Figure 6.61 is largely composed of Na, Fe, Ti and O ; this phase corresponds to the $Na_{0.75}Ti_{0.25}FeO_4$ observed in Figure 6.59b.

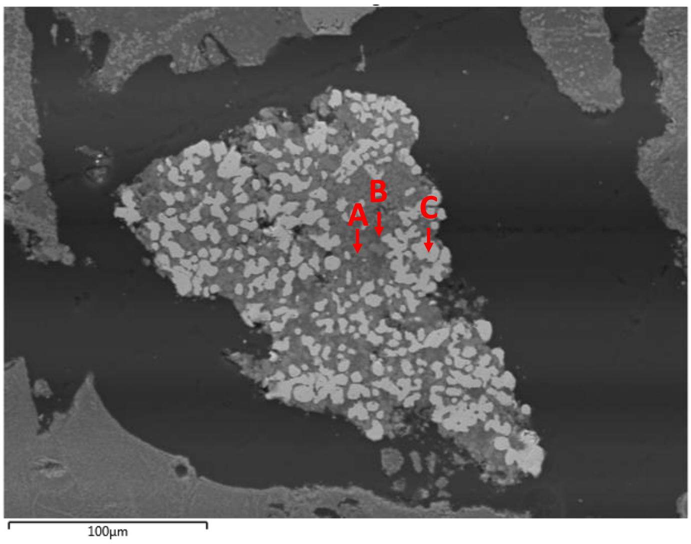

Figure 6.61 Backscattered SEM image with elemental mapping and EDX point and ID analysis of low-grade TiO_2 slag (+300 µm – 500 µm) reduced with activated carbon in the presence of Na_2CO_3 at 1273 K in the rotary kiln and collected after the fourth pass.

Table 6.12 Elemental composition of areas A to C on Figure 6.61.

Weight.%	Ti	Fe	O	Na	Al	V	Si	Ca	Mg	Mn	K
A	29.1	19.3	31.6	16.3	-	0.4	0.3	0.4	2.2	0.5	-
B	11.4	5.6	38.0	19.7	12.4	0.3	8.8	1.5	1.3	0.6	0.3
C	2.2	94.0	1.8	1.7	-	-	-	0.3	-	-	-

6.4 Chapter Summary

$CaTiO_3$ was the dominant phase formed during reductive alkali roasting of T2 due to the reaction of Na_2CO_3 with the slag matrix as the phase crystallised out. The XRPD results agree with standard Gibbs free energy change calculations which showed $CaTiO_3$ formation being more thermodynamically feasible than Na_2TiO_3 from the reaction between the slag matrix and Na_2CO_3 in the presence of carbon.

Where good fitting of experimental TGA data was observed for both the Interface and G.B models the reactions were considered to be under mixed-control. Further fitting using the mixed-control model, comprised of the combined Interface and G.B. models, was performed. Rate constants derived from the mixed-control model – which also demonstrated high goodness of fit – were utilised for determining the apparent activation energy of the global reaction which accounted for the impact of chemical reaction and diffusion on the reaction. The apparent activation energy of T1 reduction in the absence of Na_2CO_3 was determined as 258 kJ.mol^{-1}. By comparison, two distinct regimes were observed for T1 reduction in the presence of Na_2CO_3, where high temperature regime activation energy was 130 kJ.mol^{-1} contrasted with 199 kJ.mol^{-1} for the low-temperature regime. Overall activation energy of T1 in the presence of K_2CO_3 was 127 kJ.mol^{-1}. Thermodynamic prediction indicated reduction in the presence of K_2CO_3 was more favourable than in the presence of Na_2CO_3. However, SEM analysis indicated a lack of phase segregation between iron and titanium dioxide. Similar observations have been made when a liquid phase formed during potassium-based alkali roasting of ilmenite.

Reductive alkali roasting of T2 using stoichiometric carbon had an apparent activation energy of 114 kJ.mol^{-1} compared to 184 kJ.mol^{-1} for experiments utilising two times stoichiometric carbon.

Alkali reduction of T2 in the rotary kiln resulted in greater ring formation in comparison to T1 likely owing to the mineralogy of T2.

7 Separation and Purification of reduced products

Chapter 7 discusses the treatment of reduced samples for extraction of metallic values including TiO_2, V_2O_5¸Fe and Al_2O_3. Techniques such as magnetic separation, water leaching, acid treatment, sulphation roasting and smelting were employed.

7.1 Processing reduced iron-rich tailings sample

7.1.1 Magnetic separation and water leaching

T1 reduced samples were milled before subjecting them to wet magnetic separation, during which the non-magnetic fraction was expected to report to the beaker along with the water-soluble compounds such as $NaAlO_2$ and $NaVO_2$ with the Fe-rich fraction remaining on the magnet. The non-magnetic fraction was water leached at 353 K for 1 hour to enhance the recovery of vanadium oxide and alkali salts. The water leach solution was sent for vanadium pentoxide and alumina extraction. V_2O_5 and Al_2O_3 recovery is discussed in 7.2.2, as the techniques for recovering these metallic values are the same for T1 and T2.

All the T1 samples reduced in the rotary kiln were subject to magnetic separation and their respective magnetic and non-magnetic fractions analysed using XRF. Table 7.1 contains a summary of all the rotary kiln processing parameters.

Graphical representation of the iron and titanium dioxide compositions of the respective magnetite and non-magnetic fractions is presented in Figure 7.1. Detailed XRF analysis is given in Table 7.2.

Sample B was considered to be the optimised rotary kiln parameters as this magnetic fraction had the highest iron content at over 91.7 weight.%, while also having the lowest amount of TiO_2 present in magnetic fraction. Sample A, the experiments carried out at 1173 K, was found to have a non-magnetic fraction with the highest TiO_2 content and the lowest iron content. Noteworthy, Sample C, reduction at 1273 K, had more iron present in the non-magnetic fraction than titanium dioxide owing to the FeO formed (see Figure 6.27) which reports to the non-magnetic magnetic fraction. Suggesting that a reduction temperature below 1273 K is preferable for rotary kiln experiments.

Table 7.1 Summary of rotary kiln operation parameters.

Sample	Temperature (K)	Particle size (µm)	Flow rate (L.min^{-1})	Angle of inclination (°)	Na_2CO_3 weight ratio	Residence time* (minutes)
A	**1173**	+106 -300	2	1.6	0.2	72
B	1223	+106 -300	2	1.6	0.2	74
C	**1273**	+106 -300	2	1.6	0.2	71
D	1223	+106 -300	**1**	1.6	0.2	73
E	1223	+106 -300	**3**	1.6	0.2	74
F	1223	**+300 -500**	2	1.6	0.2	72
G	1223	**+500 -1180**	2	1.6	0.2	68
H	1223	+106 -300	2	**1.2**	0.2	80
I	1223	+106 -300	2	**1.4**	0.2	88
J	1223	+106 -300	2	1.6	**0.16**	76

*Residence time refers to a total residence time for all four passes and not the individual pass.

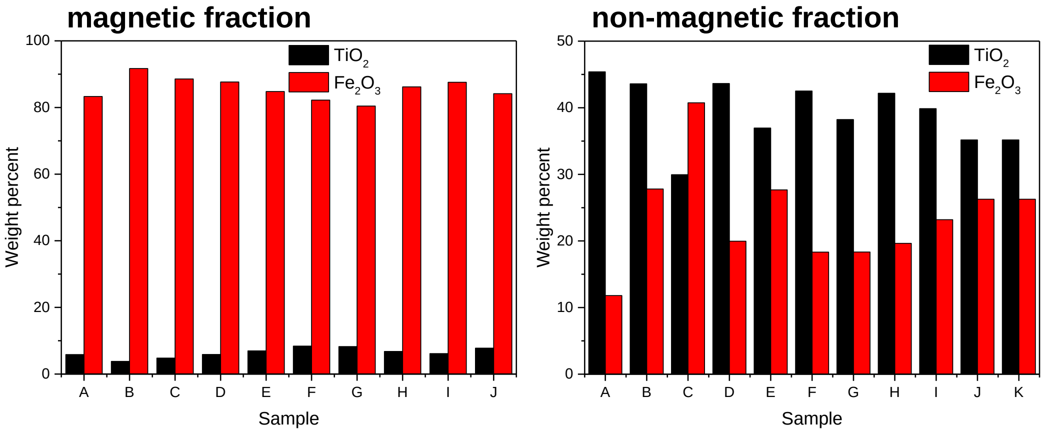

Figure 7.1 TiO_2 and Fe_2O_3 composition of magnetic and non-magnetic fraction from iron-rich tailings reduced in the rotary kiln in the presence of Na_2CO_3.

Table 7.2 Chemical composition of magnetic and non-magnetic fraction from iron-rich tailings reduced in the rotary kiln in the presence of Na_2CO_3.

Weight.%		**TiO_2**	**Fe_2O_3**	**V_2O_5**	**Al_2O_3**	**CaO**	**Cr_2O_3**	**MgO**	**MnO**	**Na_2O**	**SiO_2**	**SO_3**
NM	A	45.40	11.80	0.41	5.79	6.11	0.20	5.33	0.86	15.60	7.39	0.34
	B	43.60	27.80	0.43	3.17	3.57	0.29	2.31	0.91	11.90	5.05	-
	C	29.95	40.74	0.32	3.96	4.06	0.23	2.88	0.60	11.74	5.31	0.21
	D	43.64	19.96	0.35	4.24	5.36	0.24	4.18	0.88	13.80	6.95	0.22
	E	36.95	27.68	0.30	5.13	5.29	0.31	3.62	0.72	12.92	6.86	0.22
	F	42.51	18.32	0.33	5.09	6.05	0.25	3.93	0.79	14.46	8.02	0.25
	G	38.22	18.34	0.51	6.94	7.14	0.20	4.09	0.75	14.61	8.63	0.57
	H	42.18	19.65	0.31	4.44	5.04	0.26	3.85	0.68	15.80	7.55	0.26
	I	39.86	23.19	0.29	4.31	4.64	0.27	3.94	0.78	15.17	7.12	0.43
	J	35.17	26.27	0.57	6.37	5.94	0.25	3.73	0.62	12.50	8.10	0.49
Mag	A	5.86	83.30	-	1.40	0.50	-	0.73	0.13	6.29	1.44	-
	B	3.81	91.70	-	0.53	0.43	-	0.32	-	1.80	0.67	-
	C	4.79	88.56	0.07	1.25	0.32	0.05	0.45	0.12	3.00	1.19	0.21
	D	5.88	87.66	0.03	1.29	0.47	0.04	0.47	0.12	2.58	1.37	0.09
	E	6.96	84.79	0.04	1.16	0.37	0.11	0.52	0.16	4.19	1.45	0.24
	F	8.38	82.21	0.11	1.56	0.43	0.07	0.56	0.16	4.66	1.73	0.13
	G	8.25	80.42	0.16	1.76	0.35	0.06	0.68	0.17	6.20	1.68	0.25
	H	6.78	86.19	0.09	1.03	0.38	0.07	0.55	0.15	3.01	1.52	0.23
	I	6.13	87.58	0.04	0.95	0.40	0.07	0.51	0.13	2.65	1.38	0.15
	J	7.79	84.16	0.06	1.48	0.44	0.07	0.48	0.14	3.75	1.56	0.07

X-ray fluorescence analysis

Tube furnace experiments for alkali reduction of T1 were carried out for 90 minutes, while the carbothermic reduction in the kiln was performed over four passes.

The chemical composition analysis of magnetic and non-magnetic fractions obtained after alkali reductive roasting of T1 in the rotary kiln at 1223 K and the tube furnace at 1223 K are presented in Table 7.3. The weight percent of iron in the magnetic fraction is higher for the rotary kiln compared to the tube furnace, whereas as the TiO_2 content of the rotary kiln magnetic fraction contains a lower amount of TiO_2. The weight.% TiO_2 in the rotary kiln non-magnetic fraction is comparable to that of the tube furnace. There is a significantly greater weight percent Fe_2O_3 present for the rotary kiln magnetic fraction compared to the tube furnace magnetic fraction.

Table 7.3 Chemical composition of magnetic and non-magnetic fraction from iron-rich tailings treated in the rotary kiln and tube furnace at 1223 K.

Weight.%	**Fe_2O_3**	**TiO_2**	**V_2O_5**	**Na_2O**	**SiO_2**	**Al_2O_3**	**CaO**	**MnO**	**Cr_2O_3**	**MgO**
RK - magnetic	91.7	3.81	*255	1.8	0.66	0.53	0.43	727*	299*	0.32
RK - non-magnetic	27.8	43.6	0.43	11.9	5.05	3.17	3.57	0.91	0.293	2.31
TF - magnetic	85.72	7.01	0.02	2.48	1.85	1.73	0.43	0.18	0.12	0.56
TF - non-magnetic	6.21	45.70	0.44	10.74	7.40	12.86	10.40	0.79	0.65	4.79

*parts per million

X-ray powder diffraction analysis

The XRPD patterns for the magnetic and non-magnetic fractions obtained after reduction in the rotary kiln and the tube furnace are presented in Figure 7.2a and Figure 7.2b, respectively. It is evident from Figure 7.2a that $Na_{0.75}Ti_{0.25}Fe_{0.75}O_2$, Fe_3O_4, Fe_2TiO_4, FeO and $CaTiO_3$ are present in the rotary kiln non-magnetic fraction, whereas the tube furnace non-magnetic fraction comprised sodium titanates, sodium aluminosilicate and calcium titanate. Presence of iron oxide-bearing phases in the rotary kiln non-magnetic fraction explains the high Fe_2O_3 content observed in Table 7.3. The formation of the $CaTiO_3$ phase agrees with the thermodynamic calculations from chapter 5 that highlighted formation of the phase was more favourable than sodium titanate according to reaction 5.21 and 5.22, respectively. However, the limited amount of CaO present in the as-received T1 material allowed Na_2CO_3 to react with remaining TiO_2.

The difference in phases observed in the rotary kiln fractions and the tube furnace fractions may be due to the difference in residence time in constant temperature zone. Mixtures treated in the tube furnace were heated for 90 minutes at 1223 K, whereas as rotary kiln samples had a residence time of up to 88 minutes, However, as the constant temperature zone comprised a section of the alumina tube the exposure of rotary kiln samples to 1223 K heating would have been less than the total residence time reported.

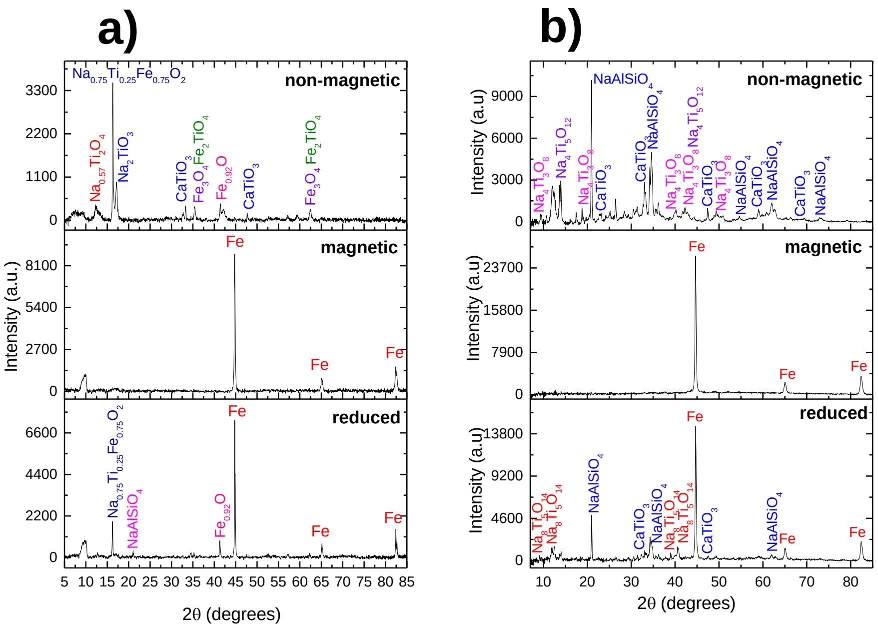

Figure 7.2. XRPD patterns of carbothermic reduction in the presence of Na_0CO_3 in the a) rotary kiln at 1223 K and the b) tube furnace at 1223 K.

Scanning electron microscopy analysis

Electron micrograph from the rotary kiln magnetic fraction is given in Figure 7.3**.** The light grey phase (see Area A on Figure 7.3) is the metallic iron, containing 97.7 weight.% Fe. The dark grey phase (see Areas B and C on Figure 7.3) shows that titanium dioxide is trapped with the iron particles. Sintering of sodium titanate to the iron grains may explain why some of the TiO_2 reports to the magnetic fraction.

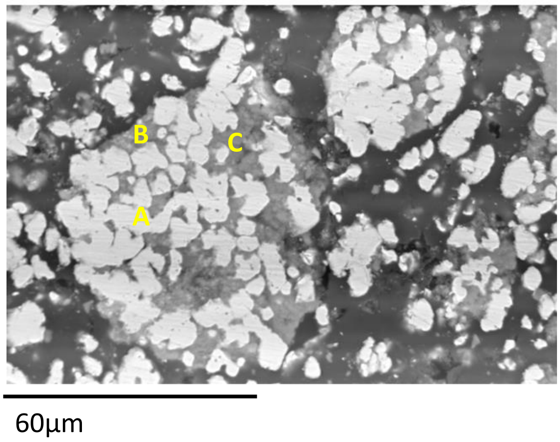

Figure 7.3. Backscattered SEM image of magnetic fraction from reduction at 1223 K in a rotary kiln.

Table 7.4. Elemental composition of areas A to C on Figure 7.3 as analysed by EDX

Weight.%	**Fe**	**Ti**	**Na**	**O**	**V**	**Si**	**Ca**	**Al**	**Mg**	**Mn**
A	97.7	0.8	-	1.4	-	-	-	-	-	-
B	9.9	41.1	9.7	34.6	0.5	1.4	0.8	0.7	1.3	-
C	4.5	47.0	9.7	35.5	0.3	0.7	0.4	0.5	0.9	0.3

The recovery iron and titanium dioxide is presented in Table 7.5. It is expected that the iron would be recovered from the magnetic fraction and the titanium dioxide would be recovered from the non-magnetic fraction. It is evident that the recovery of both is high and significantly better than results produced by El-Tawil, Morsi [119].

Table 7.5. Recovery of iron and titanium dioxide after magnetic separation for sample reduced at 1223 K.

Fraction	**Weight.% Fe**	**Weight.% TiO_2**
Magnetic	85.5	13.5
Non magnetic	14.5	86.5

7.1.2 Melting of the magnetic fraction

The rotary kiln magnetic fraction was mixed with graphite and placed in a rising hearth furnace at 1723 K for 2 hours under the flow of argon gas. Residual titanium dioxide and gangue contained in the magnetic fraction reported to the slag fraction after smelting. Low magnification SEM image (see Figure 7.4a) of the steel illustrates dark phases where slag was entrapped in the steel, indicating incomplete separation between slag and molten steel. High magnification SEM (see Figure 7.4b) show micro-alloying of steel with V. Segregation between the light TiO_2-rich phase and the dark gangue phase ($NaAlSiO_4$) in the slag is evident from the microstructure present.

Bulk analysis of the 98.1 weight.% iron ferroalloy presented in Table 7.6 indicates that the V content is 0.1 weight.% while the 1.1 weight.% C is dissolved in the steel.

Table 7.6 Chemical analysis of ferroalloy produced from magnetic fraction smelting at 1723 K.

Weight.%	Fe	V	C	S	Na
	98.1	0.1	1.1	0.04	0.2

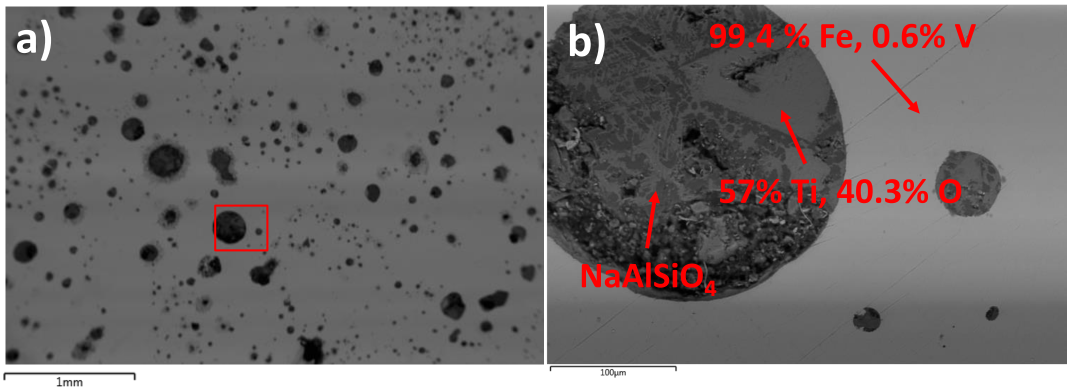

Figure 7.4. Backscattered SEM of a) low magnification and b) high magnification image of magnetic fraction smelted at 1723K for 2 hours.

7.1.3 Sulphuric acid leaching of non-magnetic fraction

The tube furnace non-magnetic fraction was leached in a 0.5 M H_2SO_4 solution under normal atmosphere for 2 hours at 313 K and the pH of the acidic medium was 1.3.

Sulphuric acid reacts with NaAlSiO4 and Na_2TiO_3 according to equations 7.1 and 7.2, respectively.

$$\mathrm{nNaAlSiO_4 + nH_2SO_4 \rightarrow H_4SiO_4 + Al_2(SO_4)_3 + Na_2SO_4 + H_2O} \qquad 7.1$$

$$\mathrm{Na_2TiO_3 + H_2SO_4 \rightarrow TiO_2 + Na_2SO_4 + H_2O} \qquad 7.2$$

The computed E_h-pH diagram of the Na-Al-Si-H_2O multi component system is given in Figure 7.5. Hydrated sodium aluminosilicate is the stable phase in basic pH range between of limits of the decomposition of water, O_2= 1 atm and H_2= 1 atm. Formation of water-soluble silicic acid (H_4SiO_4) occurs below pH 6.3 indicating the range where silica may be removed from the non-magnetic fraction. Al^{3+} ions co-exist in the same phase field as H_4SiO_4 and Na^+ at a pH less than 2, corresponding to the experimental conditions utilised during H_2SO_4 leaching.

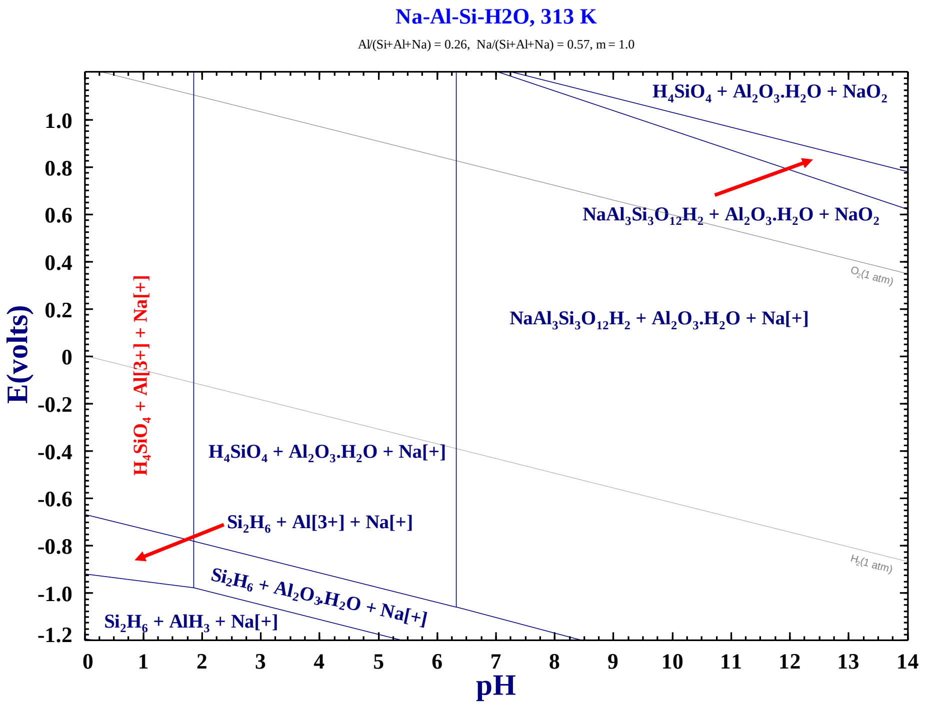

Figure 7.5. E_h-pH diagram of the Na-Al-Si-H_2O system at 313 K, computed using FactSage software [48].

Chemical analysis in Table 7.7 of the H_2SO_4 leached T1 residue show after leaching the TiO_2 content increased to 72 weight.% TiO_2. It is evident that the majority of the Na_2O, MgO, MnO, SiO_2 and Al_2O_3 were solubilised whilst CaO was only partially removed, owing to the presence of the $CaTiO_3$ compound which is insoluble in dilute acid. Dissolution of Na_2O, Al_2O_3 and SiO_2 in the acidic medium agrees with thermodynamic predictions in Figure 7.5 where solubilisation of the metallic values was predicted below pH 2.

Table 7.7 Chemical analysis of tube furnace non-magnetic fraction leached in 0.5M H_2SO_4.

Weight.%	TiO_2	Al_2O_3	Na_2O	SO_3	MgO	SiO_2	Fe_2O_3	CaO	MnO	Cr_2O_3	V_2O_5
	72.1	0.7	4.8	2.7	0.5	2.5	11.1	3.6	0.1	0.4	0.9

7.1.4 Sodium bisulphate roasting and water leaching of acid leached residue

The H_2SO_4 leached residue was roasted in air with $NaHSO_4$ at 923 K and subsequently leached in water for 1 hour at 353 K in order to solubilise that water-soluble Na_2SO_4 and $FeSO_4$ compounds. Reaction 7.3 highlights the conversion of $CaTiO_3$ into calcium sulphate ($CaSO_4$) and TiO_2 (anatase and rutile) during sodium bisulphate roasting. Residual iron and iron oxide present in the T1 acid leached residue reacts with $NaHSO_4$ to form ferrous and ferric sulphates (see equation 7.4).

$$\mathrm{CaTiO_3 + 2NaHSO_4 + \ O_2(g) \rightarrow TiO_2 + CaSO_4 + \ Na_2SO_4 + \ H_2O(g)} \qquad 7.3$$

$$\mathrm{FeO + Fe_2O_3 + \ 8NaHSO_4 + \rightarrow} Fe_2(SO_4)_3 \mathrm{+ FeSO_4 + \ 4Na_2SO_4 + \ 4H_2O(g)} \qquad 7.4$$

It should be noted that both TiO_2 and $CaSO_4$ are insoluble in water, however, two water-soluble complexes of sodium-calcium sulphate and sodium-iron sulphate (see in Figure 7.6) form during the water leaching at an acidic pH of 2.3. Figure 7.6 represents the XRPD pattern of the dried water leach solution from roasted products. $CaSO_4.(H_2O)_{0.5}$ is also observed in the XRPD pattern,

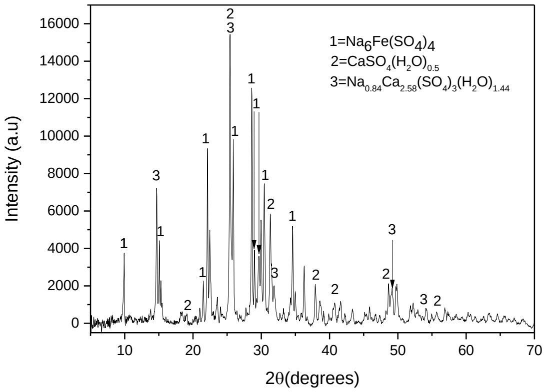

Figure 7.6 XRPD pattern of dried water leach solution from CaTiO3 roasting with $NaHSO_4$ in air followed by water leaching with $FeSO_4$.1- 1=$Na_6Fe(SO_4)_4$, 2- $CaSO_4(H_2O)_{0.5}$, 3- $Na_{0.84}Ca_{2.58}(SO4)_3(H_2O)_{1.44}$

Solids obtained after water leaching of the roasted product contained up to 92 weight.% TiO_2 with the major impurity being SiO_2, as seen in Table 7.8. Figure 7.7 illustrates the TiO_2 formed is predominantly anatase with minor amounts of rutile present.

Table 7.8 Chemical composition of TiO_2 residue.

Weight.%	**TiO_2**	**Al_2O_3**	**Na_2O**	**SO_3**	**SiO_2**	**Fe_2O_3**	**CaO**	**Cr_2O_3**	**V_2O_5**
	92.3	0.3	0.3	0.7	2.8	2.0	0.2	0.1	0.8

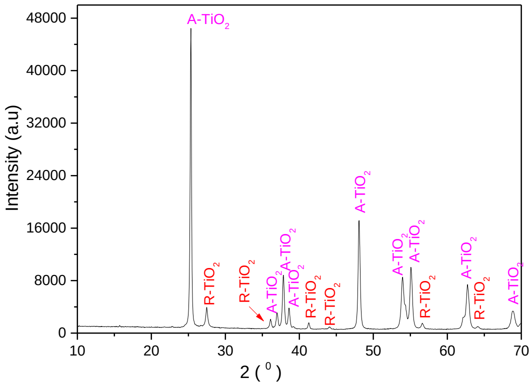

Figure 7.7 TiO_2 residue produced from iron-rich tailings. Anatase = A-TiO_2 and Rutile = R-TiO_2.

7.2 Processing reduced low-grade titanium dioxide slag

7.2.1 Water leaching of reduced low-grade TiO_2 slag

The reduced T2 material residue was leached in hot water 353 K for two hours to solubilise the sodium vanadate. During the reduction step the gangue (CaO, Al_2O_3, and MgO) was able to react with vanadium oxide to form water-insoluble vanadates [7]. Therefore, sodium carbonate is added during the water leaching to react with these water-insoluble vanadates and convert them to water-soluble sodium vanadate, according to equation 7.5 [216].

$$CaV_2O_4 + Na_2CO_3 \rightarrow NaVO_2 + CaCO_3 \qquad 7.5$$

The E_h-pH diagram in Figure 7.8 depicts the V-Al-Na-H_2O system at 353 K, illustrating the stability region of Na^+ ions and vanadates in solution. Water leaching was performed at pH 12 in air atmosphere where the solution potential would be between O_2=

1 atm and H_2=1 atm. HVO_4^{2-} anions are shown to co-exist with $Al_2O_3.H_2O$ and Na^+ cations in the same phase field, at pH greater than 11.5 and between 0.1 and -0.6 volt.

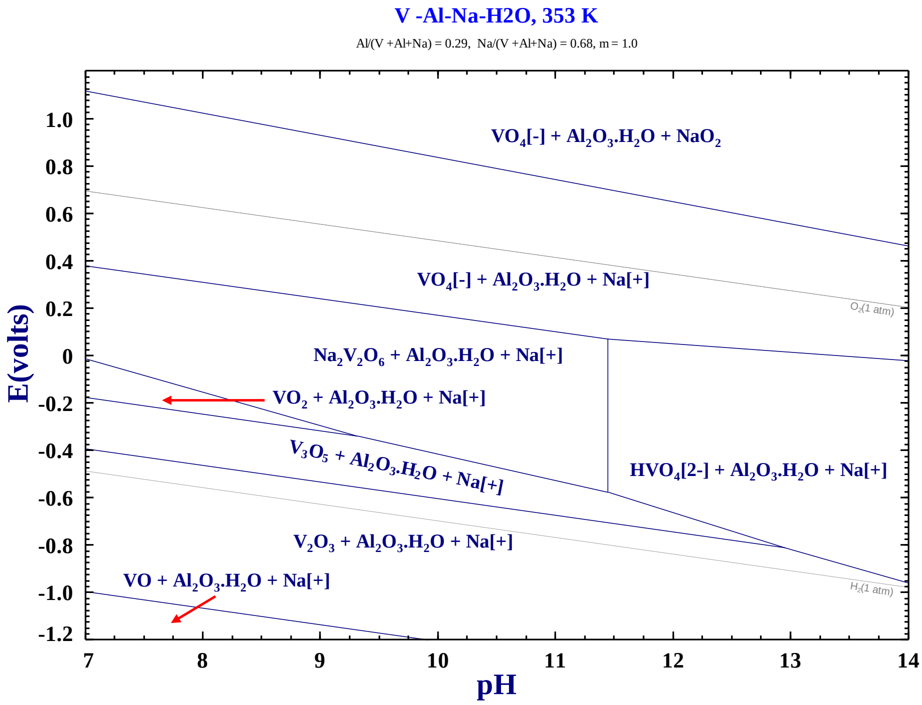

Figure 7.8. Eh-pH diagram of V-Al-Na-H_2O system at 353 K [48].

7.2.2 Recovery of vanadium pentoxide, aluminium oxide and alkali salts

Separation of Al_2O_3 and V_2O_5 dissolved in the filtered water leach solution was carried out by selective precipitation. First, the leachate was evaporated to increase the vanadium concentration in the solution with alkali salts precipitating during the evaporation process.

Sparging of CO_2 gas into the concentrated solution resulted in the pH decreasing from 12 to 8, causing alumina to precipitate and regenerating sodium carbonate, according to 7.6. Although the precipitation was selective for alumina, a limited amount of the vanadium oxide co-precipitates as the alumina residue consists of 76.9 weight.% Al_2O_3 and 2.4 weight.% V_2O_5, as seen in Table 7.9. Na_2CO_3 crystallised from the pH 8 solution contains 0.22 weight.% V_2O_5 and 94 weight.% Na_2O.

$$Na_2Al_2O_4 + CO_2(g) + H_2O \rightarrow Na_2CO_3 + Al_2O_3.H_2O \qquad 7.6$$

Sulphuric acid was added to the solution to decrease the pH value from 8 to 5. Ammonium sulphate was added to the pH 5 solution and agitation was carried out for 4 hours in order to form ammonium metavanadate (AMV) solids seen in Figure 7.9a (see equation **7.7**). Formation of water-soluble sodium vanadate during reductive alkali roasting allows for recovery of vanadium oxide via selective precipitation while avoiding the need for solvent extraction, as would be required in the H_2SO_4 – based EHSV and Avertana processes [58, 59]. Application of selective precipitation in acidic solutions is less effective than when used in alkaline solution, highlighting an advantage of the process developed in this study over existing processes as vanadium oxide is recovered from an alkaline solution [144].

XRPD pattern of AMV presented in Figure 7.10a demonstrates that ammonium metavanadate is the dominant phase. Calcination of the AMV solids at 723 K produced black solids seen in Figure 7.9b (see equation 7.8). Chemical composition of the black solids indicated 93 weight.% V_2O_5 present with 5 weight.% Na_2O also contained in the material (see Table 7.9). $Na_{0.282}V_2O_5$ is the major phase observed in the XRPD pattern (Figure 7.10b) with minor peaks for V_2O_5 also visible in the XRPD pattern, indicating residual Na_2O in the AMV reacted with vanadium oxide solids during calcination at 723 K to give sodium-deficient sodium vanadate. Purity of vanadium oxide solids can be enhanced by dissolving the black solids in hot ammonium hydroxide or sodium carbonate solution and subsequent AMV precipitation. Moreover, further optimisation of the precipitation conditions is necessary to improve the grade of V_2O_5 recovered avoiding the need for re-dissolution.

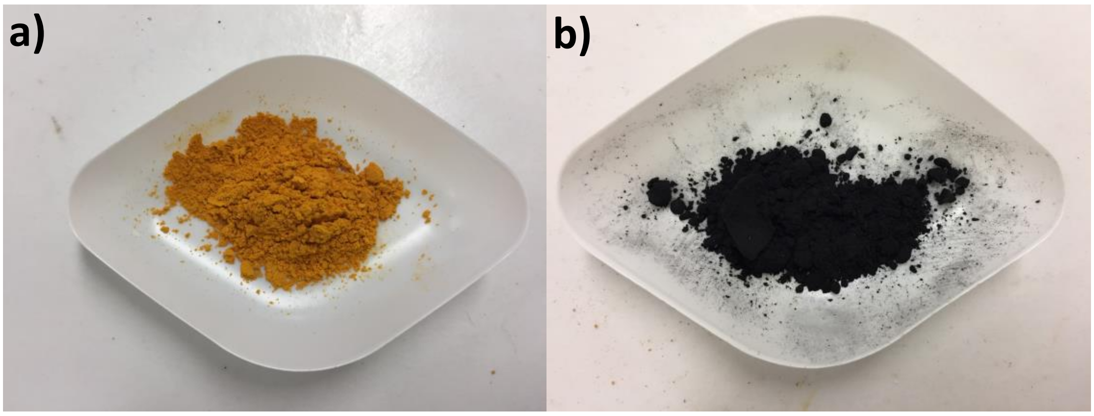

Figure 7.9 Image of a) ammonium metavanadate precipitated at pH 5 and b) of vanadium oxide solids obtained from calcination of AMV.

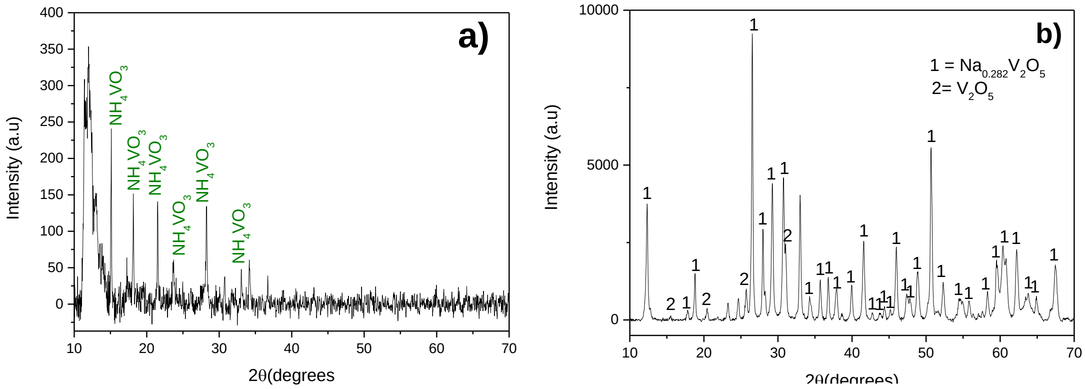

Figure 7.10 XRPD pattern of a) AMV precipitate and b) vanadium oxide solids. 1- $Na_{0.282}V_2O_5$ and 2-V_2O_5.

$$NaVO_3 + NH_4(SO)_4 \rightarrow 2NH_4VO_3 + Na_2SO_4 \qquad 7.7$$

$$2NH_4VO_3 \rightarrow V_2O_5 + 2NH_3(g) + H_2O(g) \qquad 7.8$$

Table 7.9 Chemical composition of solids recovered from water leach solution.

Weight.%	**Fe_2O_3**	**TiO_2**	**V_2O_5**	**CaO**	**Al_2O_3**	**Na_2O**	**MgO**	**SiO_2**	**SO_3**
Alumina	0.9	1.2	2.4	0.8	76.9	12.3	-	2.6	2.3
Recovered Na_2CO_3	0.07	-	0.22	0.42	1.82	94.04	0.32	0.64	1.67
V_2O_5 precipitate	0.05	-	93.27	0.03	0.15	5.68	-	0.21	0.21
Sodium sulphate	0.05	0.42	2.34	0.07	0.47	39.86	0.08	1.31	55.40

The remaining solution was evaporated yielding sodium sulphate. Chemical analysis (see Table 7.9) indicates that vanadium oxide is still present with the sodium sulphate suggesting that further optimisation of the precipitation process is required to maximise vanadium recovery from solution during AMV precipitation.

7.2.3 Hydrochloric acid leaching of T2 water leached solids

The solid T2 water leach solids were leached in air atmosphere with 0.5 M hydrochloric acid (HCl) used as a lixiviant in order to remove Al_2O_3, MgO, SiO_2 and Na_2O. The pH of the acid leach solution was maintained at 2.5 throughout. $Na_{1.74}Mg_{0.79}Al_{0.15}Si_{1.06}O_4$ and the iron in the residue reacted with HCl to form water-soluble metal chlorides and silicic acid (see equation 7.10 and 7.11). The multi component phase equilibria of the Na-Al-Si-H_2O system given in Figure 7.5 highlights the formation of silicic acid below pH 6.3.

HCl was chosen over sulphuric acid since it was observed that use of H_2SO_4 resulted in a gel phase owing to the polymerisation of silicic acid according to reaction 7.9 [217]. Polymerised silicic acid forms colloidal silica that aggregates to form a gel that adversely affects solid-liquid separation.

After filtration of the HCl leached solids, the filtrate was dried by evaporation of the aqueous medium to yield acid leach filtrate solids. The effect of increasing SiO_2 concentration in solution promotes gel formation which is evident from Figure 7.11 where silica gel is observed as the HCl leach solution volume decreases.

$$\mathrm{nSi(OH)_4 \rightarrow (OH)_3SiOSi(OH)_3 + H_2O} \qquad 7.9$$

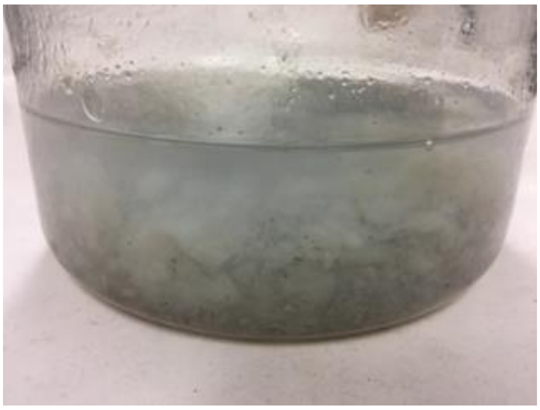

Figure 7.11 Photographic image of concentrated HCl leach solution filtrate.

Chemical composition of the dried acid leach filtrate detailed in Table 7.10 demonstrates the removal of SiO_2, MgO, Al_2O_3, Na_2O and iron from the T2 water leached solids during the HCl leaching process, which decreases the overall process acid consumption compared to the Avertana and H_2SO_4-based EHSV processes for T2 treatment [58, 59]. Silica is the major component of the acid leach filtrate solids illustrating how reductive alkali roasting results in the formation of acid-soluble silica-containing phases which precludes the need of an extra NaOH leaching step for desilication, as observed in other processes to beneficiate titania slag [79, 104, 135, 136]. However, a minor quantity of TiO_2 is lost to the solution during leaching, as the acid leach filtrate solids contain 2.18 weight.% TiO_2.

TiO_2 content of the acid leach residue has been upgraded while CaO remains the major impurity present.

$$Na_{1.74}Mg_{0.79}Al_{0.15}Si_{1.06}O_4 + nHCl \rightarrow nNaCl + nMgCl_2 + nAlCl_3 + nH_4SiO_4 \tag{7.10}$$

$$Fe + 2HCl + 0.5O_2(g) \rightarrow FeCl_2 + H_2O \tag{7.11}$$

Table 7.10 Chemical composition of acid leach solids (AL-S) and dried acid leach solution solids (AL SS).

Weight.%	**Fe_2O_3**	**TiO_2**	**V_2O_5**	**CaO**	**Al_2O_3**	**Na_2O**	**MgO**	**SiO_2**	**SO_3**	**MnO**	**Cl**	**Cr_2O_3**
AL-S	2.44	46.04	0.78	23.80	4.66	5.08	2.96	12.30	0.27	0.26	1.18	0.22
AL- SS	2.71	2.18	0.04	0.67	12.22	19.69	11.27	26.51	0.54	0.60	23.58	-

7.2.4 Sodium bisulphate roasting and water leaching of acid leach solids

$CaTiO_3$ is a difficult natural mineral to breakdown to its constituent oxides and requires an intensive treatment, as it was demonstrated with T1 material. The breakdown of $CaTiO_3$-rich was feasible by reaction with $NaHSO_4$ (see equation 7.3) at 973 K in air for 2 hrs in a furnace. However, the calcium oxide present in the T2 was greater than in the T1, whereas the iron oxide content was lower. During water leaching of the roasted residue ferrous sulphate was added to the solution in order to solubilise the $CaSO_4$. Table 7.11 shows that the final residue contained up to 85 weight.% TiO_2, primarily in the anatase form with minor amounts of rutile present, as seen in Figure 7.12.

Table 7.11 Chemical analysis of TiO_2 extracted from low-grade TiO_2 slag using $NaHSO_4$ roasting and water leaching.

Weight.%	**TiO_2**	**Fe_2O_3**	**V_2O_5**	**Na_2O**	**MgO**	**Al_2O_3**	**SiO_2**	**SO_3**	**Cl**	**CaO**	**Cr_2O_3**	**MnO**
	85.02	3.51	1.88	1.13	1.51	2.34	2.23	0.70	0.07	1.24	0.31	0.06

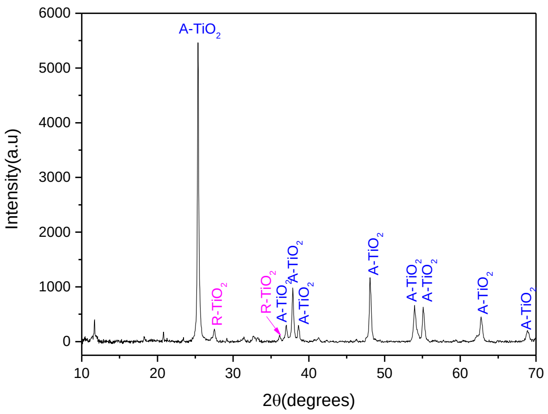

Figure 7.12 TiO_2 residue extracted from the low-grade TiO_2 slag using $NaHSO_4$ roasting followed by water leaching. A-TiO_2= anatase and R-TiO_2 = rutile.

7.2.5 Acid baking of low-grade TiO_2 slag acid leach solids

In order to produce high-grade TiO_2 and gypsum ($CaSO_4$) the $CaTiO_3$-rich residue was subjected to H_2SO_4 acid baking instead of $NaHSO_4$ roasting. The acid leach residue was baked at 473 K for 2 hours. Calcium sulphate and water- soluble titanium oxysulphate ($TiOSO_4$) were formed according to equation 7.12.

$$CaTiO_3 + H_2SO_4 \rightarrow CaSO_4 + TiOSO_4 \qquad 7.12$$

The acid baked residue was water leached to solubilise $TiOSO_4$ and leave behind a $CaSO_4$ rich residue (AB WL R), whose composition is presented in Table 7.12.

Table 7.12 Chemical composition of the TiO_2 hydrolysis precipitate (TiO_2 ppt) and acid baking-water leaching residue (AB WL R).

Weight.%	**Fe_2O_3**	**TiO_2**	**V_2O_5**	**CaO**	**Al_2O_3**	**Na_2O**	**MgO**	**SiO_2**	**SO_3**	**MnO**	**Cr_2O_3**
TiO_2 ppt	0.15	**88.23**	0.0	0.13	0.28	0.17	0.10	0.19	10.5		-
AB-WL-R	0.70	8.45	0.11	**27.03**	1.93	1.41	0.94	17.33	**41.65**	0.07	0.06

The $TiOSO_4$ in solution was hydrolysed by heating to 353 K (see equation 7.13) in order to recover TiO_2 (see Table 7.12) and regenerate dilute H_2SO_4.

$$TiOSO_4 + H_2O \rightarrow TiO_2 + H_2SO_4 \qquad 7.13$$

The TiO_2 precipitate was calcined at 1173 K to yield a synthetic rutile residue with purity greater than 95 weight.% TiO_2 (see Table 7.13). Figure 7.13 shows that the dominant phase present is rutile as the solids were heated well above the anatase-rutile transition temperature of 873 K [218].

Table 7.13 Chemical composition of synthetic rutile produced from S.A TiO_2 slag.

Weight.%	**Fe_2O_3**	**TiO_2**	**CaO**	**Al_2O_3**	**Na_2O**	**MgO**	**SiO_2**	**SO_3**
	0.50	97.98	0.18	0.51	0.22	0.15	0.42	0.12

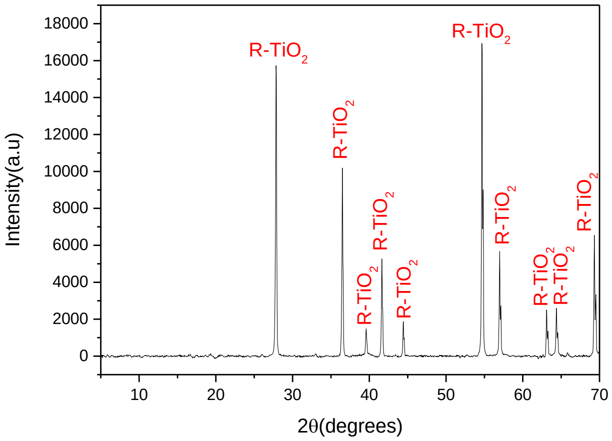

Figure 7.13 Synthetic rutile produced from S.A TiO_2 slag.

Figure 7.14a and Figure 7.14b show the TiO_2 hydrolysis precipitate and the calcined TiO_2 residue, respectively.

Figure 7.14 Photographic image of a) TiO_2 hydrolysis precipitate and b) synthetic rutile.

The treatment of T2 was validated by processing 4 kg of material for the recovery of 20 g of V_2O_5. A 400 g batch of synthetic rutile was also prepared during the same validation, of which a 100 g sample sent to Venator Materials PLC for independent analysis. Venator results are presented in Table 7.14 and a comparison of the existing high-grade TiO_2 feedstock is given. SCAPE refers to the sample sent for assaying.

Table 7.14 Venator Materials PLC analysis of SCAPE synthetic rutile compared to market synthetic rutile (SR Pr) and natural rutile (NR).

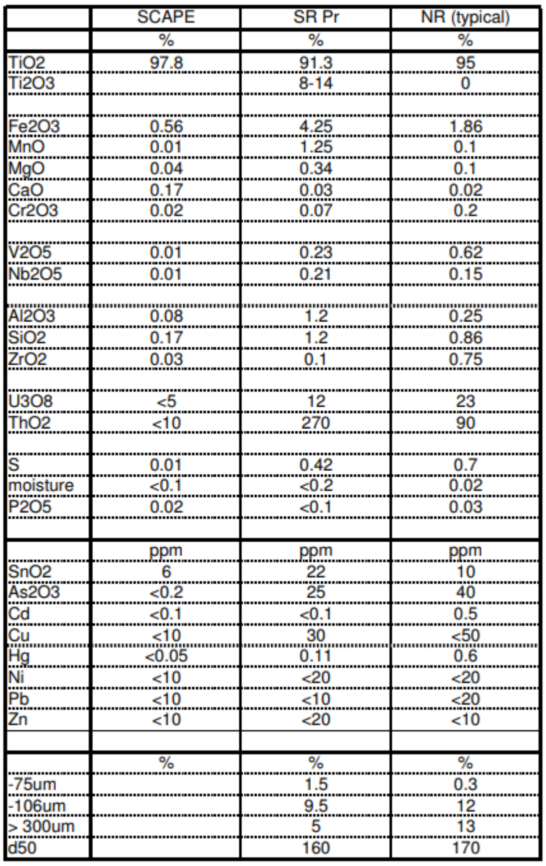

	SCAPE	SR Pr	NR (typical)
	%	%	%
TiO2	97.8	91.3	95
Ti2O3		8-14	0
Fe2O3	0.56	4.25	1.86
MnO	0.01	1.25	0.1
MgO	0.04	0.34	0.1
CaO	0.17	0.03	0.02
Cr2O3	0.02	0.07	0.2
V2O5	0.01	0.23	0.62
Nb2O5	0.01	0.21	0.15
Al2O3	0.08	1.2	0.25
SiO2	0.17	1.2	0.86
ZrO2	0.03	0.1	0.75
U3O8	<5	12	23
ThO2	<10	270	90
S	0.01	0.42	0.7
moisture	<0.1	<0.2	0.02
P2O5	0.02	<0.1	0.03
	ppm	ppm	ppm
SnO2	6	22	10
As2O3	<0.2	25	40
Cd	<0.1	<0.1	0.5
Cu	<10	30	<50
Hg	<0.05	0.11	0.6
Ni	<10	<20	<20
Pb	<10	<10	<20
Zn	<10	<20	<10
	%	%	%
-75um		1.5	0.3
-106um		9.5	12
> 300um		5	13
d50		160	170

7.3 Chapter summary

Magnetic separation of T1 sample subjected to alkali reduction in the rotary kiln yielded a non-magnetic fraction with up to 43 weight.% TiO_2 while 27 weight.% Fe_2O_3 also reported to the fraction. Phases observed in the RK non-magnetic fraction included sodium titanate, calcium titanate, sodium aluminosilicate, wustite and ulvöspinel. The presence of FeO and Fe_2TiO_4 explains the Fe_2O_3 content of the non-magnetic. The T1 magnetic fraction from the rotary kiln contained up to 91 % Fe which was melted to produce steel micro-alloyed with vanadium and a titania slag containing gangue phases.

0.5 M H_2SO_4 leaching was performed on the T1 non-magnetic fraction to give a 72 weight. % TiO_2 residue. T1 acid leach residue was roasted with $NaHSO_4$ followed by water leaching during which $CaSO_4$ dissolved in the acidic solution, owing to the presence of $FeSO_4$ and Na_2SO_4 that resulted in the formation of water-soluble sodium-calcium sulphate and sodium-iron sulphate complexes. A TiO_2 residue of up to 92 weight.% was obtained after water leaching.

T2 reduced product was water leached to dissolve water-soluble compounds including sodium vanadate. Selective precipitation of alumina (ca. 75 weight.%) was achieved by lowering the water leach solution to pH 8. Ammonium metavanadate was precipitated at pH 5 after the addition of ammonium sulphate, and H_2SO_4 to lower the pH. Ammonium metavanadate was calcined to give solids containing 93 weight.% V_2O_5. The residual T2 solids from water leaching were leached in 0.5 M HCl to yield a $CaTiO_3$-rich residue (46 weight.% TiO_2).

The calcium titanate residue was processed using two different techniques:

The first involved roasting the T2 residue with $NaHSO_4$ followed by water leaching. $FeSO_4$ was added during the water leaching step to ensure dissolution of $CaSO_4$, in order to yield an 86 weight.% TiO_2 residue.

The second technique used sulphuric acid baking of T2 forming a porous cake consisting of water-soluble $TiOSO_4$ and $CaSO_4$. Ambient temperature water leaching of the porous cake was carried out to dissolve $TiOSO_4$ and separate it from the $CaSO_4$-rich solid residue. The $TiOSO_4$ solution was hydrolysed to give a titanium dioxide hydrate precipitate. Calcination of the TiO_2 precipitate was performed to produce synthetic rutile with up to 97 weight.% TiO_2.

8 Mass and energy balance of iron-rich tailings and low-grade titanium dioxide slag processing

Blow flow diagrams outlining the processing of T1 and T2 are provided in chapter 8. Laboratory values were scaled-up to consider treatment 1000 kg of T1 or T2, with mass and energy balance results for key steps of materials treatment detailed in the chapter. Detailed mass and energy balance calculations are presented in Appendix C.

8.1 Iron-rich tailings mass and energy balance

Reductive alkali roasting of T1 (step 1)

A mixture comprised of 1000 kg T1, 200 kg Na_2CO_3 and 290 kg coal is charged into a rotary kiln operating at 1223 K. On an industrial-scale, reduction would be carried out in a direct-fired kiln where the freeboard is an oxidising atmosphere and the bed is under a reducing atmosphere due to the Boudouard reaction, similar to direct reduction of iron performed in a rotary kiln [197]. 994 kg of reduced sample exit the kiln along with 496 kg off-gas composed of 97 mol. % CO. 1034.66 k Wh is required for reduction in a rotary kiln at 1223 K, as shown in Table 8.1.

Table 8.1 Mass and energy balance for reductive alkali roasting of T1.

IN				**OUT**			
	Temperature (K)	Mass (kg)	Energy (kWh)		Temperature (K)	Mass (kg)	Energy (kWh)
T1	298	1000	-2021.39	Reduced sample	1223	994.00	-1484.81
Coal	298	290	-320.84	Off-gas	998	496.00	-415.46
Na_2CO_3	298	200	--592.71				
TOTAL		**1490**	**-2934.92**			**1490**	**-1900.27**
				Energy demand (Q)			**1034.66**

Rotary kiln off gas combustion (step 2)

Combustion of the CO-rich off gas from the rotary kiln releases -1237.11 kWh of energy. Assuming 50% heat loss, - 619 kW h can be recovered helping to lower overall process energy requirements. The combusted stream containing 763.40 kg of CO_2 that can be directed into water leach solution for use in V_2O_5 and Al_2O_3 extraction, by lowering the solution pH.

Table 8.2 Mass and energy balance for rotary kiln off-gas combustion for T1 material.

IN				**OUT**			
	Temperature (K)	Mass (kg)	Energy (kWh)		Temperature (K)	Mass (kg)	Energy (kWh)
Off - gas	998	496.04	-415.48	CO_2	998	763.40	-1736.90
Air	298	1720.28	0.00	N_2	998	1401.14	298.28
				H_2O	998	66.03	-219.77
				H_2SO_4	998	1.89	-3.50
				SO_3(g)	998	0.25	-0.90
TOTAL		**2215.87**	**-415.48**			**2215.89**	**-1663.19**
				Energy demand (Q)			**-1237.11**

Cooling of reduced sample (Step 3)

Decreasing the temperature of reduced samples exiting the rotary kiln is necessary to prevent re-oxidation of metallic iron upon exposure to open atmosphere [197]. The temperature of reduced solids exiting the kiln at 1223 K is lowered to 363 K in an indirectly-cooled rotary cooler, where water is applied to the outside shell of the cooler. 3600 L of warm water generated from the cooler can be utilised in steps 4 and 5. Overall -1.36 kW h would be generated while lowering the reduced sample temperature to 353 K.

Table 8.3 Mass and energy balance for rotary cooling of reduced solids.

IN				**OUT**			
	Temperature (K)	Mass (kg)	Energy (kWh)		Temperature (K)	Mass (kg)	Energy (kWh)
Reduced sample	1223	994.00	-1484.81	Reduced sample	353	994.00	-1715.86
H_2O	298	3600	-17628.94	H_2O	353	3600	-15636.36
TOTAL		**4594**	**-17350.86**			**4594**	**-17352.22**
				Energy demand (Q)			**-1.36**

Magnetic separation (Step 4) and water leaching of non-magnetic fraction (Step 5)

The 994 kg reduced sample is subjected to wet magnetic separation to produce a 553.26 kg Fe-rich magnetic fraction and a Ti-rich non-magnetic fraction, with sodium vanadate and sodium aluminate reporting to the solution. Water leaching of the non-magnetic fraction is performed to maximise vanadium oxide and alkali recovery and give a 191.79 kg non-magnetic fraction and a 4275.95 kg solution, as seen in Table 8.4. 3600 L of water heated in step 3 is utilised along with 400 L of make-up water for steps 4 and 5. The solution is kept for recovery of V_2O_5, Al_2O_3 and alkali salts. -68.72 k Wh is the amount of energy given off during the step 4 and step 5.

Table 8.4 Mass and energy balance of magnetic separation and water leaching of non-magnetic fraction.

IN				**OUT**			
	Temperature (K)	Mass (kg)	Energy (kWh)		Temperature (K)	Mass (kg)	Energy (kWh)
Reduced sample	353	994.00	-1713.50	Magnetic	353	553.26	-343.37
H_2O	353	3600	-15636.36	Non-magnetic	353	191.79	-500.57
H_2O	298	400	.1762.89	Solution	353	4275.98	-18314.11
TOTAL		**5023.18**	**-19114.85**			**5023.0**	**-19158.05**
				Energy demand (Q)			**-68.72**

Melting of magnetic fraction (Step 6)

The 553.26 kg magnetic fraction is melted in the presence of 6.4 kg graphite at 1723 K producing 450.16 kg steel containing vanadium and a 90.83 kg titania slag material. As indicated in Table 8.5, 200.73 kW h is needed form the melting step.

Table 8.5 Mass and energy balance for smelting of magnetic fraction.

IN				**OUT**			
	Temperature (K)	Mass (kg)	Energy (kWh)		Temperature (K)	Mass (kg)	Energy (kWh)
Magnetic	298	553.18	-347.55	Steel	1723	450.16	126.21
C	298	6.4	0	Slag	1723	90.83	-259.56
				Off gas	1500	18.64	-13.26
TOTAL		**559.58**	**-347.55**			**559.58**	**-146.61**
				Energy demand (Q)			**200.73**

Acid leaching of water leached solids (Step 7)

191.97 kg non-magnetic fraction is mixed with 90.93 kg of titania slag (from step 6). The combined residues are leached with 151 kg H_2SO_4 sulphuric in 3000 L of water at 313 K to yield a 185.25 kg acid leach residue containing carbon. -16.76 k Wh of energy is released during the acid leaching step (see Table 8.6). The 3248.58 kg acid leach solution contains dissolved gangue phases and sodium sulphate

Table 8.6 Mass and energy balance for acid leaching of non-magnetic fraction and titania slag (from step 6).

IN				**OUT**			
	Temperature (K)	Mass (kg)	Energy (kWh)		Temperature (K)	Mass (kg)	Energy (kWh)
Non magnetic	298	191.97	-502.04	Acid leached residue with C	313	185.25	-458.12
Slag	298	90.93	-297.04	Acid leach solution	313	3248.58	-13927.40
H_2SO_4	298	150.94	-347.98				
H_2O	298	3000	-132221.71				
TOTAL		**3433.83**	**-14368.77**			**-3433.83**	**-14385.53**
				Energy demand (Q)			**-16.76**

Carbon removal from acid leach residue (Step 8)

42.13 kg of excess carbon in the acid leach residue is removed by roasting with a controlled amount of air to produce a CO-rich gas which can be combusted for energy recovery. As indicated in Table 8.7, -27.27 k Wh is released during the controlled roasting process due to the exothermic nature of the reaction [35]. Combustion of the CO-rich off gas would generate -183.57 k Wh, however, after assuming 50 % heat loss the heat recovered would be -91.79 k Wh.

Table 8.7 Mass and energy balance for controlled roasting of acid leach residue containing carbon.

IN				**OUT**			
	Temperature (K)	Mass (kg)	Energy (kWh)		Temperature (K)	Mass (kg)	Energy (kWh)
Acid leached residue with C	298	185.17	-458.36	Acid leached residue	1073	143.01	-432.81
Air	298	290.27	0	Off - gas	850	332.43	-52.82
TOTAL		**475.44**	**-458.36**		**3433.83**	**475.44**	**-485.63**
				Energy demand (Q)			**-27.27**

Sodium bisulphate roasting of acid leach residue (Step 9)

143.01 kg acid leach residue is roasted in air with 148 kg sodium bisulphate ($NaHSO_4$) requiring 68.77 kW h, as seen in Table 8.8. Off gas containing 9.61 kg sulphur trioxide would be sent to a scrubber to remove harmful the gas.

Table 8.8 Mass and energy balance for $NaHSO_4$ roasting of acid leach residue.

IN				**OUT**			
	Temperature (K)	Mass (kg)	Energy (kWh)		Temperature (K)	Mass (kg)	Energy (kWh)
Acid leached residue	298	143.01	-458.36	Roast residue	923	270.16	-737.64
$NaHSO_4$	298	148	-385.69	Off gas	673	20.71	-55.57
Air	298	165.40	0	Air	673	165.56	17.94
TOTAL		**456.42**	**-844.04**			**456.42**	**-775.28**
				Energy demand (Q)			**68.77**

Water leaching of roast residue (Step 10)

270.16 kg of hot $NaHSO_4$ roasted residue is fed into a leaching tank containing 1000 L of water to solubilise sulphated impurities, giving a 94.56 kg 92 weight.% TiO_2 residue after water leaching. 17.88 kg TiO_2 is dissolved in solution owing to the formation of $TiOSO_4$, however, TiO_2 could be recovered by hydrolysis of the solution. 14.90 k Wh is needed for the hot water leaching.

Table 8.9 Mass and energy balance for water leaching of roasted residue.

IN				**OUT**			
	Temperature (K)	Mass (kg)	Energy (kWh)		Temperature (K)	Mass (kg)	Energy (kWh)
Roast residue	923	270.16	-737.64	TiO_2 residue	353	94.56	-310.63
H_2O	298	1000	-4407.24	Water leach solution	353	1176.41	-4819.63
TOTAL		**1270.27**	**-5145.17**			**1270.27**	**-5130.27**
				Energy demand (Q)			**14.90**

Extraction of metallic values from T1

Extraction of TiO_2 and V_2O_5 percentage extraction have been calculated based on the mass balance results. TiO_2 extraction is equal to 74 %, where the loss of 15 % of the TiO_2 during step 10 reduces TiO_2 recovery to a meaningful extent. 52 % of V_2O_5 was extracted from T1 during processing, including vanadium alloyed in steel.

Table 8.10 Percentage extraction of TiO_2 and V_2O_5.

	Extraction (%)
TiO_2	74
V_2O_5	52

Block flow diagram for processing of T1 material is given in Figure 8.1. Mass and energy balance results are provided for the key steps.

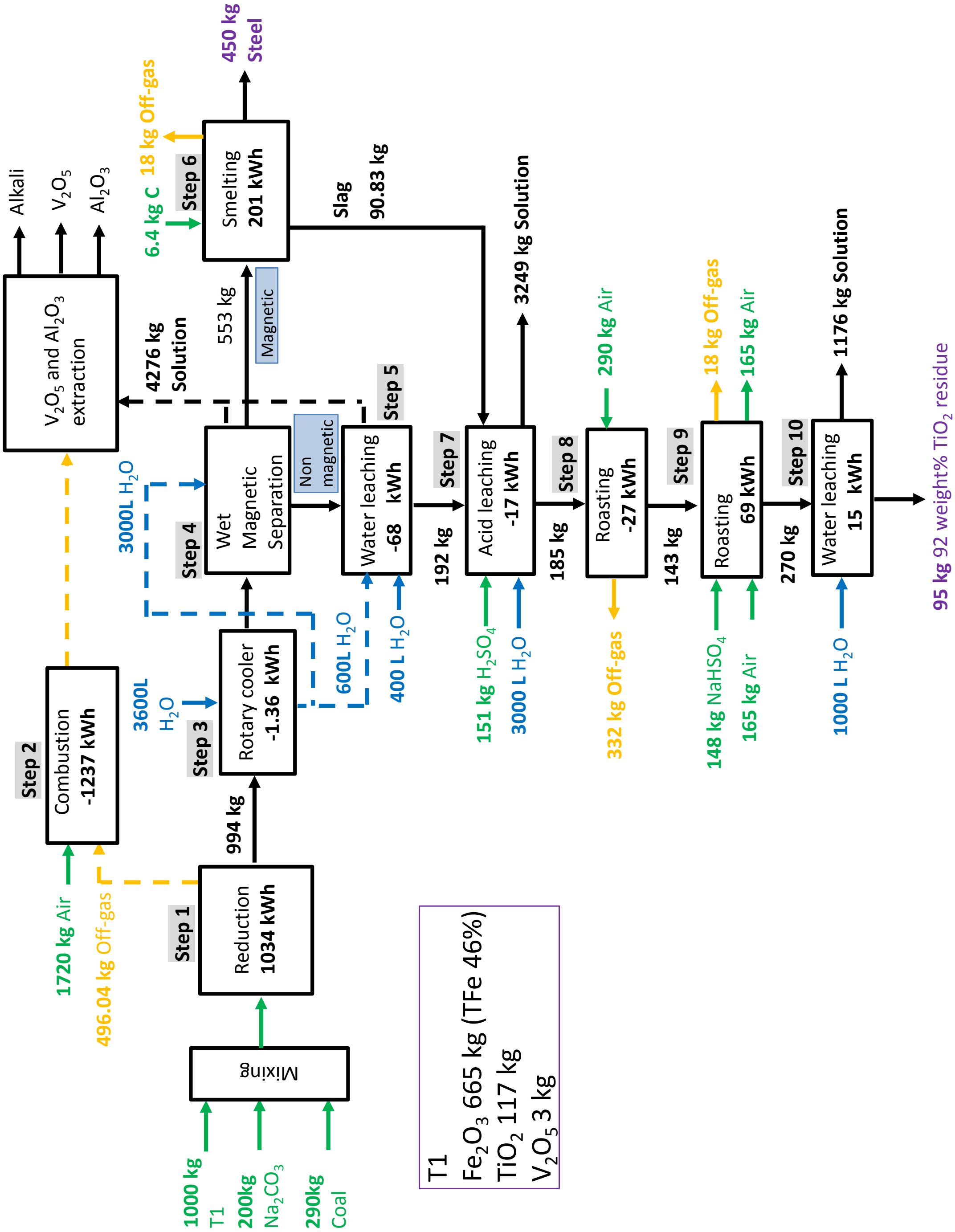

Figure 8.1 Block flow diagram for T1 processing with mass and energy balance data

8.2 Low-grade titanium dioxide slag mass and energy balance

Reductive alkali roasting of T2 (step 1)

The kiln feed made up of 1000 kg of T2 material, 450 kg of Na_2CO_3 and 67 kg of coal is fed into a rotary kiln at 298 K. The reduced sample mass of 1257.58 kg exits the kiln at 1323 K and the 259.50 kg off-gas, composed of 77 mol.% CO and 21 mol.% CO_2 [48], is assumed to exit the kiln at 1098 K. The energy demand for alkali reductive roasting step in the kiln is 674.73 kWh, as shown in summary in Table 8.11.

Table 8.11 Mass and energy balance for reductive alkali roasting of T2.

IN				**OUT**			
	Temperature (K)	Mass (kg)	Energy (kWh)		Temperature (K)	Mass (kg)	Energy (kWh)
T2	298	1000.38	-3515.51	Reduced sample	1323	1257.58	-3948.52
Coal	298	450	-73.80	Off-gas	1098	259.50	-299.65
Na_2CO_3	298	66.7	-1333.59				
TOTAL		**1517.08**	**-4922.90**			**1516.08**	**-4248.17**
				Energy demand (Q)			**674.73**

Rotary kiln off gas combustion (step 2)

The rotary kiln off-gas contains a high percentage of carbon monoxide which when combusted forms carbon dioxide and releases a significant amount of energy that can reduce the overall energy demand of the process. The 259.50 kg off gas can be combusted with 531.60 kg air and the resulting 818.1 kg CO_2 rich stream passed through a heat exchanger to recover the energy. The theoretical energy recovered by the combustion of the off gas stream is -466.97 kWh. Even assuming 50% heat loss the total energy recovered would be -233.49 kWh, as reported in Table 8.12.

Table 8.12 Mass and energy balance for rotary kiln off-gas combustion for T2 material.

IN				**OUT**			
	Temperature (K)	Mass (kg)	Energy (kWh)		Temperature (K)	Mass (kg)	Energy (kWh)
Off - gas	1098	259.50	-299.65	CO_2	1098	369.15	-826.46
Air	298	531.60	0.00	N_2	1098	407.73	106.23
				H_2O	1098	14.21	-46.39
TOTAL		**817.13**	**-299.65**			**817.13**	**-766.62**
				Energy demand (Q)			**-466.97**

Indirect cooling of T2 reduced solids (step 2)

Indirect cooling of the reduced T2 solids provides 5750 L of heated water for subsequent leaching stages, realising -7.70 kW h of energy (see Table 8.13), likely given off as steam.

Table 8.13 Mass and energy balance for indirect cooling of reduced T2 material.

IN				**OUT**			
	Temperature (K)	Mass (kg)	Energy (kWh)		Temperature (K)	Mass (kg)	Energy (kWh)
Reduced sample	1323	1257.58	-3948.52	Reduced sample	353	1257.58	-4322.98
Water	298	5750	-25341.60	Water	353	5750	-24974.74
TOTAL		**7007.49**	**-29290.02**			**7007.49**	**-29297.72**
				Energy demand (Q)			**-7.70**

Water leaching of reduced sample (step 4)

The 1257.58 kg reduced sample is then leached with 10 kg of Na_2CO_3 in 4800 kg of hot water (353 K) for two hours solubilising sodium vanadate, sodium aluminate and sodium silicate. The hot solids from the kiln could not be directly added to the water leaching tank so they would have to be cooled down first. On a large-scale the solids would pass through an indirect rotary cooler that is cooled by the flow of water on the outside of the shell. Adjusting the water flow rate for the rotary cooler would allow the temperature of the water to be raised to 353 K and then used during the water leaching stage. After water leaching solid-liquid separation is carried out, with the solids sent to step 10 and the solution taken to step 5. The energy balance calculations given in Table 8.14 indicate the release of -21.23 kWh, likely due to the formation of steam.

Table 8.14 Mass and energy balance water leaching of T2 reduced sample.

IN				OUT			
	Temperature (K)	Mass (kg)	Energy (kWh)		Temperature (K)	Mass (kg)	Energy (kWh)
Reduced sample	1323	1257.58	-4323.17	Water leach residue	353	1164.27	-4060.22
Water	353	4800	-20848.48	Water leach solution	353	4903.31	-21162.30
Na_2CO_3	298	10	-29.64				
TOTAL		**6067.57**	**-25201.29**			**6067.60**	**-25222.52**
				Energy demand (Q)			**-21.23**

Concentration and pH adjustment of water leaching solution (step 5)

The 4903.31 kg of water leach solution is transferred to a reactor where 3214.40 kg of water is evaporated in order to increase the sodium vanadate concentration. The pH of the concentrated solution is reduced from 12.34 to 8.5 by sparging in CO_2 gas. The evaporation of such a significant quantity of water is an energy intensive step which requires 1833.72 kWh. The combusted off-gas (step 2) could be scrubbed through the solution, similar to a system developed for Windimurra Vanadium by Proxawater [219]. This 818.10 kg CO_2-rich gas from the rotary kiln off-gas combustion could be utilised to adjust the pH of the solution. The decrease in pH causes the precipitation of 8.14 kg of $Al_2O_3.H_2O$ and 56.70 kg of Na_2CO_3 from the solution. The solids would be filtered before the solution is transferred to step 5.

Table 8.15 Mass and energy balance for concentration and pH adjustment of water leach solution.

IN				OUT			
	Temperature (K)	Mass (kg)	Energy (kWh)		Temperature (K)	Mass (kg)	Energy (kWh)
Water leach solution	353	4903.31	-21140.12	Concentrated solution pH 8.5	373	1998.42	-8004.70
CO_2	1098	369.15	-826.46	Water vapour	373	3214.40	-11872.82
N_2	1098	407.73	106.23	CO_2	373	9.00	-22.19
Water vapour	1098	14.21	-46.39	N_2	373	407.73	8.84
				Al_2O_3	373	8.14	-37.00
				Na_2CO_3	373	56.7	-166.75
TOTAL		**5720.44**	**-21906.74**			**5720.44**	**-20073.02**
				Energy demand (Q)			**1833.72**

Ammonium metavanadate precipitation (step 6)

The concentration is cooled from 373 K to room temperature. 18.4 kg sulphuric acid is added to the solution to decrease the pH value to 5. 26 kg ammonium sulphate is added to the solution and agitated to form 4.90 kg ammonium metavanadate (AMV), which precipitates from the solution. The addition of H_2SO_4 results in the release of CO_2 from the solution. This step requires -144.06 k Wh of energy would need to be removed from the system to decrease the temperature and facilitate AMV precipitation.

Table 8.16 Mass and energy balance for ammonium metavanadate precipitation.

IN				OUT			
	Temperature (K)	Mass (kg)	Energy (kWh)		Temperature (K)	Mass (kg)	Energy (kWh)
Concentrated solution pH 8.5	373	2000.15	-8166.12	Concentrated solution pH 5	298	2029.70	-8386.64
H_2SO_4	298	18.4	-42.42	AMV	298	4.90	-12.25
$(NH_4)_2SO_4$	298	26	-64.54	CO_2	298	7.35	-18.25
TOTAL		**2044.55**	**-8273.08**			**2041.95**	**-8417.15**
				Energy demand (Q)			**-144.06**

Condensation of water vapour (step 7)

The water vapour given off during the evaporation process in step 4 can be condensed. Condensation of the steam would generate -2044.60 kWh. Condensing the water vapour would reduce overall water consumption as the condensate could be recycled to step 2 and the energy released would reduce the overall process energy demand.

Table 8.17 Mass and energy balance for condensation of water vapour.

IN				OUT			
	Temperature (K)	Mass (kg)	Energy (kWh)		Temperature (K)	Mass (kg)	Energy (kWh)
Water vapour	373	3214.40	-11860.04	Water	368	3214.4	-13904.64
TOTAL			**-11860.04**				**-13904.64**
				Energy demand (Q)			**-2044.60**

De-ammoniation of AMV (step 8)

The AMV precipitate is filtered and calcined at 723 K requiring 2.65 kW h to produce the vanadium oxide solids, giving off 1.09 kg of ammonia (NH_3) and a minor amount of H_2O as an off gas (see Table 8.18). Scrubbing the off-gas would be necessary.

Table 8.18 Mass and energy balance for condensation of water vapour.

IN				OUT			
	Temperature (K)	Mass (kg)	Energy (kWh)		Temperature (K)	Mass (kg)	Energy (kWh)
AMV	1323	5.19	-12.87	V_2O_5	333	4.38	-9.85
Solids	298	0.28	-0.59	Off-gas	723	1.09	-0.37
TOTAL		**5.18**	**-12.87**			**5.18**	**-10.22**
				Energy demand (Q)			**2.65**

Evaporation (step 9)

The remaining solution could be pumped to a tailings dam to be allowed to naturally evaporate so that sodium sulphate could be recovered. The XRF results indicates that between 1 weight.% to 2 weight.% V_2O_5 is still present in the alkali salt and showing that further optimisation of vanadium oxide recovery is necessary.

Acid leaching of water leach residue (step 10)

The 1164.27 kg water leach residue from step 2 is acid leached using 7751.78 L of water and 394kg of 37% hydrochloric acid (HCl) aqueous solution in order to dissolve the gangue phases, leaving behind a $CaTiO_3$-rich residue. 950 L of 353 K water from the indirect cooling of the reduced sample is added to 6408 L of make-up water. The acid leaching step, utilising 8000 L of water at 313 K in total, would release -8.96 kW h as shown in Table 8.19.

Table 8.19 Mass and energy balance for acid leaching of water leached T2 solids**.**

IN				**OUT**			
	Temperature (K)	Mass (kg)	Energy (kWh)		Temperature (K)	Mass (kg)	Energy (kWh)
Water leach residue	333	1164.27	-4065.82	Acid leach residue	313	687.90	-2328.41
Water	298	6408.00	-28241.56	Acid leach solution	313	8477.25	-35712.26
Water	353	950.00	-4126.26				
37% HCl	298	394.00	-1599.26	Off-gas	313	1.2	-1.20
Air	25	1.55	0				
TOTAL		**9166.83**	**-38032.90**			**9166.84**	**-38041.86**
				Energy demand (Q)			**-8.96**

Production of synthetic rutile and calcium sulphate residue (Steps 11 – 14)

The 572 kg acid leach residue is slurred with 752 kg of 98% H_2SO_4. The acid leach residue contains moisture that reacts exothermically with H_2SO_4, evolving an off-gas that contains water vapour and SO_2/SO_3 gas that would need to be scrubbed to form sulphuric acid. The slurried mixture is placed in the furnace at 473 K for 2.5 hours to yield acid baked residue of a 1200.16 kg. During the acid baking process alkali earth sulphates and water- soluble titanium oxysulphate ($TiOSO_4$) are formed. 123.84 kg off gas containing SO_2/SO_3 and H_2O is given off as the reaction proceeds. The off gas could be combined with the early SO_2/SO_3 gas to regenerate H_2SO_4. The overall acid consumption (both HCl and H_2SO_4) for T2 processing described in this report is less than either the Avertana or H_2SO_4-based EHSV process [58, 59]. The lower acid consumption is due to the formation of acid-soluble phases during reductive alkali roasting. Removal of significant quantities of MgO and Al_2O_3 during HCl leaching results in less H_2SO_4 being required during acid baking, as these oxides would readily react with sulphuric acid.

Table 8.20 Mass balance of acid baking of acid leach residue.

IN			**OUT**		
	Temperature (K)	Mass (kg)		Temperature (K)	Mass (kg)
Acid leach residue	313	572	Acid baked residue	473	1200.16
98% sulphuric acid	313	752	Off-gas	473	123.84
TOTAL		**1324.00**	**TOTAL**		**1324.00**

The 1200.16 kg porous cake is leached with 5000 L of water at room temperature for 1 hour to solubilise $TiOSO_4$ and leave behind a $CaSO_4$ rich residue. Solid-liquid separation is carried out to separate the 433 kg solid $CaSO_4$- residue from the 3966.92 kg solution containing $TiOSO_4$ and $FeSO_4$.

Table 8.21 Mass balance of water leaching of acid baked residue.

IN			**OUT**		
	Temperature (K)	Mass (kg)		Temperature (K)	Mass (kg)
Acid baked residue	298	1200.16	$TiOSO_4$ solution	298	3966.92
Water	298	5000	$CaSO_4$ residue	298	433.24
TOTAL		**6200.16**	**TOTAL**		**6200.16**

The $TiOSO_4$ in solution is hydrolysed by heating to 353K in order to precipitate 194.49kg of $TiO_2.H_2O$ precipitate and form dilute H_2SO_4.

Table 8.22 Mass balance of water leaching of acid baked residue.

IN			**OUT**		
	Temperature (K)	Mass (kg)		Temperature (K)	Mass (kg)
$TiOSO_4$ solution	298	3966.92	TiO_2 precipitate	353	194.49
			Solution	353	3772.43
TOTAL		**3966.92**	**TOTAL**		**3966.92**

The $TiO_2.H_2O$ precipitates with sulphate ions present. Calcination in an indirect-fired rotary kiln at 1173 K yields 144 kg 98% synthetic rutile and evolves 50.49 kg off gas containing SO_3 and H_2O, with the off-gas being scrubbed to regenerate sulphuric acid.

Table 8.23 Mass balance of calcination of titanium dioxide precipitate.

IN			OUT		
	Temperature (K)	Mass (kg)		Temperature (K)	Mass (kg)
TiO_2 precipitate	353	194.49	Synthetic rutile	1173	144.00
			Off gas	948	50.49
TOTAL		**194.49**	**TOTAL**		194.49

The thermodynamic data for the $TiOSO_4$ phase was not available. Therefore, a simplified energy balance was carried out over steps 11 and 14. The calculations indicate that 307.62 k Wh of energy is required. However, these steps require more rigorous analysis to produce a more accurate result

Recovery of metallic values

Based on the mass balance data detailed above the calculated extraction of vanadium pentoxide and titanium dioxide from the T2 is presented in Table 8.24.

Table 8.24 Percentage extraction of TiO_2 and V_2O_5.

	Extraction (%)
TiO_2	85
V_2O_5	53

The block flow diagram for T2 processing presented in Figure 8.2 details the mass and energy balances for key process steps.

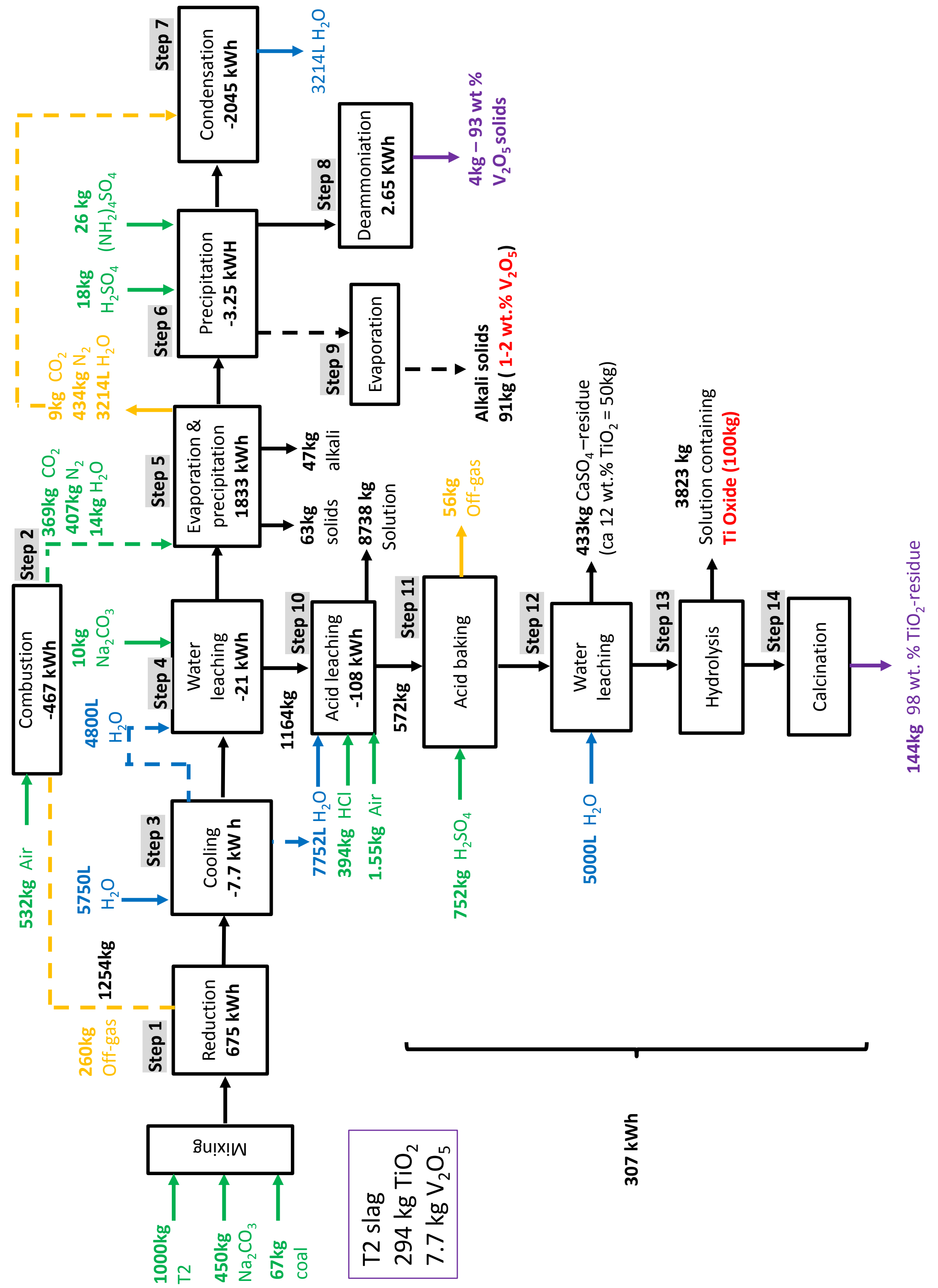

Figure 8.2 Block flow diagram for T2 processing including mass and energy balance data.

8.3 Chapter summary

The energy demand on a rotary kiln to treat 1000 kg of T1 is 1034 kW h compared to the lower value of 674 kW h to treat one tonne of T2 material in a rotary kiln. However, a greater amount of energy is released during combustion of rotary kiln off-gas from T1 processing at -1247 kW h. By comparison, combustion of the CO-rich off gas from T2 treatment generates -473 kW h. After assuming a 50 % heat loss, -623 kW h can be recovered for T1 and -236 kW h for T2.

Rotary cooling of T1 reduced solids to lower the solids temperature and prevent re-oxidation provides 3600 L of hot water (353 K) for wet magnetic separation and water leaching steps. Wet magnetic separation and water leaching of non-magnetic fractions yields 553 kg magnetics for smelting, 192 kg non magnetics and a 4276 kg solution containing V_2O_5, Al_2O_3 and alkali salts.

Melting the T1 magnetic fraction at 1723 K requires 200 kW h to produce 450 kg of steel and 91 kg of titania slag. H_2SO_4 leaching of combined non-magnetic and slag releases – 17 kW h. Excess carbon present in the T1 acid leach residue is removed by roasting with a controlled amount of air to produce a CO-rich off gas, generating – 27 kW h in the process. $NaHSO_4$ roasting at 923 K of the T1 acid leached solids without carbon requires 69 kW h. Hot water leaching of the T1 roasted solids to remove sulphated impurities, giving a 94.56 kg TiO_2 residue requires 15 kW h.

Water leaching of the hot T2 solids to solubilise sodium vanadate releases -67 kW h. Carbon dioxide produced during combustion of the kiln off-gas can be used to lower the pH of the water leach solution precipitating alumina in the process and increasing the vanadium concentration by water evaporation. 1952 kW h of energy is required to remove the necessary amount of water. Condensation of the water vapour releases – 2001 kW h, before assuming 50% heat loss.

AMV precipitation from T2 water leach solution requires 0.30 kW h while -2.58 kW h is released during de-ammoniation of AMV to yield V_2O_5 solids.

The solid T2 water leach residue is then treated with hydrochloric acid for leaching by dissolving the gangue phases and iron, upgrading the titanium dioxide content to approximately 50 weight.%. The energy balance for the acid leaching stage shows that this step would consume 58 kW h.

Owing to a lack of thermodynamic data for $TiOSO_4$, a simplified energy balance was carried out over steps 9 and 13 which indicated 263.67 kWh of energy is required.

9 Conclusions and future work

9.1 Conclusions

The objective of this thesis was to study reductive alkali roasting for purposes of recovering titanium dioxide, vanadium pentoxide, aluminium oxide and iron from waste materials produced during titanomagnetite concentrate processing.

Phase characterisation

1. XRPD analysis of titaniferous magnetite showed that magnetite, ilmenite and ulvöspinel were the major phases present and microstructure investigations indicated that V ions were dissolved in the magnetite matrix. In comparison, hematite, ilmenite and magnetite were observed in the T1 XRPD patterns.
2. SEM analysis revealed that a minor amount of vanadium was dissolved in the $FeTiO_3$-Fe_2O_3 solid solution while being enriched in sodium aluminosilicate complexes with lower Al content, whereas vanadium was absent in sodium aluminosilicates with a higher aluminium content.
3. TiO_2 in T2 was disseminated in the slag matrix and present as karooite and perovskite. Vanadium ions were dissolved in Mg_2TiO_5 and refractory $MgAl_2O_4$, occupying the octahedral sites. Vanadium was observed in metallic iron particles entrained in the slag during the previous processing.

Phase transformation of titaniferous magnetite

1. For isothermal experiments in argon and air atmospheres there was broad agreement between the experimental results in Figure 4.14a and Figure 4.14b with the thermodynamic predictions in Figure 4.17 and Figure 4.18. For example, after heating at 1273 K the main phases present after thermal treatment were Fe_2O_3, $FeTiO_3$ and Fe_2TiO_5 at 973K which agreed with the predominance area diagram that showed Fe_2O_3 and Fe_2TiO_5 co-exist in the same phase field at this temperature.
2. Microstructure for isothermal treatment in air and argon shown in Figure 4.19a and Figure 4.19b, respectively, highlighted that the titaniferous magnetite underwent spinodal decomposition in both atmospheres. In air atmosphere, the sample appeared to be more homogenous with finer grains. It was evident that

high temperature oxidation fractured that particle, giving it a more porous nature. Figure 4.19b showed that three distinct zones: top ; middle ; and bottom were formed during heating in inert atmosphere. The bottom zone had a dense morphology. The middle zone had fine interwoven grains that suggested the region was an interface between the bottom and top zone. The top zone was constituted of coarse grains that demonstrated sinusoidal behaviour.

3. The finer grains observed in the Figure 4.19a compared to Figure 4.19b may be due to the fact that the decomposition in air atmosphere is more thermodynamically favourable with a ΔG^{o} value of -168.64 kJ.mol^{-1} compared to -68.95 kJ.mol^{-1} for the treatment in argon atmosphere. Suggesting there is a greater barrier to diffusion in the inert atmosphere
4. The linescan data in Figure 4.20 illustrated the spinodal decomposition as there is unmixing between the Fe-rich areas and the Ti-rich areas, with V associated with Ti-rich regions.

Thermodynamic evaluation

1. Standard Gibbs free energy change plots versus temperature for the reduction of the iron-rich tailings of Figure 5.1 and Figure 5.2 showed that the addition of Na_2CO_3 during carbothermic reduction of ilmenite and ulvöspinel (see equations 5.7 and 5.8, respectively) made reactions more favourable than reduction in the absence of the alkali salt (see equations 5.1 and 5.3). The plots also indicated that there was a competing reaction for the formation of Na_2TiO_3 and $CaTiO_3$ with perovskite formation having a more negative standard Gibbs free energy change value below 1000 K.
2. Fe-Na-Ti-C-O multicomponent phase equilibria given in Figure 5.6a and Figure 5.6b showed that metallic iron and sodium titanate were able to co-exist in the same phase field of $\log_{10}P(CO)(atm) \approx -2.5$ and $-4 < \log_{10}P(CO_2)(atm) < -3$. However, at 1223 K there was no molten sodium titanate present, whereas at 1323 K the liquid phase was observed. Molten sodium titanate formation highlights the importance of a lower reduction temperature to avoid forming a liquid phase that would inhibit gaseous diffusion.

3. Carbothermic reduction of the S.A TM calcine using K_2CO_3 was more favourable than Na_2CO_3, according to the standard Gibbs free energy change plot in Figure 5.5.
4. The standard Gibbs free change energy plot in Figure 5.4 showed during reduction of T2 the formation of $CaTiO_3$ from reaction between Na_2CO_3 and $CaTiSiO_5$ was more favourable than the formation of Na_2TiO_3, according to reactions 5.21 and 5.22, respectively.
5. The predominance area diagram in Figure 5.9 of the Mg-Al-Na-C-O-V system at 1323 K illustrated that increasingly reducing atmosphere promotes decomposition $MgAl_2O_4$, which is necessary to liberate that V ions in the spinel lattice. It was observed that sodium vanadate co-exists with magnesium oxide and sodium aluminate at $\log_{10}P(CO)(atm) > -3.25$ and $-3.5 < \log_{10}P(CO_2)(atm) < -3$.

Carbothermic reduction of iron-rich tailings in the presence of alkali salts

1. Figure 6.1 showed that reduction of the iron-rich tailings in the absence of alkali salts results in a maximum %R of 82% at 1323 K, which is higher than what has been documented in the literature for reduction of titanomagnetites. As T1 is a waste product from oxidative alkali roasting it had been pre-oxidised, which has been reported to improve reduction of titanomagnetites. Furthermore, residual alkali remaining in the waste material may have enhanced the reduction.
2. Reaction model fitting using Interface, Ginstling and Brounshtein and Mixed-control models presented in Figure 6.4 to Figure 6.6 demonstrated that the reduction in the absence of alkali carbonate was under mixed-control, however, it was dominated by diffusion control. A single reaction regime was evident from the Arrhenius plot in Figure 6.7, where the apparent activation energy was shown to be 258 $kJ.mol^{-1}$; corresponding to C-CO_2 reaction for the gasification of activated charcoal.
3. TGA analysis demonstrated that a maximum %R of 97% was achieved at 1323 K, as shown in Figure 6.8, during reduction of T1 in the presence of Na_2CO_3. Model fitting revealed that the data fitted well for both the Interface and G.B models, meaning that the reaction was under mixed-control.
4. The electron micrograph (see Figure 6.14) of T1 sample reduced for 2 minutes and 5 minutes were analysed. After 2 iron grains were located at the core of the particle , indicating the reaction was likely under Interface-control during the initial stages of the reaction. However, after 5 minutes a product layer was

observed suggesting that reduction was under diffusion control as the reaction progresses,as gasous species would need to diffuse through the product layer.

5. XRPD patterns of T1 reduced in the presence of Na_2CO_3 (see Figure 6.9) confirmed the formation of metallic iron, sodium titanate and sodium aluminosilicate. Which showed that there was broad agreement between the experimental results and the thermodynamic predictions in chapter 5**,** where elemental iron and sodium titanate were observed to co-exist in the same phase field.
6. Microstructure analysis of the T1 sample subjected to reductive alkali roasting (see Figure 6.10) illustrated that the reaction proceeds via the shrinking-core model and showed the distinct segragation of Fe from Ti and V oxides, allowing for their separation in subsequent process steps.
7. The ln k vs 1/T plot displayed that two regimes occurred during carbothermic reduction of T1 in the presence of Na_2CO_3. Up to 1173 K the apparent activation energy was found to be 199 $kJ.mol^{-1}$, which correlates to the outward diffusion of O^{2-} ions. From 1173 K to 1323 K the calculated value was 130 $kJ.mol^{-1}$, comparing with the activation energy for the outward diffusion of Fe^{2+} ions. The diffusion is evidenced by the presence of iron at the periphery of the particle in Figure 5.17**.**
8. The proposed reaction mechanism involves the inward diffusion of Na^+ ions into the lattice where they are able to substitute with Fe^{2+} ions which diffuse towards the periphery of the particles forming a dense product layer of metallic iron. O^{2-} ions are removed by carbon during the course of the reaction.
9. Carbothermic reduction in the presence of K_2CO_3 was noted to be under- mixed control, as seen in the model fitting presented. The XRPD patterns of T1 reduced with K_2CO_3 (see Figure 6.18) showed that Fe was the dominant phase present along with minor peaks for potassium silicate and the ternary potassium iron titanate compounds, highlighting a lack of distinct phase segregation between Ti and Fe phases.
10. The apparent activation energy was 127 $kJ.mol^{-1}$, which corresponds to outward diffusion of Fe^{2+} ions. Presence of metallic Fe at the periphery of the reduced sample (shown in Figure 6.19) confirmed the outward diffusion of ferrous ions.
11. The apparent activation energy for carbothermic reduction of iron-rich tailings was lowered from 258.$kJ.mol^{-1}$ when carried out in the absence of alkali salts.

When using Na_2CO_3 there are two reaction regimes evident compared to the single reaction regimes observed in the absence of alkali carbonates and in the presence of K_2CO_3.

12. Alkali reductive roasting of the T1 was investigated in the rotary kiln and parameters such as: temperature; particle size; Na_2CO_3 weight ratio; argon gas flowrate and angle of inclination were studied to determine their impact on ring formation and extent of reduction for the waste material.
13. The general trend observed was that with each pass the percentage of input amount of material remaining in the tube decreased, as reacted material was less prone to adhering to the tube wall. After the first pass at 1273 K (see Figure 6.24) more than 50% of the feed remained in the tube, which was higher than experiments performed at 1173 K and 1223 K. The increased accumulation was to be expected as higher temperatures cause more accretion formation.
14. XRPD analysis in Figure 6.25 of accretion at the beginning of the hotzone in the alumina tube from the experiment carried out at 1173 K showed that material was partially reacted, as Fe, $Na_{0.75}Fe_{0.75}Ti_{0.25}O_2$, $NaAlSiO_4$ and FeO were present. However, peaks for the Fe_3O_4–Fe_2TiO_4 solid solution from the as-received T1 material were also present.
15. Visual inspection of the sample collected at 1223 K showed that there were grey and black particles, as seen in Figure 6.28. XRPD analysis (see Figure 6.29) of the black and grey particles showed that the grey particles were well reduced as elemental iron and sodium titanate were observed. In contrast, for the black particles Fe was the main phase present but there were peaks for FeO, $Na_{0.75}Fe_{0.75}Ti_{0.25}O_2$ and the Fe_3O_4 – Fe_2TiO_4 solid solution. A broad amorphous peak was present indicating significant amounts of carbon was present, which is to be expected as the black particles are activated carbon that had begun to react with T1 and Na_2CO_3.
16. It was evident that partially reacted black particles were located at the centre of partially formed grey particles, indicating that the black particles served as the nucleus of the growing nodules.
17. The SEM (see Figure 6.30a) of the black particles showed that core of the particle was largely unreacted, although a minor amount Na^+ ions had diffused to the centre of the particle. The ternary Na-Fe-Ti-O ternary complex was located at the interface of the Fe product layer at the periphery of the particle, demonstrating

that $Na_{0.75}Fe_{0.75}Ti_{0.25}O_2$ is an intermediate phase that forms due to incomplete carbothermic reduction in the presence of Na_2CO_3. Ternary compounds were observed by El Tawil et al [119] even though they carried out their experiments at 1473 K. Electron micrograph shown in Figure 6.30b confirmed that the grey particles were composed of metallic iron and sodium titanate.

18. When larger particles of T1 sized +500 µm -1180 µm were treated the percentage of material accumulating in the kiln tube appeared to remain constant (see Figure 6.31), owing to the increase in reaction surface area causing more Na_2CO_3 to melt as the feed entered the hotzone.
19. The decreased amount of Na_2CO_3 added to T1:Na_2CO_3:C 1:0.16:0.23 weight ratio resulted in the percentage of material remaining in the tube increasing in the second pass instead of decreasing (see Figure 6.33), as was observed for the 1:0.2:0.23 weight ratio. The photographic images of the two samples collected after the fourth pass (see Figure 6.34) showed larger nodules formed using the 1:0.2:23 weight ratio, suggesting that Na_2CO_3 plays a key role in promoting growth of the nodules that ultimately lower ring formation in subsequent passes.

Carbothermic reduction of low-grade TiO_2 slag in the presence of Na_2CO_3

1. TGA analysis of the T2:Na_2CO_3:C weight ratio of 1:0.45:0.04 experiments (see Figure 6.40) showed that the %R attained at 1323 K was 96%. The reaction model fitting indicated that the reaction was under mixed-control.
2. $CaTiO_3$, $Na_{1.74}Mg_{0.79}Al_{0.15}Si_{1.06}O_4$ and $Na_{0.75}Fe_{0.75}Ti_{0.25}O_2$ were the phases formed during the reduction, broadly agreeing with the phase equilibria calculations presented in Table 5.2.
3. The ln k vs 1/T plot derived from the model fitting data demonstrated that there was a single reaction regime and the apparent activation energy was 114 $kJ.mol^{-1}$. The value is consistent with the diffusion of Na^+ ions through soda-lime glass.
4. The maximum %R in the TGA apparatus for the S.A TiO_2 slag:Na_2CO_3:C weight ratio of 1:0.45:0.09 was 98% at 1323 K. Similar to the 1:0.45:0.04 weight ratio the reaction was under mixed-control. However, the apparent activation energy value of 184 $kJ.mol^{-1}$ was calculated from the ln vs 1/T plot (see Figure 6.54). The increased value corresponds to the gasification of activated charcoal when catalysed by alkali salts.
5. The activation energy has increased with an increase in carbon ratio and this is due to the gasification of carbon. In short, the C – CO_2 reaction dominated at the

higher carbon ratio. Furthermore, the contact areas between Na_2CO_3 and slag decreased as carbon concentration increased.

6. The suggested reaction mechanism involves the diffusion of Na_2O into the slag matrix where the basic oxide modifies the tetrahedral silicate structure. Na^+ ions replace Ca^{2+} ions to form ionic bonds with the silicate non-bridging and give the slag a partially ionic structure. Displaced Ca^{2+} results in the crystallisation of $CaTiO_3$, as seen in microstructure of alkali reduced T2 shown in Figure 6.44. Decomposition of the $MgAl_2O_4$ to $Na_2Al_2O_4$ and MgO results in these products being dissolved in the reacted slag matrix to form $Na_{1.74}Mg_{0.79}Al_{0.15}Si_{1.06}O_4$.
7. Varying the Na_2CO_3 addition by using the S.A TiO_2 slag:Na_2CO_3:C weight ratios of 1:0.35:0.09 and 1:0.35:0.09, 1:0.40:0.09 showed that the alkali carbonate was sufficient to decompose the slag matrix and promote formation of $CaTiO_3$ and $Na_{1.74}Mg_{0.79}Al_{0.15}Si_{1.06}O_4$ as seen in the XRPD pattern in Figure 6.57. However, $MgAl_2O_4$ was not fully decomposed at any of the ratios, as most of the Na^+ ions were consumed to breakdown the slag matrix.
8. The percentage of material remaining in the tube increased as the S.A TiO_2 slag particle size increased (see Figure 6.58). Slag particles sized +500µm -1180µm were only partially reacted seen in XRPD patterns and backscattered SEM images shown in Figure 6.59 and Figure 6.60, respectively. Microstructure (see Figure 6.61) revealed the formation of metallic iron within the slag matrix, likely from residual Fe_2TiO_4 from the original titanomagnetite.

Treatment of reduced samples

Treatment of reduced iron-rich tailings

1. Wet magnetic separation of the sample reduced in the rotary kiln at 1223 K yielded a magnetic fraction containing 91.7 weight.% Fe and 4 weight.% TiO_2. 43.7 weight.% TiO_2 was present in the non-magnetic fraction along with 23 weight.% Fe_2O_3. The high iron content is due to the presence of FeO, Fe_2TiO_4 $Na_{0.75}Fe_{0.75}Ti_{0.25}O_2$ phases which report to the non-magnetic fraction.
2. Evaluating the magnetic and non-magnetic fractions of the T1 samples reduced in the rotary kiln (see Table 7.2) showed that the non-magnetic fraction from the experiment at 1273 K contained more iron oxide than titanium dioxide. The presence of the FeO in the reduced sample (see Figure 6.27) explaining the

significant amount of iron oxide in the non-magnetic fraction. However, the corresponding magnetic fraction contained 88 weight.% iron.

3. Experiments carried out at 1223 K using the parameters described as sample B in Table 7.1 produced the highest grade of iron in the magnetic fraction at 91.7 weight.%.
4. Sodium titanates, calcium titanate and sodium aluminosilicates were the dominant phases observed in the non-magnetic fraction from tube furnace experiments.
5. Magnetic fraction was smelted at 1723 K to produce steel micro-alloyed with 0.1% V and a TiO_2 slag.
6. T1 non-magnetic fraction was leached in 0.5M H_2SO_4 solution to upgrade the TiO_2 content to 72 weight.%.
7. Roasting the acid leached non-magnetic residue with $NaHSO_4$ at 923 K, followed by water leaching produced a 92 weight.% TiO_2 residue that was primarily anatase with minor amounts of rutile. Solubilisation of $CaSO_4$ in the acidic solution containing $FeSO_4$ and Na_2SO_4 was observed, owing to the formation of $Na_6Fe(SO_4)_4$ and $Na_{0.84}Ca_{2.58}(SO_4)_3(H_2O)_{1.44}$ water-soluble complexes

Treatment of reduced low-grade TiO_2 slag

1. T2 reduced sample was water leached in air atmosphere to solubilise the sodium vanadate and sodium aluminate. Extraction of up to 50% vanadium was achieved by the addition Na_2CO_3 during the leaching step
2. CO_2 gas was sparged into the filtered water leach solution to adjust pH from 12 to 8, resulting in alumina precipitation (76 weight.% Al_2O_3).
3. H_2SO_4 was added to adjust pH value to 5. After addition of $(NH_4)_2SO_4$ the solution was agitated for 4 hours to precipitate ammonium metavanadate (AMV).
4. AMV was calcined at 723 K to produce 93.27 weight.% V_2O_5.
5. Water leached solids were leached in 0.5 M HCl to give a $CaTiO_3$-rich residue.
6. $CaTiO_3$ residue roasted was with $NaHSO_4$ at 923 K followed by water leaching. Due to limited amount of iron present a minor amount of $FeSO_4$ was added to the solution to ensure solubilisation of $CaSO_4$, yielding an 86 weight.% TiO_2 residue, mainly in the anatase form.
7. $CaTiO_3$ residue was separately acid baked with H_2SO_4 at 473 K to give $CaSO_4$ residue and water-soluble $TiOSO_4$. TiO_2 was precipitated from $TiOSO_4$ solution by hydrolysis.

8. 97 weight.% TiO_2 synthetic rutile was produced by calcining TiO_2 precipitate at 1173 K.

9.2 Major achievements

1. Process steps developed for extraction of Fe, titanium dioxide and vanadium pentoxide from iron-rich tailings. Alkali reductive roasting of iron-rich tailings reported below 1273 K, with effective separation of Fe-rich rich magnetic fraction from TiO_2-rich non-magnetic fraction.
2. Smelting of magnetic fraction to produce steel micro-alloyed with V
3. Treatment of non-magnetic fraction in acid medium shown to upgrade TiO_2 content to approximately 70 weight%. Subsequent sodium bisulphate roasting and water leaching yielded a 92 wt.% TiO_2 residue from T1 material.
4. 93 weight% Vanadium oxide and alumina recovered from low-grade titanium dioxide slag by employing alkali reduction and water leaching succeeded by selective precipitation of metallic values from water leaching solution.
5. Synthetic rutile (97.8 weight.%) produced from reduced T2 material by dilute acid leaching and acid baking-hydrolysis.
6. Demonstrated carbothermic reduction of titanium-bearing waste materials in the presence of Na_2CO_3 using a kiln.

9.3 Future work

1. Optimisation of V_2O_5 recovery and increasing purity to a minimum of 99.6%.
2. Computational fluid dynamics modelling of alkali reductive roasting in the rotary kiln of the titanium-bearing waste materials.
3. Further optimisation of process steps.
4. Economic analysis of the processing T1 and T2.
5. Water and acid leaching kinetics studies for treatment of T1 and T2.
6. Control of synthetic rutile particle size during hydrolysis.

10 References

1. Habashi, F., *Handbook of Extractive Metallurgy*. 1997: John Wiley & Sons.
2. Kogel, J.E., *Industrial minerals & rocks: commodities, markets, and uses*. 2006: SME.
3. Yang, F. and V. Hlavacek, *Effective extraction of titanium from rutile by a low-temperature chloride process.* AIChE journal, 2000. **46**(2): p. 355-360.
4. Habashi, F., *Handbook of extractive metallurgy*. 1997: Wiley-VCH.
5. Rosenbaum, J.B., *Titanium technology trends.* JOM, 1982. **34**(6): p. 76-80.
6. Mackey, T.S., *Upgrading ilmenite into a high-grade synthetic rutile.* Jom, 1994. **46**(4): p. 59-64.
7. Bauer, G., V. Güther, H, Hess, A. Otto, O. Roidl, H. Roller, S. Sattleberger, S. Köther-Becker and T. Beyer, *Vanadium and vanadium compounds.* Ullmann's Encyclopedia of Industrial Chemistry, 2000.
8. Kelley, K.D., C. Scott, D. Polyyak and B. Kimball,*Vanadium*. U.S Geological Survey 2017: 1802-U. p. 48.
9. Yang, J., Y. Tang, K. Yang, A. Rouff, E. Elzinga and J. Huang, *Leaching characteristics of vanadium in mine tailings and soils near a vanadium titanomagnetite mining site.* Journal of hazardous materials, 2014. **264**: p. 498-504.
10. Goldwaser, I., D. Gefel, E. Gershonov, M. Fridkin and Y. Shechter, *Insulin-like effects of vanadium: basic and clinical implications.* Journal of Inorganic Biochemistry, 2000. **80**(1): p. 21-25.
11. McCrindle, C.M., E. Mokantla, and N. Duncan, *Peracute vanadium toxicity in cattle grazing near a vanadium mine.* Journal of Environmental Monitoring, 2001. **3**(6): p. 580-582.
12. Naeem, A., P. Westerhoff, and S. Mustafa, *Vanadium removal by metal (hydr)oxide adsorbents.* Water Research, 2007. **41**(7): p. 1596-1602.
13. World Health Organization, *Vanadium*. 1988.
14. Gummow, B., C. Botha, J. Noordhuizen and J. Heesterbeek, *The public health implications of farming cattle in areas with high background concentrations of vanadium*. Preventive veterinary medicine, 2005. **72**(3-4): p. 281-290.
15. Ren, X., *Application status and market prospects of rare metal vanadium.* Chin J Rare Metals, 2003. **6**: p. 038.
16. Lindsley, D. and S. Haggerty, *Oxide Minerals Petrologic and Magnetic Significance.* Oxide Minerals Petrologic and Magnetic Significance, 1991. **25**.
17. Sole, K.C., *Recovery of titanium from the leach liquors of titaniferous magnetites by solvent extraction: Part 1. Review of the literature and aqueous thermodynamics.* Hydrometallurgy, 1999. **51**(2): p. 239-253.
18. Taner, M.F., T.S. Ercit, and R.A. Gault, *Vanadium-bearing magnetite from the Matagami and Chibougamau mining districts, Abitibi, Quebec, Canada.* Exploration and Mining Geology, 1998. **7**(4): p. 299-311.
19. Balan, E., J. De Villiers, S. Eeckhout, P. Glatzel, M. Toplis, E. Fristch, T. Allard, L. Galoisy and G. Calas, *The oxidation state of vanadium in titanomagnetite from layered basic intrusions.* American Mineralogist, 2006. **91**(5-6): p. 953-956.

20. O’Neill, H.S.C. and A. Navrotsky, *Cation distributions and thermodynamic properties of binary spinel solid solutions.* American Mineralogist, 1984. **69**(7-8): p. 733-753.
21. Sievwright, R., J. Wilkinson, H. O’Neil and A. Berry, *Thermodynamic controls on element partitioning between titanomagnetite and andesitic–dacitic silicate melts.* Contributions to Mineralogy and Petrology, 2017. **172**(8): p. 62.
22. Howard, R.L., S. Richards, B, Welch and J. Moore, *Vanadium distribution in melts intermediate to ferroalloy production from vanadiferous slag.* Metallurgical and Materials Transactions B, 1994. **25**(1): p. 27-32.
23. Righter, K., S. Sutton, M. Newville, L. Le, C. Schwandt, H. Uchida, B. Lavina and R. Downs, *An experimental study of the oxidation state of vanadium in spinel and basaltic melt with implications for the origin of planetary basalt.* American Mineralogist, 2006. **91**(10): p. 1643-1656.
24. Burns, R.G., *Mineralogical applications of crystal field theory*. Vol. 5. 1993: Cambridge University Press.
25. Porter, D.A. and K.E. Easterling, *Phase Transformations in Metals and Alloys, Third Edition (Revised Reprint)*. 1992: Taylor & Francis.
26. Kostorz, G., *Phase Transformations in Materials*. 2001: Wiley.
27. Smallman, R.E. and R.J. Bishop, *Modern Physical Metallurgy and Materials Engineering - Science, Process, Applications (6th Edition)*. Elsevier. p. 273-274.
28. Hillert, M., *Phase Equilibria, Phase Diagrams and Phase Transformations: Their Thermodynamic Basis*. 2007: Cambridge University Press.
29. Von Gruenewaldt, G., D. Klemm, J. Henckel and R. Dehm, *Exsolution features in titanomagnetites from massive magnetite layers and their host rocks of the Upper Zone, Eastern Bushveld Complex*. Economic Geology, 1985. **80**(4): p. 1049-1061.
30. Putnis, A., *An Introduction to Mineral Sciences*. 1992: Cambridge University Press.
31. Mcenroe, S.A., P. Robinson, and P.T. Panish, *Chemical and petrographic characterization of ilmenite and magnetite in oxide-rich cumulates of the Sokndal region, Rogaland, Norway.* NORGES GEOLOGISKE 32. Buddington, A. and D. Lindsley, *Iron-titanium oxide minerals and synthetic equivalents.* Journal of petrology, 1964. **5**(2): p. 310-357.
32. Buddington, A. and D. Lindsley, *Iron-titanium oxide minerals and synthetic equivalents.* Journal of petrology, 1964. **5**(2): p. 310-357.
33. Mücke, A., *Magnetite, ilmenite and ulvite in rocks and ore deposits: petrography, microprobe analyses and genetic implications.* Mineralogy and Petrology, 2003. **77**(3-4): p. 215-234.
34. Spencer, K.J. and D.H. Lindsley, *A solution model for coexisting iron-titanium oxides.* American mineralogist, 1981. **66**(11-12): p. 1189-1201.
35. Roine, A. and H. Outokumpu, *Chemistry for Windows: Chemical Reaction and Equilibrium Software with Extensive Thermodynamical Database, Version 5.1, User’s Guide.* Outokumpu Research Oy, Finland, 2002.
36. Wilson, N.C., J. Muscat, D. Mkhonto, P. Ngoepe and N. Harrison, *Structure and properties of ilmenite from first principles.* Physical Review B, 2005. **71**(7): p. 075202.
37. Klein, C. and A. Philpotts, *Earth materials: introduction to mineralogy and petrology*. 2012: Cambridge University Press.
38. Price, G.D., *Subsolidus phase relations in the titanomagnetite solid solution series.* 1981.
39. Bodsworth, C., *The extraction and refining of metals*. Vol. 2. 1994: CRC Press.

40. Gilchrist, J.D., *Extraction Metallurgy*. Pergamon Press plc, 1989, 1989: p. 431.
41. Coudurier, L., D.W. Hopkins, and I. Wilkomirsky, *Fundamentals of metallurgical processes*. 1985: Pergamon Press.
42. Sano, N., W. Lu, P. Riboud and M. Maeda, *Advanced physical chemistry for process metallurgy*. Vol. 1. 1997: Academic Press San Diego, CA.
43. Rosenqvist, T., *Principles of Extractive Metallurgy*. 1983: Mcgraw-Hill Book Comp.
44. Moore, J.J., *Chemical Metallurgy*. 2013: Elsevier Science.
45. DeVries, R., R. Roy, and E. Osborn, *Phase Equilibria in the System CaO–$Ti0_2$*. The Journal of Physical Chemistry, 1954. **58**(12): p. 1069-1073.
46. DeVries, R., R. Roy, and E. Osborn, *Phase Equilibria in the System CaO-TiO_2–SiO_2*. Journal of the American Ceramic Society, 1955. **38**(5): p. 158-171.
47. Braun, J.H., A. Baidins, and R.E. Marganski, *TiO_2 pigment technology: a review*. Progress in organic coatings, 1992. **20**(2): p. 105-138.
48. Bale, C., P. Chartrand, S. Degterov, G. Eriksson, K. Hack, R. Mahfoud, J. Melançon, A. Pelton and S. Petersen, *FactSage thermochemical software and databases*. Calphad, 2002. **26**(2): p. 189-228.
49. Auer, G., P. Woditsch, A. Westerhaus, J. Kischkewitz, W. Griebler and M. De Liedekerke, *Pigments, Inorganic, 2. White Pigments*, in *Ullmann's Encyclopedia of Industrial Chemistry*. 2000, Wiley-VCH Verlag GmbH & Co. KGaA.
50. Green, D.W., *Perry's chemical engineer's handbook 8/e section 2 physical & chem data (POD)*. 2007: McGraw-Hill Education.
51. Zhang, L., W. Zhang, J. Zhang and G. Li, *Effects of additives on the phase transformation, occurrence state, and the interface of the Ti component in Ti-bearing blast furnace slag*. International Journal of Minerals, Metallurgy, and Materials, 2016. **23**(9): p. 1029-1040.
52. Sironi, G., R. Sacerdote, and F. Ferrero, *Process for the purification of titanium tetrachloride*. 1971, Google Patents.
53. Middlemas, S., Z.Z. Fang, and P. Fan, *A new method for production of titanium dioxide pigment*. Hydrometallurgy, 2013. **131–132**(0): p. 107-113.
54. Kroll, W., *Method for manufacturing titanium and alloys thereof*. 1940, Google Patents.
55. Zhang, W., Z. Zhu, and C.Y. Cheng, *A literature review of titanium metallurgical processes*. Hydrometallurgy, 2011. **108**(3–4): p. 177-188.
56. Meng, X., M. Guo, J. Zhang, T. Wan and L. Kong, *Beneficiation of titanium oxides from ilmenite by self-reduction of coal bearing pellets*. Journal of Iron and Steel Research, International, 2006. **13**(2): p. 6-9.
57. Kronos. *Kronos TiO_2 Sulfate process*. 2018 [cited 2018 12 08]; Sulfate process]. Available from: https://kronostio2.com/en/about-tio2/sulfate-process.
58. Becker, J.H. and D.F. Dutton, *Recovery of titanium from titanium bearing materials*. 2007, Google Patents.
59. Hassell, D.J., J. Obern, S. Molloy, S. Ibrahim and M. Ali, *Extraction of products from titanium-bearing minerals*. 2017, Google Patents.
60. Kahn, J., *Non-Rutile Feedstocks for the Production of Titanium*. JOM, 1984. **36**(7): p. 33-38.
61. Pistorius, P., *Ilmenite smelting: the basics*. Journal of the Southern African Institute of Mining and Metallurgy, 2008. **108**(1): p. 35-43.
62. Pistorius, P.C. and C. Coetzee, *Physicochemical aspects of titanium slag production and solidification*. Metallurgical and Materials Transactions B, 2003. **34**(5): p. 581-588.

63. Sahu, K.K., T. Alex, D. Mishra and A. Agrawal, *An overview on the production of pigment grade titania from titania-rich slag.* Waste management & research, 2006. **24**(1): p. 74-79.
64. TiZir. *TiZir Titanium and Iron*. [cited 2015 17 May]; Available from: http://www.tizir.co.uk/projects-operations/tyssedal-tio2/.
65. McRae, L., E. Pothas, P. Jochens and D. Howat, *Physico-chemical properties of titaniferous slags.* Journal of the South African Institute of Mining and Metallurgy, 1969. **69**(11): p. 577-&.
66. Filippou, D. and G. Hudon, *Iron removal and recovery in the titanium dioxide feedstock and pigment industries.* JOM, 2009. **61**(10): p. 36-42.
67. Kale, A. and K. Bisaka, *Review of titanium feedstock selection for fluidized bed chlorinators.*
68. Stanaway, K., *Overview of titanium dioxide feedstocks.* Mining engineering, 1994. **46**(12): p. 1367-1370.
69. Pistorius, P., *Equilibrium interactions between freeze lining and slag in ilmenite smelting.* Journal of the Southern African Institute of Mining and Metallurgy, 2004. **104**(7): p. 417-422.
70. van der Westhuizen, J. and D. Bessinger, *EVALUATION OF REFRACTORY BRICKS FOR TITANIA SLAGS.*
71. Mohanty, B.P. and K.A. Smith, *Alkali metal catalysis of carbothermic reduction of ilmenite.* Transactions of the Institution of Mining and Metallurgy, Section C: Mineral Processing and Extractive Metallurgy, 1993. **102**: p. C163-C173.
72. Iluka resources. *Synthetic rutile*. Mineral Sands Technical Information 2009 [cited 2018 10 August]; Available from: https://www.iluka.com/docs/default-source/3.3-operations/synthetic-rutile.pdf.
73. Farrow, J., I. Ritchie, and P. Mangano, *The reaction between reduced ilmenite and oxygen in ammonium chloride solutions.* Hydrometallurgy, 1987. **18**(1): p. 21-38.
74. Geetha, K. and G. Surender, *Experimental and modelling studies on the aeration leaching process for metallic iron removal in the manufacture of synthetic rutile.* Hydrometallurgy, 2000. **56**(1): p. 41-62.
75. Becher, R., R. Canning, B. Goodheart and S. Uusna, *A new process for upgrading ilmenitic mineral sands.* in *Australasian inst mining met proc*. 1965.
76. Noubactep, C., *Metallic iron for environmental remediation: Learning from the Becher process.* Journal of Hazardous Materials, 2009. **168**(2): p. 1609-1612.
77. Borowiec, K., et al., *Method to upgrade titania slag and resulting product*. 1998, Google Patents.
78. Borowiec, K., A. Grau, M. Guegin and J. Turgeon, *TiO_2 containing product including rutile, pseudo-brookite and ilmenite*. 2003, Google Patents.
79. Goso, X., J. Peterson, J. Nell and K. Bisaka, *Scoping study of the upgrading of fluxed and fluxless titaniferous magnetite slag using the upgraded slag process.* Proceedings of Hydrometallurgy 2016: Sustainable Hydrometallurgical Extraction of Metals, 2016: p. 423-432.
80. Walpole, E. and J. Winter. *The Austpac ERMS and EARS processes for the manufacture of high-grade synthetic rutile by the hydrochloric acid leaching of ilmenite.* in *Chloride Metallurgy 2002—International Conference on the Practice and Theory of Chloride/Metal interaction*. 2002.
81. Walpole, E.A., *Synthetic rutile production from Murray Basin ilmenite by the Austpac ERMS process.* Murray Basin mineral sands, extended abstracts. Mildura: Australian Institute of Geoscientists, 1999: p. 164-8.

82. Habashi, F. *A New Process to Upgrade Ilmenite to Synthetic Rutile*. in *Proceedings Conference of Metallurgists, Canadian Institute of Mining, Metallurgy, and Petroleum, Montreal 2014*. 2014.
83. Kamaleddine, F.F., *Production of high-grade synthetic rutile from low-grade titanium-bearing ores*. 2015, Google Patents.
84. Cao, G. and R. Orrù, *Current Environmental Issues and Challenges*. 2014: Springer Netherlands.
85. El-Guindy, M. and W. Davenport, *Kinetics and mechanism of llmenite reduction with graphite.* Metallurgical Transactions, 1970. **1**(6): p. 1729-1734.
86. El-Tawil, S., I. Morsi, and A. Francis, *Kinetics of solid-state reduction of ilmenite ore.* Canadian metallurgical quarterly, 1993. **32**(4): p. 281-288.
87. Jones, D.G., *Kinetics of gaseous reduction of ilmenite.* Journal of Applied Chemistry and Biotechnology, 1975. **25**(8): p. 561-582.
88. Wang, Y., Z. Yuan, Z. Guo, Q. Tan, Z. Li and W. Jiang, *Reduction mechanism of natural ilmenite with graphite.* Transactions of Nonferrous Metals Society of China, 2008. **18**(4): p. 962-968.
89. Chen, Y., T. Hwang, and J. Williams, *Ball milling induced low-temperature carbothermic reduction of ilmenite.* Materials Letters, 1996. **28**(1): p. 55-58.
90. Kucukkaragoz, C. and R. Eric, *Solid state reduction of a natural ilmenite.* Minerals Engineering, 2006. **19**(3): p. 334-337.
91. Wouterlood, H.J., *The reduction of ilmenite with carbon.* Journal of Chemical Technology and Biotechnology, 1979. **29**(10): p. 603-618.
92. Bodsworth, C., *Physical chemistry of iron and steel manufacture*. 1963: Longmans.
93. Chatterjee, A., *Sponge Iron Production By Direct Reduction Of Iron Oxide*. 2010: PHI Learning.
94. Gupta, S.K., V. Rajakumar, and P. Grieveson, *The influence of weathering on the reduction of llmenite with carbon.* Metallurgical Transactions B, 1989. **20**(5): p. 735-745.
95. Pierson, H.O., *Handbook of Carbon, Graphite, Diamonds and Fullerenes: Processing, Properties and Applications*. 2012: Elsevier Science.
96. Zhao, Y. and F. Shadman, *Kinetics and mechanism of ilmenite reduction with carbon monoxide.* AIChE Journal, 1990. **36**(9): p. 1433-1438.
97. Foley, E. and K.P. MacKinnon, *Alkaline roasting of ilmenite.* Journal of Solid State Chemistry, 1970. **1**(3–4): p. 566-575.
98. Lahiri, A., *Influence of ascorbate and oxalic acid for the removal of iron and alkali from alkali roasted ilmenite to produce synthetic rutile.* Industrial & Engineering Chemistry Research, 2010. **49**(18): p. 8847-8851.
99. Lahiri, A. and A. Jha, *Kinetics and Reaction Mechanism of Soda Ash Roasting of Ilmenite Ore for the Extraction of Titanium Dioxide.* Metallurgical and Materials Transactions B, 2007. **38**(6): p. 939-948.
100. Sanchez-Segado, S., A. Lahiri, and A. Jha, *Alkali roasting of bomar ilmenite: rare earths recovery and physico-chemical changes.* Open Chemistry, 2015. **13**(1).
101. Ephraim, J.K. and A. Jha, *Leaching studies of alkali roasted bomarilmenite and anatase during the processing of synthetic rutile.* Hydrometallurgy, 2015. **152**: p. 113-119.
102. Jha, A., A. Lahiri, and E. Kumari, *Beneficiation of titaniferous ores by selective separation of iron oxide, impurities and rare earth oxides for the production of high grade synthetic rutile.* Mineral Processing and Extractive Metallurgy, 2008. **117**(3): p. 157-165.

103. Jarish, B., *Upgrading Sorelslag for production of synthetic rutile*. 1977, Google Patents.
104. Lasheen, T., *Soda ash roasting of titania slag product from Rosetta ilmenite.* Hydrometallurgy, 2008. **93**(3-4): p. 124-128.
105. Dong, H., T. Jiang, Y. Guo, J. Chen and X. Fan, *Upgrading a Ti-slag by a roast-leach process.* Hydrometallurgy, 2012. **113**: p. 119-121.
106. Yahui, L., M. Fancheng, F. Fuqiang, W. Weijing, C. Jinglong and Q. Tao, *Preparation of rutile titanium dioxide pigment from low-grade titanium slag pretreated by the NaOH molten salt method.* Dyes and Pigments, 2016. **125**: p. 384-391.
107. Elger, G.W. and R.A. Holmes, *Purifying titanium-bearing slag by promoted sulfation*. 1982, Google Patents.
108. Huhn, F., J. Klein, and H. Jüntgen, *Investigations on the alkali-catalysed steam gasification of coal: Kinetics and interactions of alkali catalyst with carbon.* Fuel, 1983. **62**(2): p. 196-199.
109. McKee, D.W., *Mechanisms of the alkali metal catalysed gasification of carbon.* Fuel, 1983. **62**(2): p. 170-175.
110. McKee, D.W., C. Spiro, P. Kosky and E. Lamby, *Catalysis of coal char gasification by alkali metal salts.* Fuel, 1983. **62**(2): p. 217-220.
111. Van Niekerk, W., R. Dippenaar, and D. Kotze, *The influence of potassium on the reactivity and strength of coke, with special reference to the role of coke ash.* JS Afr. Inst. Min. Metall, 1986. **86**(1): p. 25-29.
112. Veraa, M.J. and A.T. Bell, *Effect of alkali metal catalysts on gasification of coal char.* Fuel, 1978. **57**(4): p. 194-200.
113. Kapteijn, F. and J.A. Moulijn, *Kinetics of the potassium carbonate-catalysed* CO_2 *gasification of activated carbon.* Fuel, 1983. **62**(2): p. 221-225.
114. Li, S. and Y. Cheng, *Catalytic gasification of gas-coal char in* CO_2. Fuel, 1995. **74**(3): p. 456-458.
115. Zhu, D., T. Chun, J. Pan and X. Wei, *Upgrading iron and removing phosphorus from high-phosphorus iron ore [J]*. Journal of Central South University (Science and Technology), 2011. **3**: p. 001.
116. Li, G., S. Zhang, M. Rao, Y. Zhang and T. Jiang, *Effects of sodium salts on reduction roasting and Fe–P separation of high-phosphorus oolitic hematite ore.* International Journal of Mineral Processing, 2013. **124**: p. 26-34.
117. Bai, S., S. Wen, D. Liu, W. Zhang and Q. Cao, *Beneficiation of high phosphorus limonite ore by sodium-carbonate-added carbothermic reduction.* ISIJ international, 2012. **52**(10): p. 1757-1763.
118. Chun, T., H. Long, and J. Li, *Alumina-iron separation of high alumina iron ore by carbothermic reduction and magnetic separation.* Separation Science and Technology, 2015. **50**(5): p. 760-766.
119. El-Tawil, S., I. Morsi, A, Yehia and A. Francis, *Alkali reductive roasting of ilmenite ore.* Canadian metallurgical quarterly, 1996. **35**(1): p. 31-37.
120. Tathavadkar, V. and A. Jha. *The effect of molten sodium titanate and carbonate salt mixture on the alkali roasting of ilmenite and rutile minerals*. in *VII International Conference on Molten Slags Fluxes and Salts*. 2004.
121. Bouaziz, R. and M. Mater, *The binary sodium oxide-titanium dioxide.* Comptes rendus de l'Académie des sciences, 1971. **272**(C): p. 1874-1877.
122. Gupta, C., *Extractive metallurgy of niobium, tantalum, and vanadium.* International Metals Reviews, 1984. **29**(1): p. 405-444.

123. Rohrmann, B., *Vanadium in South Africa (Metal Review Series no. 2).* Journal of the Southern African Institute of Mining and Metallurgy, 1985. **85**(5): p. 141-150.
124. Cardarelli, F., *Materials Handbook: A Concise Desktop Reference*. 2008: Springer London.
125. Hukkanen, E. and H. Walden, *The production of vanadium and steel from titanomagnetites.* International Journal of Mineral Processing, 1985. **15**(1-2): p. 89-102.
126. Steinberg, W., W. Geyser, and J. Nell, *The history and development of the pyrometallurgical processes at Evraz Highveld Steel & Vanadium.* Journal of the Southern African Institute of Mining and Metallurgy, 2011. **111**(10): p. 705-710.
127. Nickens, K.P., S.R. Patierno, and S. Ceryak, *Chromium genotoxicity: a double-edged sword.* Chemico-biological interactions, 2010. **188**(2): p. 276-288.
128. Diao, J., B. Xie, C. Ji, X. Guo, Y. Wang and X. Li, *Growth of spinel crystals in vanadium slag and their characterization.* Crystal Research and Technology: Journal of Experimental and Industrial Crystallography, 2009. **44**(7): p. 707-712.
129. Taylor, P.R., S. Shuey, E. Vidal and J. Gomez, *Extactive metallurgy of vanadium-containing titaniferous magnetite ores: A review.* Minerals and Metallurgical Processing, 2006. **23**(2): p. 80-86.
130. Hu, T., X. Lv C. Bai, Z. Lun and G . Qiu, *Reduction behavior of Panzhihua titanomagnetite concentrates with coal.* Metallurgical and Materials Transactions B, 2013. **44**(2): p. 252-260.
131. Hu, T., X. Lü, C. Bai and G. Qiu, *Isothermal reduction of titanomagnetite concentrates containing coal.* International Journal of Minerals, Metallurgy, and Materials, 2014. **21**(2): p. 131-137.
132. Samanta, S., S. Mukherjee, and D. Rajib, *Oxidation behaviour and phase characterization of titaniferous magnetite ore of eastern India.* Transactions of Nonferrous Metals Society of China, 2014. **24**(9): p. 2976-2985.
133. Chen, D., B. Song, L. Wang, T. Qi, Y. Wang and W. Wang, *Solid state reduction of Panzhihua titanomagnetite concentrates with pulverized coal.* Minerals Engineering, 2011. **24**(8): p. 864-869.
134. Jena, B.C., W. Dresler, and I.G. Reilly, *Extraction of titanium, vanadium and iron from titanomagnetite deposits at pipestone lake, Manitoba, Canada.* Minerals Engineering, 1995. **8**(1–2): p. 159-168.
135. Chen, D., L. Zhao, Y. Liu, T. Qi, J. Wang amd L. Wang, *A novel process for recovery of iron, titanium, and vanadium from titanomagnetite concentrates: NaOH molten salt roasting and water leaching processes.* Journal of hazardous materials, 2013. **244**: p. 588-595.
136. Zhao, L., L. Wang, T. Qi, D. Chen, H. Zhao and Y. Liu, *A novel method to extract iron, titanium, vanadium, and chromium from high-chromium vanadium-bearing titanomagnetite concentrates.* Hydrometallurgy, 2014. **149**: p. 106-109.
137. Zhong, B., T. Xue, L.Zhao, H. Zhao, T. Qi amd W. Chen, *Preparation of Ti-enriched slag from V-bearing titanomagnetite by two-stage hydrochloric acid leaching route.* Separation and Purification Technology, 2014. **137**: p. 59-65.
138. Lekobotja, M., M. Mojapelo. X. Goso and H. Lagendijk, *Recovery of vanadium from discard titaniferous magnetite slag using the soda ash roast-leach process.* In 3rd Young Professionals Conference Innovation Hub, Pretoria, 9-10 March. 2017.

139. Gomez-Bueno, C., D. Spink, and G. Rempel, *Extraction of vanadium from Athabasca tar sands fly ash.* Metallurgical Transactions B, 1981. **12**(2): p. 341-352.
140. Kim, J.-H., H.-C. Cho, and K. Han, *Leaching behavior of U and V from a Korean uranium ore using Na_2CO_3 and KOH.* Geosystem Engineering, 2014. **17**(2): p. 113-119.
141. Okudan, M.D., A. Akcil, A. Tunuck and H. Deveci, *Effect of parameters on vanadium recovery from by-products of the Bayer process.* Hydrometallurgy, 2015. **152**: p. 76-83.
142. Gladyshev, S., A. Akcil, R. Abdukvaliyev, K. Beisembekova, S. Temirova and H . Deveci, *Recovery of vanadium and gallium from solid waste by-products of Bayer process.* Minerals Engineering, 2015. **74**: p. 91-98.
143. Crabtree, E.H. and V.E. Padilla, *The treatment of vanadium ores for the recovery of vanadium pentoxide.* Journal of the Less Common Metals, 1961. **3**(6): p. 437-442.
144. Navarro, R., J. Guzman, I . Saucedo, J. Revilla and E. Guibal, *Vanadium recovery from oil fly ash by leaching, precipitation and solvent extraction processes.* Waste Management, 2007. **27**(3): p. 425-438.
145. Vitolo, S., M. Seggiani, and F. Falaschi, *Recovery of vanadium from a previously burned heavy oil fly ash.* Hydrometallurgy, 2001. **62**(3): p. 145-150.
146. Gardner, H.E., *Recovery of vanadium and nickel from petroleum residues*. 1989, Google Patents.
147. Kelmers, A.D., *Preparation of ammonium metavanadate*. 1962, Google Patents.
148. Nasyrov, G.Z. and I.V. Ravdonikas, *Method of preparing vanadium pentoxide*. 1977, Google Patents.
149. Vitolo, S., M. Seggiani, S. Filippi and C. Brocchini, *Recovery of vanadium from heavy oil and Orimulsion fly ashes.* Hydrometallurgy, 2000. **57**(2): p. 141-149.
150. Li, X., C. Wei, Z. Deng, M. Li, C. Li and G. Fan, *Selective solvent extraction of vanadium over iron from a stone coal/black shale acid leach solution by D2EHPA/TBP.* Hydrometallurgy, 2011. **105**(3-4): p. 359-363.
151. Li, M., C. Wei, G. Fan, C. Li, Z. Deng and X. Li, *Extraction of vanadium from black shale using pressure acid leaching.* Hydrometallurgy, 2009. **98**(3): p. 308-313.
152. Tavakoli, M.R. and D.B. Dreisinger, *Separation of vanadium from iron by solvent extraction using acidic and neutral organophosporus extractants.* Hydrometallurgy, 2014. **141**: p. 17-23.
153. Li, W., Y. Zhang, T. Liu, J. Huang and Y. Wang, *Comparison of ion exchange and solvent extraction in recovering vanadium from sulfuric acid leach solutions of stone coal.* Hydrometallurgy, 2013. **131**: p. 1-7.
154. Lozano, L.J. and C. Godinez, *Comparative study of solvent extraction of vanadium from sulphate solutions by primene 81R and alamine 336.* Minerals Engineering, 2003. **16**(3): p. 291-294.
155. El-Nadi, Y.A., N.S. Awwad, and A.A. Nayl, *A comparative study of vanadium extraction by Aliquat-336 from acidic and alkaline media with application to spent catalyst.* International Journal of Mineral Processing, 2009. **92**(3): p. 115-120.
156. Zeng, L. and C.Y. Cheng, *Recovery of molybdenum and vanadium from synthetic sulphuric acid leach solutions of spent hydrodesulphurisation catalysts using solvent extraction.* Hydrometallurgy, 2010. **101**(3): p. 141-147.
157. Bragg, W.H. and W.L. Bragg, *The reflection of X-rays by crystals.* Proc. R. Soc. Lond. A, 1913. **88**(605): p. 428-438.

158. Culity, B. and S. Stock, *Elements of X-ray Diffraction*. Reading: Addition-Wesley, 1978.
159. Egerton, R., *Physical Principles of Electron Microscopy: An Introduction to TEM, SEM, and AEM*. 2005: Springer.
160. Goldstein, J., D. Newbury, P. Echlin, D. Joy, A. Roming, C. Lyman, C. FFiori and E. Lifshin, *Scanning Electron Microscopy and X-Ray Microanalysis: A Text for Biologists, Materials Scientists, and Geologists*. 2012: Springer US.
161. Gill, R., *Modern Analytical Geochemistry: An Introduction to Quantitative Chemical Analysis Techniques for Earth, Environmental and Materials Scientists*. 2014: Taylor & Francis.
162. Jones, M.P., *Applied mineralogy: a quantitative approach*. 1987: Taylor & Francis US.
163. Peacock, A., *Handbook of Polyethylene: Structures: Properties, and Applications*. 2000: Taylor & Francis.
164. Rigaku. *Comparison of wavelength dispersive X-ray fluorescence and energy dispersive X-ray fluorescence techniques*. [cited 2018 27 July]; Available from: https://www.rigaku.com/en/products/xrf/primini/app004.
165. Klein, C. and A.R. Philpotts, *Earth materials: introduction to mineralogy and petrology*. 2013: Cambridge University Press.
166. Klemm, D., J. Henckel, R. Dehm and G. Von Gruenewaldt, *The geochemistry of titanomagnetite in magnetite layers and their host rocks of the eastern Bushveld Complex*. Economic Geology, 1985. **80**(4): p. 1075-1088.
167. Goso, X., J. Nell, and J. Petersen. *Review of liquidus surface and phase equilibria in the TiO_2-SiO_2-Al_2O_3-MgO-CaO slag system at pO_2 applicable in fluxed titaniferous magnetite smelting*. In Advances in Molten Slags, Fluxes, and Salts: Proceedings of the 10th International Conference on Molten Slags, Fluxes and Salts 2016. 2016. Springer.
168. Li, J., Z. Zhang, L. Liu, W. Wang and X. Wang, *Influence of basicity and TiO_2 content on the precipitation behavior of the Ti-bearing blast furnace slags*. ISIJ international, 2013. **53**(10): p. 1696-1703.
169. Lycett, R., P. Jochens, D. Howat and F. Fric, *The crystallization of rutile from titaniferous slags*. Journal of the South African Institute of Mining and Metallurgy, 1975. **76**(2): p. 20-24.
170. Djuric, Z.Z., O. Aleksic, M. Nikolic, N. Labus, M. Radovanovic abd M. Lukovic, *Structural and electrical properties of sintered Fe_2O_3/TiO_2 nanopowder mixtures*. Ceramics International, 2014. **40**(9): p. 15131-15141.
171. Rosenqvist, T., *Principles of extractive metallurgy*. 2004: Tapir academic press.
172. Hu, M., L. Liu, X. Lv, C. Bai and S. Zhang, *Crystallization behavior of perovskite in the synthesized high-titanium-bearing blast furnace slag using confocal scanning laser microscope*. Metallurgical and Materials Transactions B, 2014. **45**(1): p. 76-85.
173. Liu, L., et al., *Effect of cooling rate on the crystallization behavior of perovskite in high titanium-bearing blast furnace slag*. International Journal of Minerals, Metallurgy, and Materials, 2014. **21**(11): p. 1052-1061.
174. Gao, J., Y. Zhong, and Z. Guo, *Selective Separation of Perovskite ($CaTiO_3$) from Titanium Bearing Slag Melt by Super Gravity*. ISIJ International, 2016. **56**(8): p. 1352-1357.
175. Liu, L., M. Hu, Y. Xu, C. Bai and Y. Gan, *Structure, growth process, and growth mechanism of perovskite in high-titanium-bearing blast furnace slag*. Metallurgical and Materials Transactions B, 2015. **46**(4): p. 1751-1759.

176. Gueguin, M. and F. Cardarelli, *Chemistry and mineralogy of titania-rich slags. Part 1—hemo-ilmenite, sulphate, and upgraded titania slags.* Mineral Processing and Extractive Metallurgy Review, 2007. **28**(1): p. 1-58.
177. Diao, J., B. Xie, Y. Wang, and C. Ji *Mineralogical characterisation of vanadium 0slag under different treatment conditions.* Ironmaking & Steelmaking, 2009. **36**(6): p. 476-480.
178. Sadykhov, G. and I. Karyazin, *Titanium-vanadium slags produced upon the direct reduction of iron from titanomagnetite concentrates.* Russian Metallurgy (Metally), 2007. **2007**(6): p. 447-454.
179. Antony, M., et al., *The soda-ash roasting of chromite ore processing residue for the reclamation of chromium*. Metallurgical and Materials transactions B, 2001. **32**(6): p. 987-995.
180. Chamberland, B. and S.K. Porter, *A study on the preparation and physical property determination of NaVO2.* Journal of Solid State Chemistry, 1988. **73**(2): p. 398-404.
181. Spencer, W.D. and B. Topley, *CCCLIV.—Chemical kinetics of the system* $Ag_2CO_3 \rightleftharpoons Ag_2O + CO_2$. Journal of the Chemical Society (Resumed), 1929: p. 2633-2650.
182. Ginstling, A.M. and B.I. Brounshtein, *The diffusion kinetics of reaction in spherical particles.* Journal of Applied Chemistry USSR, , 1950. **23**: p. 1327-1338.
183. Zhao, L., L. Wang, D. Chen, H. Zhao, Y. Liu and T. Qi, *Behaviors of vanadium and chromium in coal-based direct reduction of high-chromium vanadium-bearing titanomagnetite concentrates followed by magnetic separation.* Trans. Nonferrous Met. Soc. China, 2015. **25**(1325): p. 1333.
184. Levenspiel, O., *Chemical reaction engineering*. 1999: Wiley.
185. Matsui, I., D. Kunii, and T. Furusawa, *Study of char gasification by carbon dioxide. 1. Kinetic study by thermogravimetric analysis.* Industrial & engineering chemistry research, 1987. **26**(1): p. 91-95.
186. Dutta, S., C. Wen, and R. Belt, *Reactivity of coal and char. 1. In carbon dioxide atmosphere*. Industrial & Engineering Chemistry Process Design and Development, 1977. **16**(1): p. 20-30.
187. Turkdogan, E.T., *Physical chemistry of high temperature technology.* 1980.
188. Kingery, W.D., H.K. Bowen, and D.R. Uhlmann, *Introduction to Ceramics*. Wiley series on the science and technology of materials. 1976, New York: John Wiley. 1032.
189. Jha, A. and S.J. Yoon, *Formation of titanium carbonitride phases via the reduction of* TiO_2 *with carbon in the presence of nitrogen.* Journal of Materials Science, 1999. **34**(2): p. 307-322.
190. Parirenyatwa, S., L. Escudero-Castejon, S. Sanchez-Segado, Y. Hara and A. Jha, *Investigation of Molten Salt Phase Formation during Alkali Roasting of Titaniferous Minerals with Sodium and Potassium Hydroxide.* Journal for Manufacturing Science and Production, 2016. **16**(4): p. 299-308.
191. Tathavadkar, V. and A. Jha. *The effect of molten sodium titanate and carbonate salt mixture on the alkali roasting of ilmenite and rutile minerals*. In VIIInternational Conference on Molten Slags Fluxes and Salts, The South African Institute of Mining and Metallurgy,[2004],(255-261). 2004.
192. Pisaroni, M., R. Sadi, and D. Lahaye, *Counteracting ring formation in rotary kilns.* Journal of Mathematics in Industry, 2012. **2**(1): p. 3.
193. Chatterjee, A., *Beyond the Blast Furnace*. 2017: CRC Press.

194. Sullivan, J.D., M. , C.G., and R. , O.C., *Passage of solid particles through rotary cylindrical kilns.* U.S. Bureau of Mines Technical Paper, 1927(384).
195. Habashi, F., *Principles of extractive metallurgy*. Vol. 1. 1969: CRC Press.
196. Vignes, A., *Extractive Metallurgy 2: Metallurgical Reaction Processes*. 2013: Wiley.
197. Sarangi, A. and B. Sarangi, *Sponge Iron Production in rotary kiln*. 2011: PHI Learning Pvt. Ltd.
198. Bai, S., S. Wen, D. Liu, W. Zhang and Y. Xian, *Catalyzing carbothermic reduction of siderite ore with high content of phosphorus by adding sodium carbonate.* ISIJ international, 2011. **51**(10): p. 1601-1607.
199. Freek, K., P. Hans, and M.J. A., *CO_2 gasification of activated carbon catalyzed by earth alkaline elements.* AIChE Journal, 1986. **32**(4): p. 691-695.
200. Li, J. and A. Van Heiningen, *Reaction kinetics of gasification of black liquor char*. The Canadian Journal of Chemical Engineering, 1989. **67**(4): p. 693-697.
201. Radović, L.R., P.L. Walker Jr, and R.G. Jenkins, *Importance of carbon active sites in the gasification of coal chars.* Fuel, 1983. **62**(7): p. 849-856.
202. Balluffi, R.W., S. Allen, and W.C. Carter, *Kinetics of materials*. 2005: John Wiley & Sons.
203. Richardson, F.D., *Physical Chemistry of Melts in Metallurgy*. 1974: Academic Press.
204. Mills, K., *The estimation of slag properties.* Short course presented as part of Southern African Pyrometallurgy, 2011. **7**.
205. Sadykhov, G., *Oxidation of titanium-vanadium slags with the participation of Na_2O and its effect on the behavior of vanadium*. Russian Metallurgy (Metally), 2008. **2008**(6): p. 449-458.
206. Nakada, H. and K. Nagata, *Crystallization of $CaO–SiO_2–TiO_2$ slag as a candidate for fluorine free mold flux*. ISIJ international, 2006. **46**(3): p. 441-449.
207. Cheng, H., D.B. Reiser, and S. Dean Jr, *On the mechanism and energetics of Boudouard reaction at FeO (1 0 0) surface: $2CO \rightarrow C + CO_2$*. Catalysis Today, 1999. **50**(3-4): p. 579-588.
208. Marsh, H. and D.W. Taylor, *Carbon gasification in the Boudouard reaction.* Fuel, 1975. **54**(3): p. 218-220.
209. Rao, Y., A. Adjorlolo, and J. Haberman, *On the mechanism of catalysis of the Boudouard reaction by alkali-metal compounds.* Carbon, 1982. **20**(3): p. 207-212.
210. Le Losq, C., D. Neuville, P. Florian, G. Henderson and D. Massiot, *The role of Al^{3+} on rheology and structural changes in sodium silicate and aluminosilicate glasses and melts.* Geochimica et Cosmochimica Acta, 2014. **126**: p. 495-517.
211. Mills, K., L. Yuan, and R. Jones, *Estimating the physical properties of slags.* Journal of the Southern African Institute of Mining and Metallurgy, 2011. **111**(10): p. 649-658.
212. Li, H.-Y., H. Fang, K. Wang, W. Zhou, Z. Yang, X. Yan, W. Ge, Q. Li and B. Xie, *Asynchronous extraction of vanadium and chromium from vanadium slag by stepwise sodium roasting–water leaching.* Hydrometallurgy, 2015. **156**: p. 124-135.
213. Gaurav, G.K. and S. Khanam, *Computational fluid dynamics analysis of sponge iron rotary kiln.* Case Studies in Thermal Engineering, 2017. **9**: p. 14-27.
214. Greening, N.R., *Elimination of Water Pollution by Recycling Cement Plant Kiln Dust*. 1976: U.S. Environmental Protection Agency, Office of Research and Development, Industrial Environmental Research Laboratory.
215. Hewlett, P., *Lea's Chemistry of Cement and Concrete*. 2003: Elsevier Science.

216. Shi, P., B. Zhang, and M. Jiang, *Kinetics of the carbonate leaching for calcium Metavanadate*. Minerals, 2016. **6**(4): p. 102.
217. Kazadi, D.M., et al., *Control of silica polymerisation during ferromanganese slag sulphuric acid digestion and water leaching*. Hydrometallurgy, 2016. **166**: p. 214-221.
218. Hanaor, D.A. and C.C. Sorrell, *Review of the anatase to rutile phase transformation*. Journal of Materials science, 2011. **46**(4): p. 855-874.
219. Proxawater. *PROXA protects environment by cleaning off-gasses from vanadium plant in Australia*. 2008 [cited 2017 6 August]; Available from: https://www.proxawater.com/2017/03/07/windmurra-vanadium-australia/.

Appendix A

Table A.1 X-ray fluorescence analysis of standards using semi-quantitative programme.

Standard	**Fe_2O_3** Std value	**Fe_2O_3** EZ scan	**TiO_2** Std value	**TiO_2** EZ scan	**V_2O_5** Std value	**V_2O_5** EZ scan	**SO_3** Std value	**SO_3** EZ scan	**Na_2O** Std value	**Na_2O** EZ scan	**Al_2O_3** Std value	**Al_2O_3** EZ scan	**SiO_2** Std value	**SiO_2** EZ scan	**MnO** Std value	**MnO** EZ scan	**CaO** Std value	**CaO** EZ scan	**MgO** Std value	**MgO** EZ scan
1	95.00	9.47	5.00	7.45	0.00	0.00	0.00	0.21	0.00	0.56	0.00	0.24	0.00	0.52	0.00	0.00	0.00	0.73	0.00	0.00
2	90.00	88.85	1.00	9.62	0.00	0.00	0.00	0.27	0.00	0.68	0.00	0.23	0.00	0.48	0.00	0.00	0.00	0.66	0.00	0.00
3	8.00	79.42	2.00	19.18	0.00	0.00	0.00	0.15	0.00	0.53	0.00	0.15	0.00	0.29	0.00	0.00	0.00	0.59	0.00	0.00
4	6.00	59.97	4.00	36.59	0.00	0.00	0.00	0.25	0.00	1.43	0.00	0.25	0.00	0.66	0.00	0.00	0.00	0.90	0.00	0.00
5	4.00	41.22	6.00	55.96	0.00	0.00	0.00	0.19	0.00	1.23	0.00	0.24	0.00	0.48	0.00	0.00	0.00	0.65	0.00	0.00
6	2.00	22.23	8.00	76.13	0.00	0.00	0.00	0.12	0.00	0.43	0.00	0.19	0.00	0.36	0.00	0.00	0.00	0.43	0.00	0.00
7	1.00	1.95	9.00	87.15	0.00	0.00	0.00	0.98	0.00	0.65	0.00	0.19	0.00	0.33	0.00	0.00	0.00	0.46	0.00	0.00
8	3.00	4.90	95.00	92.62	2.00	0.00	0.00	0.19	0.00	0.77	0.00	0.27	0.00	0.79	0.00	0.00	0.00	0.14	0.00	0.00
9	1.50	1.83	98.00	95.49	0.50	0.00	0.00	0.20	0.00	0.52	0.00	0.29	0.00	0.72	0.00	0.00	0.00	0.82	0.00	0.00
10	15.00	17.97	35.00	35.76	0.00	0.00	0.00	0.22	23.00	2.53	15.00	12.55	5.00	5.75	0.00	0.00	5.00	4.43	2.00	1.66
11	15.00	18.27	35.00	36.62	0.00	0.00	0.00	0.13	15.00	13.51	1.00	8.29	1.00	9.73	0.00	0.00	10.00	9.33	5.00	4.14
12	15.00	17.63	35.00	36.51	0.00	0.00	0.00	0.15	0.00	0.35	5.00	4.22	15.00	14.92	0.00	0.00	20.00	17.75	10.00	8.25
13	15.00	18.22	35.00	37.25	0.00	0.00	0.00	0.13	0.00	0.18	3.00	2.53	2.00	2.32	0.00	0.00	30.00	26.79	15.00	12.36
14	5.00	7.00	6.00	7.26	0.50	0.54	0.50	0.75	5.00	5.73	80.00	75.27	2.00	2.89	0.50	0.61	0.00	0.69	0.00	0.00
15	8.00	10.00	18.00	20.44	1.00	1.11	1.00	1.19	10.00	9.59	60.00	54.42	0.00	0.46	1.00	1.20	0.00	0.18	0.00	0.00
16	8.00	9.75	29.00	30.47	2.00	2.17	1.00	1.13	15.00	14.73	40.00	34.18	0.00	0.91	2.00	2.39	0.00	0.16	0.00	0.00
17	8.00	9.55	63.00	63.36	5.00	4.82	2.00	1.99	20.00	16.88	0.00	0.19	0.00	0.36	2.00	2.35	0.00	0.57	0.00	0.00

Table A.1 X-ray fluorescence analysis of standards using semi-quantitative programme (continued).

Standard	**Fe_2O_3** **Std value**	**Fe_2O_3** **EZ scan**	**TiO_2** **Std value**	**TiO_2** **EZ scan**	**V_2O_5** **Std value**	**V_2O_5** **EZ scan**	**SO_3** **Std value**	**SO_3** **EZ scan**	**Na_2O** Std value	**Na_2O** **EZ scan**	**Al_2O_3** **Std value**	**Al_2O_3** **EZ scan**	**SiO_2** **Std value**	**SiO_2** **EZ scan**	**MnO** **Std value**	**MnO** **EZ scan**	**CaO** **Std value**	**CaO** **EZ scan**	**MgO** **Std value**	**MgO** **EZ scan**
18	8.00	9.89	11.00	12.66	1.00	1.84	3.00	3.58	25.00	22.16	0.00	0.27	0.00	0.53	3.00	3.65	40.00	36.35	0.00	0.00
19	4.00	4.96	33.00	33.67	25.00	24.70	4.00	4.00	3.00	26.52	0.00	0.32	0.00	0.59	4.00	4.78	0.00	0.97	0.00	0.00
2	4.00	4.82	46.00	46.96	0.00	0.00	5.00	4.97	35.00	29.79	0.00	0.28	0.00	0.51	10.00	12.01	0.00	0.92	0.00	0.00
21	2.00	2.53	0.00	0.00	50.00	52.54	1.00	1.67	21.00	19.49	10.00	8.88	5.00	5.53	0.00	0.00	0.00	0.12	0.00	0.00
22	1.00	1.38	0.00	0.00	80.00	81.56	0.00	0.15	8.00	7.52	8.00	6.76	2.00	2.77	0.00	0.00	0.00	0.80	0.00	0.00
23	0.20	0.39	0.00	0.00	98.50	96.14	0.00	0.15	0.80	1.67	0.00	0.22	0.20	0.64	0.00	0.00	0.00	0.64	0.00	0.00
Synthetic Rutile	2.34	3.69	92.70	9.19	0.27	0.00	1.50	0.14	0.00	0.83	1.38	1.47	0.88	1.20	0.93	1.43	0.17	0.70	0.29	0.46

Table A.2 X-ray fluorescence analysis of standards using quantitative programme.

Standard	**Fe_2O_3** Std value	**Fe_2O_3** scan	**TiO_2** Std value	**TiO_2** scan	**V_2O_5** Std value	**V_2O_5** scan	**SO_3** Std value	**SO_3** scan	**Na_2O** Std value	**Na_2O** scan	**Al_2O_3** Std value	**Al_2O_3** scan	**SiO_2** Std value	**SiO_2** scan	**MnO** Std value	**MnO** scan	**CaO** Std value	**CaO** scan	**MgO** Std value	**MgO** scan
1	95.0	85.8	5.0	9.3	0.0	0.6	0.0	0.3	0.0	-0.9	0.0	-0.7	0.0	0.0	0.0	-0.1	0.0	0.0	0.0	0.4
2	90.0	83.1	10.0	11.1	0.0	0.6	0.0	0.3	0.0	-0.8	0.0	-0.6	0.0	-0.1	0.0	-0.1	0.0	0.0	0.0	0.3
3	80.0	76.6	20.0	21.6	0.0	0.5	0.0	0.2	0.0	-1.4	0.0	-0.7	0.0	-0.2	0.0	-0.1	0.0	0.0	0.0	0.2
4	60.0	59.7	40.0	40.7	0.0	0.3	0.0	0.3	0.0	0.3	0.0	-0.7	0.0	-0.1	0.0	-0.1	0.0	0.0	0.0	0.3
5	40.0	40.7	60.0	60.0	0.0	0.2	0.0	0.2	0.0	-0.3	0.0	-0.7	0.0	-0.2	0.0	-0.2	0.0	0.0	0.0	0.2
6	20.0	21.1	80.0	79.8	0.0	0.0	0.0	0.2	0.0	-1.3	0.0	-0.7	0.0	-0.2	0.0	-0.2	0.0	0.0	0.0	0.2
7	10.0	10.6	90.0	93.4	0.0	-0.1	0.0	0.2	0.0	-1.1	0.0	-0.7	0.0	0.0	0.0	-0.2	0.0	0.0	0.0	0.3
8	3.0	3.6	95.0	93.3	2.0	2.7	0.0	0.2	0.0	-1.0	0.0	-0.7	0.0	-0.2	0.0	-0.2	0.0	0.0	0.0	0.2
9	1.5	1.7	98.0	98.5	0.5	0.6	0.0	0.2	0.0	-1.1	0.0	-0.5	0.0	1.1	0.0	-0.2	0.0	0.0	0.0	0.3
10	15.0	13.2	35.0	31.6	0.0	0.4	0.0	0.2	23.0	22.8	15.0	14.7	5.0	4.2	0.0	-0.1	5.0	4.6	2.0	1.8
11	15.0	13.7	35.0	32.7	0.0	0.5	0.0	0.2	15.0	14.7	10.0	9.8	10.0	8.8	0.0	-0.1	10.0	9.5	5.0	4.5
12	15.0	15.4	35.0	37.2	0.0	0.5	0.0	0.2	0.0	-1.5	5.0	5.0	15.0	15.5	0.0	-0.2	20.0	20.9	10.0	9.8
13	15.0	16.0	35.0	38.7	0.0	0.5	0.0	0.2	0.0	-1.6	3.0	2.8	2.0	1.9	0.0	-0.2	30.0	31.7	15.0	15.0
14	5.0	4.5	6.0	7.5	0.5	1.2	0.5	0.8	5.0	4.5	80.0	79.8	2.0	2.3	0.5	0.4	0.0	0.6	0.0	0.4
15	8.0	7.4	18.0	18.2	1.0	1.6	1.0	1.3	10.0	10.1	60.0	60.8	0.0	0.1	1.0	0.9	0.0	0.1	0.0	0.4
16	8.0	7.0	29.0	27.3	2.0	2.6	1.0	1.2	15.0	15.5	40.0	39.2	0.0	0.5	2.0	1.9	0.0	0.1	0.0	0.3
17	8.0	7.6	63.0	57.4	5.0	5.5	2.0	2.1	20.0	20.2	0.0	-0.6	0.0	0.0	2.0	2.0	0.0	0.0	0.0	0.2
18	8.0	7.5	11.0	12.5	10.0	12.1	3.0	3.0	25.0	25.0	0.0	-0.5	0.0	0.2	3.0	3.2	40.0	37.8	0.0	0.6

Table A.2 X-ray fluorescence analysis of standards using quantitative programme (continued).

19	4.0	3.6	33.0	28.6	25.0	24.4	4.0	3.7	30.0	28.7	0.0	-0.5	0.0	0.2	4.0	3.9	0.0	0.0	0.0	0.3
20	4.0	3.5	46.0	39.5	0.0	0.4	5.0	4.7	35.0	33.9	0.0	-0.5	0.0	0.2	10.0	9.8	0.0	0.0	0.0	0.3
21	2.0	1.9	0.0	1.5	50.0	51.8	10.0	10.4	21.0	22.5	10.0	10.7	5.0	5.1	0.0	-0.2	0.0	0.1	0.0	0.4
22	1.0	0.9	0.0	1.5	80.0	78.9	0.0	0.3	8.0	8.0	8.0	8.2	2.0	2.5	0.0	-0.2	0.0	0.0	0.0	0.3
23	0.2	0.4	0.0	1.5	98.5	98.2	0.0	0.3	0.8	0.4	0.0	-0.5	0.2	0.3	0.0	-0.2	0.0	0.0	0.0	0.3
Synthetic Rutile	2.3	3.6	92.7	93.8	0.3	0.2	1.1	0.2	0.0	-0.2	1.4	1.2	0.9	1.0	0.9	0.9	0.0	0.0	0.3	0.7

Appendix B

Table B.1 Effect of operating parameters on reductive alkali roasting of iron rich tailings in the rotary kiln.

Experiment	Feed	Weight ratio	Particle size (μm)	Angle of inclination	Temperature (K)	Gas flowrate (L.min^{-1})	Input (g)	Sample collected (g)	Sample tube (g)	Sample screw (g)	Percentage tube
1	T1:Na_2CO_3:C	1:0.2:0.23	+106 -300	1.6	1173	2	288	178.42	58.26	3.57	20.23
							240.25	211.47	4.34	2.69	1.81
							218.5	185	10.94	1.89	5.01
							197.83	173	8.13	2.1	4.11
2	T1:Na_2CO_3:C	1:0.2:0.23	+106 -300	1.6	1223	2	287	58.96	191.17	6.72	66.61
							256.85	148.77	75.17	4.54	29.27
							228.48	197.89	15.15	3.37	6.63
							216.41	149.69	6.56	2.62	3.03
3	T1:Na_2CO_3:C	1:0.2:0.23	+106 -300	1.6	1273	2	287	46.55	163.35	5.96	56.92
							215.86	35.78	143.31	2.96	66.39
							182.05	166.35	6.61	1.53	3.63
							174.49	159.85	2.37	9.04	1.36
4	T1:Na_2CO_3:C	1:0.2:0.23	+300 -500	1.6	1223	2	287	192.47	45.5	4.61	15.85
							242.58	197.21	15.96	3.97	6.58
							217.14	188.38	5.07	3.97	2.33
							197.42	188.15	0.46	2.41	0.23
5	T1:Na_2CO_3:C	1:0.2:0.23	+500 -1180	1.6	1223	2	287	160.36	87.89	5.22	30.62
							253.47	163.35	61.26	3.75	24.17
							228.36	146.62	53.65	2.35	23.49
							202.62	156.67	40.49	1.98	19.98
6	T1:Na_2CO_3:C	1:0.16:0.23	+106 -300	1.6	1223	2	277	122.52	102.43	36.98	6.94
							231.89	116.51	112.24	48.40	4.41
							233.16	201.75	2.08	0.89	4.84
							208.67	193.98	1.41	0.68	3

Table B.1 Effect of operating parameters on reductive alkali roasting of iron rich tailings in the rotary kiln (continued).

Experiment	Feed	Weight ratio	Particle size (μm)	Angle of inclination (°)	Temperature (K)	Gas flowrate (L.min^{-1})	Input (g)	Sample collected (g)	Sample tube (g)	Sample screw (g)	Percentage tube
7	T1:Na_2CO_3:C	1:0.2:0.23	+106 -300	1.6	1223	1	287	131	102	5	35.54
							238	192	15	0.5	6.30
							207.5	192	1	1	0.48
							194	176.17	9.06	1.46	4.67
8	T1:Na_2CO_3:C	1:0.2:0.23	+106 -300	1.6	1223	3	287	190.24	36.08	5.32	12.57
							231.64	204.44	2.43	3.69	1.05
							210.56	194.33	1.23	2.85	0.58
							198.41	189	1.95	2.62	0.98
9	T1:Na_2CO_3:C	1:0.2:0.23	+106 -300	1.2	1223	2	287	102.82	136.29	6.23	47.49
							245.34	167.84	38.59	6.77	15.73
							238.85	193.49	0.69	2.62	0.29
							192.16	188.85	1.75	2.3	0.91
10	T1:Na_2CO_3:C	1:0.2:0.23	+106 -300	1.4	1223	2	287	146.56	75.79	5.63	26.41
							227.98	196.68	1.71	4.64	0.75
							203.03	186.55	1.44	3.24	0.71
							191.23	183.83	1.4	2.6	0.73

Table B.2 Effect of low-grade TiO_2 slag particle size on reductive alkali roasting in the rotary kiln.

Experiment	Feed	Weight ratio	Particle size (μm)	Angle of inclination (°)	Temperature (K)	Gas flowrate ($L.min^{-1}$)		Sample collected (g)	Sample tube (g)	Sample screw (g)	Percentage tube
1	T2:Na_2CO_3:C	1:0.45:0.09	+106 -300	1.6	1273	2	308	122.33	157.36	6.69	51.09
							286.38	239.11	27.26	3.42	9.52
							269.79	257	4.1	2.36	1.52
							263.46	259.45	4.83	2.88	1.83
2	T2:Na_2CO_3:C	1:0.45:0.09	+300 -500	1.6	1273	2	308	67.02	227.48	5	73.86
							299.5	70.45	209.13	4.39	69.83
							283.97	152.18	110.57	4.61	38.94
							267.36	206.45	39.57	2.91	14.80
3	T2:Na_2CO_3:C	1:0.45:0.09	+500 -1180	1.6	1273	2	308	49.35	248.02	4	80.53
							301.37	25.83	264.89	3.76	87.90
							294.48	34.96	246.34	4.58	83.65
							285.88	89.99	183.49	3.18	64.18

Appendix C

Table C.1 Mass and energy balance calculations for alkali reduction of iron-rich tailings. Computed using HSC 5.1 software [35].

INPUT SPECIES Formula	Temperature (K)	Amount kmol	Amount kg	Amount Nm3	Latent H kWh	Total H kWh	Latent H	Total H	MW
Mineral	298.150	8.693	993.000	6.101	0.00	-2021.06			
Fe2O3	298.150	4.164	665.000	0.127	0.00	-952.00	0.000	-228.611	159.692
TiO2	298.150	1.464	117.000	0.028	0.00	-384.29	0.000	-262.430	79.899
V2O5	298.150	0.016	3.000	0.001	0.00	-7.11	0.000	-430.833	181.880
CaO	298.150	0.285	16.000	0.005	0.00	-50.32	0.000	-176.367	56.079
Al2O3	298.150	0.490	50.000	0.013	0.00	-228.26	0.000	-465.470	101.961
Na2O	298.150	0.904	56.000	0.025	0.00	-104.91	0.000	-116.106	61.979
MgO	298.150	0.099	4.000	0.001	0.00	-16.58	0.000	-167.111	40.304
SiO2	298.150	0.965	58.000	0.022	0.00	-244.24	0.000	-253.016	60.084
SO3(g)	298.150	0.262	21.000	5.879	0.00	-28.84	0.000	-109.935	80.058
MnO	298.150	0.042	3.000	0.001	0.00	-4.53	0.000	-107.006	70.937
Coal	298.150	18.612	289.990	39.725	0.00	-320.84			
C	298.150	15.742	189.080	0.072	0.00	0.00	0.000	0.000	12.011
CH4(g)	298.150	1.518	24.360	34.034	0.00	-31.47	0.000	-20.722	16.043
C2H4(g)	298.150	0.217	6.090	4.866	0.00	3.16	0.000	14.556	28.054
H2O	298.150	0.213	3.840	0.004	0.00	-16.92	0.000	-79.397	18.015
Fe2O3	298.150	0.006	1.030	0.000	0.00	-1.47	0.000	-228.611	159.692
TiO2	298.150	0.018	1.420	0.000	0.00	-4.66	0.000	-262.430	79.899
V2O5	298.150	0.000	0.019	0.000	0.00	-0.05	0.000	-430.833	181.880
CaO	298.150	0.008	0.450	0.000	0.00	-1.42	0.000	-176.367	56.079
Al2O3	298.150	0.230	23.480	0.006	0.00	-107.19	0.000	-465.470	101.961
Na2O	298.150	0.007	0.450	0.000	0.00	-0.84	0.000	-116.106	61.979
MgO	298.150	0.003	0.129	0.000	0.00	-0.53	0.000	-167.111	40.304
SiO2	298.150	0.616	36.990	0.014	0.00	-155.77	0.000	-253.016	60.084
SO3(g)	298.150	0.032	2.600	0.728	0.00	-3.57	0.000	-109.935	80.058
Cr2O3	298.150	0.000	0.052	0.000	0.00	-0.11	0.000	-315.195	151.990
Soda Ash	298.150	1.887	200.000	0.079	0.00	-592.71			
Na2CO3	298.150	1.887	200.000	0.079	0.00	-592.71	0.000	-314.102	105.989
OUTPUT SPECIES Formula	**Temperature (K)**	**Amount kmol**	**Amount kg**	**Amount Nm3**	**Latent H kWh**	**Total H kWh**	**Lat H**	**Tot H**	**MW**
Reduced sample	1223.000	14.487	1000.558	0.115	241.72	-1484.81			
Fe	1223.000	7.299	407.627	0.052	72.80	72.80	9.974	9.974	55.847
FeO	1223.000	0.811	58.267	0.010	11.76	-48.45	14.503	-59.738	71.846
Na2O*TiO2	1223.000	1.189	168.693	0.000	47.58	-464.89	40.019	-390.991	141.878
CaO*TiO2	1223.000	0.293	39.842	0.010	9.25	-125.93	31.553	-429.780	135.978
NaVO3	1223.000	0.033	4.024	0.000	1.35	-9.17	40.858	-277.934	121.929
NaAlSiO4	1223.000	1.441	204.700	0.000	60.35	-778.10	41.881	-539.969	142.054
Na2SiO3	1223.000	0.089	10.864	0.004	3.52	-35.08	39.568	-394.162	122.063
Mg2SiO4	1223.000	0.051	7.175	0.002	2.11	-28.73	41.457	-563.247	140.693
FeS	1223.000	0.000	0.000	0.000	0.00	0.00	16.904	-11.338	87.907
Na2Cr2O4	1223.000	0.001	0.214	0.000	0.05	-0.40	53.262	-401.549	213.969
C	1223.000	2.225	26.724	0.010	10.36	10.36	4.657	4.657	12.011
FeS	1223.000	0.231	20.307	0.004	3.90	-2.62	16.904	-11.338	87.907
MnS	1223.000	0.042	3.654	0.001	0.58	-1.92	13.725	-45.775	86.998
Na2O	1223.000	0.782	48.468	0.021	18.10	-72.70	23.146	-92.960	61.979
Off gas	998.150	21.041	496.002	479.959	125.66	-415.43			
CO(g)	998.150	17.276	483.900	393.735	103.80	-426.67	6.008	-24.698	28.010
CO2(g)	998.150	0.078	3.418	1.770	0.72	-7.77	9.252	-100.055	44.010
H2(g)	998.150	3.637	7.331	83.312	20.76	20.76	5.707	5.707	2.016
H2O(g)	998.150	0.028	0.508	0.632	0.20	-1.69	7.212	-59.962	18.015
H2S(g)	998.150	0.019	0.656	0.438	0.15	0.04	7.773	2.079	34.076
COS(g)	998.150	0.003	0.188	0.071	0.03	-0.09	9.956	-29.405	60.070
Balance	**Temperature (K)**	**Amount kmol**	**Amount kg**	**Amount Nm3**	**Latent H kWh**	**Total H kWh**			
IN1		29.193	1482.990	45.905	0.00	-2934.61			
OUT1		35.528	1496.560	480.074	367.38	-1900.24			
BALANCE		6.335	13.570	434.169	367.38	1034.37			

Table C.2 Mass and energy balance calculations for combustion of rotary kiln off-gas from of iron-rich tailings. Computed using HSC 5.1 software [35].

INPUT SPECIES Formula	**Temperature (K)**	**Amount kmol**	**Amount kg**	**Amount Nm3**	**Latent H kWh**	**Total H kWh**	**Latent H**	**Total H**	**MW**
Off gas	998.000	20.835	495.586	475.238	124.45	-416.63			
CO(g)	998.000	17.276	483.900	393.735	103.77	-426.69	6.007	-24.699	28.010
CO2(g)	998.000	0.078	3.418	1.770	0.72	-7.77	9.250	-100.057	44.010
H2(g)	998.000	3.431	6.916	78.591	19.58	19.58	5.706	5.706	2.016
H2O(g)	998.000	0.028	0.508	0.632	0.20	-1.69	7.211	-59.963	18.015
H2S(g)	998.000	0.019	0.656	0.438	0.15	0.04	7.772	2.077	34.076
COS(g)	998.000	0.003	0.188	0.071	0.03	-0.09	9.953	-29.408	60.070
Air	298.150	59.930	1720.283	1365.988	0.00	0.00			
N2(g)	298.150	49.529	1387.464	1128.937	0.00	0.00	0.000	0.000	28.013
O2(g)	298.150	10.401	332.820	237.051	0.00	0.00	0.000	0.000	31.999
OUTPUT SPECIES Formula	**Temperature (K)**	**Amount kmol**	**Amount kg**	**Amount Nm3**	**Latent H kWh**	**Total H kWh**	**Lat H**	**Tot H**	**MW**
Combusted off gas	998.000	70.369	2215.891	1602.605	480.37	-1653.75			
CO2(g)	998.000	17.359	763.970	395.634	160.57	-1736.90	9.250	-100.057	44.010
H2O(g)	998.000	3.459	62.316	77.531	24.94	-207.42	7.211	-59.963	18.015
N2(g)	998.000	49.529	1387.464	1128.937	294.38	294.38	5.944	5.944	28.013
SO3(g)	998.000	0.003	0.251	0.070	0.04	-0.30	13.205	-96.730	80.058
H2SO4(g)	998.000	0.019	1.890	0.432	0.43	-3.50	22.434	-181.769	98.073
Balance	**Temperature (K)**	**Amount kmol**	**Amount kg**	**Amount Nm3**	**Latent H kWh**	**Total H kWh**			
IN1		80.764	2215.869	1841.226	124.45	-416.63			
OUT1		70.369	2215.891	1602.605	480.37	-1653.75			
BALANCE		-10.395	0.022	-238.621	355.91	**-1237.11**			

Table C.3 Mass and energy balance calculations for indirect cooling of iron-rich tailings reduced sample. Computed using HSC 5.1 software [35].

INPUT SPECIES Formula	Temperature (K)	Amount kmol	Amount kg	Amount Nm3	Latent H kWh	Total H kWh	Latent H	Total H	MW
Reduced sample	**1223**	**14.49**	**1000.56**	**0.11**	**241.72**	**-1484.81**			
Fe	1223	7.30	407.63	0.05	72.80	72.80	9.97	9.97	55.85
FeO	1223	0.81	58.27	0.01	11.76	-48.45	14.50	-59.74	71.85
Na2O*TiO2	1223	1.19	168.69	0.00	47.58	-464.89	40.02	-390.99	141.88
CaO*TiO2	1223	0.29	39.84	0.01	9.25	-125.93	31.55	-429.78	135.98
NaVO3	1223	0.03	4.02	0.00	1.35	-9.17	40.86	-277.93	121.93
NaAlSiO4	1223	1.44	204.70	0.00	60.35	-778.10	41.88	-539.97	142.05
Na2SiO3	1223	0.09	10.86	0.00	3.52	-35.08	39.57	-394.16	122.06
Mg2SiO4	1223	0.05	7.18	0.00	2.11	-28.73	41.46	-563.25	140.69
FeS	1223	0.00	0.00	0.00	0.00	0.00	16.90	-11.34	87.91
Na2Cr2O4	1223	0.00	0.21	0.00	0.05	-0.40	53.26	-401.55	213.97
C	1223	2.23	26.72	0.01	10.36	10.36	4.66	4.66	12.01
FeS	1223	0.23	20.31	0.00	3.90	-2.62	16.90	-11.34	87.91
MnS	1223	0.04	3.65	0.00	0.58	-1.92	13.73	-45.77	87.00
Na2O	1223	0.78	48.47	0.02	18.10	-72.70	23.15	-92.96	61.98
Cooling water	**298.15**	**199.83**	**3600.00**	**3.93**	**0.00**	**-15866.05**			
H2O	298.15	199.83	3600.00	3.93	0.00	-15866.05	0.00	-79.40	18.02
OUTPUT SPECIES Formula	**Temperature (K)**	**Amount kmol**	**Amount kg**	**Amount Nm3**	**Latent H kWh**	**Total H kWh**	**Lat H**	**Tot H**	**MW**
Reduced sample	**353**	**14.49**	**1000.56**	**0.11**	**10.67**	**-1715.86**			
Fe	353	7.30	407.63	0.05	2.84	2.84	0.39	0.39	55.85
FeO	353	0.81	58.27	0.01	0.62	-59.59	0.77	-73.47	71.85
Na2O*TiO2	353	1.19	168.69	0.00	2.32	-510.15	1.95	-429.06	141.88
CaO*TiO2	353	0.29	39.84	0.01	0.45	-134.72	1.55	-459.78	135.98
NaVO3	353	0.03	4.02	0.00	0.05	-10.47	1.56	-317.23	121.93
NaAlSiO4	353	1.44	204.70	0.00	2.72	-835.73	1.89	-579.96	142.05
Na2SiO3	353	0.09	10.86	0.00	0.16	-38.44	1.78	-431.95	122.06
Mg2SiO4	353	0.05	7.18	0.00	0.10	-30.74	1.91	-602.80	140.69
FeS	353	0.00	0.00	0.00	0.00	0.00	0.88	-27.36	87.91
Na2Cr2O4	353	0.00	0.21	0.00	0.00	-0.45	2.78	-452.03	213.97
C	353	2.23	26.72	0.01	0.32	0.32	0.14	0.14	12.01
FeS	353	0.23	20.31	0.00	0.20	-6.32	0.88	-27.36	87.91
MnS	353	0.04	3.65	0.00	0.03	-2.47	0.76	-58.74	87.00
Na2O	353	0.78	48.47	0.02	0.85	-89.95	1.09	-115.02	61.98
Warm water	**353**	**199.83**	**3600.00**	**3.93**	**229.69**	**-15636.36**			
H2O	353	199.83	3600.00	3.93	229.69	-15636.36	1.15	-78.25	18.02
Balance	**Temperature (K)**	**Amount kmol**	**Amount kg**	**Amount Nm3**	**Latent H kWh**	**Total H kWh**			
IN1		214.32	4600.56	4.04	241.72	-17350.86			
OUT1		214.32	4600.56	4.04	240.36	-17352.22			
BALANCE		0.00	0.00	0.00	-1.36	-1.36			

Table C.4 Mass and energy balance calculations for magnetic separation and water leaching of iron-rich tailings reduced sample. Computed using HSC 5.1 software [35].

INPUT SPECIES Formula	**Temperature (K)**	**Amount kmol**	**Amount kg**	**Amount Nm3**	**Latent H kWh**	**Total H kWh**	**Latent H**	**Total H**	**MW**
Reduced sample	353	16.37	1023.18	0.12	10.94	-1715.59			
Fe	353	7.30	407.63	0.05	2.84	2.84	0.39	0.39	55.85
FeO	353	0.81	58.27	0.01	0.62	-59.59	0.77	-73.47	71.85
Na2O*TiO2	353	1.19	168.69	0.00	2.32	-510.15	1.95	-429.06	141.88
CaO*TiO2	353	0.29	39.84	0.01	0.45	-134.72	1.55	-459.78	135.98
NaVO3	353	0.03	4.02	0.00	0.05	-10.47	1.56	-317.23	121.93
NaAlSiO4	353	1.44	204.70	0.00	2.72	-835.73	1.89	-579.96	142.05
Na2SiO3	353	0.09	10.86	0.00	0.16	-38.44	1.78	-431.95	122.06
Mg2SiO4	353	0.05	7.18	0.00	0.10	-30.74	1.91	-602.80	140.69
FeS	353	0.00	0.00	0.00	0.00	0.00	0.88	-27.36	87.91
Na2Cr2O4	353	0.00	0.21	0.00	0.00	-0.45	2.78	-452.03	213.97
C	353	4.11	49.34	0.02	0.59	0.59	0.14	0.14	12.01
FeS	353	0.23	20.31	0.00	0.20	-6.32	0.88	-27.36	87.91
MnS	353	0.04	3.65	0.00	0.03	-2.47	0.76	-58.74	87.00
Na2O	353	0.78	48.47	0.02	0.85	-89.95	1.09	-115.02	61.98
Water	353	222.03	4000.00	4.36	255.21	-17373.73			
H2O	353	222.03	4000.00	4.36	255.21	-17373.73	1.15	-78.25	18.02
OUTPUT SPECIES Formula	**Temperature (K)**	**Amount kmol**	**Amount kg**	**Amount Nm3**	**Latent H kWh**	**Total H kWh**	**Latent H**	**Totat H**	**MW**
Magnetic fraction	353	9.63	553.25	0.08	4.54	-343.37			
Fe	353	7.30	407.63	0.05	2.84	2.84	0.39	0.39	55.85
FeO	353	0.69	49.21	0.01	0.53	-50.33	0.77	-73.47	71.85
Al2O3	353	0.07	7.55	0.00	0.09	-34.35	1.25	-464.22	101.96
Na2O*TiO2	353	0.20	27.95	0.00	0.38	-84.52	1.95	-429.06	141.88
V2O5	353	0.00	0.55	0.00	0.01	-1.29	2.04	-428.80	181.88
TiO2	353	0.32	25.73	0.01	0.28	-84.22	0.88	-261.55	79.90
MnS	353	0.01	0.61	0.00	0.01	-0.41	0.76	-58.74	87.00
Cr2O3	353	0.00	0.61	0.00	0.01	-1.25	1.83	-313.36	151.99
CaO*TiO2	353	0.06	8.16	0.00	0.09	-27.59	1.55	-459.78	135.98
C	353	0.78	9.34	0.00	0.11	0.11	0.14	0.14	12.01
MgTiO3	353	0.07	7.81	0.00	0.10	-28.30	1.47	-435.35	120.20
SiO2	353	0.14	8.11	0.00	0.10	-34.06	0.72	-252.29	60.08
Non magnetic fraction	353	4.50	191.79	0.12	2.48	-500.57			
Na2O*TiO2	353	0.56	79.95	0.00	1.10	-241.78	1.95	-429.06	141.88
CaO*TiO2	353	0.10	13.70	0.00	0.16	-46.32	1.55	-459.78	135.98
NaAlSiO4	353	0.20	28.41	0.00	0.38	-115.99	1.89	-579.96	142.05
Al2SiO5	353	0.07	11.80	0.00	0.15	-54.19	2.01	-744.37	162.05
Cr2O3	353	0.00	0.61	0.00	0.01	-1.27	1.83	-313.36	151.99
MgSiO3	353	0.05	5.39	0.00	0.08	-23.02	1.56	-428.57	100.39
V2O5	353	0.00	0.75	0.00	0.01	-1.76	2.04	-428.80	181.88
MnO	353	0.01	1.00	0.00	0.01	-1.50	0.68	-106.32	70.94
FeO	353	0.12	8.32	0.00	0.09	-8.51	0.77	-73.47	71.85
C	353	3.33	39.99	0.02	0.48	0.48	0.14	0.14	12.01
SO3(g)	353	0.00	0.37	0.10	0.00	-0.50	0.81	-109.13	80.06
MgO	353	0.04	1.50	0.00	0.02	-6.20	0.60	-166.51	40.30
Water leach solution	353	224.76	4275.98	4.43	257.95	-18314.11			
NaAlO2(ia)	353	0.07	6.01	0.00	0.00	-23.85	0.00	-325.34	81.97
Na2SiO3	353	0.02	1.94	0.00	0.03	-6.87	1.78	-431.95	122.06
NaVO3	353	0.02	2.20	0.00	0.03	-5.72	1.56	-317.23	121.93
Fe2O3	353	0.00	0.05	0.00	0.00	-0.07	1.67	-226.94	159.69
Na2O*TiO2	353	0.00	0.27	0.00	0.00	-0.82	1.95	-429.06	141.88
NaOH	353	0.67	26.64	0.01	0.62	-78.15	0.94	-117.34	40.00
H2O	353	221.75	3994.87	4.36	254.88	-17351.45	1.15	-78.25	18.02
Na2SiO3	353	1.10	134.76	0.05	1.97	-476.87	1.78	-431.95	122.06
NaAlO2(ia)	353	0.87	71.64	0.00	0.00	-284.35	0.00	-325.34	81.97
CaSO4	353	0.13	17.56	0.01	0.21	-51.31	1.60	-397.74	136.14
MnSO4	353	0.02	3.17	0.00	0.03	-6.18	1.62	-294.28	151.00
FeSO4	353	0.11	16.86	0.00	0.18	-28.46	1.61	-256.40	151.90
Balance	**Temperature (K)**	**Amount kmol**	**Amount kg**	**Amount Nm3**	**Latent H kWh**	**Total H kWh**			
IN1		238.40	5023.18	4.49	266.15	-19089.33			
OUT1		238.89	5021.03	4.64	264.98	-19158.05			
BALANCE		0.49	-2.15	0.15	-1.17	-68.72			

Table C.5 Mass and energy balance calculations for smelting of iron-rich tailings magnetic fraction. Computed using HSC 5.1 software [35].

INPUT SPECIES Formula	**Temperature (K)**	**Amount kmol**	**Amount kg**	**Amount Nm3**	**Latent H kWh**	**Total H kWh**	**Latent H**	**Total H**	**MW**
Magnetic fraction	**298.15**	**9.63**	**553.18**	**0.08**	**0.00**	**-347.55**			
Fe	298.15	7.30	407.63	0.05	0.00	0.00	0.00	0.00	55.85
FeO	298.15	0.69	49.24	0.01	0.00	-50.88	0.00	-74.24	71.85
Al2O3	298.15	0.07	7.50	0.00	0.00	-34.24	0.00	-465.47	101.96
Na2O*TiO2	298.15	0.20	27.90	0.00	0.00	-84.75	0.00	-431.01	141.88
V2O5	298.15	0.00	0.60	0.00	0.00	-1.42	0.00	-430.83	181.88
TiO2	298.15	0.32	25.72	0.01	0.00	-84.46	0.00	-262.43	79.90
MnS	298.15	0.01	0.60	0.00	0.00	-0.41	0.00	-59.50	87.00
Cr2O3	298.15	0.00	0.60	0.00	0.00	-1.24	0.00	-315.19	151.99
CaO*TiO2	298.15	0.06	8.16	0.00	0.00	-27.68	0.00	-461.33	135.98
C	298.15	0.78	9.34	0.00	0.00	0.00	0.00	0.00	12.01
MgTiO3	298.15	0.06	7.80	0.00	0.00	-28.35	0.00	-436.82	120.20
SiO2	298.15	0.13	8.10	0.00	0.00	-34.11	0.00	-253.02	60.08
Graphite	**298.15**	**0.53**	**6.40**	**0.00**	**0.00**	**0.00**			
C	298.15	0.53	6.40	0.00	0.00	0.00	0.00	0.00	12.01
OUTPUT SPECIES Formula	**Temperature (K)**	**Amount kmol**	**Amount kg**	**Amount Nm3**	**Latent H kWh**	**Total H kWh**	**Lat H**	**Tot H**	**MW**
Steel	**1723**	**7.06**	**450.16**	**0.05**	**122.98**	**126.21**			
Fe	1723	6.54	365.32	0.05	100.11	100.11	15.30	15.30	55.85
Fe3C	1723	0.46	83.30	0.00	22.15	25.39	47.75	54.72	179.55
V	1723	0.01	0.34	0.00	0.08	0.08	12.13	12.13	50.94
S	1723	0.01	0.20	0.00	0.08	0.08	13.41	13.41	32.06
Na	1723	0.04	1.00	0.00	0.55	0.55	12.75	12.75	22.99
Slag	**1723**	**1.03**	**90.83**	**0.03**	**37.90**	**-259.56**			
FeO	1723	0.05	3.66	0.00	1.53	-2.25	30.03	-44.21	71.85
Na2O*TiO2	1723	0.11	15.25	0.00	7.03	-39.31	65.36	-365.65	141.88
NaAlSiO4	1723	0.14	19.18	0.00	9.03	-69.52	66.90	-514.95	142.05
CaO*TiO2	1723	0.06	8.16	0.00	3.09	-24.59	51.42	-409.91	135.98
SO3(g)	1723	0.00	0.06	0.02	0.02	-0.06	29.34	-80.59	80.06
Cr2O3	1723	0.00	0.60	0.00	0.20	-1.05	49.93	-265.27	151.99
MnO	1723	0.01	0.49	0.00	0.15	-0.59	21.29	-85.72	70.94
C	**1723**	**0.18**	**2.16**	**0.00**	**1.43**	**1.43**	**7.96**	**7.96**	**12.01**
MgTiO3	1723	0.07	7.81	0.00	3.26	-25.13	50.20	-386.62	120.20
Al2O3	1723	0.01	0.61	0.00	0.29	-2.51	47.84	-417.63	101.96
TiO2	1723	0.41	32.84	0.01	11.88	-95.98	28.90	-233.53	79.90
Off gas	1469	0.67	18.65	15.18	6.98	-13.47			
CO(g)	1469	0.67	18.65	15.18	6.98	-13.47	10.49	-20.22	28.01
Balance	**Temperature (K)**	**Amount kmol**	**Amount kg**	**Amount Nm3**	**Latent H kWh**	**Total H kWh**			
IN1		10.16	559.58	0.08	0.00	-347.55			
OUT1		8.75	559.65	15.26	167.87	-146.82			
BALANCE		-1.41	0.07	15.18	167.87	200.73			

Table C.6 Mass and energy balance calculations for acid leaching of combined non-magnetic and smelting slag fractions from iron-rich tailings. Computed using HSC 5.1 software [35].

INPUT SPECIES Formula	Temperature (K)	Amount kmol	Amount kg	Amount Nm3	Latent H kWh	Total H kWh	Latent H	Total H	MW
Non magnetic fraction	**333**	**4.50**	**191.97**	**0.13**	**1.55**	**-502.04**			
Na2O*TiO2	333	0.56	80.02	0.00	0.69	-242.40	1.23	-429.78	141.88
CaO*TiO2	333	0.10	13.73	0.00	0.10	-46.50	0.97	-460.36	135.98
NaAlSiO4	333	0.20	28.41	0.00	0.23	-116.14	1.17	-580.68	142.05
Al2SiO5	333	0.07	11.83	0.00	0.09	-54.39	1.25	-745.13	162.05
Cr2O3	333	0.00	0.61	0.00	0.00	-1.26	1.18	-314.01	151.99
MgSiO3	333	0.05	5.42	0.00	0.05	-23.17	0.99	-429.15	100.39
V2O5	333	0.00	0.73	0.00	0.01	-1.72	1.28	-429.56	181.88
MnO	333	0.01	0.99	0.00	0.01	-1.49	0.43	-106.57	70.94
FeO	333	0.12	8.33	0.00	0.06	-8.56	0.49	-73.75	71.85
C	333	3.33	40.00	0.02	0.29	0.29	0.09	0.09	12.01
SO3(g)	333	0.01	0.40	0.11	0.00	-0.55	0.50	-109.43	80.06
MgO	333	0.04	1.49	0.00	0.01	-6.17	0.37	-166.74	40.30
Slag	**333**	**1.03**	**90.93**	**0.04**	**0.69**	**-297.04**			
FeO	333	0.05	3.66	0.00	0.02	-3.76	0.49	-73.75	71.85
Na2O*TiO2	333	0.11	15.32	0.00	0.13	-46.42	1.23	-429.78	141.88
NaAlSiO4	333	0.14	19.18	0.00	0.16	-78.39	1.17	-580.68	142.05
CaO*TiO2	333	0.06	8.16	0.00	0.06	-27.62	0.97	-460.36	135.98
SO3(g)	333	0.00	0.08	0.02	0.00	-0.11	0.50	-109.43	80.06
Cr2O3	333	0.00	0.61	0.00	0.00	-1.26	1.18	-314.01	151.99
MnO	333	0.01	0.50	0.00	0.00	-0.75	0.43	-106.57	70.94
C	333	0.18	2.16	0.00	0.02	0.02	0.09	0.09	12.01
MgTiO3	333	0.07	7.81	0.00	0.06	-28.33	0.92	-435.90	120.20
Al2O3	333	0.01	0.61	0.00	0.00	-2.79	0.78	-464.69	101.96
TiO2	333	0.41	32.84	0.01	0.23	-107.63	0.55	-261.88	79.90
Acid		**168.07**	**3150.93**	**3.35**	**0.00**	**-13569.69**			
H2O	298.15	166.53	3000.00	3.27	0.00	-13221.71	0.00	-79.40	18.02
H2SO4	298.15	1.54	150.93	0.08	0.00	-347.98	0.00	-226.11	98.07
OUTPUT SPECIES Formula	**Temperature (K)**	**Amount kmol**	**Amount kg**	**Amount Nm3**	**Latent H kWh**	**Total H kWh**	**Lat H**	**Tot H**	**MW**
Acid leach resdiue	**313**	**5.16**	**185.25**	**0.05**	**0.52**	**-458.12**			
FeO	313	0.12	8.39	0.00	0.02	-8.65	0.21	-74.04	71.85
TiO2	313	1.18	94.48	0.02	0.27	-310.04	0.23	-262.20	79.90
NaVO3	313	0.00	0.51	0.00	0.00	-1.33	0.41	-318.38	121.93
Na2Cr2O4	313	0.00	0.43	0.00	0.00	-0.91	0.74	-454.07	213.97
CaO*TiO2	313	0.13	17.17	0.00	0.05	-58.20	0.41	-460.92	135.98
MgSO4	313	0.05	5.78	0.00	0.02	-17.16	0.40	-357.60	120.36
NaMnO4	313	0.01	0.85	0.00	0.00	-2.80	0.00	-467.33	141.93
Na2SiO3	313	0.05	5.61	0.00	0.02	-19.93	0.47	-433.26	122.06
NaAlO2(ia)	313	0.12	9.67	0.00	0.00	-38.39	0.00	-325.34	81.97
C	313	3.51	42.16	0.02	0.13	0.13	0.04	0.04	12.01
MgO	313	0.01	0.20	0.00	0.00	-0.83	0.16	-166.96	40.30
Acid leach solution	**313**	**169.61**	**3248.79**	**3.38**	**52.96**	**-13927.40**			
FeSO4	313	0.05	7.60	0.00	0.02	-12.88	0.42	-257.59	151.90
Na2SO4	313	0.73	103.33	0.04	0.39	-280.08	0.53	-384.99	142.04
Al2(SO4)3	313	0.19	64.15	0.02	0.21	-179.00	1.10	-954.67	342.14
CaSO4	313	0.04	4.76	0.00	0.01	-13.96	0.42	-398.92	136.14
Cr2O3	313	0.01	0.91	0.00	0.00	-1.89	0.51	-314.68	151.99
MgSO4	313	0.10	12.40	0.00	0.04	-36.83	0.40	-357.60	120.36
MnSO4	313	0.02	2.26	0.00	0.01	-4.43	0.42	-295.48	151.00
SiO2	313	0.42	25.00	0.01	0.08	-105.18	0.19	-252.83	60.08
VOSO4	313	0.00	0.65	0.00	0.00	-1.45	0.55	-363.12	163.00
H2O	313	168.07	3027.72	3.30	52.20	-13291.69	0.31	-79.09	18.02
Balance	**Temperature (K)**	**Amount kmol**	**Amount kg**	**Amount Nm3**	**Latent H kWh**	**Total H kWh**			
IN1		173.60	3433.83	3.52	2.24	-14368.77			
OUT1		174.77	3434.04	3.43	53.48	-14385.53			
BALANCE		1.18	0.21	-0.09	51.24	-16.76			

Table C.7 Mass and energy balance calculations for carbon removal from acid leach residue from iron-rich tailings. Computed using HSC 5.1 software [35].

INPUT SPECIES Formula	Temperature (K)	Amount kmol	Amount kg	Amount Nm3	Latent H kWh	Total H kWh	Latent H	Total H	MW
Acid leach residue	**313**	**5.16**	**185.17**	**0.05**	**0.52**	**-457.84**			
FeO	313	0.12	8.41	0.00	0.02	-8.66	0.21	-74.04	71.85
TiO2	313	1.18	94.44	0.02	0.27	-309.92	0.23	-262.20	79.90
NaVO3	313	0.00	0.49	0.00	0.00	-1.27	0.41	-318.38	121.93
Na2Cr2O4	313	0.00	0.43	0.00	0.00	-0.91	0.74	-454.07	213.97
CaO*TiO2	313	0.13	17.13	0.00	0.05	-58.08	0.41	-460.92	135.98
MgSO4	313	0.05	5.78	0.00	0.02	-17.16	0.40	-357.60	120.36
NaMnO4	313	0.01	0.85	0.00	0.00	-2.80	0.00	-467.33	141.93
Na2SiO3	313	0.05	5.61	0.00	0.02	-19.93	0.47	-433.26	122.06
NaAlO2(ia)	313	0.12	9.67	0.00	0.00	-38.39	0.00	-325.34	81.97
C	313	3.51	42.16	0.02	0.13	0.13	0.04	0.04	12.01
MgO	313	0.01	0.20	0.00	0.00	-0.83	0.16	-166.96	40.30
Air	**298.15**	**10.11**	**290.27**	**230.49**	**0.00**	**0.00**			
O2(g)	298.15	1.76	56.16	40.00	0.00	0.00	0.00	0.00	32.00
N2(g)	298.15	8.36	234.11	190.49	0.00	0.00	0.00	0.00	28.01
OUTPUT SPECIES Formula	**Temperature (K)**	**Amount kmol**	**Amount kg**	**Amount Nm3**	**Latent H kWh**	**Total H kWh**	**Latent H**	**Total H**	**MW**
Acid leach residue	**1073.15**	**1.65**	**143.01**	**0.03**	**25.56**	**-432.80**			
FeO	1073.15	0.12	8.41	0.00	1.40	-7.28	11.98	-62.26	71.85
TiO2	1073.15	1.18	94.44	0.02	17.75	-292.44	15.02	-247.41	79.90
NaVO3	1073.15	0.00	0.49	0.00	0.14	-1.14	34.94	-283.86	121.93
Na2Cr2O4	1073.15	0.00	0.43	0.00	0.09	-0.82	44.01	-410.81	213.97
CaO*TiO2	1073.15	0.13	17.13	0.00	3.28	-54.85	26.05	-435.29	135.98
MgSO4	1073.15	0.05	5.78	0.00	1.36	-15.83	28.26	-329.74	120.36
NaMnO4	1073.15	0.01	0.85	0.00	0.00	-2.80	0.00	-467.33	141.93
Na2SiO3	1073.15	0.05	5.61	0.00	1.48	-18.47	32.26	-401.47	122.06
NaAlO2(ia)	1073.15	0.12	9.67	0.00	0.00	-38.39	0.00	-325.34	81.97
MgO	1073.15	0.01	0.20	0.00	0.05	-0.78	10.18	-156.93	40.30
Off gas	**850**	**11.87**	**332.43**	**270.49**	**54.95**	**-52.82**			
CO(g)	850	3.51	98.32	80.00	16.36	-91.42	4.66	-26.05	28.01
N2(g)	850	8.36	234.11	190.49	38.60	38.60	4.62	4.62	28.01
Balance	**Temperature (K)**	**Amount kmol**	**Amount kg**	**Amount Nm3**	**Latent H kWh**	**Total H kWh**			
IN1		15.28	475.44	230.54	0.52	-457.84			
OUT1		13.52	475.44	270.52	80.51	-485.62			
BALANCE		-1.76	0.00	39.98	79.99	-27.79			

Table C.8 Mass and energy balance calculations for sodium bisulphate roasting of iron-rich tailings acid leach residue (without carbon). Computed using HSC 5.1 software [35].

INPUT SPECIES Formula	**Temperature (K)**	**Amount kmol**	**Amount kg**	**Amount Nm3**	**Latent H kWh**	**Total H kWh**	**Latent H**	**Total H**	**MW**
Acid leach residue	**298**	**1.65**	**143.01**	**0.03**	**0.00**	**-458.36**			
FeO	298	0.12	8.41	0.00	0.00	-8.69	0.00	-74.24	71.85
TiO2	298	1.18	94.44	0.02	0.00	-310.19	0.00	-262.43	79.90
NaVO3	298	0.00	0.49	0.00	0.00	-1.28	0.00	-318.80	121.93
Na2Cr2O4	298	0.00	0.43	0.00	0.00	-0.91	-0.01	-454.82	213.97
CaO*TiO2	298	0.13	17.13	0.00	0.00	-58.13	0.00	-461.34	135.98
MgSO4	298	0.05	5.78	0.00	0.00	-17.18	0.00	-358.00	120.36
NaMnO4	298	0.01	0.85	0.00	0.00	-2.80	0.00	-467.33	141.93
Na2SiO3	298	0.05	5.61	0.00	0.00	-19.95	0.00	-433.73	122.06
NaAlO2(ia)	298	0.12	9.67	0.00	0.00	-38.39	0.00	-325.34	81.97
MgO	298	0.01	0.20	0.00	0.00	-0.84	0.00	-167.11	40.30
Sodium bisulphate roasting	**298**	**6.99**	**313.40**	**131.33**	**-0.01**	**-385.69**			
NaHSO4	298	1.23	148.00	0.00	0.00	-385.68	0.00	-312.86	120.06
O2(g)	298	1.00	32.00	22.79	0.00	0.00	0.00	0.00	32.00
N2(g)	298	4.76	133.40	108.54	-0.01	-0.01	0.00	0.00	28.01
OUTPUT SPECIES Formula	**Temperature (K)**	**Amount kmol**	**Amount kg**	**Amount Nm3**	**Latent H kWh**	**Total H kWh**	**Latent H**	**Total H**	**MW**
Roasted residue	**923**	**2.44**	**270.16**	**0.08**	**49.97**	**-737.64**			
Fe2O3	923	0.00	0.70	0.00	0.11	-0.90	24.24	-204.38	159.69
FeSO4	923	0.11	16.27	0.00	2.51	-25.13	23.42	-234.60	151.90
TiO2	923	1.31	104.56	0.02	15.58	-327.85	11.91	-250.52	79.90
CaSO4	923	0.12	16.28	0.01	2.71	-45.04	22.70	-376.64	136.14
Na2SO4	923	0.73	103.47	0.04	23.82	-257.04	32.69	-352.84	142.04
MgSO4	923	0.04	5.10	0.00	0.93	-14.24	21.93	-336.07	120.36
Al2(SO4)3	923	0.05	15.46	0.01	2.86	-40.34	63.17	-892.59	342.14
MnSO4	923	0.00	0.69	0.00	0.11	-1.25	23.30	-272.60	151.00
Cr2O3	923	0.00	0.10	0.00	0.01	-0.18	20.91	-294.28	151.99
V2O5	923	0.00	0.38	0.00	0.06	-0.84	27.54	-403.30	181.88
Al2O3	923	0.01	1.41	0.00	0.26	-6.17	19.03	-446.44	101.96
SiO2	923	0.05	2.76	0.00	0.51	-11.13	11.14	-241.87	60.08
Cr2(SO4)3	923	0.00	0.68	0.00	0.11	-1.29	64.91	-743.64	392.16
MgSO4	923	0.01	1.32	0.00	0.24	-3.70	21.93	-336.07	120.36
CaSO4	923	0.01	0.88	0.00	0.15	-2.43	22.70	-376.64	136.14
Na2SO4	923	0.00	0.00	0.00	0.00	0.00	32.69	-352.84	142.04
MnO	923	0.00	0.09	0.00	0.01	-0.12	8.66	-98.34	70.94
Off gas	**673**	**6.50**	**186.27**	**134.15**	**24.50**	**-37.64**			
SO3(g)	673	0.12	9.61	2.69	0.78	-12.42	6.47	-103.46	80.06
H2O	673	0.62	11.11	0.01	5.79	-43.16	9.39	-70.01	18.02
O2(g)	673	1.01	32.16	22.91	3.24	3.24	3.23	3.23	32.00
N2(g)	673	4.76	133.40	108.54	14.69	14.69	3.09	3.09	28.01
Balance	**Temperature (K)**	**Amount kmol**	**Amount kg**	**Amount Nm3**	**Latent H kWh**	**Total H kWh**			
IN1		8.65	456.41	131.36	-0.01	-844.05			
OUT1		8.95	456.42	134.23	74.48	-775.28			
BALANCE		0.30	0.02	2.87	74.49	68.77			

Table C.9 Mass and energy balance calculations for water leaching of iron-rich tailings roasted residue. Computed using HSC 5.1 software [35].

INPUT SPECIES Formula	**Temperature (K)**	**Amount kmol**	**Amount kg**	**Amount Nm3**	**Latent H kWh**	**Total H kWh**	**Latent H**	**Total H**	**MW**
Roasted residue	**923**	**2.44**	**270.27**	**0.08**	**50.00**	**-737.93**			
Fe2O3	923	0.00	0.64	0.00	0.10	-0.82	24.24	-204.38	159.69
FeSO4	923	0.11	16.25	0.00	2.51	-25.10	23.42	-234.60	151.90
TiO2	923	1.31	104.59	0.02	15.58	-327.94	11.91	-250.52	79.90
CaSO4	923	0.12	16.34	0.01	2.72	-45.20	22.70	-376.64	136.14
Na2SO4	923	0.73	103.55	0.04	23.83	-257.22	32.69	-352.84	142.04
MgSO4	923	0.04	5.06	0.00	0.92	-14.11	21.93	-336.07	120.36
Al2(SO4)3	923	0.05	15.40	0.01	2.84	-40.17	63.17	-892.59	342.14
MnSO4	923	0.01	0.75	0.00	0.12	-1.36	23.30	-272.60	151.00
Cr2O3	923	0.00	0.15	0.00	0.02	-0.29	20.91	-294.28	151.99
V2O5	923	0.00	0.36	0.00	0.06	-0.81	27.54	-403.30	181.88
Al2O3	923	0.01	1.43	0.00	0.27	-6.25	19.03	-446.44	101.96
SiO2	923	0.05	2.76	0.00	0.51	-11.13	11.14	-241.87	60.08
Cr2(SO4)3	923	0.00	0.78	0.00	0.13	-1.49	64.91	-743.64	392.16
MgSO4	923	0.01	1.32	0.00	0.24	-3.70	21.93	-336.07	120.36
CaSO4	923	0.01	0.82	0.00	0.14	-2.26	22.70	-376.64	136.14
Na2SO4	923	0.00	0.00	0.00	0.00	0.00	32.69	-352.84	142.04
MnO	923	0.00	0.07	0.00	0.01	-0.10	8.66	-98.34	70.94
Water	**298.15**	**55.51**	**1000.00**	**1.09**	**0.00**	**-4407.24**			
H2O	298.15	55.51	1000.00	1.09	0.00	-4407.24	0.00	-79.40	18.02
OUTPUT SPECIES Formula	**Temperature (K)**	**Amount kmol**	**Amount kg**	**Amount Nm3**	**Latent H kWh**	**Total H kWh**	**Lat H**	**Tot H**	**MW**
TiO2 residue	**353**	**1.15**	**94.56**	**0.02**	**1.06**	**-310.63**			
Fe2O3	353	0.01	0.80	0.00	0.01	-1.13	1.67	-226.94	159.69
TiO2	353	1.09	86.69	0.02	0.96	-283.78	0.88	-261.55	79.90
V2O5	353	0.00	0.36	0.00	0.00	-0.86	2.04	-428.80	181.88
SiO2	353	0.01	0.30	0.00	0.00	-1.26	0.72	-252.29	60.08
MnO	353	0.00	0.09	0.00	0.00	-0.13	0.68	-106.32	70.94
Cr2O3	353	0.00	0.15	0.00	0.00	-0.31	1.83	-313.36	151.99
CaSO4	353	0.01	0.82	0.00	0.01	-2.39	1.60	-397.74	136.14
MgO	353	0.00	0.16	0.00	0.00	-0.67	0.60	-166.51	40.30
MgSO4	353	0.01	0.72	0.00	0.01	-2.14	1.53	-356.47	120.36
NaAlSiO4	353	0.03	3.98	0.00	0.05	-16.24	1.89	-579.96	142.05
Na2SiO3	353	0.00	0.49	0.00	0.01	-1.73	1.78	-431.95	122.06
Water leach solution	**353**	**56.79**	**1176.41**	**1.15**	**66.11**	**-4819.63**			
FeSO4	353	0.11	16.27	0.00	0.17	-27.46	1.61	-256.40	151.90
CaSO4	353	0.12	16.28	0.01	0.19	-47.56	1.60	-397.74	136.14
Na2SO4	353	0.73	103.47	0.04	1.47	-279.39	2.02	-383.51	142.04
TiO2	353	0.22	17.88	0.00	0.20	-58.54	0.88	-261.55	79.90
Cr2(SO4)3	353	0.00	0.68	0.00	0.01	-1.40	4.55	-804.01	392.16
MnSO4	353	0.00	0.69	0.00	0.01	-1.35	1.62	-294.28	151.00
SiO2	353	0.01	0.57	0.00	0.01	-2.39	0.72	-252.29	60.08
MgSO4	353	0.04	5.10	0.00	0.06	-15.10	1.53	-356.47	120.36
Al2(SO4)3	353	0.05	15.46	0.01	0.19	-43.00	4.28	-951.49	342.14
H2O	353	55.51	1000.00	1.09	63.80	-4343.43	1.15	-78.25	18.02
Balance	**Temperature (K)**	**Amount kmol**	**Amount kg**	**Amount Nm3**	**Latent H kWh**	**Total H kWh**			
IN1		57.95	1270.27	1.17	50.00	-5145.17			
OUT1		57.94	1270.97	1.17	67.17	-5130.27			
BALANCE		-0.01	0.70	0.00	17.17	**14.90**			

Table C.10 Mass and energy balance calculations for alkali reduction of low-grade TiO_2 slag. Computed using HSC 5.1 software [35].

INPUT SPECIES Formula	**Temperature (K)**	**Amount kmol**	**Amount kg**	**Amount Nm3**	**Latent H kWh**	**Total H kWh**	**Latent H**	**Total H**	**MW**
Mineral	**298.15**	**15.07**	**1000.38**	**3.63**	**0.00**	**-3515.51**			
Fe2O3	298.15	0.21	33.82	0.01	0.00	-48.42	0.00	-228.61	159.69
TiO2	298.15	3.69	294.49	0.07	0.00	-967.25	0.00	-262.43	79.90
V2O5	298.15	0.04	7.70	0.00	0.00	-18.24	0.00	-430.83	181.88
CaO	298.15	2.78	155.66	0.05	0.00	-489.55	0.00	-176.37	56.08
Al2O3	298.15	1.25	127.22	0.03	0.00	-580.76	0.00	-465.47	101.96
Na2O	298.15	0.93	57.53	0.03	0.00	-107.78	0.00	-116.11	61.98
MgO	298.15	2.64	106.44	0.03	0.00	-441.33	0.00	-167.11	40.30
SiO2	298.15	3.29	197.91	0.08	0.00	-833.41	0.00	-253.02	60.08
SO3(g)	298.15	0.15	11.91	3.34	0.00	-16.36	0.00	-109.93	80.06
MnO	298.15	0.09	6.26	0.00	0.00	-9.44	0.00	-107.01	70.94
Cr2O3	298.15	0.01	1.44	0.00	0.00	-2.99	0.00	-315.19	151.99
Coal	**298.15**	**4.28**	**66.70**	**9.14**	**0.00**	**-73.80**			
C	298.15	3.62	43.49	0.02	0.00	0.00	0.00	0.00	12.01
CH4(g)	298.15	0.35	5.60	7.83	0.00	-7.24	0.00	-20.72	16.04
C2H4(g)	298.15	0.05	1.40	1.12	0.00	0.73	0.00	14.56	28.05
H2O	298.15	0.05	0.88	0.00	0.00	-3.89	0.00	-79.40	18.02
Fe2O3	298.15	0.00	0.24	0.00	0.00	-0.34	0.00	-228.61	159.69
TiO2	298.15	0.00	0.33	0.00	0.00	-1.07	0.00	-262.43	79.90
V2O5	298.15	0.00	0.00	0.00	0.00	-0.01	0.00	-430.83	181.88
CaO	298.15	0.00	0.10	0.00	0.00	-0.33	0.00	-176.37	56.08
Al2O3	298.15	0.05	5.40	0.00	0.00	-24.65	0.00	-465.47	101.96
Na2O	298.15	0.00	0.10	0.00	0.00	-0.20	0.00	-116.11	61.98
MgO	298.15	0.00	0.03	0.00	0.00	-0.12	0.00	-167.11	40.30
SiO2	298.15	0.14	8.51	0.00	0.00	-35.83	0.00	-253.02	60.08
SO3(g)	298.15	0.01	0.60	0.17	0.00	-0.82	0.00	-109.93	80.06
Cr2O3	298.15	0.00	0.01	0.00	0.00	-0.02	0.00	-315.19	151.99
Soda Ash	**298.15**	**4.25**	**450.00**	**0.18**	**0.00**	**-1333.59**			
Na2CO3	298.15	4.25	450.00	0.18	0.00	-1333.59	0.00	-314.10	105.99
OUTPUT SPECIES Formula	**Temperature (K)**	**Amount kmol**	**Amount kg**	**Amount Nm3**	**Latent H kWh**	**Total H kWh**	**Latent H**	**Total H**	**MW**
Reduced sample	**1323.15**	**11.20**	**1257.57**	**0.15**	**391.02**	**-3948.52**			
Fe	1323.15	0.43	23.85	0.00	4.67	4.67	10.94	10.94	55.85
CaO*TiO2	1323.15	2.46	334.51	0.08	86.95	-1047.93	35.34	-425.99	135.98
Na2O*TiO2	1323.15	1.23	174.51	0.00	55.21	-474.93	44.89	-386.12	141.88
NaVO3	1323.15	0.02	2.58	0.00	0.95	-5.80	44.81	-273.98	121.93
NaAlSiO4	1323.15	2.60	369.34	0.00	121.84	-1390.97	46.86	-534.99	142.05
MgO	1323.15	2.54	102.17	0.03	34.96	-388.67	13.79	-153.32	40.30
CaV2O6	1323.15	0.03	7.56	0.00	1.51	-19.03	47.48	-599.54	237.96
Ca3MgSi2O8	1323.15	0.11	34.51	0.00	8.30	-124.05	79.02	-1181.39	328.71
NaMnO4	1323.15	0.09	12.51	0.00	0.00	-41.21	0.00	-467.33	141.93
Na2Cr2O4	1323.15	0.01	2.03	0.00	0.56	-3.74	59.56	-395.25	213.97
Na2SO4	1323.15	0.15	21.16	0.01	9.33	-48.11	62.62	-322.91	142.04
*2Na2O*SiO2	1323.15	0.63	116.13	0.00	40.02	-329.23	63.42	-521.75	184.04
Na2O	1323.15	0.92	56.71	0.02	26.72	-79.52	29.20	-86.90	61.98
Off-gas	**1098.15**	**9.18**	**259.50**	**209.15**	**68.49**	**-299.65**			
CO(g)	1098.15	7.15	200.19	162.89	49.58	-169.87	6.94	-23.77	28.01
CO2(g)	1098.15	1.24	54.62	28.28	13.38	-122.27	10.78	-98.53	44.01
H2(g)	1098.15	0.60	1.20	13.63	3.90	3.90	6.56	6.56	2.02
H2O(g)	1098.15	0.19	3.49	4.35	1.63	-11.41	8.38	-58.79	18.02
Balance	**Temperature (K)**	**Amount kmol**	**Amount kg**	**Amount Nm3**	**Latent H kWh**	**Total H kWh**			
IN1		23.60	1517.08	12.94	0.00	-4922.90			
OUT1		20.38	1517.07	209.30	459.51	-4248.17			
BALANCE		-3.22	-0.01	196.36	459.51	674.73			

Table C.11 Mass and energy balance calculations for low-grade TiO_2 slag rotary kiln off-gas combustion. Computed using HSC 5.1 software [35].

INPUT SPECIES Formula	**Temperature (K)**	**Amount kmol**	**Amount kg**	**Amount Nm3**	**Latent H kWh**	**Total H kWh**	**Latent H**	**Total H**	**MW**
Off- gas	**1098.15**	**9.18**	**259.50**	**209.15**	**68.49**	**-299.65**			
CO(g)	1098.15	7.15	200.19	162.89	49.58	-169.87	6.94	-23.77	28.01
CO2(g)	1098.15	1.24	54.62	28.28	13.38	-122.27	10.78	-98.53	44.01
H2(g)	1098.15	0.60	1.20	13.63	3.90	3.90	6.56	6.56	2.02
H2O(g)	1098.15	0.19	3.49	4.35	1.63	-11.41	8.38	-58.79	18.02
Air	**298.15**	**19.36**	**557.63**	**441.16**	**0.00**	**0.00**			
N2(g)	298.15	15.48	433.76	352.94	0.00	0.00	0.00	0.00	28.01
O2(g)	298.15	3.87	123.87	88.22	0.00	0.00	0.00	0.00	32.00
OUTPUT SPECIES Formula	**Temperature (K)**	**Amount kmol**	**Amount kg**	**Amount Nm3**	**Latent H kWh**	**Total H kWh**	**Latent H**	**Total H**	**MW**
Combusted gas	**1098.15**	**24.66**	**817.13**	**561.79**	**203.25**	**-766.62**			
CO2(g)	1098.15	8.39	369.15	191.17	90.41	-826.46	10.78	-98.53	44.01
H2O(g)	1098.15	0.79	14.21	17.68	6.61	-46.39	8.38	-58.79	18.02
N2(g)	1098.15	15.48	433.76	352.94	106.23	106.23	6.86	6.86	28.01
Balance	**Temperature (K)**	**Amount kmol**	**Amount kg**	**Amount Nm3**	**Latent H kWh**	**Total H kWh**			
IN1		28.53	817.13	650.31	68.49	-299.65			
OUT1		24.66	817.13	561.79	203.25	-766.62			
BALANCE		-3.87	0.00	-88.52	134.76	-466.97			

Table C.12 Mass and energy balance calculations for indirect cooling of low-grade TiO_2 slag reduced sample. Computed using HSC 5.1 software [35].

INPUT SPECIES Formula	**Temperature (K)**	**Amount kmol**	**Amount kg**	**Amount Nm3**	**Latent H kWh**	**Total H kWh**	**Latent H**	**Total H**	**MW**
Reduced sample	**1323.00**	**11.20**	**1257.49**	**0.15**	**390.93**	**-3948.42**			
Fe	1323.00	0.43	23.85	0.00	4.67	4.67	10.94	10.94	55.85
CaO*TiO2	1323.00	2.46	334.51	0.08	86.93	-1047.95	35.34	-425.99	135.98
Na2O*TiO2	1323.00	1.23	174.51	0.00	55.20	-474.94	44.88	-386.13	141.88
NaVO3	1323.00	0.02	2.56	0.00	0.94	-5.75	44.81	-273.98	121.93
NaAlSiO4	1323.00	2.60	369.34	0.00	121.82	-1390.99	46.85	-535.00	142.05
MgO	1323.00	2.54	102.17	0.03	34.95	-388.68	13.79	-153.32	40.30
CaV2O6	1323.00	0.03	7.61	0.00	1.52	-19.19	47.48	-599.54	237.96
Ca3MgSi2O8	1323.00	0.11	34.51	0.00	8.30	-124.05	79.01	-1181.41	328.71
NaMnO4	1323.00	0.09	12.49	0.00	0.00	-41.13	0.00	-467.33	141.93
Na2Cr2O4	1323.00	0.01	1.93	0.00	0.54	-3.56	59.55	-395.26	213.97
Na2SO4	1323.00	0.15	21.16	0.01	9.33	-48.11	62.61	-322.92	142.04
*2Na2O*SiO2	1323.00	0.63	116.13	0.00	40.01	-329.23	63.41	-521.77	184.04
Na2O	1323.00	0.92	56.71	0.02	26.72	-79.52	29.20	-86.91	61.98
Cooling water		**319.17**	**5750.00**	**6.27**	**0.00**	**-25341.60**			
H2O	298.15	319.17	5750.00	6.27	0.00	-25341.60	0.00	-79.40	18.02
OUTPUT SPECIES Formula	**Temperature (K)**	**Amount kmol**	**Amount kg**	**Amount Nm3**	**Latent H kWh**	**Total H kWh**	**Latent H**	**Total H**	**MW**
Reduced sample	**353.00**	**11.20**	**1257.49**	**0.15**	**16.37**	**-4322.98**			
Fe	353.00	0.43	23.85	0.00	0.17	0.17	0.39	0.39	55.85
CaO*TiO2	353.00	2.46	334.51	0.08	3.81	-1131.07	1.55	-459.78	135.98
Na2O*TiO2	353.00	1.23	174.51	0.00	2.40	-527.74	1.95	-429.06	141.88
NaVO3	353.00	0.02	2.56	0.00	0.03	-6.66	1.56	-317.23	121.93
NaAlSiO4	353.00	2.60	369.34	0.00	4.91	-1507.90	1.89	-579.96	142.05
MgO	353.00	2.54	102.17	0.03	1.51	-422.11	0.60	-166.51	40.30
CaV2O6	353.00	0.03	7.61	0.00	0.08	-20.62	2.54	-644.48	237.96
Ca3MgSi2O8	353.00	0.11	34.51	0.00	0.34	-132.01	3.22	-1257.20	328.71
NaMnO4	353.00	0.09	12.49	0.00	0.00	-41.13	0.00	-467.33	141.93
Na2Cr2O4	353.00	0.01	1.93	0.00	0.03	-4.07	2.78	-452.03	213.97
Na2SO4	353.00	0.15	21.16	0.01	0.30	-57.14	2.02	-383.51	142.04
*2Na2O*SiO2	353.00	0.63	116.13	0.00	1.80	-367.45	2.85	-582.33	184.04
Na2O	353.00	0.92	56.71	0.02	0.99	-105.24	1.09	-115.02	61.98
Water	**353.00**	**319.17**	**5750.00**	**6.27**	**366.86**	**-24974.74**			
H2O	353.00	319.17	5750.00	6.27	366.86	-24974.74	1.15	-78.25	18.02
Balance	**Temperature (K)**	**Amount kmol**	**Amount kg**	**Amount Nm3**	**Latent H kWh**	**Total H kWh**			
IN1		330.38	7007.49	6.42	390.93	-29290.02			
OUT1		330.38	7007.49	6.42	383.23	-29297.72			
BALANCE		0.00	0.00	0.00	-7.70	-7.70			

Table C.13 Mass and energy balance calculations for water leaching of low-grade TiO_2 slag reduced sample. Computed using HSC 5.1 software [35].

INPUT SPECIES Formula	Temperature (K)	Amount kmol	Amount kg	Amount Nm3	Latent H kWh	Total H kWh	Latent H	Total H	MW
Reduced sample	**353.00**	**11.20**	**1257.57**	**0.15**	**16.37**	**-4323.17**			
Fe	353.00	0.43	23.85	0.00	0.17	0.17	0.39	0.39	55.85
CaO*TiO2	353.00	2.46	334.51	0.08	3.81	-1131.07	1.55	-459.78	135.98
Na2O*TiO2	353.00	1.23	174.51	0.00	2.40	-527.74	1.95	-429.06	141.88
NaVO3	353.00	0.02	2.58	0.00	0.03	-6.72	1.56	-317.23	121.93
NaAlSiO4	353.00	2.60	369.34	0.00	4.91	-1507.90	1.89	-579.96	142.05
MgO	353.00	2.54	102.17	0.03	1.51	-422.11	0.60	-166.51	40.30
CaV2O6	353.00	0.03	7.56	0.00	0.08	-20.46	2.54	-644.48	237.96
Ca3MgSi2O8	353.00	0.11	34.51	0.00	0.34	-132.01	3.22	-1257.20	328.71
NaMnO4	353.00	0.09	12.51	0.00	0.00	-41.21	0.00	-467.33	141.93
Na2Cr2O4	353.00	0.01	2.03	0.00	0.03	-4.28	2.78	-452.03	213.97
Na2SO4	353.00	0.15	21.16	0.01	0.30	-57.14	2.02	-383.51	142.04
*2Na2O*SiO2	353.00	0.63	116.13	0.00	1.80	-367.45	2.85	-582.33	184.04
Na2O	353.00	0.92	56.71	0.02	0.99	-105.24	1.09	-115.02	61.98
Soda Ash	**298.15**	**0.09**	**10.00**	**0.00**	**0.00**	**-29.64**			
Na2CO3	298.15	0.09	10.00	0.00	0.00	-29.64	0.00	-314.10	105.99
Water	**353.00**	**266.44**	**4800.00**	**5.23**	**306.25**	**-20848.48**			
H2O	353.00	266.44	4800.00	5.23	306.25	-20848.48	1.15	-78.25	18.02
OUTPUT SPECIES Formula	**Temperature (K)**	**Amount kmol**	**Amount kg**	**Amount Nm3**	**Latent H kWh**	**Total H kWh**	**Latent H**	**Total H**	**MW**
Water leach residue	**353.15**	**10.23**	**1164.28**	**0.13**	**15.01**	**-4060.22**			
CaO*TiO2	353.15	2.46	334.51	0.08	3.83	-1131.05	1.56	-459.78	135.98
Fe	353.15	0.43	23.85	0.00	0.17	0.17	0.39	0.39	55.85
Na2O*TiO2	353.15	1.17	166.00	0.00	2.29	-501.99	1.96	-429.05	141.88
NaAlSiO4	353.15	2.42	343.77	0.00	4.58	-1403.50	1.89	-579.96	142.05
MgO	353.15	2.51	100.96	0.03	1.50	-417.12	0.60	-166.51	40.30
CaV2O6	353.15	0.02	5.24	0.00	0.06	-14.18	2.55	-644.47	237.96
Ca3MgSi2O8	353.15	0.11	34.51	0.00	0.34	-132.00	3.23	-1257.19	328.71
NaMnO4	353.15	0.09	12.51	0.00	0.00	-41.21	0.00	-467.33	141.93
Na2Cr2O4	353.15	0.01	2.03	0.00	0.03	-4.28	2.79	-452.02	213.97
*2Na2O*SiO2	353.15	0.63	116.13	0.00	1.80	-367.45	2.85	-582.33	184.04
Na2O	353.15	0.38	23.68	0.01	0.42	-43.94	1.09	-115.02	61.98
CaCO3	353.15	0.01	1.10	0.00	0.01	-3.67	1.34	-333.82	100.09
Water leach solution	**353.15**	**267.52**	**4903.31**	**5.26**	**308.46**	**-21162.30**			
H2O	353.15	265.91	4790.37	5.22	306.47	-20805.80	1.15	-78.24	18.02
NaVO3	353.15	0.04	4.90	0.00	0.06	-12.74	1.57	-317.23	121.93
Na2O*TiO2	353.15	0.06	8.51	0.00	0.12	-25.74	1.96	-429.05	141.88
NaAlSiO4	353.15	0.18	25.57	0.00	0.34	-104.39	1.89	-579.96	142.05
MgO	353.15	0.03	1.21	0.00	0.02	-5.00	0.60	-166.51	40.30
Na2SO4	353.15	0.15	21.16	0.01	0.30	-57.14	2.02	-383.50	142.04
NaOH	353.15	1.07	42.80	0.02	1.01	-125.55	0.94	-117.34	40.00
Na2CO3	353.15	0.08	8.80	0.00	0.15	-25.93	1.75	-312.35	105.99
Balance	**Temperature (K)**	**Amount kmol**	**Amount kg**	**Amount Nm3**	**Latent H kWh**	**Total H kWh**			
IN1		277.74	6067.57	5.39	322.62	-25201.29			
OUT1		277.75	6067.60	5.38	323.48	-25222.52			
BALANCE		0.01	0.02	-0.01	0.86	-21.23			

Table C.14 Mass and energy balance calculations for evaporation and concentration of water leach solution from low-grade TiO_2 slag processing. Computed using HSC 5.1 software [35].

INPUT SPECIES Formula	**Temperature (K)**	**Amount kmol**	**Amount kg**	**Amount Nm3**	**Latent H kWh**	**Total H kWh**	**Latent H**	**Total H**	**MW**
Water leach solution	**353.15**	**267.52**	**4903.31**	**5.26**	**308.66**	**-21140.12**			
H2O	353.15	266.44	4800.00	5.23	307.09	-20847.64	1.15	-78.24	18.02
NaVO3	353.15	0.04	4.90	0.00	0.06	-12.74	1.57	-317.23	121.93
Na2O*TiO2	353.15	0.06	8.51	0.00	0.12	-25.74	1.96	-429.05	141.88
NaAlSiO4	353.15	0.18	25.57	0.00	0.34	-104.39	1.89	-579.96	142.05
MgO	353.15	0.03	1.21	0.00	0.02	-4.99	0.60	-166.51	40.30
Na2SO4	353.15	0.15	21.16	0.01	0.30	-57.14	2.02	-383.50	142.04
Na2O	353.15	0.54	33.16	0.01	0.58	-61.53	1.09	-115.02	61.98
Na2CO3	353.15	0.08	8.80	0.00	0.15	-25.93	1.75	-312.35	105.99
Off-gas	**1098.15**	**24.66**	**817.13**	**561.79**	**203.25**	**-766.62**			
CO2(g)	1098.15	8.39	369.15	191.17	90.41	-826.46	10.78	-98.53	44.01
H2O(g)	1098.15	0.79	14.21	17.68	6.61	-46.39	8.38	-58.79	18.02
N2(g)	1098.15	15.48	433.76	352.94	106.23	106.23	6.86	6.86	28.01
OUTPUT SPECIES Formula	**Temperature (K)**	**Amount kmol**	**Amount kg**	**Amount Nm3**	**Latent H kWh**	**Total H kWh**	**Latent H**	**Total H**	**MW**
Concentrated solution	**373.15**	**89.47**	**2000.25**	**1.62**	**129.20**	**-8004.70**			
H2O	373.15	81.25	1463.70	1.60	127.86	-6323.00	1.57	-77.82	18.02
NaVO3	373.15	0.04	4.88	0.00	0.09	-12.67	2.17	-316.63	121.93
Na2O*TiO2	373.15	0.06	8.51	0.00	0.16	-25.70	2.68	-428.33	141.88
Al2O3	373.15	0.03	2.85	0.00	0.05	-12.98	1.75	-463.72	101.96
SiO2	373.15	0.18	10.82	0.00	0.18	-45.36	1.01	-252.01	60.08
MgO	373.15	0.03	1.21	0.00	0.02	-4.99	0.83	-166.28	40.30
Na2SO4	373.15	0.15	21.16	0.01	0.42	-57.03	2.79	-382.73	142.04
Na2O	373.15	0.00	0.00	0.00	0.00	0.00	1.50	-114.61	61.98
Na2CO3	373.15	0.17	18.34	0.01	0.42	-53.92	2.41	-311.69	105.99
H2CO3(a)	373.15	7.56	468.78	0.00	0.00	-1469.05	0.00	-194.37	62.03
Off-gas	**373.15**	**194.12**	**3657.16**	**4356.79**	**135.18**	**-11872.82**			
H2O(g)	373.15	178.43	3214.40	3999.19	125.61	-11860.04	0.70	-66.47	18.02
CO2(g)	373.15	0.20	9.00	4.66	0.17	-22.19	0.81	-108.50	44.01
N2(g)	373.15	15.48	433.76	352.94	9.40	9.40	0.61	0.61	28.01
Precipitated solids	**373.15**	**0.60**	**63.03**	**0.02**	**1.40**	**-195.50**			
Al2O3	373.15	0.06	6.32	0.00	0.11	-28.75	1.75	-463.72	101.96
Na2CO3	373.15	0.54	56.70	0.02	1.29	-166.75	2.41	-311.69	105.99
Balance	**Temperature (K)**	**Amount kmol**	**Amount kg**	**Amount Nm3**	**Latent H kWh**	**Total H kWh**			
IN1		292.18	5720.44	567.05	511.90	-21906.74			
OUT1		284.18	5720.44	4358.43	265.78	-20073.02			
BALANCE		-8.00	0.00	3791.38	-246.12	1833.72			

Table C.15 Mass and energy balance calculations for condensation of evaporated water. Computed using HSC 5.1 software [35].

INPUT SPECIES Formula	**Temperature (K)**	**Amount kmol**	**Amount kg**	**Amount Nm3**	**Latent H kWh**	**Total H kWh**	**Latent H**	**Total H**	**MW**
H2O(g)	373.15	178.43	3214.40	3999.19	125.61	-11860.04	0.70	-66.47	18.02
OUTPUT SPECIES Formula	**Temperature (K)**	**Amount kmol**	**Amount kg**	**Amount Nm3**	**Latent H kWh**	**Total H kWh**	**Latent H**	**Total H**	**MW**
H2O	368.15	178.43	3214.40	3.51	261.98	-13904.64	1.47	-77.93	18.02
Balance	**Temperature (K)**	**Amount kmol**	**Amount kg**	**Amount Nm3**	**Latent H kWh**	**Total H kWh**			
IN1		178.43	3214.40	3999.19	125.61	-11860.04			
OUT1		178.43	3214.40	3.51	261.98	-13904.64			
BALANCE		0.00	0.00	-3995.69	136.37	-2044.60			

Table C.16 Mass and energy balance calculations for ammonium metavanadate precipitation from low-grade TiO_2 slag processing. Computed using HSC 5.1 software [35].

INPUT SPECIES Formula	**Temperature (K)**	**Amount kmol**	**Amount kg**	**Amount Nm3**	**Latent H kWh**	**Total H kWh**	**Latent H**	**Total H**	**MW**
Concentrated solution pH 8	**373**	**94.83**	**2000.15**	**1.77**	**140.81**	**-8166.12**			
H2O	373	88.81	1599.84	1.74	139.48	-6911.39	1.57	-77.83	18.02
NaVO3	373	0.04	4.90	0.00	0.09	-12.72	2.16	-316.63	121.93
Na2O*TiO2	373	0.06	8.51	0.00	0.16	-25.70	2.68	-428.33	141.88
Al2O3	373	0.03	2.85	0.00	0.05	-12.98	1.75	-463.72	101.96
SiO2	373	0.18	10.82	0.00	0.18	-45.36	1.01	-252.01	60.08
MgO	373	0.03	1.21	0.00	0.02	-4.99	0.83	-166.29	40.30
Na2SO4	373	0.15	21.16	0.01	0.42	-57.03	2.79	-382.74	142.04
Na2CO3	373	0.17	18.34	0.01	0.42	-53.92	2.41	-311.69	105.99
H2CO3(a)	373	5.36	332.52	0.00	0.00	-1042.02	0.00	-194.37	62.03
Additives	**298.15**	**0.38**	**44.40**	**0.02**	**0.00**	**-106.96**			
H2SO4	298.15	0.19	18.40	0.01	0.00	-42.42	0.00	-226.11	98.07
(NH4)2SO4	298.15	0.20	26.00	0.01	0.00	-64.54	0.00	-328.01	132.13
OUTPUT SPECIES Formula	**Temperature (K)**	**Amount kmol**	**Amount kg**	**Amount Nm3**	**Latent H kWh**	**Total H kWh**	**Latent H**	**Total H**	**MW**
Concentrated solution pH 5	**298.15**	**95.25**	**2029.70**	**1.79**	**0.00**	**-8386.64**			
H2O	298.15	89.09	1605.04	1.75	0.00	-7073.79	0.00	-79.40	18.02
Na2O*TiO2	298.15	0.06	8.51	0.00	0.00	-25.86	0.00	-431.01	141.88
Al2O3	298.15	0.03	2.85	0.00	0.00	-13.03	0.00	-465.47	101.96
SiO2	298.15	0.18	10.82	0.00	0.00	-45.54	0.00	-253.02	60.08
MgO	298.15	0.03	1.21	0.00	0.00	-5.01	0.00	-167.11	40.30
Na2SO4	298.15	0.32	44.88	0.02	0.00	-121.83	0.00	-385.53	142.04
Na2CO3	298.15	0.01	0.64	0.00	0.00	-1.88	0.00	-314.10	105.99
H2CO3(a)	298.15	5.36	332.52	0.00	0.00	-1042.02	0.00	-194.37	62.03
(NH4)2SO4	298.15	0.18	23.23	0.01	0.00	-57.68	0.00	-328.01	132.13
AMV precipitate	**298.15**	**0.04**	**4.90**	**0.00**	**0.00**	**-12.25**			
NH4VO3	298.15	0.04	4.90	0.00	0.00	-12.25	0.00	-292.50	116.98
Off-gas	**298.15**	**0.17**	**7.35**	**3.81**	**0.00**	**-18.25**			
CO2(g)	298.15	0.17	7.35	3.81	0.00	-18.25	0.00	-109.31	44.01
Balance	**Temperature (K)**	**Amount kmol**	**Amount kg**	**Amount Nm3**	**Latent H kWh**	**Total H kWh**			
IN1		95.21	2044.55	1.79	140.81	-8273.08			
OUT1		95.46	2041.95	5.59	0.00	-8417.15			
BALANCE		0.25	-2.60	3.80	-140.81	-144.06			

Table C.17 Mass and energy balance calculations for AMV de-ammoniation from low-grade TiO_2 slag. Computed using HSC 5.1 software [35].

INPUT SPECIES Formula	Temperature (K)	Amount kmol	Amount kg	Amount Nm3	Latent H kWh	Total H kWh	Latent H	Total H	MW
AMV precipitate	**298.15**	**0.05**	**5.19**	**0.00**	**0.00**	**-12.87**			
NH4VO3	298.15	0.04	4.91	0.00	0.00	-12.28	0.00	-292.50	116.98
Na2O	298.15	0.00	0.25	0.00	0.00	-0.47	0.00	-116.11	61.98
SiO2	298.15	0.00	0.01	0.00	0.00	-0.04	0.00	-253.02	60.08
Al2O3	298.15	0.00	0.01	0.00	0.00	-0.03	0.00	-465.47	101.96
Na2SO4	298.15	0.00	0.02	0.00	0.00	-0.04	0.00	-385.53	142.04
OUTPUT SPECIES Formula	**Temperature (K)**	**Amount kmol**	**Amount kg**	**Amount Nm3**	**Latent H kWh**	**Total H kWh**	**Latent H**	**Total H**	**MW**
Vanadium oxide solids	**723.15**	**0.03**	**4.38**	**0.00**	**0.45**	**-9.85**			
V2O5	723.15	0.02	4.10	0.00	0.40	-9.31	17.90	-412.93	181.88
Na2O	723.15	0.00	0.25	0.00	0.04	-0.43	9.56	-106.55	61.98
SiO2	723.15	0.00	0.01	0.00	0.00	-0.04	6.99	-246.02	60.08
Al2O3	723.15	0.00	0.01	0.00	0.00	-0.03	12.33	-453.14	101.96
CaO	723.15	0.00	0.00	0.00	0.00	0.00	5.71	-170.66	56.08
Na2SO4	723.15	0.00	0.02	0.00	0.00	-0.04	22.14	-363.38	142.04
Off gas	**723.15**	**0.05**	**0.81**	**1.09**	**0.24**	**-0.37**			
NH3(g)	723.15	0.05	0.81	1.09	0.24	-0.37	5.01	-7.75	17.03
Balance	**Temperature (K)**	**Amount kmol**	**Amount kg**	**Amount Nm3**	**Latent H kWh**	**Total H kWh**			
IN1		0.05	5.19	0.00	0.00	-12.87			
OUT1		0.07	5.19	1.09	0.69	-10.22			
BALANCE		0.03	0.00	1.09	0.69	2.65			

Table C.18 Mass and energy balance calculations for acid leaching of low-grade TiO_2 slag water leach residue. Computed using HSC 5.1 software [35].

INPUT SPECIES Formula	Temperature (K)	Amount kmol	Amount kg	Amount Nm3	Latent H kWh	Total H kWh	Latent H	Total H	MW
Water leach residue	**333.15**	**10.23**	**1164.28**	**0.13**	**9.42**	**-4065.82**			
CaO*TiO2	333.15	2.46	334.51	0.08	2.40	-1132.48	0.98	-460.36	135.98
Fe	333.15	0.43	23.85	0.00	0.10	0.10	0.25	0.25	55.85
Na2O*TiO2	333.15	1.17	166.00	0.00	1.45	-502.84	1.24	-429.77	141.88
NaAlSiO4	333.15	2.42	343.77	0.00	2.85	-1405.23	1.18	-580.67	142.05
MgO	333.15	2.51	100.96	0.03	0.94	-417.68	0.37	-166.74	40.30
CaV2O6	333.15	0.02	5.24	0.00	0.04	-14.20	1.62	-645.40	237.96
Ca3MgSi2O8	333.15	0.11	34.51	0.00	0.21	-132.13	2.02	-1258.40	328.71
NaMnO4	333.15	0.09	12.51	0.00	0.00	-41.21	0.00	-467.33	141.93
Na2Cr2O4	333.15	0.01	2.03	0.00	0.02	-4.29	1.76	-453.05	213.97
*2Na2O*SiO2	333.15	0.63	116.13	0.00	1.14	-368.11	1.81	-583.37	184.04
Na2O	333.15	0.38	23.68	0.01	0.26	-44.09	0.69	-115.42	61.98
CaCO3	333.15	0.01	1.10	0.00	0.01	-3.68	0.84	-334.33	100.09
Hydrochloric acid	**298.15**	**24.63**	**643.00**	**0.60**	**0.00**	**-1599.26**			
H2O	298.15	13.82	249.00	0.27	0.00	-1097.40	0.00	-79.40	18.02
HCl(ia)	298.15	10.81	394.00	0.33	0.00	-501.86	0.00	-46.44	36.46
Water	**298.15**	**408.43**	**7358.00**	**8.02**	**60.61**	**-32367.82**			
H2O	353	52.73	950.00	1.04	60.61	-4126.26	1.15	-78.25	18.02
H2O	298.15	355.70	6408.00	6.99	0.00	-28241.56	0.00	-79.40	18.02
Air	**298.15**	**0.05**	**1.55**	**1.23**	**0.00**	**0.00**			
O2(g)	298.15	0.01	0.34	0.25	0.00	0.00	0.00	0.00	32.00
N2(g)	298.15	0.04	1.20	0.98	0.00	0.00	0.00	0.00	28.01
OUTPUT SPECIES Formula	**Temperature (K)**	**Amount kmol**	**Amount kg**	**Amount Nm3**	**Latent H kWh**	**Total H kWh**	**Latent H**	**Total H**	**MW**
Acid leach residue	**313.15**	**7.30**	**687.90**	**0.18**	**2.18**	**-2328.41**			
CaO*TiO2	313.15	2.46	334.51	0.08	1.02	-1133.86	0.41	-460.92	135.98
TiO2	313.15	1.17	93.48	0.02	0.27	-306.77	0.23	-262.20	79.90
CaV2O6	313.15	0.02	5.24	0.00	0.02	-14.22	0.69	-646.32	237.96
Fe	313.15	0.19	10.72	0.00	0.02	0.02	0.10	0.10	55.85
Na2O	313.15	1.00	61.82	0.03	0.29	-115.53	0.29	-115.82	61.98
Cr2O3	313.15	0.01	1.37	0.00	0.00	-2.83	0.52	-314.68	151.99
MnO	313.15	0.02	1.56	0.00	0.00	-2.35	0.18	-106.82	70.94
Ca3MgSi2O8	313.15	0.11	34.51	0.00	0.09	-132.26	0.85	-1259.57	328.71
Al2O3	313.15	0.36	37.01	0.01	0.12	-168.85	0.33	-465.14	101.96
MgO	313.15	0.50	19.95	0.01	0.08	-82.64	0.16	-166.95	40.30
SiO2	313.15	1.46	87.72	0.03	0.28	-369.13	0.19	-252.83	60.08
Acid leach solution	**313.15**	**438.58**	**8477.25**	**8.72**	**136.75**	**-35712.26**			
H2O	313.15	427.66	7704.40	8.40	134.17	-33820.92	0.31	-79.08	18.02
FeCl2	313.15	0.23	29.66	0.01	0.08	-22.11	0.32	-94.48	126.75
MgCl2	313.15	2.01	191.37	0.08	0.60	-359.13	0.30	-178.67	95.21
NaCl	313.15	6.16	360.01	0.17	1.30	-702.17	0.21	-113.99	58.44
VOCl	313.15	0.00	0.20	0.00	0.00	-0.33	0.26	-167.10	102.39
CaCl2	313.15	0.01	1.22	0.00	0.00	-2.43	0.30	-220.64	110.99
MnCl2	313.15	0.07	8.43	0.00	0.02	-8.94	0.31	-133.39	125.84
SiO2	313.15	1.59	95.59	0.04	0.30	-402.25	0.19	-252.83	60.08
Al2O3	313.15	0.85	86.36	0.02	0.28	-393.98	0.33	-465.14	101.96
Off-gas	**313.15**	**0.05**	**1.69**	**1.23**	**0.01**	**-1.20**			
CO2(g)	313.15	0.01	0.48	0.25	0.00	-1.20	0.16	-109.15	44.01
N2(g)	313.15	0.04	1.20	0.98	0.01	0.01	0.12	0.12	28.01
Balance	**Temperature (K)**	**Amount kmol**	**Amount kg**	**Amount Nm3**	**Latent H kWh**	**Total H kWh**			
IN1		443.34	9166.83	9.98	70.03	-38032.90			
OUT1		445.93	9166.84	10.14	138.94	-38041.86			
BALANCE		2.59	0.01	0.16	68.92	-8.96			

Table C.19 Mass and energy balance calculations for TiO_2 recovery from low-grade TiO_2 slag acid leach residue. Computed using HSC 5.1 software [35].

INPUT SPECIES Formula	Temperature (K)	Amount kmol	Amount kg	Amount Nm3	Latent H kWh	Total H kWh	Latent H	Total H	MW
Acid leach residue	**298.15**	**7.24**	**684.35**	**0.18**	**0.00**	**-2326.24**			
CaO*TiO2	298.15	2.46	334.51	0.08	0.00	-1134.88	0.00	-461.33	135.98
TiO2	298.15	1.17	93.48	0.02	0.00	-307.04	0.00	-262.43	79.90
CaV2O6	298.15	0.02	5.24	0.00	0.00	-14.23	0.00	-647.02	237.96
Fe	298.15	0.17	9.49	0.00	0.00	0.00	0.00	0.00	55.85
Na2O	298.15	0.96	59.50	0.03	0.00	-111.46	0.00	-116.11	61.98
Cr2O3	298.15	0.01	1.37	0.00	0.00	-2.84	0.00	-315.19	151.99
MnO	298.15	0.02	1.56	0.00	0.00	-2.35	0.00	-107.01	70.94
Ca3MgSi2O8	298.15	0.11	34.51	0.00	0.00	-132.34	0.00	-1260.42	328.71
Al2O3	298.15	0.36	37.01	0.01	0.00	-168.97	0.00	-465.47	101.96
MgO	298.15	0.50	19.95	0.01	0.00	-82.72	0.00	-167.11	40.30
SiO2	298.15	1.46	87.72	0.03	0.00	-369.40	0.00	-253.02	60.08
Sulphuric acid	**298.15**	**8.35**	**752.00**	**0.42**	**0.00**	**-1765.34**			
H2SO4	298.15	7.51	736.96	0.40	0.00	-1699.06	0.00	-226.11	98.07
H2O	298.15	0.83	15.04	0.02	0.00	-66.28	0.00	-79.40	18.02
Air	298.15	0.36	10.51	8.31	0.00	0.00			
O2(g)	298.15	0.07	2.33	1.66	0.00	0.00	0.00	0.00	32.00
N2(g)	298.15	0.29	8.17	6.65	0.00	0.00	0.00	0.00	28.01
Hydrolysis water	**298.15**	**277.54**	**5000.00**	**5.45**	**0.00**	**-22036.18**			
H2O	298.15	277.54	5000.00	5.45	0.00	-22036.18	0.00	-79.40	18.02
OUTPUT SPECIES Formula	**Temperature (K)**	**Amount kmol**	**Amount kg**	**Amount Nm3**	**Latent H kWh**	**Total H kWh**	**Latent H**	**Total H**	**MW**
Acid bake residue	**1173.15**	**287.81**	**6142.10**	**5.82**	**453.72**	**-25077.26**			
TiO2	1173.15	2.38	190.53	0.05	40.82	-584.98	17.12	-245.31	79.90
TiO2	353.00	1.25	100.00	0.02	1.10	-327.35	0.88	-261.55	79.90
CaSO4	353.00	2.80	380.78	0.13	4.47	-1112.48	1.60	-397.74	136.14
VOSO4	353.00	0.04	7.17	0.00	0.09	-15.91	2.05	-361.61	163.00
FeSO4	353.00	0.17	25.82	0.01	0.27	-43.59	1.61	-256.40	151.90
MgSO4	353.00	0.60	72.22	0.03	0.92	-213.88	1.53	-356.47	120.36
MnSO4	353.00	0.02	3.32	0.00	0.04	-6.47	1.62	-294.28	151.00
SiO2	353.00	1.67	100.34	0.04	1.21	-421.33	0.72	-252.29	60.08
Na2SO4	1173.15	0.96	136.36	0.05	51.96	-318.15	54.12	-331.41	142.04
Al2(SO4)3	1173.15	0.36	124.20	0.05	33.57	-313.38	92.47	-863.30	342.14
H2O	353.00	277.54	5000.00	5.45	319.01	-21717.17	1.15	-78.25	18.02
Cr2O3	1173.15	0.01	1.37	0.00	0.27	-2.57	29.78	-285.42	151.99
Off gas	**473.15**	**10.47**	**305.25**	**234.84**	**19.35**	**-742.88**			
H2O(g)	473.15	8.35	150.41	187.13	13.87	-546.96	1.66	-65.51	18.02
SO3(g)	473.15	1.21	96.67	27.06	3.34	-129.40	2.76	-107.17	80.06
N2(g)	473.15	0.29	8.17	6.65	0.41	0.41	1.42	1.42	28.01
H2O(g)	473.15	0.00	0.00	0.00	0.00	0.00	1.66	-65.51	18.02
SO3(g)	473.15	0.62	50.00	14.00	1.73	-66.93	2.76	-107.17	80.06
Balance	**Temperature (K)**	**Amount kmol**	**Amount kg**	**Amount Nm3**	**Latent H kWh**	**Total H kWh**			
IN1		293.49	6446.85	14.36	0.00	-26127.76			
OUT1		298.29	6447.35	240.66	473.07	-25820.14			
BALANCE		4.79	0.50	226.30	473.07	307.62			